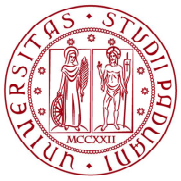

UNIVERSITÀ
DEGLI STUDI
DI PADOVA

Università degli Studi di Padova

Dipartimento di Scienze Biomediche

CORSO DI DOTTORATO DI RICERCA IN SCIENZE BIOMEDICHE
31° CICLO

MECHANISMS UNDERLYING THE INCREASED SUSCEPTIBILITY TO CORTICAL SPREADING DEPRESSION IN A MOUSE MODEL OF FAMILIAL HEMIPLEGIC MIGRAINE TYPE 2

Coordinatore: Ch.mo Prof. Paolo Bernardi
Supervisore: Ch.mo Prof. Pietrobon Daniela

Dottorando: Crivellaro Giovanna

CONTENTS

RIASSUNTO

L'emicrania è un disturbo neurologico episodico, altamente invalidante che colpisce più del 12% della popolazione mondiale e che si manifesta con attacchi ricorrenti di mal di testa pulsante ed unilaterale con determinate caratteristiche associate. In un terzo dei pazienti il mal di testa è preceduto da disturbi sensoriali transitori la cosiddetta "aura emicranica". Il meccanismo neurofisiologico alla base dell'aura emicranica è la *cortical spreading depression* (CSD), un'onda di forte depolarizzazione cellulare che propaga lentamente ed ha un ruolo chiave nella patogenesi dell'emicrania grazie alla sua capacità di attivare il sistema trigeminovascolare (Pietrobon and Moskowitz, 2013). I meccanismi alla base dell'emicrania e dell'aumentata suscettibilità del cervello umano alla CSD sono tutt'ora in gran parte sconosciuti.

L'emicrania emiplegica familiare di tipo 2 (FHM2) è rara forma monogenica di emicrania con aura, causata da una mutazione missenso associata a perdita di funzione del gene *ATP1A2*, codificante per la subunità α_2 della Na^+, K^+ ATPase (α_2 NKA). La α_2 NKA è espressa quasi esclusivamente negli astrociti nel cervello adulto dove si trova colocalizzata con vari trasportatori ionici, compresi i trasportatori del glutammato (GluTs) (Cholet *et al*., 2002). Nel cervello dei topi eterozigoti in cui è stata inserita la mutazione umana W887R che causa l'FHM2 (FHM2 KI), i livelli di espressione della proteina α_2 NKA sono dimezzati rispetto ai topi con genotipo wild-type (WT). Studi *in vivo* hanno dimostrato che nei topi FHM2 KI la soglia per l'innesco della CSD è minore e la velocità di propagazaione della CSD è maggiore rispetto ai topi WT (Leo *et al*., 2011).

Lo scopo del mio progetto di ricerca durante il dottorato è stato quello di studiare i meccanismi tutt'ora sconosciuti alla base della facilitazione della CSD in un modello animale di FHM2.

Ho contribuito a verificare l'ipotesi che la rimozione del glutammato (Glu) fosse compromessa nei topi FHM2 KI, che questo portasse ad un'aumentata neurotrasmissione glutammatergica e quindi alla facilitazione della CSD nel modello murino di FHM2. Precedentemente in laboratorio è stato dimostrato che il tempo di decadimento della corrente attivata sinapticamente mediata dai

trasportatori del glutammato (STC), il quale fornisce una misura relativa della velocità di rimozione del Glu nella fessura sinaptica da parte degli astrociti, è più lento nei topi FHM2 KI rispetto ai WT. E' anche stato dimostrato che il rallentamento della rimozione del Glu è più lento in seguito ad un treno di impulsi rispetto che ad impulso singolo. Inoltre, grazie ad una collaborazione con il Prof. Fiorenzo Conti (Univ. di Ancona), è stato dimostrato che la densità dei trasportatori gliali del glutammato 1a (GLT-1a) è ridotta del 48% nei processi astrocitari che circondano le sinapsi eccitatorie dei topi FHM2 KI rispetto ai WT. Tale riduzione riflette la riduzione dell'espressione della α_2 NKA causata dalla mutazione, suggerendo uno specifico accoppiamento strutturale e funzionale tra α_2 NKA e GLT-1a.

Ho contribuito inoltre a condurre degli esperimenti con lo scopo di testare se fosse possibile riprodurre *in vitro* i risultati ottenuti *in vivo* relativamente alla facilitazione della CSD nei topi FHM2 KI. A tale scopo abbiamo indotto sperimentalmente la CSD in fettine di cervello mediante l'applicazione di brevi pulsi di durata crescente di una soluzione ad alta concentrazione di KCl. In questo modo abbiamo verificato che, anche *in vitro*, la CSD risultasse facilitata nei topi FHM2 KI in quanto la soglia per la sua induzione era minore e la velocità con cui si propagava maggiore rispetto ai topi WT.

Alla luce di questi risultati ho studiato se vi fosse una relazione causa-effetto tra la ridotta velocità di rimozione del Glu da parte degli astrociti corticali e la facilitazione della CSD nei topi FHM2 KI, attraverso due differenti approcci.

Con il primo approccio ho verificato se il trattamento farmacologico dei topi FHM2 KI con il Ceftriaxone (Cef), un farmaco che aumenta l'espressione in membrana dei GLT-1 nella neocorteccia dei topi WT, potesse ripristinare soglia e velocità di propagazione della CSD. Il trattamento farmacologico dei topi FHM2 KI con Cef è risultato in un leggero ma significativo aumento della soglia per l'innesco della CSD senza influenze però sulla velocità di propagazione. Questa piccola efficacia del trattamento farmacologico con Cef nel ripristinare soglia e velocità di propagazione della CSD potrebbe essere spiegata dal fatto che, sorprendentemente, il medesimo trattamento, nei topi FHM2 KI, non aumenta la densità dei GLT-1a nei

processi astrocitari perisinaptici (PAPs), bensì la aumenta nei terminali assonici (AxTs).

Con il secondo approccio ho testato se la riduzione farmacologica della velocità di rimozione del Glu nei topi WT, in misura simile ai topi FHM2 KI, abbassasse la soglia per l'innesco della CSD e ne aumentasse la velocità di propagazione in modo simile alla mutazione. Come prima cosa ho identificato la concentrazione di un inibitore dei GluTs, il DL-TBOA (TBOA), in grado di rallentare la velocità di ricaptazione del Glu nei WT in modo simile ai topi FHM2 KI. Ho successivamente confrontato la soglia di innesco e la velocità di propagazione della CSD in fettina di cervello di topo in assenza ed in presenza della concentrazione di inibitore sopra identificata. Ho trovato che la concentrazione di TBOA in grado di rallentare la rimozione del Glu nei topi WT similmente agli FHM2 KI, riduce la soglia di attivazione della CSD in modo simile alla mutazione e ne aumenta la velocità di propagazione in modo simile, ma quantitativamente inferiore, rispetto alla mutazione FHM2. Questi dati supportano la conclusione che la ridotta velocità di rimozione del Glu rende conto della maggior parte della facilitazione dell'induzione della CSD e di una larga parte della facilitazione della propagazione della CSD nei topi FHM2 KI.

Grazie ad una collaborazione con il Dr. Mirko Santello (Univ. di Zurigo) la velocità di rimozione del Glu è stata ulteriormente studiata utilizzando un sensore fluorescente geneticamente codificato per il glutammato (iGluSnFr). Sia topi WT che FHM2 KI sono stati iniettati con un virus adeno-associato con il promotore GFAP per far esprimere selettivamente il sensore nella membrana degli astrociti corticali. Le cinetiche di decadimento dei transienti di Glu evocati da stimolazione extracellulare nello strato 1 della corteccia somatosensoriale sono risultate più lente nei topi FHM2 KI rispetto ai WT, supportando ulteriormente la conclusione che la velocità di rimozione del Glu durante l'attività neuronale è compromessa nei topi FHM2 KI.

I meccanismi alla base dell'innesco della CSD sperimentale sono tutt'ora controversi sebbene ci siano evidenze farmacologiche che supportano un ruolo chiave dei recettori *N*-methyl-D-aspartate (NMDARs) (Pietrobon and Moskowitz, 2014). I dati ottenuti nei topi FHM1 KI (Tottene *et al*., 2009) sono coerenti con un

modello di inizio della CSD in cui il rilascio di Glu mediato dai canali $Ca_v2.1$ e l'attivazione dei recettori NMDA hanno un ruolo chiave nel ciclo a feedback positivo di innesco della CSD.

Per studiare le conseguenze della ridotta velocità di rimozione del Glu sulla neurotrasmissione sinaptica eccitatoria ed in particolare sull'attivazione dei recettori NMDA, ho misurato la corrente postsinaptica eccitatoria mediata dai recettori NMDA (NMDARs-EPSC) nelle cellule piramidali dello strato 2/3, evocata da stimolazione extracellulare nello strato 1 della corteccia somatosensoriale dei topi FHM2 KI e WT. Ho condotto degli esperimenti preliminari per verificare se la concentrazione di TBOA in grado di rallentare la velocità di rimozione del Glu nei topi WT in modo simile ai topi FHM2 KI (1.5 μM), aumentasse l'attivazione dei recettori NMDA. Ho trovato che 1.5 μM TBOA aumenta effettivamente l'attivazione dei recettori NMDA come si evince sia dall'aumento dell'ampiezza che dal rallentamento delle cinetiche di decadimento dell'NMDARs-EPSC nelle cellule piramidali, nei topi WT.

Ho registrato pertanto l'NMDARs-EPSC sia in topi WT che FHM2 KI ed ho trovato che, in seguito ad un singolo stimolo, l'ampiezza della corrente è maggiore e le cinetiche di decadimento più lente, nel topo FHM2 KI rispetto al topo WT. Come risultato dell'aumento dell'ampiezza e del rallentamento delle cinetiche di decadimento, anche la carica totale mediata dai recettori NMDA, misurata come area sottesa alla curva, è maggiore nei topi FHM2 KI rispetto ai WT. Come precedentemente dimostrato per la rimozione del Glu, anche l'aumentata attivazione dei recettori NMDA nei topi FHM2 KI sembra essere dipendente dall'attività, infatti è maggiore in seguito a treni di impulsi ad alta frequenza rispetto a stimolazione singola. Complessivamente questi dati dimostrano che c'è un'aumentata attivazione dei recettori NMDA negli FHM2 KI rispetto ai topi WT. Inoltre, il confronto con l'STC ed i transienti di Glu supportano la conclusione che l'aumentata attivazione dei recettori NMDA riflette la ridotta velocità di rimozione del Glu da parte degli astrociti durante l'attività neuronale alle sinapsi corticali eccitatorie, suggerendo che l'aumento dell'attivazione degli NMDARs sia probabilmente una conseguenza dello spillover del Glu.

Alla luce di questi risultati, ho studiato il profilo farmacologico dei recettori NMDA attivati come conseguenza della ridotta velocità di rimozione del Glu nei topi FHM2 KI. I recettori glutammatergici NMDA sono canali ionotropici attivati da ligando che si assemblano come eterotetrameri. Gli NMDARs si possono trovare come di dieteromeri, composti da due subunità recettoriali GluN2A (GluN2AR) o due subunità GluN2B (GluN2BR), oppure come trieteromeri, composti da una subunità GluN2A ed una subunità GluN2B (GluN2A-2BR), assieme a due subunità costitutive GluN1. Le due subunità GluN2 conferiscono al recettore proprietà elettriche, biochimiche e farmacologiche caratteristiche (Paoletti *et al*., 2013). I dieteromeri GluN2BRs hanno una maggiore affinità per il Glu rispetto sia ai dieteromeri GluN2ARs che ai trieteromeri GluN2A-2BRs, quindi potrebbero essere preferenzialmente attivati dallo spillover del Glu. Ho perciò studiato il contributo di questi recettori nell'NMDARs-EPSC in fettine di cervello di topi WT e FHM2 KI utilizzando Ro25-6981, un inibitore selettivo della subunità GluN2B dei recettori NMDA. Ho trovato che 1 μM, la concentrazione di Ro25-6981 che inibisce selettivamente i dieteromeri GluN2BRs, inibisce solo una piccola frazione dell'NMDARs-EPSC nei topi WT, con un effetto trascurabile sulle cinetiche di decadimento. Utilizzando una concentrazione di Ro25-6981 più alta, 20 μM, che dovrebbe inibire anche i trieteromeri GluN2A-2BRs, sebbene non completamente, senza comunque inibire i dieteromeri GluN2ARs (Fischer *et al*., 1997; Hansen *et al*., 2014; Volianskis *et al*., 2013; Stroebel *et al*., 2018), ho trovato che gran parte dell'NMDARs-EPSC viene inibita nei topi WT. Questi dati dimostrano che la maggior parte dell'NMDARs-EPSC nei topi WT è mediata dall'attivazione di recettori trieteromerici GluN2A-2B e solo una piccola parte è mediata dall'attivazione dei recettori dieteromerici GluN2B e (forse) GluN2A. Nei topi FHM2 KI, l'inibizione dell'ampiezza dell'NMDARs-EPSC dovuta a 1 μM Ro25-6981 è maggiore rispetto ai WT e le cinetiche di decadimento della corrente dopo l'applicazione dell'inibitore sono più veloci, indicando che nei topi FHM2 KI una frazione maggiore dell'NMDARs-EPSC è mediata dall'attivazione dei recettori dieteromerici GluN2B rispetto ai topi WT. Questi dati sono coerenti con un reclutamento preferenziale dei GluN2BRs da parte dall'aumentato spillover del Glu, nei topi FHM2 KI.

I dati ottenuti nel modello murino di FHM2 e quelli precedentemente ottenuti nel modello di FHM1 supportano l'idea che un'eccessiva neurotrasmissione glutammatergica ed un'eccessiva attivazione dei recettori NMDA esercitino un ruolo cruciale nella facilitazione della CSD indotta sperimentalmente in entrambi i modelli di FHM.

Precedenti studi nei topi FHM1 hanno rivelato che la neurotrasmissione inibitoria risultava inalterata a numerose sinapsi inibitorie corticali, contrariamente, la neurotrasmissione eccitatoria risultava aumentata alle sinapsi delle cellule piramidali corticali (Tottene *et al*., 2009 e dati non pubblicati ottenuti in laboratorio). Questo effetto differenziale della mutazione FHM1 alle sinapsi eccitatorie ed inibitorie ci ha portato a formulare l'ipotesi di lavoro che un'alterato bilanciamento tra eccitazione ed inibizione (E/I) in specifici circuiti corticali possa essere uno dei meccanismi patogenetici chiave nell'FHM.

Per testare questa ipotesi abbiamo deciso di studiare se e come le mutazioni FHM alterino la regolazione del bilanciamento E/I durante attività ricorrente di network indotta dall'attivazione di cellule corticali piramidali attraverso stimolazione optogenetica con vari tipi di stimoli luminosi, che presumibilmente mimano differenti tipi di attività fisiologiche.

L'elettroporazione *in utero* al 15 giorno e mezzo di gestazione permette di esprimere selettivamente la channelrhodopsin-2 (ChR2) nelle cellule piramidali dello strato 2/3 della corteccia (Szczurkowska *et al*., 2016). Ho contribuito ad implementare questa tecnica e ad ottimizzare il protocollo descritto in Szczurkowska *et al*., 2016. In particolare, ho ottimizzato le strategie di accoppiamento per ottenere un maggior numero di femmine gravide da elettroporare, ho ottimizzato la concentrazione ed il volume di cDNA e di Fast Green FCF da iniettare al fine di aumentare la sopravvivenza dei cuccioli.

Dopo aver ottenuto una buona e selettiva espressione della ChR2 è possibile registrare correnti eccitatorie ed inibitorie evocate da stimoli luminosi in cellule piramidali dello strato 2/3 della corteccia somatosensoriale che non esprimono channelrhodopsin-2 (ChR2-). Abbiamo condotto esperimenti preliminari registrando Pyrs ChR2- dello strato 2/3 e misurato correnti eccitatorie ed inibitorie evocate da stimoli luminosi clampando il voltaggio dei singoli neuroni a +10 e -68

mV, i potenziali di reversione (E_{rev}) del potenziale post-sinaptico eccitatorio (EPSP) ed inibitorio (IPSP), rispettivamente. Per mimare l'attività sensoriale che avviene in condizioni fisiologiche dopo uno stimolo sensoriale sono stati usati brevi stimoli singoli di luce blu lunghi 2 ms ad intensità crescenti, con lo scopo di attivare un numero crescente di cellule piramidali ChR2+ e caratterizzare così il reclutamento crescente di eccitazione ed inibizione nel network attivo ricorrente (Shao *et al*., 2013). La quantità di corrente è stata misurata integrando i primi 50 ms della risposta ed utilizzata per calcolare la E/(E+I) ratio. In un esperimento preliminare abbiamo trovato che, all'aumentare dell'intensità della luce, la E/(E+I) ratio diminuiva nelle cellule piramidali ChR2- (eccetto vicino all'intensità di luce soglia per evocare l'EPSC), riflettendo un reclutamento preferenziale dell'inibizione sull'eccitazione all'aumentare dell'attivazione del network.

SUMMARY

Migraine is a common disabling episodic neurological disorder affecting more than 12% of the world population that manifests as recurrent attacks of typically throbbing and unilateral headache with certain associated features. In a third of patients headache is preceded by transient sensory disturbances (migraine aura) whose neurophysiological correlate is cortical spreading depression (CSD), a slowly propagating wave of strong depolarization of brain cells (Pietrobon and Moskowitz, 2013). Given the ability to activate trigeminal nociception and trigger the headache mechanisms, CSD is considered to play a key role in migraine pathogenesis. The mechanisms underlying the onset of migraine attacks and the susceptibility to CSD in the human brain are still largely unknown.

Familial Hemiplegic Migraine type 2 (FHM2) is a rare monogenic form of migraine with aura, caused by loss-of-function missense mutations in *ATP1A2*, the gene encoding for the α_2 subunit of the Na^+, K^+ ATPase (α_2 NKA), which is expressed almost exclusively in astrocytes in the adult brain, where it is colocalized with various ion transporters, including the glutamate transporters (GluTs) (Cholet *et al*., 2002). In the brain of heterozygous knockin (KI) mice carrying the W887R FHM2 mutation, the α_2 NKA protein is halved compared to WT. *In vivo* studies in these mice demonstrated that the threshold for CSD induction is lower and the velocity of CSD propagation is higher than in wild type (WT) mice (Leo *et al*., 2011).

The aim of my PhD research project was to investigate the unknown mechanisms leading to facilitation of CSD in the FHM2 mouse model.

I contributed to test the working hypothesis that glutamate (Glu) clearance is impaired in FHM2 KI mice and this leads to enhanced glutamatergic transmission and hence to facilitation of CSD induction and propagation. Previous experiments in my lab demonstrated that the time course of the synaptically activated glutamate transporter current (STC), which reflects the rate of Glu clearance from the extracellular space, is slower in FHM2 KI compared to WT mice and that the slowing is activity-dependent. Moreover in collaboration with Fiorenzo Conti (Univ. of Ancona), it was shown that the density of GLT-1a in the astrocytic

processes surrounding glutamatergic synapses is 48% reduced in FHM2 KI mice compared to WT, a reduction that mirrors the reduction of α_2 NKA caused by the mutation, thus suggesting a specific tight coupling between α_2 NKA and GLT-1a.

I contributed to perform *in vitro* experiments to test whether I could reproduce the *in vivo* findings that CSD induction and propagation are facilitated in FHM2 KI. We induced experimental CSD in acute cortical slices, by application of brief pressure-ejection pulses of high KCl of increasing duration. We found that, *in vitro*, experimental CSD was facilitated since the threshold for CSD induction was lower and the velocity of CSD propagation was higher in FHM2 KI compared to WT mice.

In light of these results I investigated whether there was a causative link between the reduced rate of Glu clearance by cortical astrocytes and CSD facilitation in FHM2 KI mice, using two different approaches.

In the first approach I investigated whether treatment of FHM2 KI mice with Ceftriaxone (Cef), a drug that increases the membrane expression of GLT-1 in neocortex of WT mice, rescues CSD facilitation. I found that Cef-treatment increased slightly, but significantly, CSD threshold in FHM2 KI mice without affecting CSD propagation velocity. This small efficacy of Cef-treatment in the rescue of CSD facilitation could be explained by the striking finding that Cef-treatment did not increase the density of GLT-1a in perisynaptic astrocytic processes (PAPs) in FHM2 KI mice (in contrast with the 50% increase in WT mice), but it increased it in the axon terminals (AxTs).

In the second approach I investigated whether pharmacological reduction of the rate of Glu clearance in WT mice to a value similar to that of FHM2 KI mice, lowered the threshold for CSD induction and increased the velocity of CSD propagation to values similar to those observed in FHM2 KI mice. I first identified the concentration of TBOA, a Glu transporters inhibitor, able to produce a slowing of the rate of Glu clearance in WT similar to that in FHM2 KI mice. I then compared CSD induction and velocity in WT slices perfused with or without TBOA and I found that the threshold for CSD induction was reduced to a value similar to that in FHM2 KI mice and also that the velocity of CSD propagation was increased but less than in the FHM2 mutants. These data support the conclusion

that the reduced rate of Glu clearance can account for most of the facilitation of CSD induction and for a large fraction of the facilitation of CSD propagation in the FHM2 mice.

Glu clearance in FHM2-KI mice has been further investigated using the genetically encoded fluorescent glutamate sensor iGluSnFr, thanks to a collaboration with Dr. Mirko Santello (Univ. of Zurich). WT and FHM2-KI mice were injected with adeno-associated virus under the GFAP promoter to drive the expression of iGluSnFr selectively in the membrane of cortical astrocytes. The decay kinetics of the Glu transients elicited in L1 by extracellular stimulation, were slower in FHM2-KI compared to WT mice, and this provided additional support to the conclusion that Glu clearance during neuronal activity is impaired in FHM2 KI mice.

The mechanisms underlying ignition of experimental CSD are still controversial but there is pharmacological support for a key role of *N*-methyl-D-aspartate receptors (NMDARs) (Pietrobon and Moskowitz, 2014). Data obtained in FHM1 KI mice (Tottene *et al*., 2009) are consistent with a model of CSD ignition in which $Ca_v2.1$ dependent Glu release and activation of NMDARs play crucial roles in the positive feedback cycle that ignites CSD.

To investigate the consequences of the reduced rate of Glu clearance on excitatory synaptic transmission and in particular the activation of NMDARs, I measured the NMDARs-mediated excitatory postsynaptic current (NMDARs-EPSC) in L2/3 pyramidal cells (Pyrs) elicited by extracellular stimulation in L1 of the barrel cortex in acute cortical slices from WT and FHM2 KI mice. In preliminary experiments I verified that 1.5 μM TBOA (the concentration that slows the rate of Glu clearance in WT mice to a similar extent as the FHM2 KI mice) did increase NMDARs activation, as shown by both an increased amplitude and a slowing of the decay kinetics of NMDARs-EPSC in WT Pyrs. I then recorded NMDARs-EPSC in both WT and FHM2 mice and I found that after a single stimulus both the amplitude and the half time of decay of NMDARs-EPSC were larger in FHM2 KI compared to WT mice and, as a result, the total charge carried by NMDARs was increased. As shown for the Glu clearance, the increased activation of NMDARs in FHM2 KI mice appears activity-dependent since it is

larger after high frequency train than after a single stimulus. Taken together these data demonstrate that there is an increased activation of the NMDARs in FHM2 KI compared to WT mice. Moreover the comparison with the STC and Glu transients supports the conclusion that the increased NMDARs activation reflects the reduced rate of Glu clearance by astrocytes at cortical excitatory synapses during neuronal activity, suggesting that the increased NMDARs activation is presumably a consequence of increased Glu spillover.

I then investigated the pharmacological profile of the NMDARs activated as a consequence of the reduced rate of Glu clearance in FHM2 KI mice. NMDARs are ligand-gated ionotropic Glu receptors that assemble as heterotetramers and can exist as diheteromers with either two GluN2A subunits (GluN2AR) or two GluN2B subunits (GluN2BR) and as triheteromers, with one GluN2A and one GluN2B subunit (GluN2A-2BR) besides two mandatory GluN1 subunits. The different GluN2 subunits impart distinct electrical, biochemical and pharmacological properties to the ion channel (Paoletti *et al*., 2013). Interestingly GluN2BRs have a higher affinity for Glu than both GluN2ARs and GluN2A-2BRs and thus should be preferentially activated by Glu spillover. I therefore investigated the contribution of these receptors to the NMDARs-EPSC in WT and FHM2 KI acute cortical brain slices, using Ro25-6981, a GluN2B-selective NMDARs-antagonist. Using 1 µM Ro25-6981, a concentration that specifically inhibits the diheteromers GluN2BRs, I found that, only a very small fraction of the NMDARs-EPSC, was inhibited in WT mice, with negligible effects on its kinetics. Using, 20 µM Ro25-6981, that also inhibits the triheteromers GluN2A-2BRs, although not completely, without affecting the GluN2ARs (Fischer *et al*., 1997; Hansen *et al*., 2014; Volianskis *et al*., 2013; Stroebel *et al*., 2018), I found that a large fraction of the WT NMDARs-EPSC was inhibited. These data show that the large majority of the NMDARs-EPSC in WT mice is due to activation of triheteromers GluN2A-2BRs, with only a very small fraction due to activation of diheteromers GluN2BRs and (perhaps) GluN2ARs.

In FHM2 KI mice, the inhibition of the NMDARs-EPSC by 1 µM Ro25-6981 was significantly larger than in WT mice, and the decay of the remaining NMDARs current was faster, indicating that a larger fraction of the NMDARs-EPSC is due to

activation of GluN2BRs in FHM2 compared to WT mice. This is consistent with preferential recruitment of GluN2BRs by increased Glu spillover in FHM2 KI mice.

Taken together the findings in the FHM2 mouse model with previous findings in the FHM1 model (Tottene e*t al*., 2009) support the idea that excessive glutamatergic transmission and excessive activation of NMDARs play a crucial role in the facilitation of experimental CSD in the FHM mouse models.

Previous findings from the lab in FHM1 KI mice demonstrated an unaltered inhibitory transmission at several cortical inhibitory synapses, in contrast with increased excitatory neurotransmission at cortical Pyrs synapses (Tottene *et al*., 2009). This differential effect of FHM1 mutation at excitatory and inhibitory synapses suggests the working hypothesis that a dysfunctional excitatory/inhibitory (E/I) balance in specific cortical circuits might be the key pathogenic mechanisms in FHM.

As a first test of this hypothesis we decided to investigate whether FHM mutations alter the dynamic regulation of the E/I balance in L2/3 during recurrent network activity induced by optogenetic activation of L2/3 pyramidal cells with different types of light stimuli, that presumably mimick different types of physiological activity.

In utero electroporation at day 15.5 of gestation allows to selectively express channelrhodopsin-2 (ChR2) in L2/3 Pyrs (Szczurkowska *et al*., 2016). I contributed to implement this technique in the lab and to optimize the protocol described in Szczurkowska *et al*., 2016. In particular, I optimized the mating strategies to obtain a higher number of pregnant females to be electroporated, I implemented some strategies and optimized the concentration and the volume of injection of cDNA and Fast Green FCF in order to increase the survival of the pups.

Once obtained a good, selective expression of ChR2 we can then record light-evoked excitatory and inhibitory currents in voltage-clamped Pyr neurons not expressing ChR2 (ChR2-). We performed preliminary recordings in L2/3 Pyrs not expressing Chr2- and measured light-evoked excitatory and inhibitory currents in isolation by voltage clamping individual Pyrs at +10 mV and -68 mV, the reversal potential (E_{rev}) for EPSP (excitatory post-synaptic potential) and IPSP (inhibitory

post-synaptic potential), respectively. For these experiments single short 2 ms blue light pulses, to mimic transient sensory-driven spiking (Shao *et al*., 2013), were delivered at increasing photostimulus intensity to induce spiking in an increasing number of Pyrs and characterize the progressive recruitment of excitation and inhibition in the active recurrent network. Synaptic charges were derived by integrating the currents over the first 50 ms, and used to calculate the E/(E+I) ratio.

In a preliminary experiment we found that increasing the intensity of the 2 ms light pulses, the E/I ratio in ChR2- cells decreased (except at close to EPSC threshold light intensities), reflecting preferential recruitment of inhibition over excitation as the L2/3 network activation increases.

1. INTRODUCTION

1.1 Migraine

Migraine is one of the most disabling neurological disorder that affects 12% of the population in occidental countries with a higher prevalence in women (18%) than in man (6%) (Lipton *et al.*, 2007). Given the heavy impact in the quality of life caused by the disorder, that predominantly affect people during middle life, migraine is considered one of the 20 most disabling diseases by the World Health Organization and has high direct and indirect socio-economic costs (Leonardi *et al.*, 2005). In most of the cases migraine consists of episodic manifestation of severe headache, that lasts from a few hours up to 72 hours, accompanied by throbbing unilateral head pain, pain in the neck and shoulders, nausea and vomiting; autonomic phenomena such as reddening of the eyes, tearing, flushing or pallor, and finally sensory amplifications, such as photo-, phono-, and osmo-phobia and cutaneous allodynia (MO) (Brennan and Pietrobon, 2018). In 1-2% of the cases it persists for more than 15 days a month and is considered chronic (May and Schulte, 2016).

In one third of patients the headache is preceded by the so called “migraine aura”, which lasts at least 1 hour and consists in typically sensory hallucination, with visual or somatic percepts that do not exist in the environment; it can also reversibly affects speech function (MA) (Brennan and Pietrobon, 2018). Visual aura is the most common form and usually consists in a scotoma, a propagating area in the visual field with loss of vision and scintillating borders (Pietrobon and Striessnig, 2003). Up to 72 hours before an attack, some patients experience premonitory symptoms: cognitive changes, hunger/thirst, euphoria or irritability. Following the attack, sensory function typically does not immediately return to normal; milder pain and sensory amplifications can persist for hours to days (Goadsby *et al.*, 2002; Olesen *et al.*, 2013 reviewed in Brennan and Pietrobon, 2018).

Migraine has a strong genetic component (up to 50%), higher in MA than in MO, characterized by a multifactorial polygenic inheritance. The complexity of the disease has hampered the identification of a common susceptibility variants.

Indeed, a lot of external and internal factors can modulate the inherent migraine threshold, and several loci have been linked to migraine but causative genes have not been identified yet, except for Familial Hemiplegic Migraine (FHM). FHM is a rare autosomal subtype of MA characterized by dominant inheritance for which three different causative gene have been identified, all encoding ion channels or transporters (Pietrobon and Moskowitz, 2014; Vecchia and Pietrobon, 2012).

1.2 Neurobiology of migraine

1.2.1 Migraine headache

The typical premonitory symptoms that many patients manifest up to 12 hours before the attack, (see above), together with the nature of some typical migraine triggers (stress, sleep deprivation or oversleeping, hunger and prolonged sensory stimulation) indicate that migraine attacks start in the brain (Giffin *et al.*, 2003; Hauge *et al.*, 2011). This evidence is also supported by the fact that in the period between attacks, migraineurs show hypersensitivities to sensory stimuli and abnormal processing of sensory information (Coppola *et al.*, 2007).

It is generally believed that migraine headache depends on the activation and the sensitization of the trigeminovascular system (TGVS). Within the skull, pain sensitivity is primarily restricted to the meningeal blood vessel, which are densely innervated by nociceptive sensory afferent fibers of the oftalmic division of the trigeminal nerve (Pietrobon and Striessnig, 2003; Pietrobon and Moskowitz, 2013). The activation of the meningeal TGV afferents leads to the activation of the trigeminocervical complex (TCC) which comprises the C1 and C2 dorsal horns of the cervical spinal cord and the caudal division of the spinal trigeminal nucleus (TNC). The TCC makes direct ascending connections with different areas in the brain stem [e.g., superior salivary nucleus, rostral ventromedial medulla (RVM), ventrolateral periacqueductal gray (vlPAG)] and with higher structures including several hypothalamic and thalamic nuclei [particularely ventroposteromedial (VPM) and posterior (Po)], which in turn make ascending connections with the cortex (Pietrobon and Moskowitz, 2013) (Fig 1.1 a). VPM thalamic neurons project mainly in the trigeminal primary and secondary somatosensory (S1 and S2) cortices and the insular (Ins) cortex. S1, S2 and Ins cortices are part of the so-called “pain

matrix" and are likely involved in the perception of headache. TGV neurons belonging to Po thalamus mainly project to beyond the pain matrix into non-trigeminal S1 cortex, as well as into auditory, visual, retrosplenial, ecthorinal and parietal association cortices, thus they are thought to be involved in other aspects of migraine, as disturbances in neurological functions involved on vision, audition, memory, motor and limbic functions and cognitive performances (Pietrobon and Moskowitz, 2013 and references therein).

The TCC receive descending projections from brainstem and hypothalamic nociceptive modulatory nuclei that may mediate descending modulation of trigeminovascular nociceptic traffic. The TCC also receives the descending cortical projection from layer 5 (L5) pyramidal cells (Pyrs) of the contralateral S1 cortex and caudal Ins cortex (Pietrobon and Moskowitz, 2013 and references therein) (Fig. 1.1 b).

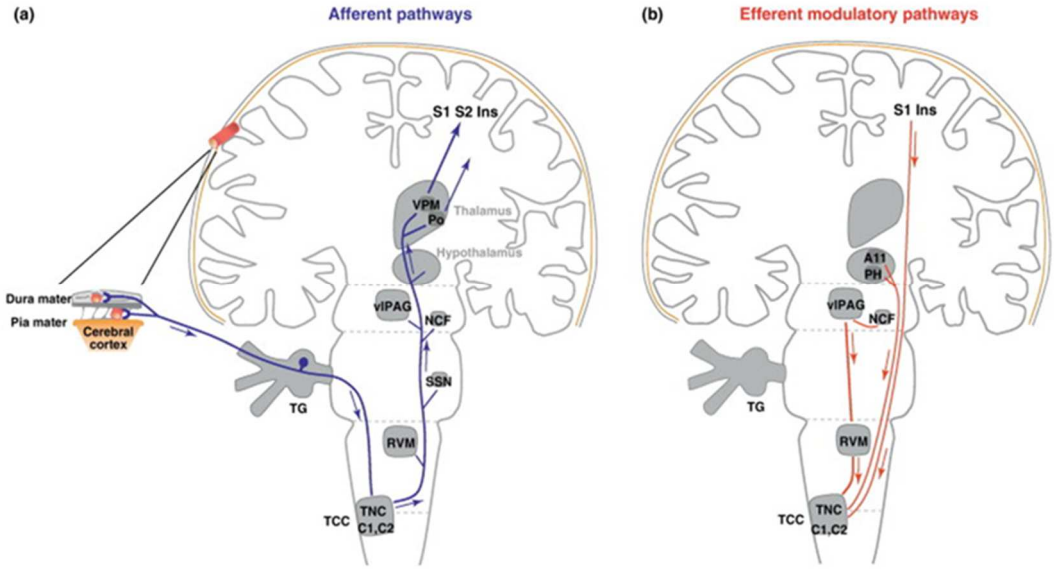

Figure 1.1 Neuronal structures and pathways involved in the trigeminovascular activation underlying migraine headache (Vecchia and Pietrobon, 2012).
Schematic illustration of important neuronal structures connected in the trigeminovascular pathways involved in migraine headache. a) Afferent pathways b) Efferent pathways.
TG trigeminal ganglion; TCC trigeminocervical complex which comprises C1 and C2, dorsal horns of the cervical spinal cord, and TNC, caudal division of the spinal trigeminal nucleus; RVM rostral ventromedial medulla; SSN salivatory nucleus; NCF the nucleus cuneiformis; vlPAG ventrolateral periacqueductal gray; VPM ventroposteromedial thalamic nucleus; Po posterior thalamic nucleus; S1 and S2 somatosensory cortex; Ins insular cortex; Ph posterior hypothalamus; A11 dopaminergic hypothalamic nucleus.

Two main open questions in the neurobiology of migraine are: “which is the primary dysfunction in migraine headache that leads to activation of the TGVS?” and “which is the mechanism of pain generation after activation of the TGVS?” (Pietrobon and Striessnig, 2003). The widely accepted “vascular theory of migraine” according to which the transient ischemia, induced by vasoconstriction, is the cause of migraine aura and also induces, as a rebound effect, an abnormal vasodilation of intracranial arteries that activate the perivascular sensory fibers, has been overcome. Recent studies, supported also by clinical observations, show that vasodilation of meningeal and/or extracranial arteries is neither necessary nor sufficient to cause migraine pain (Pietrobon and Moskowitz, 2013; Brennan and Charles, 2010). It is now generally accepted that the primary cause of the migraine headache resides in the brain but its cellular and molecular mechanisms remains unknown (Pietrobon and Striessnig, 2003).

The two main pain mechanisms are: the neurogenic inflammation of the meninges and the peripheral and central trigeminal sensitization. Increasing evidence from animal and clinical studies showed that meningeal inflammation is a key mechanism that may activate and sensitize perivascular meningeal afferents and lead to migraine pain. Numerous studies provided evidence for an increased level of various inflammatory mediators in the cephalic venous outflow during spontaneous migraine attacks. Activation of the meningeal nociceptor *in vivo* causes the release of vasoactive proinflammatory peptides, among them calcitonine gene-related peptide (CGRP), which is a potent vasodilator (Pietrobon and Striessnig, 2003), and substance P. These peptides result in vasodilation of the meningeal blood vessels, plasma extravasation and local activation of the dural mast cells, with ensuing release of cytokines and other inflammatory mediators resulting in neurogenic inflammation (Vecchia and Pietrobon 2012, and reference herein). The sensitization of the mechanosensitive meningeal afferents to the *dura mater* provides a mechanism that may explain the throbbing nature of the migraine headache (typically attributed to vascular pulsation) and the exacerbation of headache during events that increase intracranial pressure.

The nature and the mechanisms of the primary brain dysfunction that lead to the episodic activation of the TGVS remain largely unknown. The idea that different

primary mechanisms of migraine onset exist comes from the wide genetic and clinical heterogeneity of the disorder (Pietrobon and Moskowitz, 2013).

1.2.2 Cortical spreading depression (CSD)

CSD is now recognized as the neurophysiological correlate of migraine aura. CSD is a slowly propagating wave (2-6 mm/min) of sustained nearly complete depolarization that generates a transient, intense spike activity as it progresses into the tissue, followed by neural suppression that can lasts for minutes (Pietrobon and Striessnig, 2003). CSD is characterized by the collapse of ions homeostasis, the profound disruption of transmembrane ionic gradients and the release of neurotransmitters and other molecules from the cellular compartments. CSD causes no cell death or long-lasting damage in a normally metabolizing brain but imposes a considerably burden on tissue (Pietrobon and Moskowitz, 2014).

CSD can be experimentally induced by different stimuli, including chemical stimulation with high KCl concentration and electrical stimulation.

CSD is a complex phenomenon which consists of several phases that have been characterized by both extracellular and intracellular recordings in the hippocampus at the dendrite and soma (Canals *et al*., 2005). The extracellular recordings showed that the field potential in the dendrite layer is characterized by a rapidly attained early peak followed by either a less negative plateau or, after a brief decline (the so called “notch”), a slow second negative peak and displays a typical inverted saddle shape (Canals *et al.*, 2005; Pietrobon and Moskowitz, 2014) (Fig 1.2 a, top traces). Intracellular recordings showed that CSD consists mainly in three different phases: during the early phase, which lasts a few seconds, the apical dendrites of hippocampal pyramidal cells (Pyrs) are almost completely depolarized while the soma is only partially depolarized; during the main phase, which lasts 15-20 sec, the entire somatodendritic membrane is completely depolarized and during the late phase only a narrow band of the proximal apical dendrites remains fully depolarized while the soma is partially repolarized (Canals *et al.*, 2005; Pietrobon and Moskowitz, 2014) (Fig 1.2 a, bottom trace). Once the CSD starts, it self-propagates in the contiguous gray matter as a wave and, given that CSD-related depolarization initiates from the apical dendrites of Pyrs, the leading edge

propagates in layers containing apical dendrites (Pietrobon and Moskowitz, 2014 and reference therein). Collective Pyrs depolarization is accompanied by a rapid field potential change during the early phase, characterized by a rapid increase of the $[K^+]_e$, a rapid decrease of $[Na^+]_e$, $[Cl^-]_e$, and $[Ca^{2+}]_e$ (Fig. 1.2 b). The reduction of the $[Na^+]_e$ is greater than the increase of $[K^+]_e$, hence electroneutrality is probably maintained by the efflux of organic anions, including glutamate (Glu) and aspartate released during CSD (Pietrobon and Moskowitz, 2014). During CSD events there is a large increase of the intracellular calcium ($[Ca^{2+}]_i$) levels primarily in neurons, temporarily followed by astrocytes. The increase of $[Ca^{2+}]_i$ parallels the neuronal depolarization sites during the three CSD phases, in fact, the increase of $[Ca^{2+}]_i$ occurs first in the apical dendrites and then in the somata and lasts longer in dendrites than in somata (Aiba and Shuttleworth, 2012). The CSD-associated neuronal $[Ca^{2+}]_i$ wave is unaffected by the suppression of the $[Ca^{2+}]_i$ increase in astrocytes (Peters *et al*., 2003; Chuquet *et al*., 2007, reviwed in Pietrobon and Moskowitz, 2014).

Besides these changes in ions homeostasis, pH transiently increase during the early phase and immediately decrease in the sustained phase. The increase reflects the transient proton influx into (and/or HCO_3^- efflux from) neurons, as it is accompanied by a transient decrease in intracellular pH in neurons. Astrocytes depolarization during CSD seems to be largely passive and is caused by an increase in $[K^+]_e$ (Pietrobon and Moskowitz, 2014). A characteristic feature of the CSD is the neuronal swelling that is visible both *in vivo* and *in vitro* (see also 5.11.1 in "Materials and Methods"). Neurons swell upon the influx of Na^+, Cl^- and water and the interstitial space shrinks by 40-70%. By contrast, astrocytes display only passive swelling in response to CSD-inducing high $[K^+]$ solutions in cortical slices and do not swell *in vivo* (Pietrobon and Moskowitz, 2014). During depolarization cortical layer 2 (L2) dendrites show various morphological changes (e.g beading and loss of spines) that are reversible within 8-10 minutes, similar to the time for recovery from suppression of electroencephalogram activity in the rabbit cerebral cortex (Pietrobon and Moskowitz, 2014).

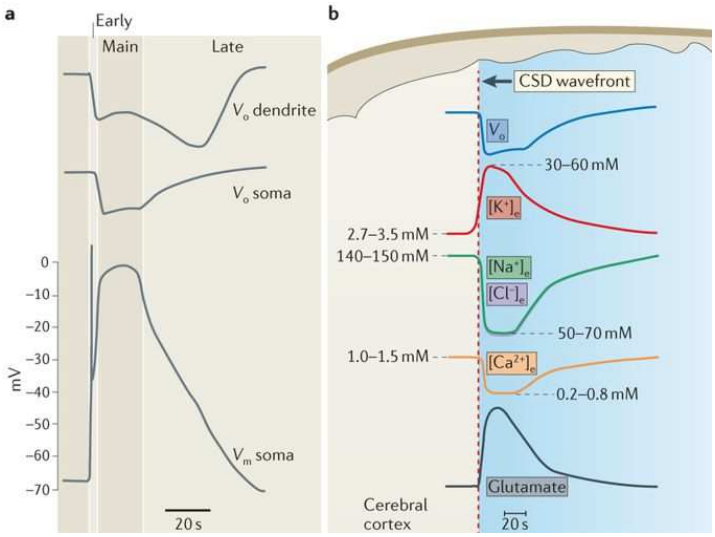

Figure 1.2 Electrophysiological features and ionic changes during CSD (Pietrobon and Moskowitz, 2014; Canals *et al.*, 2005)
a Two top traces showing the extracellular potential (V_o) recorded simultaneously in the apical dendrite and at the Pyrs soma regions in the hippocampus during a CSD. The trace at the bottom shows the membrane potential (V_m) recorded from a Pyr during CSD.
b Changes in the extracellular K^+ ($[K^+]_e$), of Na^+ ($[Na^+]_e$), of Cl^- ($[Cl^-]_e$), of Ca^{2+} ($[Ca^{2+}]_e$) and of glutamate (Glu) during CSD depolarization. The rapid V_o change during the early phase of CSD is accompanied by $[K^+]_e$ increase from 2.7-3.5 mM to 30-60 mM, a $[Na^+]_e$ and $[Cl^-]_e$ decrease from 140-150 mM to 50-70 mM and a $[Ca^{2+}]_e$ decrease from 1.0-1.5 mM to 0.2-0.8 mM. In the panel CSD depolarization and associated ionic changes are assumed to propagate across the cerebral cortex from right to left.

1.2.3 Mechanisms of initiation of experimental CSD

The experimental stimuli that have been found to induce CSD in the healthy brain cause depolarization of the brain cells, an increase in local $[K^+]_e$ and the release of Glu and other neurotrasmitters as a consequence of the depolarization of presynaptic terminals and activation of voltage-gated Ca^{2+} (Ca_v) channels (Pietrobon and Moskowitz, 2014) (Fig 1.3 b). Experimental data and modeling studies support the idea that an increase in $[K^+]_e$ above a certain concentration is the key initiating event and the generation of a net self-sustaining inward current across the membrane is necessary to initiate the positive feed-back cycle that makes the initial gradual neuronal depolarization self-regenerative and confers it all or none characteristic (Pietrobon and Moskowitz, 2014). This occurs when sufficient number of voltage-gated and/or $[K^+]_e$-dependent channels carrying an inward current, are activated by CSD-inducing stimuli. The net inward current leads to

membrane depolarization and an increase in $[K^+]_e$, which in turn leads to further activation of voltage-gated and/or $[K^+]_e$-dependent channels, further depolarization and further increase in local $[K^+]_e$. This results in complete neuronal depolarization if the removal of K^+ from the interstitium, does not keep pace with its release (Pietrobon and Moskowitz, 2014) (Fig 1.3 a).

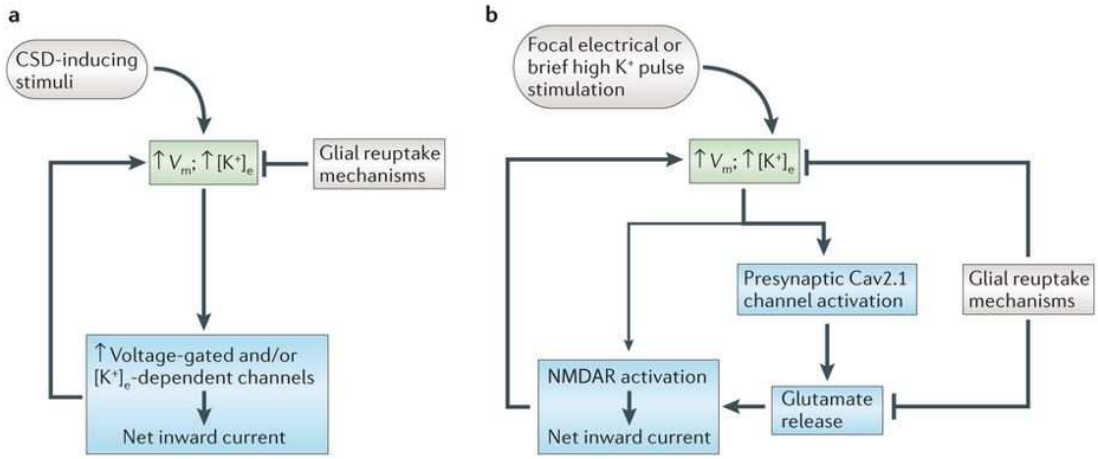

Figure 1.3 Models of CSD initiation (Pietrobon and Moskowitz, 2014)
a Schematic diagram of the requirements for CSD induction in the healthy brain tissue. Stimuli that can induce CSD increase the local $[K^+]_e$ above a certain concentration and produce neuronal depolarization. The initiation of the positive feed-back cycle requires the generation of a net inward current as a consequence of the activation of a sufficient number of voltage-gated and/or $[K^+]_e$-dependent channels carrying an inward current. This leads to the complete neuronal depolarization when the glial mechanisms of K^+ removal from the interstitium are overwhelmed by its release.
b Schematic diagram of the mechanisms of experimental CSD initiation. CSD is induced by brief K^+ pulse or by electrical stimulation. P/Q type Ca^{2+} channel-dependent release of Glu from cortical Pyrs and activation of N-methyl-D-aspartate receptors (NMDARs) exert a key role in the positive feed-back cycle that initiate CSD. Within this scheme, glial reuptake mechanisms have a role in the uptake of K^+ and Glu.

Summarizing, it is generally accepted that the regenerative increase of $[K^+]_e$ is fundamental in the positive feed-back mechanisms that ignites CSD and that the activation of ion channels located in the apical dendrite of Pyrs are crucial for CSD initiation. What is still unknown and controversial is the nature of the cationic channels involved in the generation of the initial net inward current and in local K^+ release. Most findings in this regard derive from pharmacological studies on experimental CSD. These studies are hampered by the fact that CSD involves

different phases and this makes difficult to distinguish between them (Pietrobon and Moskowitz, 2014).

There is a strong pharmacological support from *in vivo* and *in vitro* studies in cortical slices, regarding the involvement of *N*-methyl-D-aspartate receptors (NMDARs) in CSD phenomenon. These studies showed that saturating concentrations of NMDARs antagonist but not *α*-amino-3-hydroxy-5-methyl-4-isoxazole-propionic acid (AMPA) or kainate receptors antagonists completely block CSD even when the intensity of stimulation is several times larger than threshold. This leads to conclude that NMDARs are necessary for CSD initiation or propagation, or for both (Pietrobon and Moskowitz, 2014).

NMDARs implicated in the ignition of CSD are activated by Glu released from synaptic terminals after the openings of Ca_v channels. Three different main data support this conclusion: the first work showing that in a free Ca^{2+} medium or after blocking Ca_v channels with either Cd^{2+} or Ni^{2+} propagating CSD is abolished in brain slices (Footitt and Newberry, 1998; Jing *et al*., 1993). The second work has been done by Ayata *et al*., who demonstrate that *Leaner* mice, carrying a $Ca_v2.1$ mutation with a reduced channel open probability and a shifted activation curve to more depolarized voltages, showed an elevation in the threshold for CSD induction and a slower velocity, beside more frequent failures, of CSD propagation (Ayata *et al*., 2000). The third evidence comes from familial hemiplegic type 1 (FHM1) knockin (KI) mice which carry gain-of-function mutations in the gene encoding the $Ca_v2.1$ channels and which showed increased action potential-evoked glutamate release at cortical synapses (Tottene *et al*., 2009). These mice have a lower threshold for CSD induction and an increased velocity of CSD propagation both *in vivo* (van den Maagdenberg *et al*., 2004 and 2010) and in cortical slices (Tottene *et al*., 2009). Moreover in brain slices, partial inhibition of $Ca_v2.1$ channels that restored evoked Glu release to the wild type (WT) value, increased CSD threshold to the WT value in FHM1 KI mice, thus suggesting a causative link between the increased $Ca_v2.1$-dependent Glu release and facilitation of CSD initiation (Tottene *et al*., 2009). These data support a model of CSD initiation in which $Ca_v2.1$ channel-dependent Glu release from cortical Pyrs and activation of NMDARs exert

a key role in the positive feed-back cycle that ignites CSD (Pietrobon and Moskowitz, 2014) (Fig 1.3 b).

Astrocytes also seem to be involved in CSD ignition. In the brain of adult mice the α2 NKA is expressed almost exclusively in astrocytes (Cholet *et al*., 2002) where it is involved in the clearance of K^+ and of Glu, given a functional coupling with glutamate transporters (GluTs) during neuronal activity (Capuani *et al*., 2016; Pietrobon and Moskowitz, 2014 and references herein). Familial hemiplegic migraine type 2 (FHM2) KI mice, carrying a loss-of-function mutation in the gene encoding for the α2 NKA that reduces the protein expression by 50% *in vivo*, showed a lowered electrical threshold for CSD induction and an increased velocity of CSD propagation (Leo *et al*., 2011). A recent study shows that also in brain slices from FHM2 KI mice the threshold for CSD induction is lower while the velocity of its propagation is increased compared to WT mice (Capuani *et al*., 2016).

1.2.4 Mechanisms of propagation of experimental CSD

The mechanisms of CSD propagation are still debated but the slow rate of CSD propagation suggests that CSD propagation is mediated by the diffusion of a chemical substance. Indeed two of the four hypothesis proposed are based on interstitial diffusion of a humoral agent K^+ or Glu (van Harreveld, 1959). The other two hypothesis involve intracellular diffusion and opening of gap junctions in either glial cells or neurons. The role of gap-junctions in CSD is challenged by the findings that carbenoxolone, a gap-junction blocker, does not inhibit propagation (Somjen 2001; Herreras *et al*., 1994). The involvement of humoral mechanisms is supported by the finding that dilution of mediating substance (or substances) by intracerebral microdialysis of a physiological solution inhibits CSD (van Harreveld, 1959; Pietrobon and Moskowitz 2013).

The release of K^+ and Glu in the extracellular space during CSD produces a large increase of their extracellular concentration (Fig 1.2 b). As discussed in 1.2.3 a local increase of $[K^+]_e$ above a critical value and $[K^+]_e$-induced Glu release are key elements in the positive feed-back cycle that ignites CSD (Fig 1.3 b). Thus both K^+ and Glu may mediate CSD propagation through their diffusion and ignition of

CSD in the contiguous gray matter. Several evidences point to a key role of K^+ rather than Glu in CSD propagation (Pietrobon and Moskowitz 2014). For example, CSD propagation is restored after its inhibition by intracerebral dialysis using high levels of K^+ but not Glu (Obrenovitch *et al*., 1995). Moreover the enhancing effect of electric field on propagation velocity is consistent with a positively, but not negative, charged diffusing substance (Grafstein, 1956) and this is consistent with a more efficient mechanism of Glu rather than K^+ clearance (Okubo and Iino, 2011; Meeks and Mennerick 2007).

Conflicting results are reported regarding the $[K^+]_e$ rise preceding the fast depolarization associated with CSD (Pietrobon and Moskowitz, 2014 and references herein). According to a recent *in vivo* study measuring simultaneously the concentration of extracellular Glu using the genetically encoded glutamate sensor iGluSnFr, $[K^+]_e$ and V_0, the $[K^+]_e$ increase precedes both the neuronal depolarization and the increase of the extracellular Glu concentration (Enger *et al*., 2015). In brain slices the propagating K^+ wave is accompanied by a wave of $[K^+]_e$-induced synaptic Glu release at the CSD wave-front that is essential for the activation of the NMDARs that are involved in mediating CSD (Pietrobon and Moskowitz, 2014).

Overall, these data support a model of CSD propagation in which interstitial K^+ diffusion initiates the positive feed-back cycle that ignites CSD in the contiguous dendritic regions and astrocytes limit the rate of CSD propagation by buffering both K^+ and Glu (Pietrobon and Moskowitz, 2014).

1.2.5 Migraine aura and CSD

The neuropsychologist Karl Lashley during the 40s analyzed the progression of his own visual aura, which consisted in a scotoma (an area characterized by loss of vision within the visual field) with scintillating borders drifting slowly across the visual field. He hypothesized that the scotoma resulted from a region of depression of neuronal activity and that the scintillations resulted from a bordening region of intense cortical excitation and calculated that they spread across the visual cortex at a rate of 3 mm/min. A few years later Leão discovered a possible physiological correlate in the rabbit cerebral cortex and named it CSD (Leão, 1944). He showed

that CSD is characterized by a slowly propagating wave of sustained strong neuronal depolarization followed by neuronal suppression that can last for minutes. Moreover, Leão found that the velocity of the phenomenon reported by Lashley and the CSD elicited by focal stimulation were similar (3 and 2-6 mm/min, respectively) (Leão, 1944) (Pietrobon and Striessnig, 2003) (Fig 1.4 b). The similarities between migraine visual aura and CSD led to the hypothesis that CSD is responsible for the aura. Data obtained with blood-oxygen-level-dependent functional magnetic resonance imaging (BOLD fMRI) supported this hypothesis given that a specific temporal correlation was established between the initial features of the aura percept and the initial increase in the mean BOLD signal changes, reflecting cortical hyperaemia (Hadjikhani *et al*., 2001). The subsequent decrease in BOLD signal was temporally correlated with the following scotoma and finally the BOLD signals migrated towards more anterior regions of the visual cortex well correlating with the progressive movement of the scotoma from the center of vision towards the periphery (Pietrobon and Striessnig, 2003).

As the knowledge increases, the clearer the link between the aura, the CSD and migraine becomes. As discussed above (see paragraph 1.2.3) one major discovery is that genetic mutations that cause FHM, increase the risk of migraine aura in humans and facilitate CSD in mouse models (Pietrobon and Moskowitz, 2013; Vecchia and Pietrobon, 2012). Another evidence is that CSD activates the TGVS in animal model and cause headache, in fact a single CSD can lead to a long-lasting increase in ongoing activity of dural nociceptors and central TGV neurons in the superficial and deep laminae of the TCC (Zhang *et al*., 2010-2011). It has been proposed that such immediate activation, may be mediated by peptidergic nociceptors with axon collateral extending to the pia, where immediate activation may be mediated by increase of K^+, hydrogen (H^+) ions, nitric oxide (NO), arachidonic acid and prostaglandine and or other noxious mediators released in the wake of the CSD wave (Vecchia and Pietrobon, 2012; Pietrobon and Moskowitz, 2013). These substances may activate trigeminal nociceptors innervating pial blood vessels and, via axon collaterals, dural trigeminal afferents and/or the meningeal afferents, leading to activation of central TGV neurons in the TCC. Activation of the meningeal afferents leads to release of the proinflammatory vasoactive

neuropeptides (e.g CGRP, substance P and neurokinin A), that may promote neurogenic inflammation in the dura and possibly sustain the activation of the TGV afferents and lead to their sensitization (Pietrobon and Moskowitz, 2013) (Fig 1.4 c).

Another evidence that links the aura, CSD and migraine is that electrical and chemical threshold to evoke a CSD is raised by prophylactic drugs, as a mechanism of prevention. At least five clinically used migraine-preventing drugs, such as topiramate or valproate, which reduce the frequency of migraine attacks with or without aura, increase the threshold for CSD induction in rodents (Ayata, 2009; Ayata *et al*., 2006).

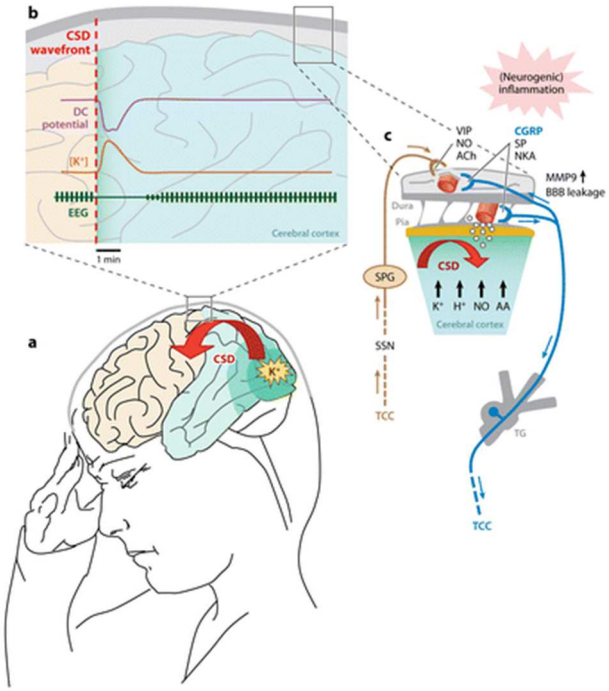

Figure 1.4 CSD and trigeminovascular nociception activation (Pietrobon and Moskowitz, 2013)
a Increase of the local $[K^+]_e$ above a certain level is belived to initiatiate CSD. **b** Schematic representation of the CSD, a slowly propagating wave of strong glial and neuronal depolarization accompanied by depression of spontaneous and evoked EEG activity and by a large increase in $[K^+]_e$. **c** Schematic representation of the noxious mediators released during CSD (H^+, NO arachidonic acid, serotonin, glutamate and others). These substances may activate trigeminal nociceptors innervating pial blood vessel, dural trigeminal afferents and/or meningeal afferents leading to activation of central TGV neurons in the TCC. Meningeal activation leads to release of proinflammatory vasoactive neuropeptide (e.g CGRP, substance P and neurokinin A) that may promote neurogenic inflammation and sustained the activation of the TGV afferents and lead to their sensitization. The blue pathway represent the meningeal TGV afferents, the brown pathway represent a parasympathetic reflex involving the activation of the superior salivatory nucleus (SSN) and the sphenopalatine ganglion (SPG) leading to release of vasoactive intestinal peptide (VIP), NO and acetylcholine (Ach) from the meningeal parasympathetic efferents.

1.3 Familial hemiplegic migraine

Familial hemiplegic migraine (FHM) is a rare autosomal-dominant subtype of migraine with aura which is characterized by obligatory motor aura symptoms that consist of motor weakness or paralysis, which is often, but not always, unilateral (Pietrobon and Striessnig, 2003; Pietrobon, 2007; Pietrobon and Moskowitz, 2013). Beside the characteristic motor aura a typical FHM attack resembles a MA attack. At least three, but more often four, different aura symptoms are copresent: visual, sensory, motor and sometimes aphasic and they last longer than in MA. Also the headache duration is longer in FHM than in MA but all the other headache characteristics are very similar (Pietrobon, 2007). FHM patients can experience alternatively both FHM and MA attacks and compared with the general population FHM patients have an almost eight times higher risk of MA (Thomsen *et al*., 2003) suggesting that FHM and MA have some common aspects and may share some pathogenic mechanisms (Pietrobon, 2007). Another feature that characterize FHM among the other types of migraine is that some FHM patients can experience atypical severe attacks with even coma, diffuse encephalopathy, confusion, seizures and/or prolonged hemiplegia that lasts for several days. Furthermore, about 20% of the FHM families show permanent cerebellar ataxia with or without nystagmus (Thomsen *et al*., 2003). Typical triggers of FHM attacks are emotional stress and minor head trauma (Thomsen *et al*., 2003; Ducros *et al*., 2001). FHM is a genetically heterogeneous pathology of which three different causative gene have been identified, all involved in the coding of ion channels or transporters.

1.3.1 Familial hemiplegic migraine type 1

FHM1 is caused by missense mutations in the gene *CACNA1A* at chromosome 19p13 which encodes for the pore-forming α1 subunit of the neuronal voltage-dependent P/Q-type Ca^{2+} ($Ca_v2.1$) channels (Ophoff *et al*., 1996). These channels play a fundamental role in neurotransmitters release at excitatory and inhibitory synapses in the CNS (Pietrobon, 2005) (Fig 1.5). More than 25 missense mutations are known (Sutherland and Griffiths, 2017), which may be associated with a broad spectrum of clinical features besides hemiplegic migraine, such as cerebellar ataxia, epilepsy, both during or independent from the FHM attack (Carreño *et al*., 2013;

Pietrobon and Moskowitz, 2013). $Ca_v2.1$ channels are widely expressed in the nervous system, including all the structures implicated in the pathogenesis of migraine (e.g. cerebral cortex, trigeminal ganglia, brainstem nuclei involved in the central control of nociception) (Pietrobon, 2005; Pietrobon, 2010). The somato-dendritic localization of $Ca_v2.1$ channels point to additional post-synaptic roles, e.g in neural excitability, besides their key presynaptic role (Pietrobon, 2007). In particular, the expression of $Ca_v2.1$ channels in the cerebellum is high and this might explain the cerebellar symptoms caused by some FHM1 mutations (Pietrobon, 2010). In the TGVS these channels account for a large part of the Ca^{2+} current of dissociated trigeminal ganglion neurons, are involved in CGRP release from perivascular terminals of meningeal nociceptors and trigeminal ganglion, as well as in control of Glu release from trigeminal ganglion neurons in culture. Finally they are involved in controlling the tonic inhibition of trigeminal nucleus caudalis neurons that regulate the trigeminal and spinal pain transmission (Pietrobon, 2013).

Analysis of the single channel properties of mutant recombinant human P/Q-type Ca^{2+} channels revealed that FHM1 mutations produce gain-of-function of the $Ca_v2.1$ channels mainly due to increased channel open probability and to a shift to lower voltages of the channel activation curve (Tottene *et al*., 2002-2005; Mullner *et al*., 2004; Kraus *et al*., 1998-2000; Hans *et al*., 1999; Melliti *et al*., 2003).

Two transgenic FHM1 KI mouse models have been generated: mice expressing the R192Q CACNA1A mutation which in humans cause pure FHM and mice expressing the S218L CACNA1A mutation, which in humans cause a more severe clinical phenotype which may include cerebellar ataxia, spontaneous seizures, coma, fever, long-lasting cerebral edema and cerebral and/or cerebellar atrophy (Kors *et al*., 2001; Pietrobon, 2005).

It has been demonstrated that R192Q KI mice have enhanced cortical excitatory synaptic transmission, as a consequence of increased action potential-evoked Ca^{2+} influx and Glu release at Pyrs synapses. In striking contrast, inhibitory synaptic transmission at fast spiking (FS) interneurons synapses was unaltered, despite being initiated by P/Q-type Ca^{2+} channels (Tottene *et al*., 2009).

FHM1 KI models show a lower threshold for CSD induction and a higher velocity of CSD propagation (van den Maagdenberg *et al*., 2004-2010; Tottene *et al*., 2009). Induction and propagation of CSD in FHM1 R192Q KI mice were rescued to WT values using sub-saturating concentrations of ω-agatoxin IVA, a selective P/Q-type Ca^{2+} channel blocker, that reduced Glu release to a value similar to that in WT mice, suggesting a causative link between enhanced Glu release and CSD facilitation in FHM1 R192Q KI mice (Tottene *et al*., 2009).

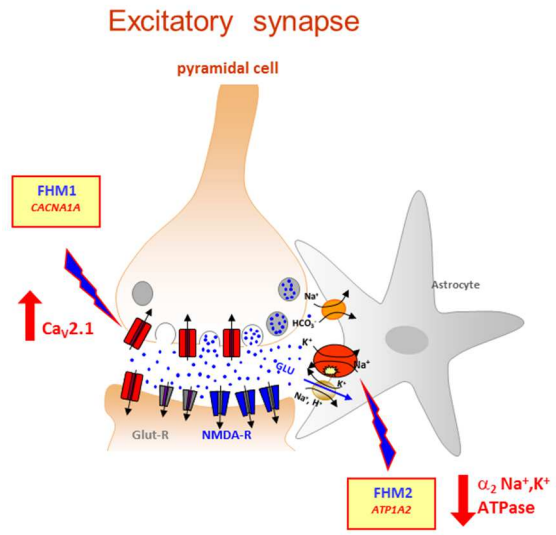

Figure 1.5 Location of FHM1 and 2 proteins in brain cells and effect of FHM mutation on their function (adapted from Pietrobon, 2017)
The $Ca_V2.1$ channels (the mutant proteins in FHM1) are located at the active zones of both excitatory and inhibitory synaptic terminals throughout the brain. FHM1 mutations produce gain-of-function of the $Ca_V2.1$ channels in excitatory cortical pyramidal cells, but do not affect the $Ca_V2.1$ channels in multipolar cortical inhibitory interneurons. In the adult brain, the α2 Na^+/K^+ ATPase (the mutant proteins in FHM2) are located almost exclusively in astrocytes, where they are colocalized with glutamate transporters in astrocyte processes surrounding excitatory, but not inhibitory, synapses.

1.3.2 Familial hemiplegic migraine type 2

FHM2 is caused by mutations in the gene *ATP1A2* at chromosome 1q23 which encodes for the α2 subunit of the Na^+/K^+ ATPase (De Fusco *et al*., 2003; Bøttger *et al*., 2012) (Fig 1.5). More than 50 FHM2 mutations have been identified and almost all are missense mutations that cause a complete or partial loss-of-function of recombinant α2 NKA due to loss or reduction of catalytic activity or impairment of plasma membrane delivery (Pietrobon 2007; Leo *et al*., 2011; Tavraz *et al*., 2008-2009). Most of the *ATP1A2* mutations are associated with pure FHM, however some are associated to complications including cerebellar ataxia, childhood convulsions, epilepsy and mental retard. Some other *ATP1A2* mutations are associated with non-hemiplegic migraine but resemble common migraine features

(Russel and Ducros, 2011). In the murine brain α2 NKA is expressed primarily in neurons during embryonic development and at time of birth, and almost exclusively in astrocytes in the adult brain (Moseley *et al*., 2003; Fink *et al*., 1996). The α2 NKA is located in the astrocytic processes surrounding glutamatergic synapses (Cholet *et al*., 2002) where it is colocalized with the glial glutamate transporters 1 (GLT-1), which mediates the majority of the Glu clearance during neuronal activity, while it is not present at GABAergic synapses (Cholet *et al*., 2002). It is also colocalized with the the Na^+/K^+ exchanger in microdomains that overlie subplasmalemmal endoplasmic reticulum (Lencesova *et al*., 2004; Golovina *et al*., 2003). The colocalization of the α2 NKA with GLT-1 suggests a specific role in the clearance of Glu, and the colocalization with the Na^+/K^+ exchanger a role in the regulation of intracellular Ca^{2+}, particularly in the endoplasmic reticulum (Juhaszova and Blaustein, 1997). Indeed elevated levels of Ca^{2+} ions in the cytoplasm and in the endoplasmic reticulum were measured in cultured astrocytes from *ATP1A2*$^{-/-}$ knock-out mice (Golovina *et al*., 2003).

In 2011 Leo *et al*., generated the first FHM2 KI mice by introducing the human FHM2 W887R mutations into the orthologous genes (Leo *et al*., 2011). The W887R mutation localizes to the extracellular loop between transmembrane domain (M) 7 and M8, which includes the β subunit binding site (Jorgensen *et al*., 2003) and was shown to produce an almost complete loss-of-function of the mutated pump (De Fusco *et al*., 2003; Koenderink *et al*., 2005) (see also above). In the fetal brain of homozygous FHM2 KI mice carrying the W887R mutation the α2 NKA protein is barely detectable, while its expression is reduced by 50% in the adult brain of heterozygous FHM2 KI compared to WT mice (Fig. 1.6 a), likely due to the retention in the endoplasmic reticulum and sequent proteasomal degradation (Leo *et al*., 2011). Homozygous W887R KI mice die at birth because of lack of spontaneous respiratory activity, probably as a result of elevated $[Cl^-]_i$ which would switch the GABA response from hyperpolarization to depolarization, suggesting a necessary coupling of α2 NKA with neuron-specific K^+/Cl^- cotransporter, which exclude the Cl^- ions from the cytosol in respiratory central neurons (Ikeda *et al*., 2004). Heterozygous W887R KI mice behaviour was tested using a modified SHIRPA protocol (Rogers *et al*., 1997) that provides comparable quantitative data

on animal motor, sensory, autonomic and neuropsychiatric functions. Using this method, no significant differences were observed in the sensory-motor functions between heterozygous W887R KI and WT mice, except for a higher fear and anxiety in mutants at the specific test of transfer arousal and fear (Leo *et al*., 2011). Heterozygous W887R KI mice are viable and fertile and do not show apparent clinical phenotype, however they display, as the FHM1 KI, enhanced susceptibility to CSD. Leo *et al*., in 2011 and more recently Capuani *et al*. in 2016, demonstrated that CSD threshold is lower while CSD propagation velocity is higher in FHM2 KI with a reduced expression of the α2 NKA compared to WT mice, *in vivo* and *in vitro*, respectively (Fig. 1.6 b).

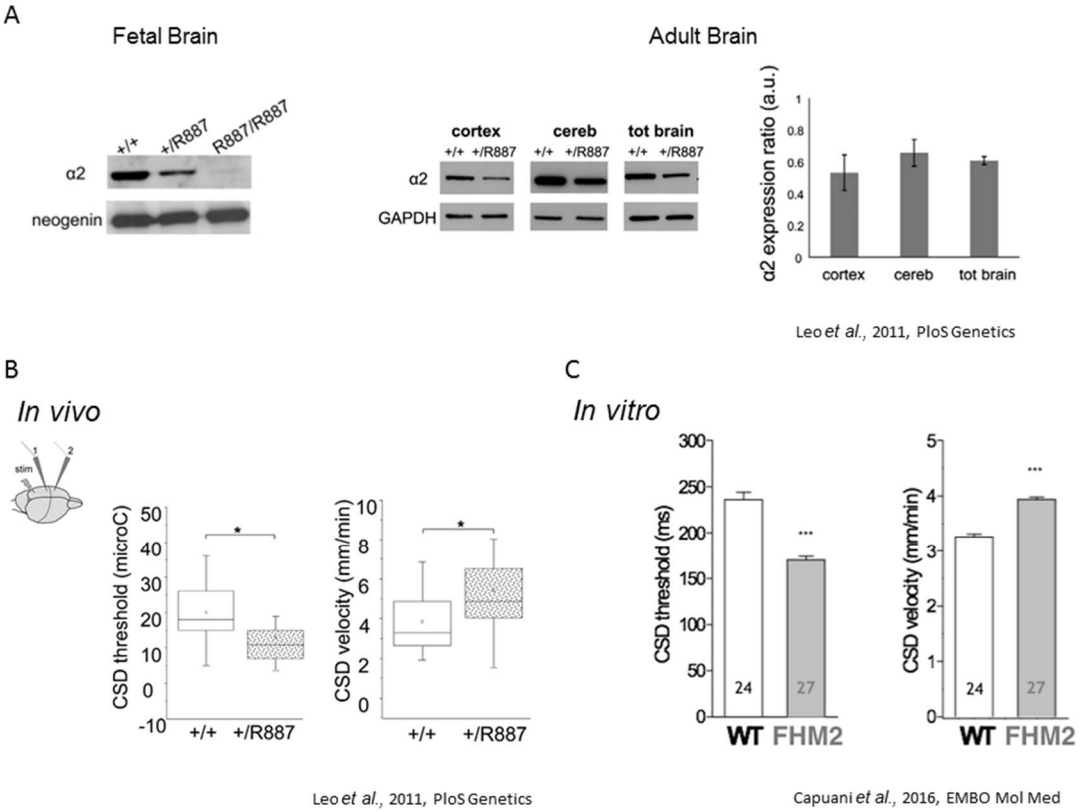

Figure 1.6 *In vivo* expression of mutant *ATP1A2* and facilitation of CSD *in vivo* and in acute cortical slices of FHM2 W887R KI mice (adapted from: Leo *et al*., 2011; Capuani *et al*., 2016)
a Protein expression measured using a western-blot of microsomal fraction probed with anti-α2 NKA and anti-neogenin as loading control in both fetal (left) and adult (right) brain of WT $^{+/+}$, heterozygous FHM2 W887R KI $^{+/R887}$ and omozygous FHM2 W887R KI $^{R887/R887}$. The α2 NKA and neogenin bands weight 110 and 52 kD, respectively. On the right quantification of the α2 NKA expression ratio in three different brain areas. **b**

Schematic representation of the position of the electrical stimulating (Stim) and the recording electrodes. Box plot showing CSD threshold and propagation velocity in WT $^{+/+}$ and heterozygous FHM2 W887R KI $^{+/R887}$. Heterozygous animals are more sensitive to CSD induction (13.00 ± 1.7 μC, n = 20 versus 19.90 ± 1.9 μC, n = 18. Unpaired *t*-test: ***P* <0.01). CSD velocity of propagation is increased in heterozygous FHM2 W887R KI $^{+/R887}$ compared to WT $^{+/+}$ (5.41 ± 0.41 mm/min, n = 20 versus 3.85 ± 0.35 mm/min, n = 18. Unpaired *t*-test: ***P* <0.01). Data are mean ± SEM. **c** Stimulation threshold for CSD induction (CSD threshold) and rate of CSD propagation (CSD velocity) measured in WT and FHM2 KI mice brain slices in which CSD is induced by brief pressure ejection pulses of increasing duration of high KCl. As *in vivo*, also in brain slices heterozygous FHM2 KI animals are more sensitive to both, CSD induction than WT (170 ± 4 ms, n = 27, *N* = 8 versus 236 ± 8 ms, n = 24, *N* = 3. Mann-Whitney *U*-test: ****P* <0.0001) and to CSD propagation velocity (3.94 ± 0.04 mm/min, n = 27, *N* = 8 vs 3.26 ± 0.05 mm/min, n = 24, *N* = 3. Unpaired *t*-test: ****P* <0.0001). Data are mean ± SEM.

1.3.3 Familial hemiplegic migraine type 3

FHM3 is caused by missense mutations in the gene *SCNA1A* which encodes for the α1 subunit of the voltage-gated sodium (Na^+) channels $Na_v1.1$ (Dichgans *et al*., 2005). $Na_v1.1$ channels are expressed primarily in the central nervous system (CNS) in the late postnatal stage and more in caudal than rostral region. $Na_v1.1$ channels are expressed in many types of neurons, including hippocampal and cortical Pyrs but especially in inhibitory interneurons where they are specifically localized in the axon initial segment (Ogiwara *et al*., 2007; Yu *et al*., 2006; Hedrich *et al*., 2014) (Fig 1.7). Studies of the functional effects of FHM3 mutations on recombinant human $Na_v1.1$ channels expressed in non-neuronal cells reported conflicting results, indeed both gain- or loss-of-function were reported depending on the mutation and/or the splice variants of $Na_v1.1$ (Cestèle *et al*., 2008; Kahlig 2008). However, recent studies of L1649Q mutant $Na_v1.1$ that was not-functional if expressed in a non-neuronal cell line, showed a gain-of-function if expressed in cortical interneurons. Moreover it could sustain high-frequency firing better than the WT channel (Cestèle *et al*., 2008). Taken together these data suggest that FHM3 is more likely associated with a gain of function of $Na_v1.1$ channels and consequent selective hyperexcitability of cortical interneurons (Pietrobon, 2017). FHM3 can manifest with the typical feature of pure hemiplegic migraine or in association with epileptic seizure or repetitive daily blindness attacks that are independent from the hemiplegic migraine attacks (Vecchia and Pietrobon, 2012).

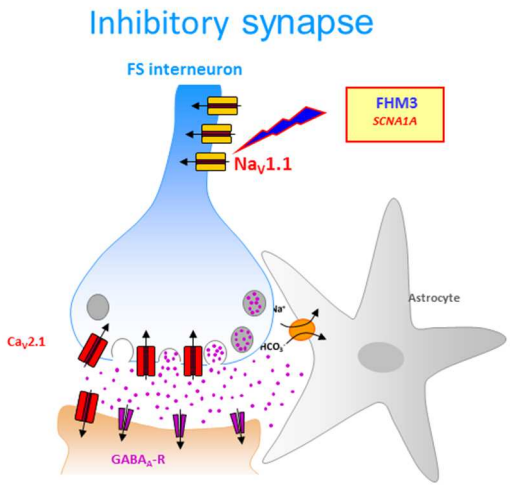

Figure 1.7 Location of FHM3 protein in brain cells and effect of familial hemiplegic migraine mutation on their function (adapted from Pietrobon, 2017)
The $Na_V1.1$ channels (the mutant proteins in FHM3) are located in cortical inhibitory interneurons, especially at the axon initial segment, and play an important role in interneuron (but not Pyrs) excitability, particularly in sustaining high-frequency firing. FHM3 mutations produce gain-of-function of $Na_V1.1$ channels in cortical interneurons.

1.4 Astrocyte-neuron signaling in the "Tripartite synapses"

In vertebrates, glia can be divided into four major categories. In the peripheral nervous system are the Schwann cells, and in the CNS are microglia, oligodendrocytes and astrocytes, glial cells that are intimately associated with synapses: the perisynaptic Schwann cells at the neuro-muscular junction and the astrocytes of the CNS (Araque *et al.*, 1999). Experimental evidences provided by many laboratories in the last few years showed that astrocytes located in close proximity of the synapses might play important functional roles. Among all, astrocytes can actively promote the formation of nascent neuronal synapses, regulate the synapse maintenance and promote synapse elimination, thus regulating the overall architecture and activity of neuronal circuits and ultimately animal behavior (Farhy-Tselnicker and Allen, 2018). Moreover astrocytes are intimately involved in the active control of neuronal activity and synaptic neurotransmission (Araque *et al.*, 1999). This led to the concept of "tripartite synapses" composed mainly of three functional elements: the pre- and post-synaptic elements and the surrounding astrocytes (Araque *et al.*, 1999) (Fig 1.8). Accumulating findings on this argument agree that there is a dynamic reciprocal communication between astrocytes and neurons. The astrocytes express membrane receptors for almost all neurotransmitters (Haydon, 2001), many of which are metabotropic receptors, thus they are able to receive signals from neurons and actively respond to synaptic activity with cytosolic Ca^{2+} elevation (Araque *et al.*, 1999) via activation of the

inositol triphosphate pathway. Activated astrocytes have the ability to release a variety of neuroactive molecules, called gliotransmitters, including Glu, ATP, NO, prostaglandins, atrial natruretic peptide, GABA and D-serine, which in turns influences neuronal excitability (Fellin *et al*., 2006 and references herein) (Fig 1.8).

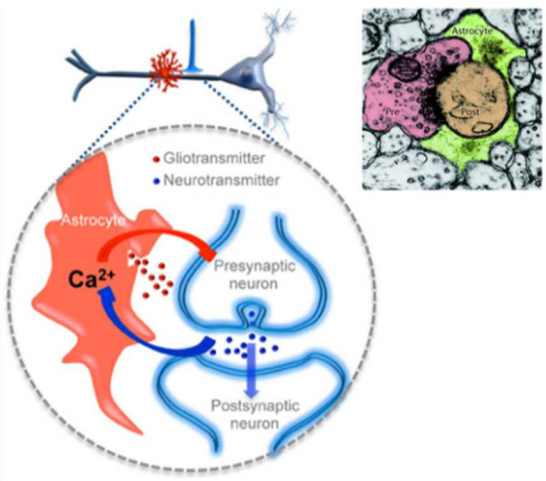

Figure 1.8 Structure and main plyers in a "tripartite synaps" (adapted from Navarrete and Araque, 2014; Fellin *et al*., 2006)
Schematic representation of one axon establishing a synapse on an apical dendrite of a prototypical Pyrs and an astrocyte (in red). The large dashed circle illustrate a magnification of the tripartite synapse, where the pre- and post-synaptic neuronal elements (in blue) are surrounded by astrocytic processes (in red). Astrocytes respond with Ca^{2+} elevation to neurotransmitters (blue dots) released during synaptic activity and, in turn, control neuronal excitability and synaptic transmission through the Ca^{2+}-dependent release of gliotransmitters (red dots). Inset: electron microscopy showing the tripartite nature of synaptic strucures with astrocytic processes (in green) associating with pre- and post-synaptic terminals.

The Ca^{2+} elevations upon astrocytic activation are mainly due to the mobilitation of Ca^{2+} stored in the endoplasmic reticulum. Astrocytic Ca^{2+} elevations can occur also spontaneously as intrinsic oscillations in the absence of neuronal activity (Perea *et al*., 2009). Several mechanisms have been described for gliotransmitter release, including Ca^{2+} and SNARE protein-dependent mechanisms through vescicle exocytosis (Perea and Araque, 2010), membrane channels or pumps.

1.4.1 Glutamate uptake

Glutamate is the major excitatory neurotransmitter in the mammalian CNS (Krnjevic, 1974; Watkins and Evans, 1981) and the control of its time course in the synapse is crucial for excitatory neurotransmission. On the other hand, Glu is also a potent neurotoxin and its accumulation in the extracellular space can trigger excessive activation of glutamatergic receptors and may lead to excitotoxicity, a characteristic hallmark of many diseases (Murphy-Royal *et al*., 2017). Therefore a

rapid removal of Glu from the extracellular space during neuronal activity is fundamental to reduce Glu spillover, thus preserving the signal specificity thought to be required for efficient information processing (Danbolt, 2001; Tzingounis and Wadiche, 2007), and to prevent overexcitation, excitotoxicity and the maintenance of the normal neuronal functions.

The GluTs present in the brain belong to five different subtypes, called excitatory amino acid transporters (EAAC) 1-5 (Danbolt, 2001). The EAAT family can be roughly divided based on cell-specific expression patterns, with glutamate-aspartate transporter (GLAST or EAAT1) and glutamate transporter 1 (GLT-1 or EAAT2) mainly located on astrocytes (~ 90% of the total GLT-1) while EAAT3-5 are exclusively neuronal (Murphy-Royal, *et al*., 2017; Melone *et al*., 2018 and references herein).

The Glu uptake mediated by astrocytes is quantitatively the most important for Glu homeostasis (Anderson and Swanson, 2000) and occurs rapidly thus ensuing temporally brief and spatially restricted Glu neurotransmission (Bergles and Jahr, 1997; Danbolt, 2001; Diamond, 2005). GLAST and GLT-1 are the predominant GluTs in glial cells (Ilarianova *et al*., 2014). GLT-1 is the quantitatively dominant GluTs in the brain and it mediates the majority of Glu clearance in the adult murine neocortex (Haugeto *et al*., 1996; Rothstein *et al*., 1996; Tanaka *et al*., 1997; Danbolt, 2001; Campbell *et al*., 2014) given its locations close to synapse (Barbour *et al*., 1994; Lehre and Danbolt, 1998). Electron microscopy studies at excitatory synapses of rat and human neocortex revealed that GLT-1 is localized in ~ 65% of cases at perisynaptic astrocytic processes (PAPs), in ~ 20% of cases in the axon terminals (AxTs), and in ~ 15% of cases in both of them (Melone *et al*., 2009-2011).

GLT-1 and GLAST are sodium dependent proteins that rely on sodium and potassium gradients generated principally by the NKA, to generate ion gradients that drive the neurotransmitter uptake (Rose *et al*., 2009). During each individual transport cycle, each transporter binds one extracellular molecule of Glu as well as 3 Na^+ and 1 H^+. The transporter undergoes a conformational change towards an inward facing conformation where these substrates are released into the cytoplasm that is followed by the binding of one internal K^+ and a switch back to an outward

facing state, completing the transport cycle. (Zerangue and Kavanaugh, 1996 and Reyes *et al*., 2013 reviewed in Murphy-Royal *et al*., 2017).

It has been demonstrated that selective deletion of neuron-specific GluTs are not vital for survival and mice lacking these transporters display no neurodegeneration despite presenting in some cases behavioral abnormalities (Petr *et al*., 2015). On the contrary, astrocytic GLT-1 has been shown to be fundamental for normal brain function in a GLT-1 knockout mouse model (Tanaka *et al*., 1997; Mitani and Tananka, 2003; Takasaki *et al*., 2008). These mice appears to be normal at birth but during the time window in which synaptic clearance of neurotransmitters shift from passive diffusion to transporters-mediated uptake (2 to 3 weeks of age), they start to suffer from hyperactivity as well as severe epileptic seizure (Ullensvang *et al*., 1997; Furuta *et al*., 1997; Thomas *et al*., 2011).

1.4.2 Roles of glutamate transporters in shaping excitatory transmission

For each quantal event it has been estimated that the transient increase of Glu reaches in the synaptic cleft the concentration of 1 mM, for approximately 1.2 ms before returning to basal level (Clements *et al*., 1992). As there are no extracellular enzymes to degrade Glu, this brief transient can only be attributed to the diffusion of Glu in the extracellular space combined with its efficient uptake by transporters. The slow transport cycle for GluTs (from 12 to 70 ms per cycle, depending on experimental conditions) relative to the time course of Glu in the synaptic cleft led to the hypothesis that thousands of transporters must be present to the synapse in order to efficiently remove this neurotransmitter on a rapid timescale. Numerous studies show that genetic and pharmacological manipulation of transporter expression and localization even if small can have significant effects on neuronal function (Armbruster *et al*., 2016 and references herein).

During a synaptic event, Glu release results in an excitatory postsynaptic current (EPSC), a flux of cations across the membrane mediated by the activation of post-synaptic Glu receptors leading to a depolarization of the cell. The kinetics of these EPSC depends mainly on the concentration and the time course of the neurotransmitter at the synapse and the properties of postsynaptic receptors activated by the neurotransmitters. The role of uptake in determining the duration

and the properties of excitatory postsynaptic currents vary among different synapses. This differential effect seems to correlate with the amount of glia and coverage and transporter expression at these synapses (Campbell and Hablitz, 2004 and references herein). The glutamate-gated ion channel receptors (named ionotropic Glu receptors iGluRs) constitute the major targets of synaptically released Glu. They can be divided in three different subtypes: non–NMDA receptors, of which there are two subtype: AMPA and kainate receptors, and NMDA receptors (NMDARs), with differing kinetics (Campbell and Hablitz, 2004 and references herein). AMPA and NMDA receptors are the main contributors to Glu-mediated excitatory neurotransmission. It has been demonstrated that the rapid decay of AMPAR-mediated EPSC is largely governed by deactivation kinetics of the receptors (Hestrin, 1992; Jonas *et al*., 1994; Silver *et al*., 1996). The decay kinetics of NMDARs-mediated EPSC (NMDARs-EPSC) instead are slower, a fact that has been attributed to its high affinity for Glu that can cause prolonged binding (Hestrin *et al*., 1990; Lester and Jahr, 1992; Lester *et al*., 1990). In light of the higher affinity of NMDARs for Glu, when its uptake is compromised for any reason, or during high frequency synaptic stimulation, they can be preferentially activated by Glu that spillovers. Indeed, in certain conditions, Glu could spillover in the synaptic cleft and could activate extrasynaptic NMDARs and/or NMDARs in the neighbouring synapses, able to detect even little amount of Glu.

1.5 *N*-methyl-D-aspartate receptors

NMDARs are glutamate-gated ion channel widely expressed in the CNS that play important roles in excitatory transmission and require simultaneous presynaptic release of Glu and postsynaptic depolarization to produce the slow Ca^{2+}-permeable component of the EPSC (Bourne and Nicoll, 1993; Volianskis *et al*., 2015). Moreover, to be activated, they do not require only the binding of Glu but also of the endogenous co-agonist glycine/D-serine (Hansen *et al*., 2017 and references herein). Given the central role of NMDARs in normal brain function, their dysregulation has been associated to a wide variety of pathologies, including migraine, pathological pain, epilepsy, schizophrenia, Alzheimer's disease and mental retardation (Hansen *et al*., 2017). Hyperactivation of NMDARs results in a

NMDAR-mediated Ca^{2+} flux into neurons which may promote neuronal death (Hansen *et al*., 2017 and references herein).

From a structural point of view, NMDARs are integral membrane proteins incorporating four large subunits that form a central ion channel pore selective for cations (Na^+, K^+ and Ca^{2+}). Each subunit is composed of an extracellular region with large globular bilobate (clam-shell like) domains comprising the amino (N)-terminal domain (NTD), which is involved in subunit assembly and allosteric regulation, and the agonist binding domain (ABD) that is formed by two discontinuous segments (S1 and S2), which binds glycine (or D-serine) in GluN1 and GluN3 subunits and Glu in GluN2 subunits. Beside the extracellular region there is a trans-membrane domain (TMD) made of three trans-membrane helices plus a pore loop (M2) that lines the ion selectivity filter; and an intracellular carboxyl (C)-terminal domain (CTD), which is involved in receptor trafficking, anchoring and coupling to signaling molecules (Paoletti *et al*., 2013) (Fig 1.9).

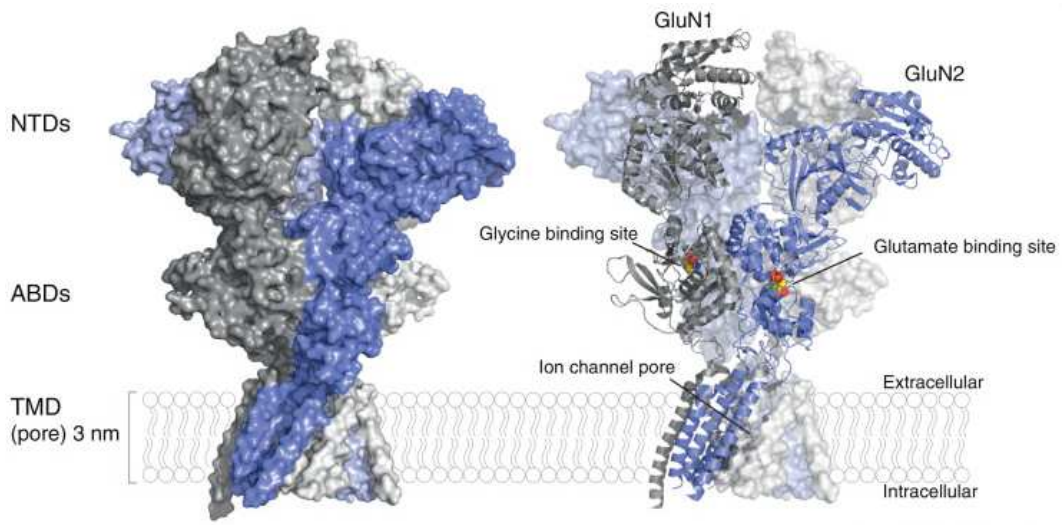

Figure 1.9 NMDARs structure (Zhu and Paoletti, 2015)
Left panel: X-ray structure of the heterotertameric NMDAR. The two GluN subunits (different shades of gray) and the two GluN2 subunits (different shades of blue) are visible. It is possible to appreciate the layered arrangement with the NTDs at the top, the ABDs binging glycine (or D-serine) in GluN1 and Glu in GluN2, and the TMD which contains the ion channel pore. Right panel: location of the orthosteric site GluN1 (bound to glycine) and GluN2 (bound to Glu), and of the ion channel pore site in the transmembrane region.

NMDARs assemble as heterotetramers associating two mandatory GluN1 subunits and two GluN2 subunits (and more rarely GluN3 subunits), of which there are four subtypes (GluN2A-D) (Zhu and Paoletti, 2015). Assembly of different GluN1 and GluN2 subtype subunits give raise to different types of NMDARs. Indeed NMDARs can exist as diheteromers associating two GluN1 subunits and two GluN2 subunits belonging to the same subtype or as triheteromers associating two GluN1 subunits and two different subtypes of GluN2 subunits. The GluN1 subunit has eight different isoforms that arise form alternative splicing of three exon within a single gene product (Hansen *et al*., 2017 and references herein). The GluN2 subunit endow NMDARs with very different pharmacological and functional properties e.g difference in sensitivity to voltage-dependent Mg^{2+} block, inhibition by endogenous modulators, different affinities for Glu and glycine/D-serine, as well as other agonist (Hansen *et al*., 2017 and references herein; Paoletti *et al*., 2013) (Fig 1.9). Importantly, the identity of the GluN2 subunits determines several gating properties including maximal channel open probability, agonist sensitivity and deactivation kinetics (τ_{decay}) (Paoletti *et al*., 2013). Data from many studies reviewed in Zhu and Paoletti, 2015 showed that diheteromers GluN2ARs have a higher open probability than diheteromers GluN2B, 2C and 2D receptors. The same studies revealed that NMDA receptor deactivation kinetics, which govern the EPSC decay, are the fastest in diheteromers GluN2ARs and the slowest in diheteromers GluN2DRs. To note is that deactivation kinetics are complicated by the fact that different GluN1 subunit isoform differently influence the decay (GluN1-1b has a faster decay than GluN1-1a) besides the GluN2 subtype (Rumbaugh *et al*., 2000; Vance *et al*., 2012). These distinct gating properties confer distinct signaling profile to each different type of NMDAR. While many information regarding the gating properties of diheteromeric receptors are available, little is known about the properties of triheteromeric receptors containing more than one type of GluN2 subunit.

The GluN1 subunit is ubiquitously expressed in the CNS at all stages of development, while the expression of GluN2 subunits varies with time and space. Indeed during development, GluN2B and 2D are the predominant subunits while GluN2A and C expression starts only later. In the adult brain the GluN2A and B are

the predominant subunits in the forebrain, while GluN2C is confined in the cerebellum and GluN2D is restricted to the midbrain (Paoletti *et al*., 2013). NMDARs are typically found at postsynaptic sites but they vary also according to subcellular localization. In the adult forebrain, at synaptic sites, diheteromeric, either GluN2ARs and GluN2BRs, or triheteromeric GluN2A-2BRs are predominant, although their ratio vary depending on the inputs. By contrast pery- and extrasynaptic sites are enriched in diheteromeric GluN2B-containing receptors, although the idea that diheteromers GluN2BRs segregates outside synapses while diheteromers GluN2ARs are principally synaptic, is an oversimplification (Paoletti *et al*., 2013 and references herein). An important feature of NMDARs is that their molecular composition is not static but varies in an activity-dependent manner, or in disease states with profound consequences on network function (Paoletti *et al*., 2013; Lau and Zukin, 2007).

2. AIMS

Familial hemiplegic migraine type 2 is caused by mutations in the *ATP1A2*, the gene encoding for the α2 subunit of the sodium potassium ATPase (De Fusco *et al*., 2003). The α2 NKA is expressed almost exclusively in the astrocytes in the adult brain (Moseley *et al*., 2003). The FHM2 mutations cause loss-of-function of recombinant α2 NKA (Bøttger *et al*., 2012). In the brain of heterozygous FHM2 KI mice carrying the human mutation W887R, the α2 NKA protein expression is reduced to half compared to WT mice (Leo *et al*., 2011). *In vivo* experiments in heterozygous FHM2 KI mice, showed facilitation of induction and propagation of the experimental CSD (Leo *et al*., 2011). The facilitation of CSD has been more recently investigated also *in vitro*, in cortical brain slices, demonstrating that the threshold for CSD induction is lower while the velocity of its propagation is higher in FHM2 KI compared to WT mice (Capuani *et al*., 2016). The specific localization and functional coupling of the α2 NKA with the GluTs in the astrocytic processes surrounding cortical glutamatergic synapses (Cholet *et* al., 2002) suggest that Glu uptake by cortical astrocytes during neuronal activity could be impaired in FHM2 KI mice with a reduced expression of the α2 NKA. Indeed, recent studies from my lab have shown that the rate of Glu clearance, obtained by measuring the time constant of decay of the synaptically activated transporter current (STC) elicited in cortical astrocytes by extracellular stimulation, is slower in an activity-dependent manner in FHM2 KI compared to WT mice (Capuani *et al*., 2016).

In light of these results the first aim of my PhD project was to investigate whether there is a relation of cause and effect between the reduced rate of Glu clearance by cortical astrocytes and CSD facilitation in FMH2 KI mice. To test this hypothesis I used two different approaches: in the first approach I tested whether the facilitation of CSD in FHM2 KI mice could be rescued by systemic treatment with ceftriaxone (Cef), a drug that increases the membrane expression of GLT-1 in the neocortex of WT mice (Bellesi *et al*., 2009). In the second approach I investigated whether pharmacological reduction of the rate of Glu clearance in WT mice to a value similar to that of FHM2 KI mice reduces the threshold for CSD

induction and increases the velocity of CSD propagation to values similar to those in the FHM2 mutants.

The second aim of my PhD project was to investigate the consequences of the reduced rate of Glu clearance on excitatory synaptic transmission and in particular the activation of NMDARs, given the key role that these receptors play in CSD initiation and propagation (Pietrobon and Moskowitz, 2014) and given the fact that, due to their higher affinity for Glu than α-amino-3-hydroxy-5-methyl-4-isoxazole-propionic acid receptors (AMPARs), they are expected to be particularly sensitive to Glu spillover, that should be increased as a consequence of the reduced rate of Glu clearance in FHM2 KI mice.

To this aim I recorded in isolation at +40 mV the NMDARs-EPSC from voltage clamped L2/3 Pyrs of the barrel cortex upon extracellular stimulation in L1 in acute cortical slices from WT and FHM2 KI mice (in the presence of Gabazine and NBQX, inhibitors of GABA and AMPA receptors, respectively). I measured the amplitude, the half time of the decay and the area under the curve of postsynaptic NMDARs-EPSC for comparison of the two phenotype.

NMDARs are ligand-gated ionotropic Glu receptors that assemble as heteroteramers associating two mandatory GluN1 subunits and two GluN2 subunits, of which there are four subtypes (GluN2A-D) (Zhu and Paoletti, 2015). The diheteromeric GluN2B receptors (GluN2BRs) display the higher affinity for glutamate among the NMDARs subtype and hence are predicted to be preferentially activated by Glu spillover (Paoletti *et al*., 2013). Therefore, the third aim of my PhD project was to investigate the pharmacological profile of the NMDARs-EPSC elicited in L2/3 Pyrs in WT and FHM2 KI mice.

Previous findings from the lab in FHM1 KI mice demonstrated an unaltered inhibitory transmission at several cortical inhibitory synapses, in contrast with increased excitatory neurotransmission at cortical Pyrs synapses (Tottene *et al*., 2009). This differential effect of FHM1 mutation at excitatory and inhibitory synapses suggests the working hypothesis that a dysfunctional excitatory/inhibitory (E/I) balance in specific cortical circuits might be the key pathogenic mechanisms in FHM.

As a first test of this hypothesis, we decided to investigate whether FHM mutations alter the dynamic regulation of the E/I balance in L2/3 during recurrent network activity induced by optogenetic activation of L2/3 pyramidal cells with different types of light stimuli, that presumably mimick different types of physiological activity. Selective expression of channelrhodopsin-2 (ChR2) in L2/3 Pyrs of the barrel cortex can be obtained by performing *in utero* electroporation at day 15.5 of gestation (Szczurkowska *et al*., 2016).

The fourth aim of my PhD research project was to implement and optimize the *in utero* electroporation protocol described in Szczurkowska *et al*., 2016, in order to improve the number of pregnant females, the number of surviving electroporated pups and to obtain a good selective expression of ChR2 in L2/3 of the somatosensory cortex.

3. RESULTS

3.1. Is there a causative relationship between the reduced rate of glutamate clearance by astrocytes and cortical spreading depression facilitation in FHM2 KI mice?

To study whether there is a causative relationship between the reduced rate of Glu clearance and CSD facilitation in FHM2 KI mice we used two different approaches.

3.1.1 Approach 1: effects on CSD facilitation of systemic treatment of FHM2 KI mice with Ceftriaxone (Cef)

As a first approach we investigated the effect of Cef in FHM2 KI mice. Cef is a β-lactam antibiotic that act to inhibit bacterial synthetic pathways and when delivered to animals increases the membrane expression of the glial glutamate transporter 1 (GLT-1), in the neocortex (Rothstein *et al.*, 2005; Bellesi *et al.*, 2009). Cef and other β-lactams were found to be potent stimulators of GLT-1 expression and this appears mediated through increased transcription of GLT-1 gene (Su *et al.*, 2003).

In collaboration with Professor Fiorenzo Conti from the University of Ancona, it has been shown that western blot of cortical crude synaptic membranes from WT mice injected for 8 days with Cef (200 mg/Kg) display a 63% increase in GLT-1a protein level (163,51 ± 9,89 versus 100,00 ± 7,98) compared to those from WT mice injected with saline alone (Fig 3.1 A). Using double-labeling immunofluorescence of GLT-1a and vesicular glutamate transporter 1 (VGLUT1, which is expressed in the large majority of cortical excitatory terminals (Kaneko *et al.*, 2002), in sections of somatosensory cortex, it has been shown that the mean size of the GLT-1a immunoreactivity (ir) positive puncta (GLT-1a+) overlapping with VGLUT1 ir positive puncta (VGLUT1+) is increased by 58% in Cef-treated compared to saline-treated control animals (0.84 ± 0.03 versus 0.53 ± 0.03 μm^2; Fig 3.1 B). Overlapping signals are consistent with a strict colocalization of GLT-1a and VGLUT1 in cortical sections and the change in size of ir puncta has been considered strongly suggestive of a change in protein expression (Bozdagi *et al.*,

2000; Bragina *et al.*, 2006; Omrani *et al.*, 2009). Therefore, these data indicate that Cef treatment increases GLT-1a expression at cortical excitatory terminals in WT mice (Capuani *et al.*, 2016).

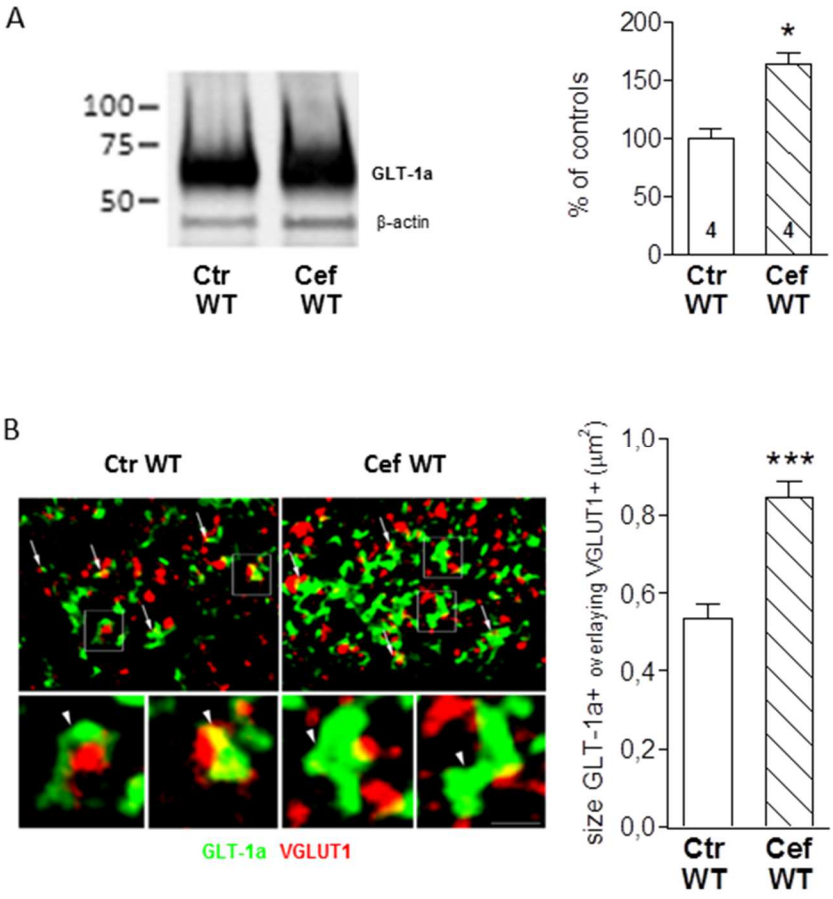

Figure 3.1 Ceftriaxone treatment increases GLT-1a expression and the mean size of the GLT-1a+ puncta overlapping with VGLUT1 in WT mice (adapted from Capuani *et al.*, 2016).

A Western blottings of GLT-1a in cortical crude synaptic membranes of P39 WT mice following Cef treatment. GLT-1a levels are significantly increased in mice treated with Cef (Cef WT, $N = 4$) compared to control saline-injected mice (Ctr WT, $N = 4$) (Mann-Whitney U-test: $^{*}P = 0.028$). Data are mean ± SEM.

B Immunofluorescence of GLT-1a+ puncta (green) and VGLUT1+ puncta (red) in sections from SI of P45-46 WT mice that were treated with saline (Ctr WT) or Cef (Cef WT). Arrows point to some GLT-1a/VGLUT1-related puncta. Framed regions (and relative magnifications below) are examples of GLT-1a/VGLUT1-related puncta (arrowheads). Right, Cef treatment increased significantly the size of GLT-1a+ puncta overlaying VGLUT1 (142 and 186 GLT-1a+ puncta analyzed from 4 Ctr WT and 4 Cef WT mice, respectively; 3 sections/animal) (Mann-Whitney U-test: $^{***}P < 0.0001$). Data are mean ± SEM. All microscopic fields are from L2/3. Scale bars: 3.5 µm for left and right upper panels and 1 µm for enlarged framed areas.

In light of these results, I measured the threshold of CSD induction and the velocity of CSD propagation in cortical slices from P30-33 FHM2 KI mice that had been injected for 8 days with either Cef (200 mg/Kg) or saline. CSD was elicited *in vitro* by application of brief pressure ejection pulses of high KCl (3M) of increasing duration, onto L2/3 of acute cortical slices of mouse somatosensory cortex as in Tottene *et al*., 2009. The duration of the first pulse eliciting a CSD was taken as CSD threshold and it was easily detectable by the typical spreading changes in the intrinsic optic signal (IOS). The rate of horizontal spread of the change in intrinsic optical signals was taken as velocity of CSD propagation (Tottene *et al*. 2009) (see also 5.11.1 of the "Materials and Methods"). I found that the threshold for CSD induction was slightly but significantly increased by 12% (162 ± 5 versus 145 ± 5 ms) in cortical slices from Cef-treated compared to saline-treated FHM2 KI mice (Fig 3.2). The velocity of CSD propagation was similar in cortical slices from Cef-treated compared to saline-treated FHM2 KI mice (3,82 ± 0,08 versus 3,83 ± 0,07 mm/min) (Fig 3.2). Moreover, the frequency of spontaneous CSDs, which at this age is relatively small (in 7 out of 47 slices from saline-injected FHM2 KI mice), decreased in Cef-treated mice (in 2 out of 40 slices).

These results indicate that Cef treatment rescues a small fraction of the facilitation of CSD induction in FHM2 KI mice without affecting the facilitation of CSD propagation.

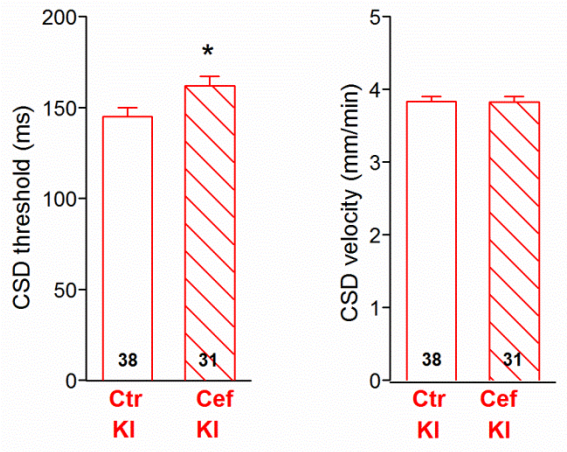

Figure 3.2 The threshold for cortical spreading depression induction is increased in cortical slices of FHM2 KI mice after ceftriaxone treatment that increases the GLT-1a expression in WT mice (adapted from Capuani *et al.*, 2016). CSD threshold and velocity of propagation in cortical slices from P30-33 KI mice that were injected with saline (Ctr KI, n = 38; N = 7) or Cef (Cef KI, n = 31; N = 6). CSD threshold is 12% higher (Mann-Whitney U-test: $^*P$ = 0.02) in Cef-treated compared to saline-treated KI mice. CSD velocity is not altered by Cef treatment (Mann-Whitney U-test: P = 0.90). Data are mean ± SEM.

Given the findings suggesting a necessary tight coupling between the α2 NKA and GLT-1a in perisynaptic astrocytic processes (PAPs) (Capuani *et al.* 2016), we asked whether Cef effectively increased the density of GLT-1a in cortical PAPs of FHM2 KI mice having a 50% reduced α2 NKA expression.

Using post-embedding immunogold electron microscopy (EM), Dr. Marcello Melone in the group of Professor Fiorenzo Conti, measured the density of GLT-1a gold particles associated with the membrane of PAPs in cortical sections from Cef- and saline-injected FHM2 KI mice. Interestingly, he found that, the density of GLT-1a gold particles in the membrane of PAPs was unaltered by Cef-treatment (23,31 ± 1,19 versus 21,13 ± 1,16 particles/μm^2) while the density of GLT-1a in AxTs was larger in Cef-treated than in saline-treated FHM2 KI mice (18,50 ± 1,18 versus 14,40 ± 1,22 particles/μm^2) (Fig 3.3 A and B) (Capuani *et al.*, 2016).

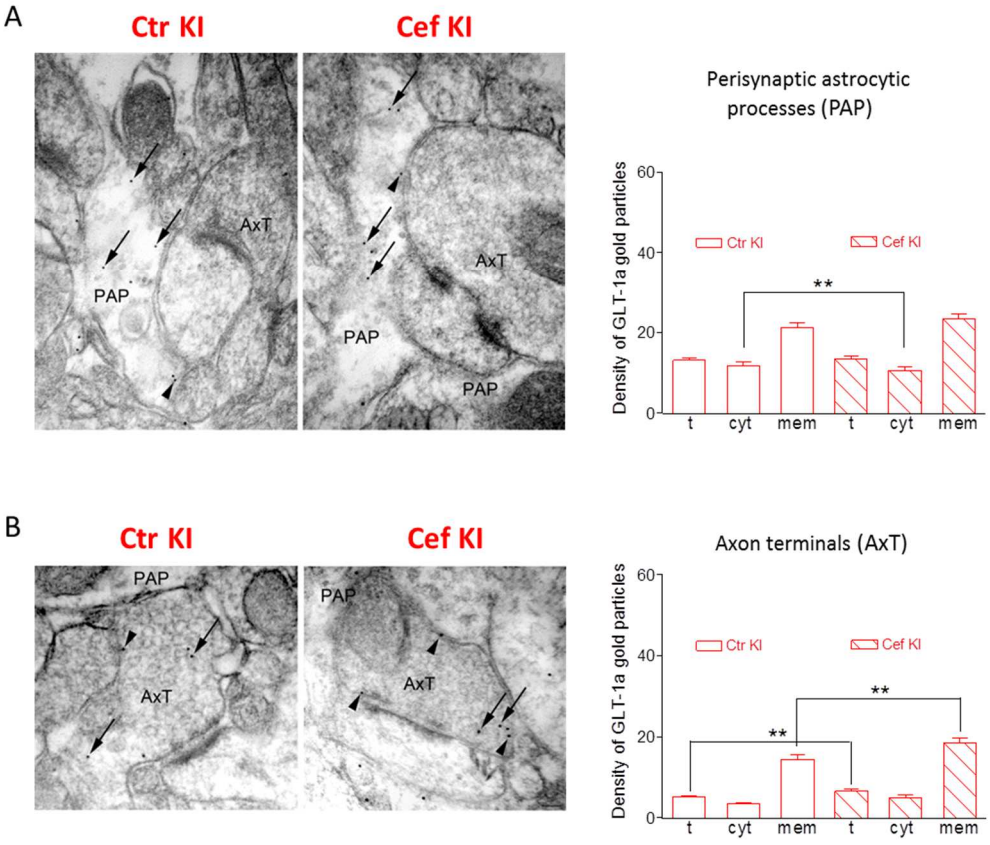

Figure 3.3 The density of GLT-1a in the membrane of cortical perisynaptic astrocytic processes is not altered by ceftriaxone treatment in W887R/+ FHM2 KI mice, while the density of GLT-1a in the axon terminals is increased (adapted from Capuani *et al.*, 2016).

A Distribution of GLT-1a gold particles in PAP of saline-injected (Ctr KI, *N* = 4) and Cef-treated KI mice (Cef KI, *N* = 4) (P45-46). Cef-treatment does not modify the density of total (Mann-Whitney *U*-test: *P* = 0.27) and membrane-associated (arrowheads) (Mann-Whitney *U*-test: *P* = 0.27) gold particles in PAP of KI mice.
B Distribution of GLT-1a gold particles in AxTs in saline-injected (Ctr KI, *N* = 4) and Cef KI mice (Cef KI, *N* = 4). The density of the membrane-associated gold particles (arrowheads) is increased in Cef-treated KI mice (Mann-Whitney *U*-test: **P* = 0.007). All microscopic fields in A and B are from L2/3. *t*, total density; cyt, cytoplasmic density; mem, membrane density. Scale bar 100 nm. Data are mean ± SEM.

Moreover, the GLT-1a protein expression level and the size of GLT-1a+ ir puncta that overlapped with VGLUT1+ ir in the cortex of Cef- and saline-treated FHM2 KI were similar (106,29 ± 8,39 versus 100,00 ± 11,18 for protein expression level and 0,47 ± 0,03 versus 0,44 ± 0,03 μm^2 for immunofluorescence data) (Fig 3.4 A and B) (Capuani *et al.*, 2016).

These findings are consistent with the relative inefficacy of Cef in the rescue of CSD facilitation in FHM2 KI mice and further support the idea that there is a tight coupling between NKA and GLT-1a in PAPs (Capuani *et al.*, 2016). The small increase in the CSD threshold after Cef treatment might be due to the increased GLT-1a expression and Glu uptake in the AxTs. However GLT-1a in the AxTs accounts for only a small fraction of total brain GLT-1a (Chen *et al.*, 2004; Furness *et al.*, 2008; Melone *et al.*, 2009).

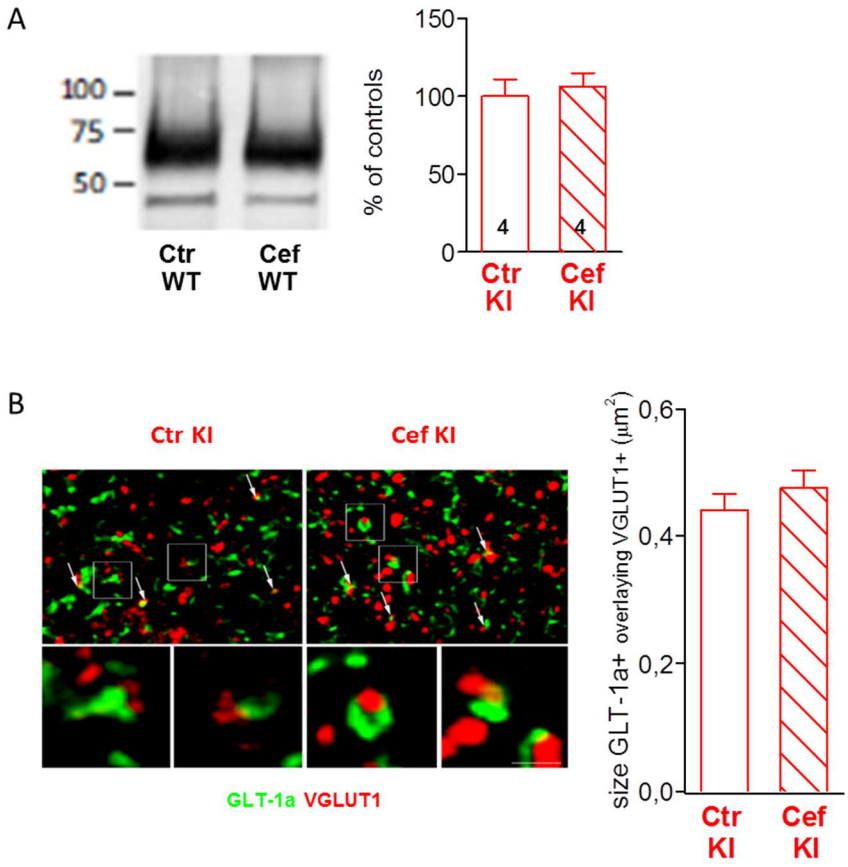

Figure 3.4 GLT-1a expression and the mean size of the GLT-1a+ puncta overlapping with VGLUT1 are similar in ceftriaxone treated mice (adapted from Capuani *et al.*, 2016).
A Western blottings of GLT-1a in cortical crude synaptic membranes of P39 KI mice following Cef treatment. GLT-1a levels are similar in Cef-treated (Cef KI, $N = 4$) and saline-injected (Ctr KI, $N = 4$)) (Mann-Whitney U-test: $P = 0.83$). Data are mean ± SEM.
B Visualization of GLT-1a+ puncta (green) and VGLUT1+ puncta (red) in KI mice that received saline (Ctr KI) and in Cef-treated KI mice (Cef KI) (P45-46). Arrows point to some GLT-1a/VGLUT1-related puncta; framed regions are examples of GLT-1a/VGLUT1-related puncta (arrowheads). Right, Cef treatment does not increase the size of GLT-1a+ puncta overlaying with VGLUT1 (160 and 175 GLT-1a+ puncta analyzed from the same 4 Ctr KI and 4 Cef KI used for post-embedding electron microscopy analysis; three sections/animal) (Mann-Whitney U-test: $P = 0.31$). Data are mean ± SEM. Scale bars: 3.5 µm for left and right upper panels and 1 µm for enlarged framed areas. All microscopic fields are from L2/3.

3.1.2 Approach 2: effects of the pharmacological inhibition of a fraction of glutamate transporters in WT mice to reduce the rate of glutamate clearance to a value similar to that in FHM2 KI mice

The first approach did not allow us to draw a clear-cut conclusion about the relationship between the reduced rate of Glu clearance by cortical astrocytes during neuronal activity and the facilitation of CSD in FHM2 KI mice. Therefore, as a

second approach, I investigated whether the pharmacological reduction of the rate of Glu clearance in WT mice to a value similar to that produced by the W887R mutation in FHM2 KI, reduces the threshold for CSD induction and increases the velocity of CSD propagation in WT mice to values similar to those in FHM2 KI mice.

It is possible to obtain a measure of the rate of Glu clearance by astrocytes taking advantage of the fact that Glu uptake by the GluTs is electrogenic. Indeed, it is coupled to the influx of 3 Na^+ and 1 H^+ ions and efflux of 1 K^+ ion, resulting in the translocation of net positive charge during each transport cycle, therefore it can be measured electrophysiologically in voltage-clamped astrocytes. The so called synaptically activated transporter current (STC) is the rapidly decaying component of the total inward current elicited in voltage-clamped astrocytes by extracellular stimulation of the neuronal afferents, as shown by its complete inhibition by TBOA. The time constant of decay of the STC gives a measure of the rate of Glu clearance by astrocytes: the larger is tau, the slower is the rate of Glu clearance (Fig 3.5 B).

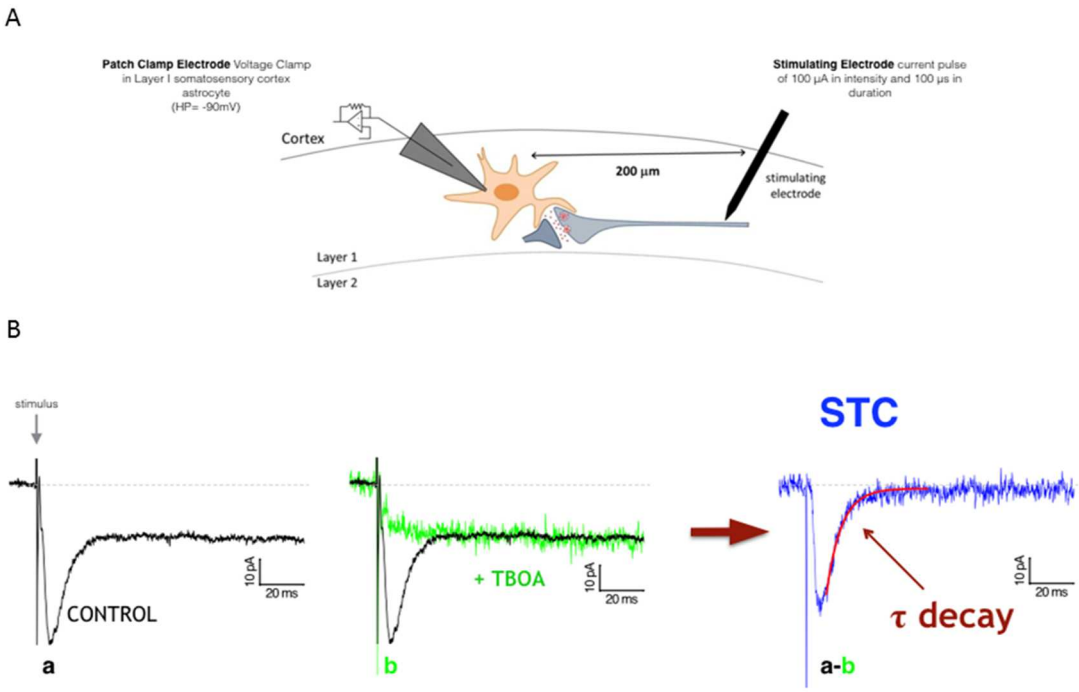

Figure 3.5 The rate of glutamate clearance by cortical astrocytes measured from the decay kinetics of the synaptically activated transporter current (Capuani *et al.*, 2016).
A Scheme of the STC recording paradigm. The currents elicited by extracellular stimulation in L1 were measured in voltage-clamped L1 astrocyte located at 200 µm from the stimulating electrode in an acute cortical slice of mouse barrel cortex.
B Time constant of decay (τ_{decay}) of the STC isolated pharmacologically. Superimposed representative traces of the inward current evoked in an astrocyte (held at -90 mV) by a single pulse stimulation (indicated by the arrow) in an acute cortical brain slice, before (trace a) and after (trace b) application of a saturating concentration of the Glu transporter inhibitor TBOA. The STC was obtained by subtracting the residual current remaining in the presence of TBOA from the total inward current (traces a – b); the decay of the STC was best fitted by a single exponential function (τ_{decay}).

To identify the concentration of the Glu transporter inhibitor DL-TBOA (TBOA), able to slow down the rate of Glu clearance in WT mice to a similar value to that in FHM2 KI mice, I measured the STC in L1 astrocytes. The STC was elicited by extracellular stimulation in L1 in acute brain slices of somatosensory cortex (Fig 3.5 A; see also 5.11.3 section in "Materials and Methods"), in the presence of 50 µM D-APV, 10 µM NBQX and Gabazine, 20 µM MK-801 and of different subsaturating concentrations of TBOA.

Using this method I found that 2.5 µM TBOA increased the time constant of decay of the STC by 32% after a single pulse stimulation, thus producing a slowdown of the rate of Glu clearance close to but larger than that produced by the mutation (32 versus 21%) (Fig 3.6 A). In the presence of 2.5 µM TBOA the CSD threshold was 36% lower than in control (142 ± 4 versus 220 ± 8 ms), and the velocity of CSD propagation was 20% higher (3,84 ± 0,09 versus 3,21 ± 0,08 mm/min) (Fig 3.6 B). Thus, pharmacological inhibition of a fraction of GluTs did facilitate CSD induction and propagation in WT mice. In correlation with the larger slowing of the rate of Glu clearance produced by 2.5 µM TBOA relative to that produced by the FHM2 mutation (32 versus 21%), the facilitation of CSD induction was also larger (36 versus 28% lower CSD threshold in 2.5 µM TBOA versus FHM2 KI, respectively; for comparison see Figs 3.6 B and 1.6 C in the "Introduction"), suggesting that the reduced rate of Glu clearance in FHM2 KI mice may account for a large part of the facilitation of CSD induction.

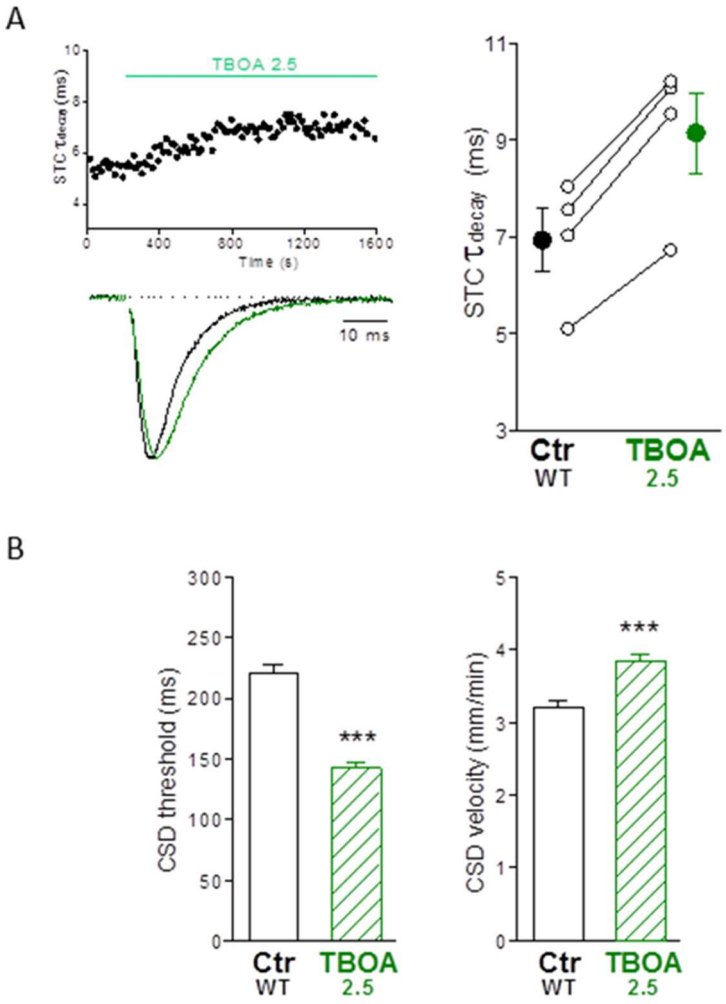

Figure 3.6 Facilitation of CSD induction and propagation after pharmacological inhibition with 2.5 µM DL-TBOA of a fraction of glutamate transporters in WT mice (Capuani *et al.*, 2016).
A τ_{decay} of the STC evoked by single pulse stimulation in L1 astrocytes in acute cortical slices from P22-23 WT mice before (Ctr WT) and after the application of 2.5 µM DL-TBOA (TBOA 2.5) (n = 4; N = 2) (right panel). The traces on the left are the corresponding average normalized STCs, isolated as in Fig 3.5 B. The STC τ_{decay} in TBOA 2.5 is 32 % higher than in Ctr WT (paired t-test: $^{**}P$ = 0,002). Data are mean ± SEM. The left top panel shows the time course of τ_{decay} of the transient component (due to the STC) of the current recorded in an astrocyte during a representative experiment in which TBOA 2.5 was applied at the time indicated by horizontal bar. The steady-state was reached after 10-15 minutes of bath application of the inhibitor.
B CSD threshold and velocity of propagation measured in cortical slices from P22-23 WT mice after perfusion for 20 minutes with extracellular solution without (Ctr WT: n = 23; N = 15) and with TBOA 2.5 (TBOA 2.5: n = 25; N = 8). CSD threshold in TBOA 2.5 is 36% lower than in Ctr WT (Mann-Whitney U-test: $^{***}P < 0.0001$) and CSD velocity is 20% higher (unpaired t-test: $^{***}P$ < 0,0001). Data are mean ± SEM.

To establish whether impaired Glu clearance in FHM2 mice may completely account for the facilitation of CSD induction, we measured the CSD threshold and velocity of propagation in the presence of a concentration of TBOA (1.5 µM) that

produced a slowing of the rate of Glu clearance quantitatively equal to that produced by the FHM2 mutation. We found that 1.5 µM TBOA lowered the threshold for CSD induction by 23% (170 ± 5 versus 220 ± 8 ms) and increased the velocity of CSD propagation by 13% compared to control (3,61 ± 0,09 versus 3,21 ± 0,08 mm/min) (Fig 3.7). These data support the conclusion that the reduced rate of Glu clearance can account for most of the facilitation of CSD induction and for a large fraction of the facilitation of CSD propagation in FHM2 KI mice.

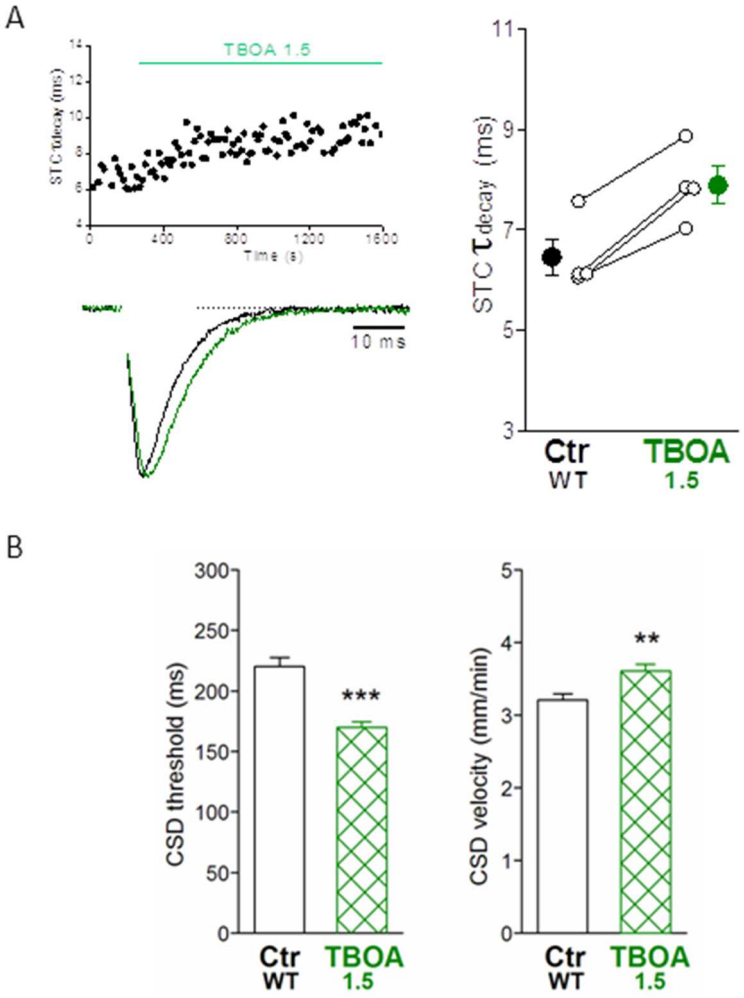

Figure 3.7 Facilitation of CSD induction and propagation after pharmacological inhibition with 1.5 µM DL-TBOA of a fraction of glutamate transporters in WT mice (Capuani *et al.*, 2016).
A τ_{decay} of the STC evoked by single pulse stimulation in L1 astrocytes in acute cortical slices from P22-23 WT mice before (Ctr WT) and after the application of 1.5 µM TBOA (TBOA 1.5) (n = 4; N = 4) (right panel). The traces on the left are the corresponding average normalized STCs, isolated as in Fig 3.5 B. The STC τ_{decay} in TBOA 1.5 is 22% higher than in Ctr WT (paired t-test: $^{**}P$ = 0,004). Data are mean ± SEM. The left top panel

shows the time course of τ_{decay} of the transient component (due to the STC) of the current recorded in astrocytes during a representative experiment in which TBOA 1.5 was applied at the time indicated by horizontal bar.
B CSD threshold and velocity of propagation measured in cortical slices from P22-23 WT mice after perfusion for 20 minutes with extracellular solution without (Ctr WT: n = 23; N = 15) and with 1.5 µM TBOA (TBOA 1.5: n = 18; N = 6). CSD threshold in TBOA 1.5 is 23% lower than in Ctr WT (Mann-Whitney U-test: ***P < 0.0001) and CSD velocity is 13% higher (unpaired t-test: **P = 0,003). Data are mean ± SEM.

3.1.3 Activity-dependent slowing of the extracellular glutamate kinetics in FHM2 KI mice somatosensory cortex

Previously in the lab it has been demonstrated that the rate of Glu clearance by cortical astrocytes during neuronal activity, as measured by decay kinetics of the STC (using the method described in 3.1.2, Fig 3.5), is impaired in FHM2 KI mice. It has been also shown that the slowing of Glu clearance in FHM2 KI mice was quantitatively larger after repetitive stimulation than after a single pulse stimulation and increased with increasing stimulation frequency (Capuani *et al.*, 2016) (Fig 3.8).

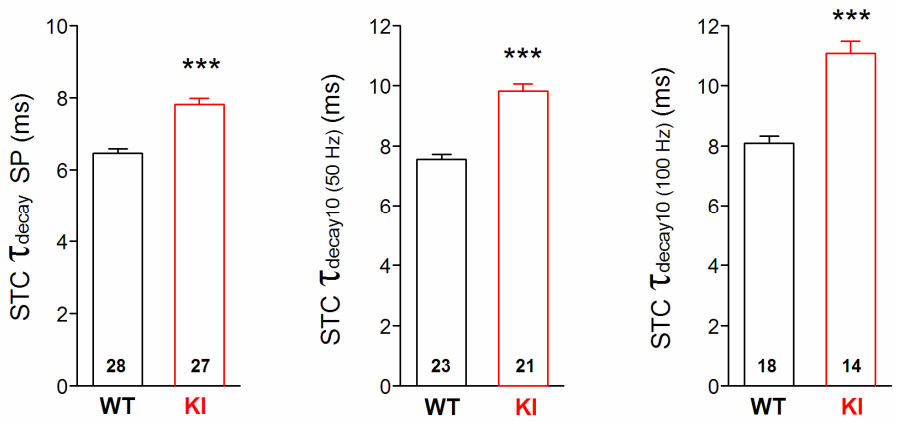

Figure 3.8 The rate of glutamate clearance by cortical astrocytes is slower in FHM2 KI relative to WT mice. The slowing down of glutamate clearance in FHM2 KI relative to WT mice is larger after train of action potentials at high frequency than after a single action potential (Capuani *et al.*, 2016).
Left: the bar plot shows the average values of τ_{decay} of the STC after a single pulse stimulation, isolated as in Fig 3.5 A-B, in cortical slices from P22-23 WT (n = 28; N = 11) and FHM2 KI mice (n = 27; N = 9). STC τ_{decay} is 21% higher in FHM2 KI compared to WT astrocytes (7,82 ± 0,16 vs 6,46 ± 0,13 ms). (unpaired t-test: ***P < 0,0001). Centre and right: bar plot showing the average values of τ_{decay} of the STC elicited by the 10th pulse of a 50 Hz ($\tau_{decay10\ (50Hz)}$, central panel) and 100 Hz ($\tau_{decay10\ (100Hz)}$, right panel) trains in L1 astrocytes in acute cortical slices from P22-23 WT (n = 23; N = 10 for 50 Hz and n = 18; N = 8 for 100 Hz) and FHM2 KI mice (n = 21; N = 9 for 50 Hz and n = 14; N = 7 for 100 Hz). The STC $\tau_{decay10\ (50Hz)}$ and $\tau_{decay10\ (100Hz)}$ are 30% (9,82 ± 0,24 vs 7,56 ± 0,16 ms) and 37% (11,08 ± 0,41 vs 8,09 ± 0,23 ms) higher in FHM2 KI compared to WT, respectively. (unpaired t-test: ***P < 0,0001 in both cases). Data are mean ± SEM.

Glutamate clearance in FHM2 KI mice has been further investigated in collaboration with Dr. Mirko Santello from the University of Zurich. He measured the Glu transients using the fluorescent genetically encoded glutamate sensor iGluSnFr, expressed in cortical astrocytes, in combination with two-photon microscopy. iGluSnFr is a biosensor composed of a glutamate binding protein coupled to a fluorescent readout that allows the measurement of extracellular Glu. WT and FHM2 KI mice were injected with adeno-associated virus under the GFAP promoter to selectively drive the expression of iGluSnFr in the membrane of cortical astrocytes. This set-up allows high spatial and temporal resolution measurements of the dynamics of synaptically released Glu after stimulation.

Glu transients were elicited in L1 of the barrel cortex of acute cortical brain slices from FHM2 KI and WT mice, by extracellular stimulation in L1 with a theta-glass pipette (Fig 3.9 A) using the same protocols as for the STC. In agreement with the previous results obtained in my lab relative to the slowing of the rate of Glu clearance, the decay kinetics of the Glu transients were significantly slower by 23% in FHM2 KI compared to WT mice after a single pulse (SP) stimulation (τ_{decay}: 58,58 ± 5,01 versus 47,69 ± 2,05 ms) (Fig 3.9 B). The slowdown of the Glu transients decay kinetics in FHM2 KI mice is activity-dependent since it was larger after a train of pulses compared to a single pulse, in fact it is slowed by 30 and 28% in FHM2 KI compared to WT mice after a train of 10 pulses at 50 and 100 Hz, respectively ($\tau_{decay10(50Hz)}$: 118,14 ± 7,6 versus 91,24 ± 3,29 ms; $\tau_{decay10(100Hz)}$: 128,44 ± 8,12 versus 100,31 ± 4,83 ms) (Fig 3.9 B). These results confirm with a different technique previous findings, obtained by measuring the time constant of decay of the STC, demonstrating a slowing of the Glu uptake by cortical astrocytes during neuronal activity.

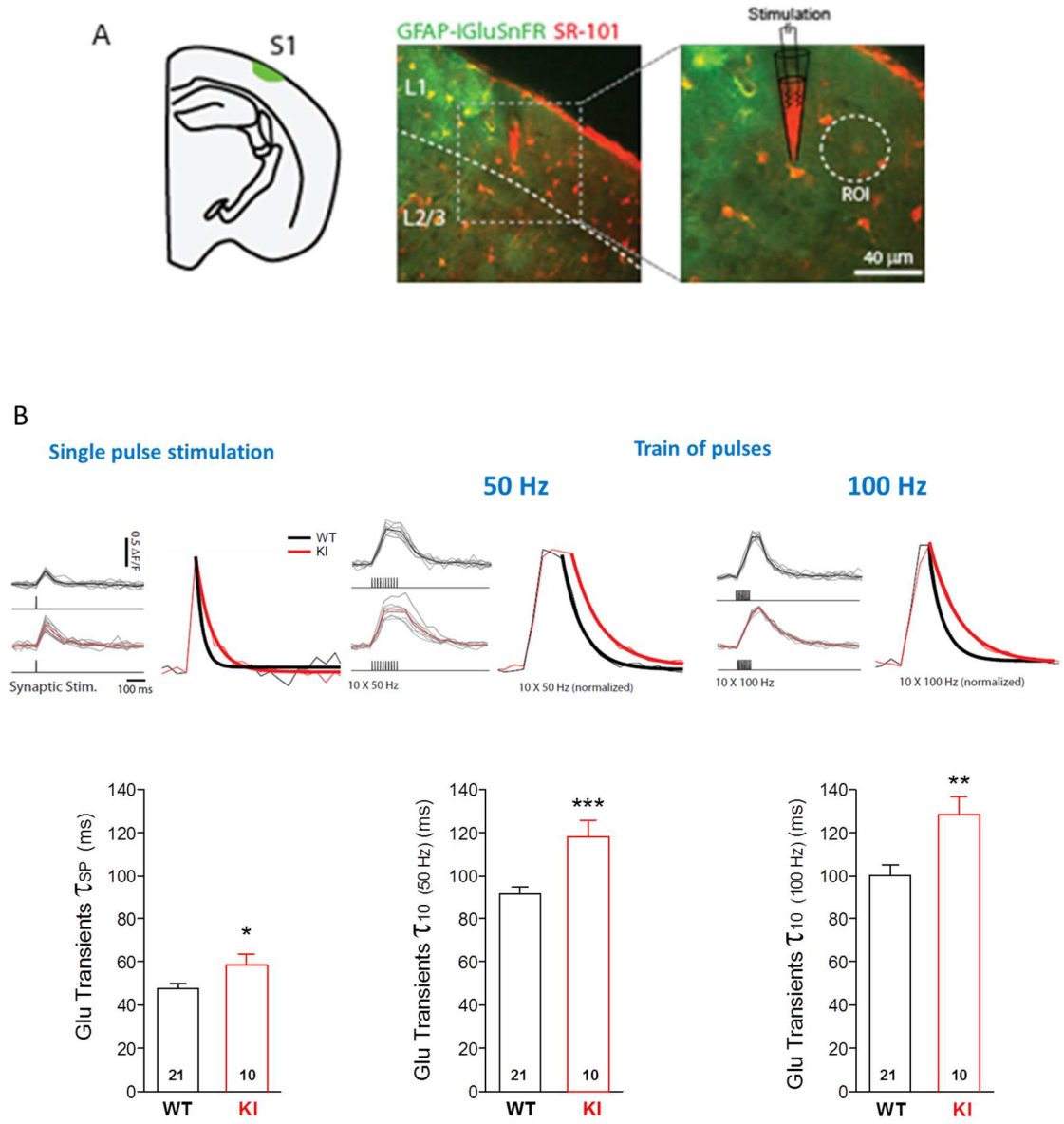

Figure 3.9 Extracellular glutamate kinetics, measured using the genetically encoded glutamate iGluSnFr sensor expressed in somatosensory cortex astrocytes, are slower in FHM2 KI mice in an activity-dependent manner.

A iGluSnFr expression in the adult mouse somatosensory cortex. The glutamate sensor (in green) is expressed by viral injection (AAV2/1.GFAP.iGluSnFr.WPRE.SV40) specifically on the plasma membrane of FHM2 KI and WT mice astrocytes. 15-18 days after viral injection, synaptic glutamate release was elicited by extracellular stimulation with a thetaglass pipette containing Sulforhodamine 101 for visualization (SR101 in red that stained astrocytes), placed in inner L1 (with similar protocols and solutions as for the STC measurements, T = 34°C). Using a galvanometer-based two-photon (2P) laser scanning system (excitation wavelength 900 nm, acquisition rate 19.2 Hz), fluorescence emission was collected from a region of interest (ROI, diameter 34 µm) 10-40 µm away from the stimulation pipette.

B Top panel: superimposed representative pooled traces resulting from the robust increase in iGluSnFr emission in WT (black) and FHM2 KI (red) mice following a single stimulation, 10 pulses at 50 Hz (10X50 Hz) and 10 pulses at 100 Hz (10X100Hz). Thick lines represent the superimposed mono-exponential fit of the decay of the iGluSnFr transients from WT (black) and FHM2 KI (red). **Bottom panel:** On the left, 23%

slowing of the τ_{decay} of the Glu transients evoked by a single stimulation (as described in A) in FHM2 KI (n = 10; N = 4) compared to WT mice (n = 21; N = 9) (unpaired t-test: $^{*}P$ = 0,02). Middle: τ_{decay} of the Glu transients evoked by trains of 10 pulses at 50 Hz. The slowing of the decay kinetics is 30% higher after trains of 10 pulses at 50 Hz frequency in FHM2 KI (n = 10; N = 4) compared to WT (n = 21; N = 9) (unpaired t-test: $^{***}P = 6{,}68\text{x}10^{-4}$). Right: τ_{decay} of the Glu transients evoked by trains of 10 pulses at 100 Hz, is higher in FHM2 KI (n = 10; N = 4) compared to WT mice (n = 21; N = 9) (unpaired t-test: $^{**}P$ = 0,003). Data are mean ± SEM.

3.2 Is there an increased activation of *N*-Methyl-D-Aspartate receptors (NMDARs) due to glutamate spillover as a consequence of the reduced rate of glutamate clearance by astrocytes in FHM2 KI mice?

Given that the rate of Glu clearance, as measured by the decay kinetics of the STC and the Glu transients, is impaired in FHM2 KI mice I studied the effect of this impairment on synaptic transmission. In particular, I studied the effect of the reduced rate of Glu uptake on the activity of NMDARs, given that pharmacological data support their key role in CSD initiation mechanisms and the fact that, given their high affinity for Glu, they are expected to be particularly sensitive to Glu spillover, that shold be increased in FHM2 KI mice. The hypothesis is that facilitation of CSD ignition in FHM2 KI mice may be due to excessive activation of NMDARs, as a consequence of the increased Glu spillover due to the reduced rate of Glu clearance. Therefore, I recorded the NMDARs-EPSC in L2/3 Pyrs elicited by extracellular stimulation in L1 in acute cortical slices from FHM2-KI mice (see also 5.11.4 in “Materials and Methods”).

It has been shown that almost saturating concentration of the GluTs inhibitor TBOA (30 µM), which produces a fourfold increase in the decay time constant of the STC, slows by 47% the decay kinetics of NMDARs-EPSC (measured at +40 mV to unlock the Mg^{2+} block) at hippocampal synapses, and produces only a small increase by 17% of the amplitude (Diamond, 2001). I performed preliminary experiments to test whether a much lower concentration of TBOA (1.5 µM), able to reduce the rate of Glu clearance in WT to a similar extent as the FHM2 KI mice (21% STC reduction, Fig 3.7 A), affects NMDARs-EPSC in L2/3 Pyrs. I measured in isolation at +40 mV the NMDARs-EPSC from whole cell voltage clamped L2/3 Pyrs upon extracellular stimulation in L1 in acute cortical slices, in the presence of

10 µM NBQX and Gabazine (for details see also 5.11.4 and Fig 5.7 in "Materials and Methods").

As shown by the representative traces in Fig 3.10, 1.5 µM TBOA, the concentration that slows the rate of Glu clearance in WT mice to a similar extent as the FHM2 mutation, exerted an effect on NMDARs-EPSC, slowing the decay kinetics and increasing the amplitude of NMDARs-mediated current elicited in cortical L2/3 Pyrs by single pulse (SP) stimulation.

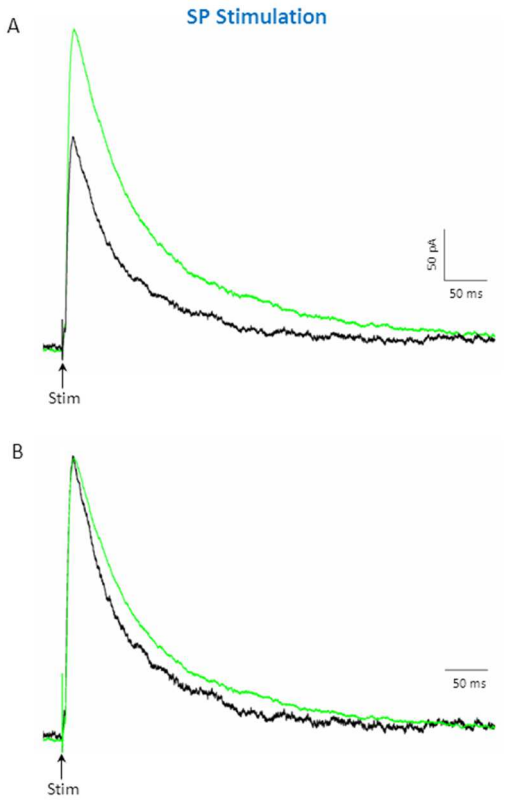

Figure 3.10 Effects of 1.5 µM DL-TBOA (the concentration that slowed the rate of glutamate clearance in WT mice to a similar extent as FHM2 mutation) on NMDARs-EPSC in WT mice.
A Representative pooled traces showing an increase by 51% of the NMDARs-EPSC amplitude evoked by a SP stimulation (as described in 5.11.4 in "Materials and Methods"), in Ctr conditions (black trace) and after 20 minutes of 1.5 µM DL-TBOA perfusion (green trace).
B Representative normalized traces corresponding to that in the upper panel showing a slowing by 33% of the decay kinetics of NMDARs-EPSC, as measured from the half time of decay, evoked as described in A, in Ctr conditions (black trace) and in the presence of 1.5 µM TBOA (green trace).

In light of the preliminary results obtained using 1.5 µM TBOA I recorded the NMDARs-EPSC in WT and FHM2 KI mice. I compared the amplitude, the decay kinetics, measured as half time of decay of the current, and the total charge transfer mediated by NMDARs, as measured from the area under the curve, in FHM2 KI and WT mice.

After a SP stimulation (50 µA of intensity, 100 µs length), I found that the amplitude of NMDARs-mediated current was increased by 45% in FHM2 KI

compared to WT mice (211,48 ± 16,26 versus 145,45 ± 14,11 pA) (Fig 3.11 traces in A, left panel, and quantification in B) and the decay, measured as half time of decay of the NMDARs-EPSC, was 22% slowed in FHM2 KI compared to WT mice (46,56 ± 1,43 versus 38,23 ± 2,05 ms) (Fig 3.11 traces in A, right panel, and quantification in B). As a result of both the significantly increased amplitude and the slowing of the decay kinetics, the total charge transfer mediated by NMDARs was 64% higher in FHM2 KI compared to WT mice (16,16 ± 1,39 versus 9,87 ± 1,34 pA*s) (Fig 3.11 B). These data show that there is an increased activation of NMDARs in FHM2 KI compared to WT mice after a SP stimulation, presumably as a consequence of the increased Glu spillover due to the reduced rate of Glu clearance by cortical astrocytes.

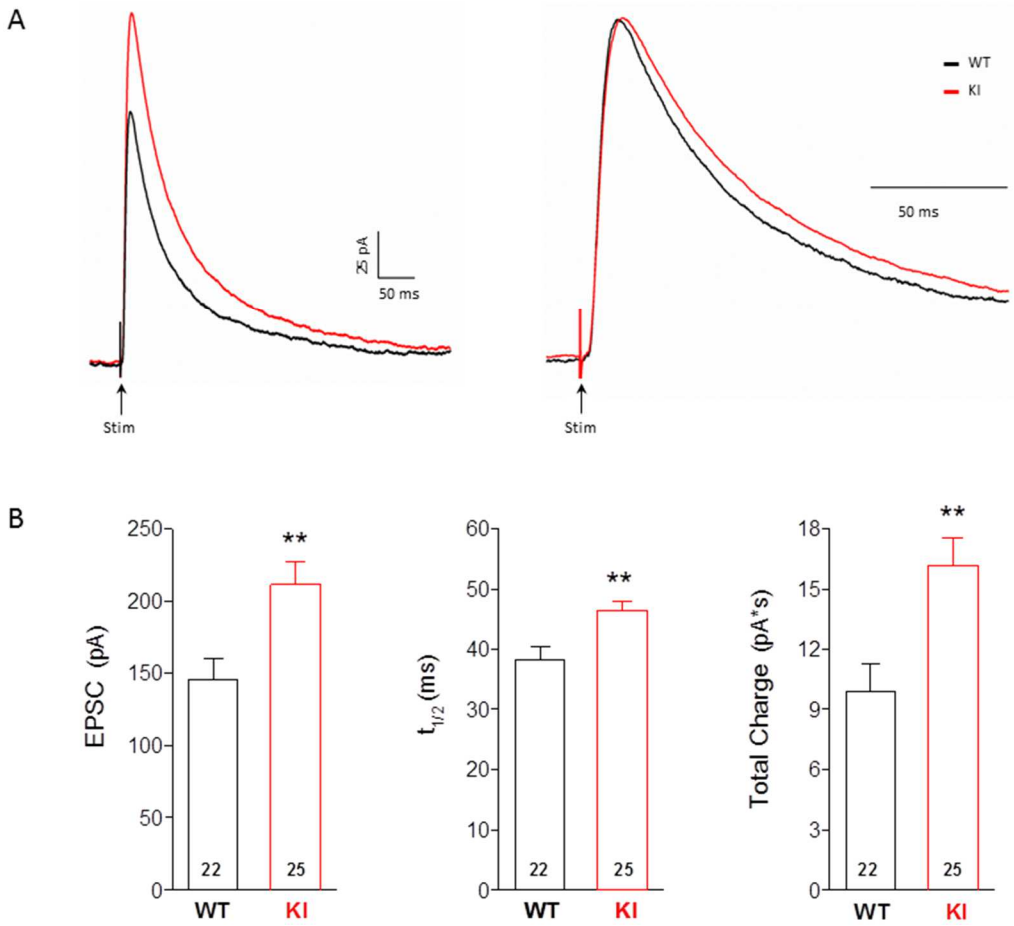

Figure 3.11 Increased activation of NMDARs after a single pulse stimulation in FHM2 KI compared to WT mice.
A Superimposed pooled traces of NMDARs-EPSC (normalized traces on the right) from WT (black trace) and FHM2 KI (red trace) mice. NMDARs-mediated current was elicited by a SP stimulation, as indicated by the arrow, in L1 somatosensory cortex and recorded from L2/3 Pyrs, from P22-23 mice of both genotypes and sex matched.
B Bar plots showing a significant increase by 45% of NMDARs-EPSC amplitude in FHM2 KI (n = 25; N = 15) compared to WT (n = 22; N = 13) mice (unpaired t-test: $^{**}P$ = 0,004) (left); a significant 22% slowing of the decay kinetics (unpaired t-test: $^{**}P$ = 0,001) (center) and a significant increase by 64% of the total charge (Mann-Whitney U-test: ** P = 0,002) (right) of NMDARs-EPSC in FHM2 KI (n = 25; N = 15) compared to WT (n = 22; N = 13). Data are mean ± SEM.

The relative slowing of the decay kinetics of NMDARs-EPSC in FHM2 KI relative to WT mice (22%) is similar to that of the decay kinetics of the STC in cortical astrocytes and extracellular Glu transients (21% and 23% slowing in FHM2 KI compared to WT mice, respectively) (Fig 3.12).

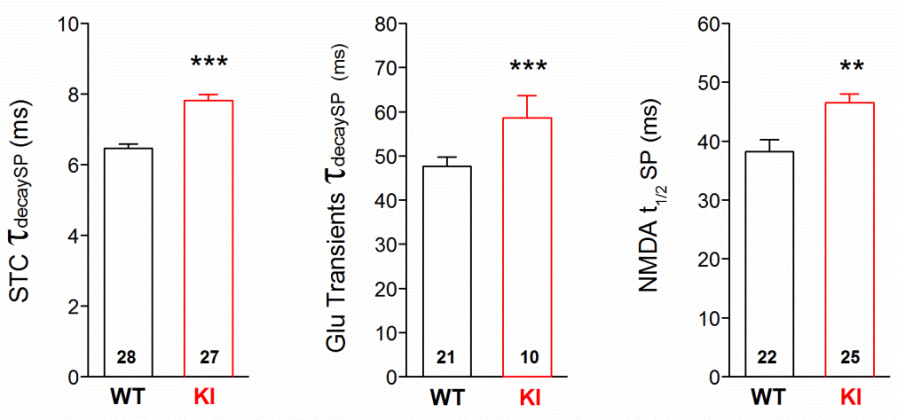

Figure 3.12 The increased activation of NMDARs after a single pulse stimulation reflects the reduced rate of glutamate clearance in FHM2 KI mice.
Bar plots showing a significant increase by 21% of the time constant of decay of the STC in FHM2 KI (n = 27; N =9) compared to WT mice (n = 28; N =11). Similar 23% increase of decay kinetics of the Glu transients in FHM2 KI (n = 10; N =4) compared to WT mice (n = 21; N =9); and of NMDARs-EPSC increased by 22% in FHM2 KI (n = 25; N = 15) compared to WT (n = 22; N = 13). Data are mean ± SEM.

Taken together these data suggest that the increased activation of NMDARs reflects the reduced rate of Glu clearance by astrocytes at cortical excitatory synapses during neuronal activity in FHM2 KI compared to WT mice.

Also the activation kinetics of NMDARs-EPSC are slower in FHM2 KI compared to WT mice, as shown from the time course of the rising phase, in fact, the time necessary for the current to reach the 95% of the peak, is 12% slower in FHM2 KI compared to WT mice (9,38 ± 0,21 versus 8,40 ± 0,38 ms) (Fig 3.13).

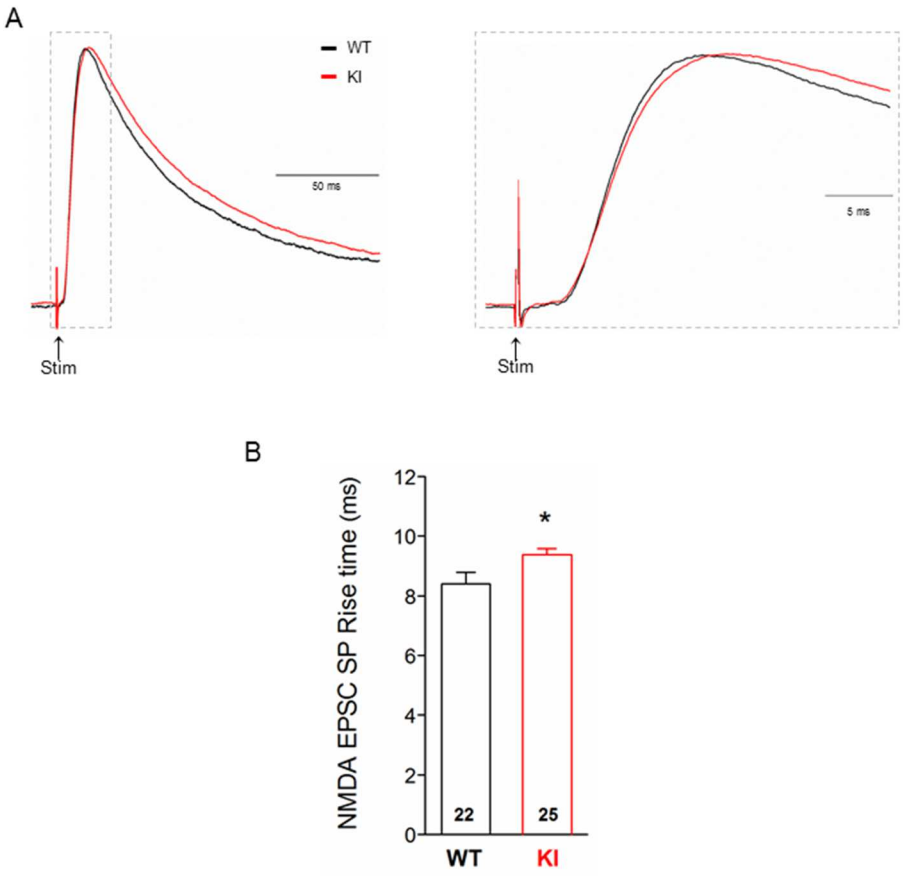

Figure 3.13 Slowing of the activation kinetics of NMDARs-EPSC elicited by a single pulse stimulation in FHM2 KI compared to WT mice.
A Left: Normalized superimposed pooled traces of NMDARs-EPSC from WT (black trace) and FHM2 KI (red trace) mice. NMDARs-mediated current was elicited by a SP stimulation, as in Fig. 3.11 A. **Right:** Magnification of the rising phase of the traces shown on the left.
B Bar plot showing a significant increase by 12% of the activation kinetics of NMDARs-EPSC in FHM2 KI (n = 25; N = 15) compared to WT (n = 22; N = 13) mice (unpaired t-test: *P = 0,02). Data are mean ± SEM.

The slowing of the decay and activation kinetics is consistent with delayed activation of NMDARs at distant sites (cooperative activation of NMDARs at

neighboring synapses and/or activation of extrasynaptic NMDARs), and/or activation of NMDARs with different subunit compositions.

In light of the results obtained using a single stimulus I tested whether the relative increase in FHM2 KI compared to WT mice is activity-dependent, as in the case of the STC and Glu transients (see 3.1.3 of the "Results"). I delivered trains of 10 pulses at 100 Hz frequency ($T_{10(100Hz)}$) using a stimulation intensity of 50 µA and, as for the SP stimulation, I compared the amplitude, the decay kinetics, and the total charge transfer mediated by NMDARs in FHM2 KI and WT mice.

After $T_{10(100Hz)}$ I found that the amplitude of NMDARs-EPSC was increased by 60% in FHM2 KI compared to WT mice (688,96 ± 52,44 versus 429,59 ± 31,51 pA) (Fig 3.14 traces in A, left panel, and quantification in B) and the half time of decay of NMDARs-EPSC was slowed by 27% in FHM2 KI compared to WT mice (123,76 ± 5,55 versus 97,55 ± 6,50 ms) (Fig 3.14 traces in A, right panel, and quantification in B). As a result of both the increased amplitude and the slowing of the decay, the total charge transfer mediated by NMDARs was 106% higher in FHM2 KI compared to WT mice (122,55 ± 12,26 versus 59,40 ± 6,24 pA*s) (Fig 3.14 B).

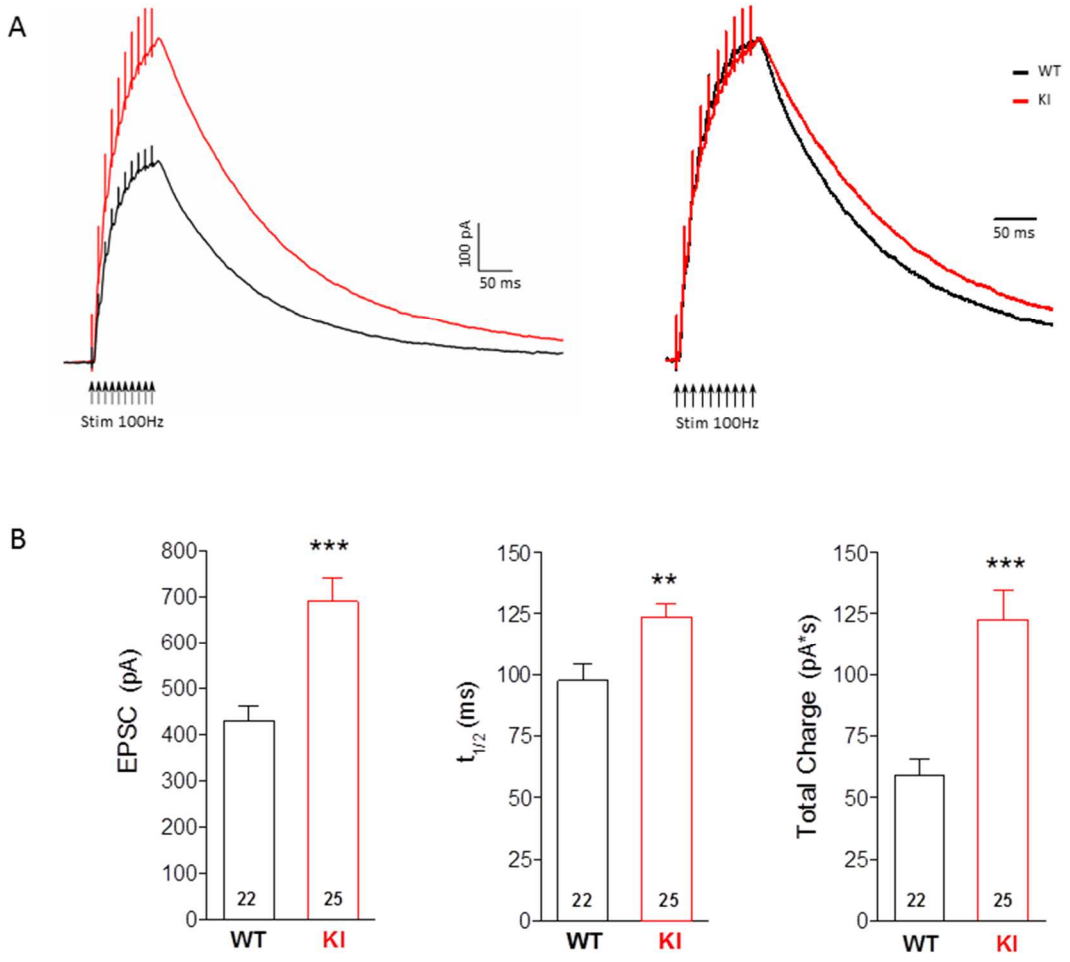

Figure 3.14 Increased activation of NMDARs after a train of 10 pulses at 100 Hz frequency in FHM2 KI compared to WT mice.

A Superimposed pooled traces of NMDARs-EPSC (normalized traces on the right) from WT (black trace) and FHM2 KI mice (red trace). NMDARs-mediated current was elicited by a train of 10 pulses at 100 Hz frequency of stimulation, as indicated by the arrows, in L1 somatosensory cortex and recorded from L2/3 Pyrs, from P22-23 mice of both genotypes and sex matched.

B Bar plots showing a significant increase by 60% of NMDARs-EPSC in FHM2 KI (n = 25; N = 15) compared to WT (n = 22; N = 13) mice (unpaired t-test: ***P = 0,0002) (left); a significant increase by 27% of the time constant of decay of NMDARs-EPSC in FHM2 KI (n = 25; N = 15) compared to WT (n = 22; N = 13) mice (unpaired t-test: **P = 0,004) (center) and a significant increase by 106% of the total charge (unpaired t-test: ***P = 0,00006) (right) of NMDARs-EPSC in FHM2 KI (n = 25; N = 15) compared to WT (n = 22; N = 13). Data are mean ± SEM.

Taken together these data demonstrate that the increased activation of NMDARs in FHM2 KI mice appears activity-dependent since it is larger after high frequency trains than after a single stimulus.

3.2.1 Both the rate of glutamate clearance and the decay kinetics of NMDARs-EPSC are slower after a high frequency stimulation compared to a single pulse stimulation

The comparison of the time constants of decay of the STC, the extracellular Glu transients and the NMDARs-EPSC elicited by a train of 10 pulses at 100 Hz frequency to those elicited by a single stimulus in WT mice (8,09 ± 0,23 versus 6,46 ± 0,13 ms for the STC; 100,31 ± 4,83 versus 47,69 ± 2,05 ms for the Glu transients and 97,55 ± 6,50 versus 38,23 ± 2,05 ms for the NMDARs-EPSC) reveals a slowing of both the rate of Glu clearance and the decay kinetics of NMDARs-EPSC after high frequency stimulation (Fig 3.15).

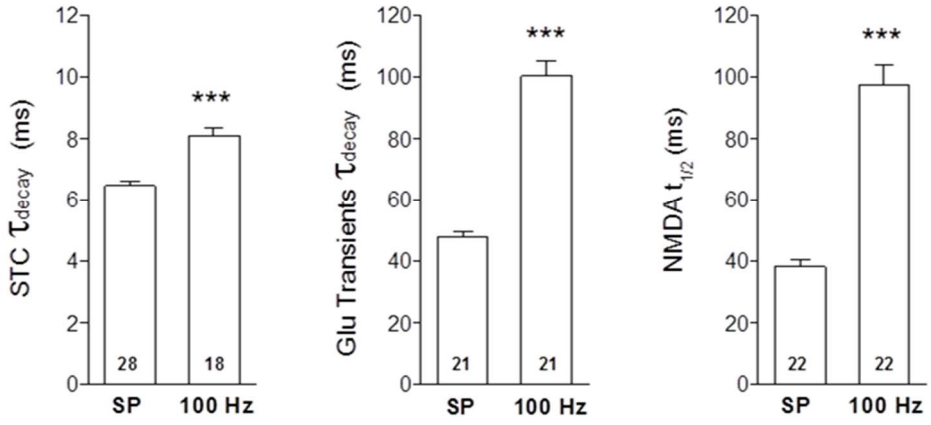

Figure 3.15 Slowing of the rate of glutamate clearance and of NMDARs-EPSC decay kinetics after a train of 10 pulses at 100 Hz compared to single pulse stimulation in WT mice.
Bar plots showing a significant increase of the time constant of decay of the STC (left), elicited in L1 cortical astrocytes of the barrel cortex by extracellular stimulation in L1, after a train of 10 pulses at 100 Hz frequency (n = 18; N = 8) compared to a SP stimulation (n = 28; N = 11) in WT mice (unpaired t-test: ***P = 0,000006). Significant increase of the time constant of decay of the glutamate transients (center) after a train of 10 pulses at 100 Hz frequency (n = 21; N = 10) compared to a SP stimulation (n = 21; N = 10) in WT mice (paired t-test: ***P = 3,16 x 10^{-11}). Significant increase in the half time of decay of the NMDARs-EPSC (right) after a train of 10 pulses at 100 Hz frequency (n = 22; N = 13) compared to a SP stimulation (n = 22; N = 13) in WT mice (paired t-test: ***P = 6,25 x 10^{-11}). Data are mean ± SEM.

These data show that the Glu clearance by cortical astrocytes in WT mice is slowed after a high frequency stimulation. The activity-induced slowing of Glu clearance results in increased decay times of postsynaptic NMDARs currents.

Quantitatively, the activity-dependent slowing of NMDARs-EPSC decay kinetics (150% slowing after a train of pulses than after a SP stimulation) better correlate with the activity-dependent slowing of the decay kinetics of the Glu transients than those of the STC (110 and 25% slowing after a train of pulses than after a SP stimulation, respectively).

The decay kinetics of the STC, the Glu transients and the NMDARs-EPSC are slower after trains of 10 pulses at 100 Hz frequency than after a single stimulus also in FHM2 KI mice (11,08 ± 0,41 versus 7,82 ± 0,16 ms for the STC; 128,44 ± 8,12 versus 58,58 ± 5,01 ms for the Glu transients and 123,76 ± 5,55 versus 46,56 ± 1,43 ms for the NMDARs-EPSC) (Fig 3.16).

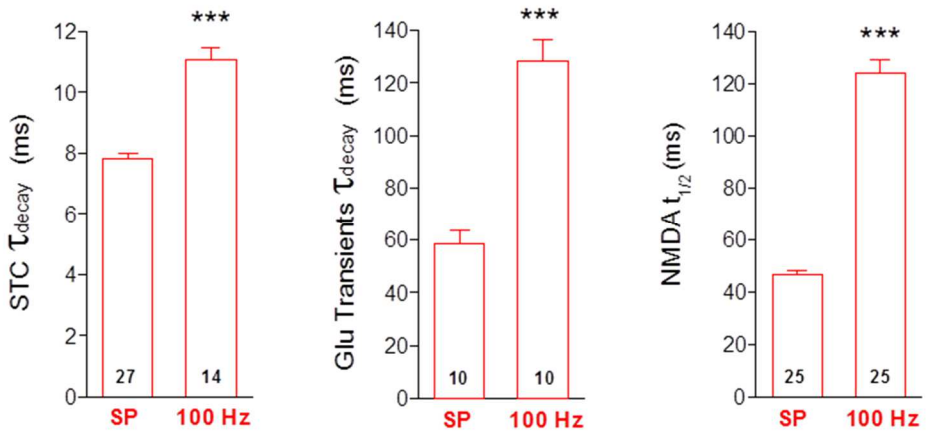

Figure 3.16 Activity-dependent slowing of the rate of glutamate clearance and of NMDARs-EPSC decay kinetics after a train of 10 pulses at 100 Hz frequency in FHM2 KI mice.
Bar plots showing a significant increase of the time constant of decay of the STC (left), elicited in L1 cortical astrocytes of the barrel cortex by extracellular stimulation in L1, after a train of 10 pulses at 100 Hz frequency (n = 27; N = 9) compared to a SP stimulation (n = 14; N = 7) in FHM2 KI mice (unpaired t-test: ***P = 4,98 x 10^{-11}). Significant increase of the time constant of decay of the Glu transients (center) after a train of 10 pulses at 100 Hz frequency (n = 10; N = 5) compared to a SP stimulation (n = 10; N = 5) in FHM2 KI mice (paired t-test: ***P = 1,42 x 10^{-5}). Significant increase of the half time of decay of the NMDARs-EPSC (right) after a train of 10 pulses at 100 Hz frequency (n = 25; N = 15) compared to a SP stimulation (n = 25; N = 15) in FHM2 KI mice (paired t-test: ***P = 1,36 x 10^{-13}). Data are mean ± SEM.

The relative increase in the time constant of decay of the STC after a train compared to a SP is higher in FHM2 KI compared to WT mice (42 versus 25%). The slowing of the decay kinetics of the Glu transients and the NMDARs-EPSC

after a high frequency train, as a trend, is larger in FHM2 KI compared to WT mice (119 versus 110% for the Glu transients and 166 versus 155% for the NMDARs-EPSC) (Fig 3.17).

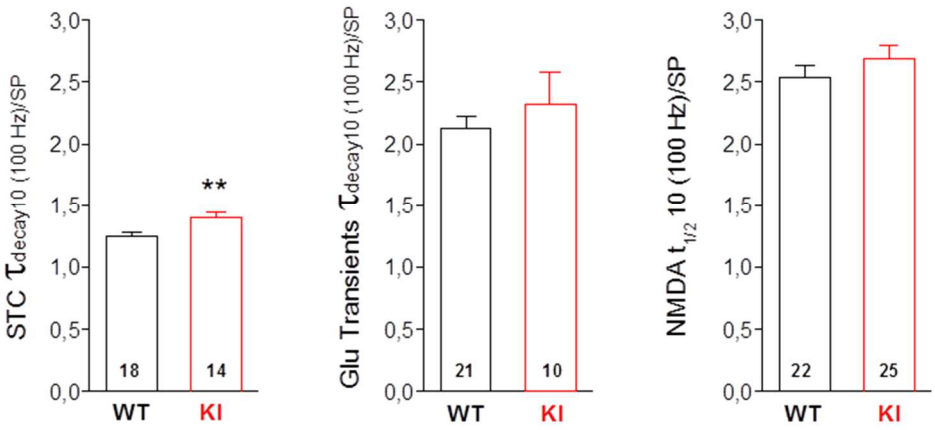

Figure 3.17 Activity-dependent slowing of the rate of glutamate clearance and of NMDARs-EPSC decay kinetics after a train of 10 pulses at 100 Hz frequency compared to a single pulse stimulation.
Bar plots showing the comparison of the averaged ratio of the decay after a train of 10 pulses at 100 Hz over that after a single stimulus, measured as time constant of decay in the case of the STC and the Glu transients and as half time of decay in the case of the NMDARs-EPSC. Significant increase of the ratio of the STC (left) in FHM2 KI (n = 14; N = 7) compared to WT mice (n = 18; N = 8) (unpaired t-test: $^{**}P$ =0,009). The averaged ratio of the Glu transients (center) in FHM2 KI compared to WT mice, as a trend, is larger in FHM2 KI (n = 10; N = 5) compared to WT mice (n = 21; N = 10) (unpaired t-test: P = 0,99). The averaged ratio of the NMDARs-EPSC, as a trend, is larger in FHM2 KI (n = 25, N = 15) compared to WT mice (n = 22, N = 13) (unpaired t-test: P = 0,09). Data are mean ± SEM.

3.3 Pharmacological profile of NMDARs activated by glutamate spillover in FHM2 KI mice

As shown in paragraphs 3.2 and 3.2.1 the activation of NMDARs is increased in FHM2 KI compared to WT mice presumably as a consequence of the increase of Glu spillover due to the reduced Glu clearance by cortical astrocytes. Diheteromers GluN2B containing NMDA receptors (GluN2BRs) have a higher affinity for Glu than both diheteromers GluN2A (GluN2ARs) and triheteromers GluN2A and GluN2B containing receptors (GluN2A-2BRs), and hence should be preferentially activated by Glu spillover. I therefore investigated the pharmacological profile of the NMDARs-EPSC in WT and FHM2 KI mice. To investigate the relative contribution of GluN2BRs I performed pharmacological experiments testing the

effect of Ro25-6981, a GluN2B-selective NMDAR allosteric antagonist, on NMDARs-EPSC in both genotypes.

3.3.1 Effects of 1 and 20 µM Ro25-6981 on NMDARs mediated EPSC in WT mice

I tested two different concentrations of Ro25-6981 in WT mice: 1 µM which should inhibits specifically diheteromers GluN2BRs and 20 µM which should inhibits also triheteromers GluN2A-2BRs, even though not completely (maximal inhibition around 50-60%) but not diheteromers GluN2ARs (Fischer *et al.*, 1997; Volianskis *et al.*, 2013). The experiments were performed recording from L2/3 Pyrs as in previous experiments (see 3.2 of the "Results"), using the same protocols. The NMDARs-EPSC was recorded in control conditions and after 20 minutes from the application of 1 or 20 µM Ro25-6981 to let it explicate its effect and the NMDARs-EPSC reach the steady state.

I found that 1 µM Ro25-6981 in WT mice inhibits only a small fraction of NMDARs-EPSC, indeed the amplitude slightly decreased on average by 9,00 ± 4,73% (n = 3; N = 3) after a SP stimulus (188,67 ± 11,61 versus 171, 00 ± 9,17 pA) with negligible effect on the decay kinetics, measured as half time of decay of the NMDARs-EPSC (44,67 ± 2,33 versus 42,33 ± 0,88 ms; 4,67 ± 3,71% decrease after Ro25-6981, n = 3; N = 3) or as measured from the τ weighted (τ_W) (see 5.11.4 in "Materials and Methods") (93,00 ± 8,62 versus 82,33 ± 3,76 ms; 10,33 ± 6,06% decrease after Ro25-6981, n = 3; N = 3) (Fig 3.18 A). These data indicate that only a very small fraction of the NMDARs-EPSC is due to the activation of the diheteromers GluN2BRs in WT mice.

I found that 20 µM Ro25-6981 inhibits a large fraction of the NMDARs-EPSC amplitude by 68 ± 1,73% (n = 3; N = 3) after a single stimulus (240,67 ± 8,69 versus 75,33 ± 7,13 pA), indicating that the large majority of the NMDARs-EPSC in WT mice is due to the activation of triheteromers GluN2A-2BRs. Moreover, 20 µM Ro25-6981 exerts an effect also on the decay kinetics that become faster 23,67 ± 4,37% (n = 3; N = 3) measured as half time of decay (62,00 ± 9,46 versus 46,67 ± 5,24 ms), or 9,33 ± 1,20%, as measured from the τ_W (122,33 ± 15,62 versus 110,00 ± 13,05 ms) of the NMDARs-EPSC (Fig 3.18 B).

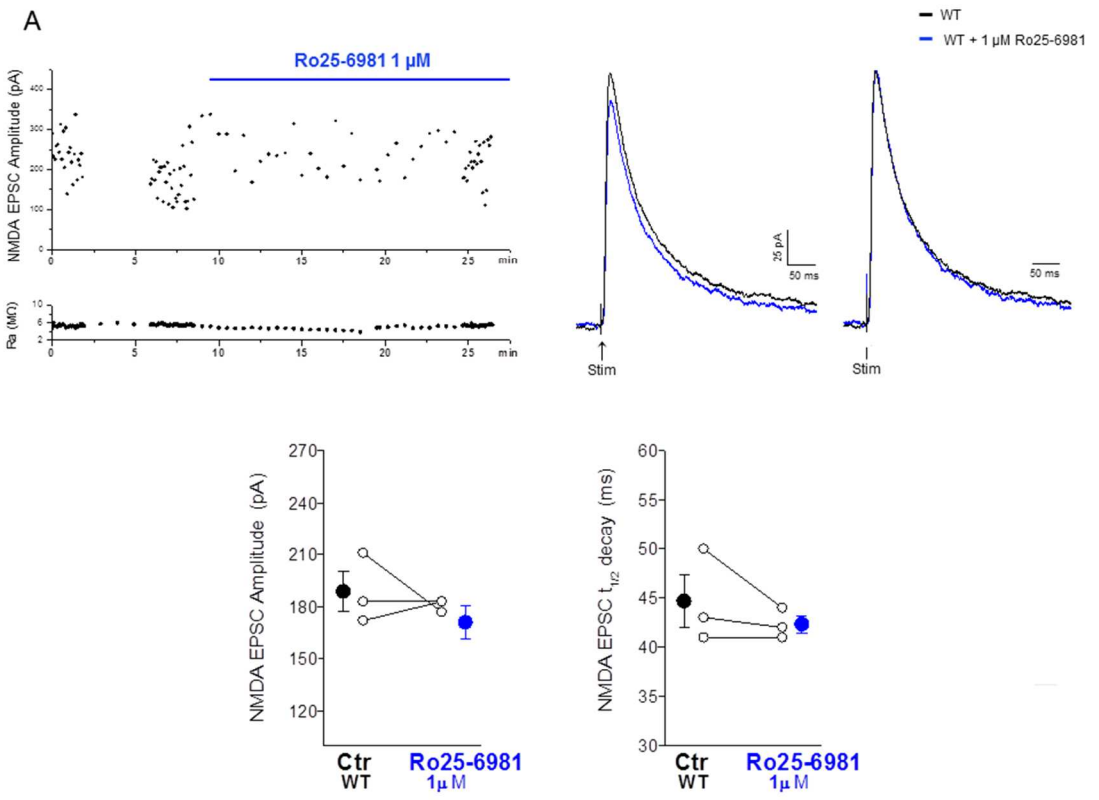
A
Ro25-6981 1 µM
NMDA EPSC Amplitude (pA)
Ra (MΩ)
min
WT
WT + 1 µM Ro25-6981
25 pA
50 ms
Stim
NMDA EPSC Amplitude (pA)
NMDA EPSC t1/2 decay (ms)
Ctr
WT
Ro25-6981
1µM

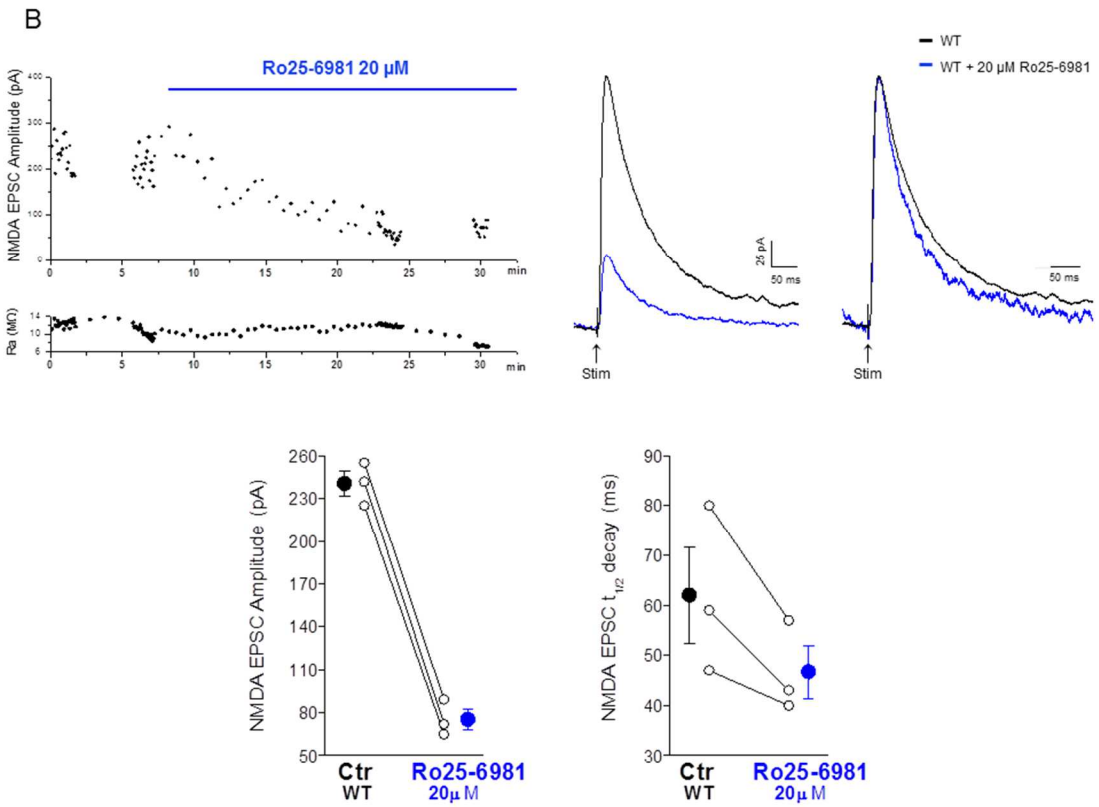
B
Ro25-6981 20 µM
NMDA EPSC Amplitude (pA)
Ra (MΩ)
min
WT
WT + 20 µM Ro25-6981
25 pA
50 ms
Stim
NMDA EPSC Amplitude (pA)
NMDA EPSC t1/2 decay (ms)
Ctr
WT
Ro25-6981
20µM

Figure 3.18 Effect of 1 and 20 µM Ro25-6981, a GluN2B-selective NMDAR antagonist, in WT mice.
A Upper panel: representative time course of the NMDARs-EPSC elicited in L2/3 Pyr by single pulse extracellular stimulation in L1 of the barrel cortex in acute cortical slices from P22-23 WT mice in control conditions and during the application of 1 µM Ro25-6981 (horizontal blue bar). At the bottom the time course of the series resistance (Ra) during the experiment (left). Representative superimposed original and normalized traces of the NMDARs-EPSC from the same experiment, in control conditions (black trace) and after 20 minutes from the application of 1 µM Ro25-6981 (blue trace) (right). **Bottom panel:** amplitude and decay kinetics, measured as half time of decay, of the NMDARs-EPSC evoked, as described above, in control conditions (Ctr WT) and after the application of 1 µM Ro25-6981 (Ro25-6981 1 µM) (n =3; N = 3).
B Upper panel: representative time course of the NMDARs-EPS, elicited as in A, in WT mice in control conditions and during the application of 20 µM Ro25-6981 (horizontal blue bar). At the bottom: the time course of the Ra during the experiment (left). Representative superimposed original and normalized traces of the NMDARs-EPSC from the same experiment in Ctr WT (black trace) and after 20 minutes from the application of 20 µM Ro25-6981 (blue trace) (right). **Bottom panel:** amplitude and decay kinetics, measured as half time of decay, of the NMDARs-EPSC evoked, as described in A, in Ctr WT and after the application of 20 µM Ro25-6981 (Ro25-6981 20 µM) (n =3; N = 3).

The remaining current after 20 µM Ro25-6981 should be due to the activation of the fraction of triheteromers GluN2A-2BRs not inhibited and the diheteromers GluN2ARs, if present. In one experiment in which the two concentrations of Ro25-6981 were sequentially added, the decay kinetics of the current remaining after 20 µM Ro25-6981 were only slightly faster than those in the presence of 1 µM Ro25-6981 (not shown).

This suggests that, depending on whether or not all GluN2BRs were fully inhibited by 1 µM Ro25-6981, only a very small fraction (or none) of the WT NMDARs-EPSC is due to diheteromers GluN2ARs, since the decay kinetics of diheteromeric recombinant GluN2A containing receptors are faster than the triheteromeric GluN2A-2BRs (Hansen *et al.*, 2014).

These data support the conclusion that the large majority of the WT NMDARs-mediated EPSC is due to the activation of triheteromeric GluN2A-2BRs, with only a very small fraction due to the activation of diheteromers GluN2BRs and maybe GluN2ARs. Consistent with this conclusion are also the decay kinetics of the NMDARs-EPSC in WT mice (τ_W = 77 ms, τ_f= 39 ms, τ_s = 204 ms, A_f = 76%), that are much faster than those reported for recombinant diheteromers GluN2BRs (τ_W = 314 ms, τ_f= 152 ms, τ_s = 496 ms, A_f = 52%) and only slightly slower than those of recombinant triheteromers GluN2A-2BRs (τ_W = 57 ms, τ_f= 39 ms, τ_s = 146 ms, A_f = 79%) (Hansen *et al.*, 2014) and similar to those reported for native hippocampal GluN2A-2BRs (in particular regarding the τ_W = 78 ms) (Tovar *et al.*, 2013).

3.3.2 Effects of 1 µM Ro25-6981 on NMDARs mediated EPSC in FHM2 KI mice

I tested the effect of Ro25-6981 at the low concentration (1 µM) that inhibits specifically the diheteromers GluN2B containing receptors in FHM2 KI mice. I found that the inhibition of the NMDARs-EPSC after 1 µM Ro25-6981, is larger in FHM2 KI than in WT mice as regards both, the amplitude and the decay kinetics. Indeed the NMDARs-EPSC amplitude decreased by 35,33 ± 5,49% (213,00 ± 25,42 versus 135,33 ± 5,70 pA) and the decay kinetics were faster by 14,25 ± 5,27% (44,00 ± 3,11 versus 51,25 ± 1,11ms) and by 18,00 ± 3,37% (80,25 ± 7,32 versus 97,75 ± 6,97 ms), as measured by the half time of decay or the weighted time constant, respectively (Fig 3.19).

These data show that a larger fraction of the NMDARs-EPSC is due to the activation of the diheteromers GluN2BRs in FHM2 KI compared to WT mice. This is consistent with the preferential recruitment of GluN2B containing receptors by the increased Glu spillover in FHM2 KI mice.

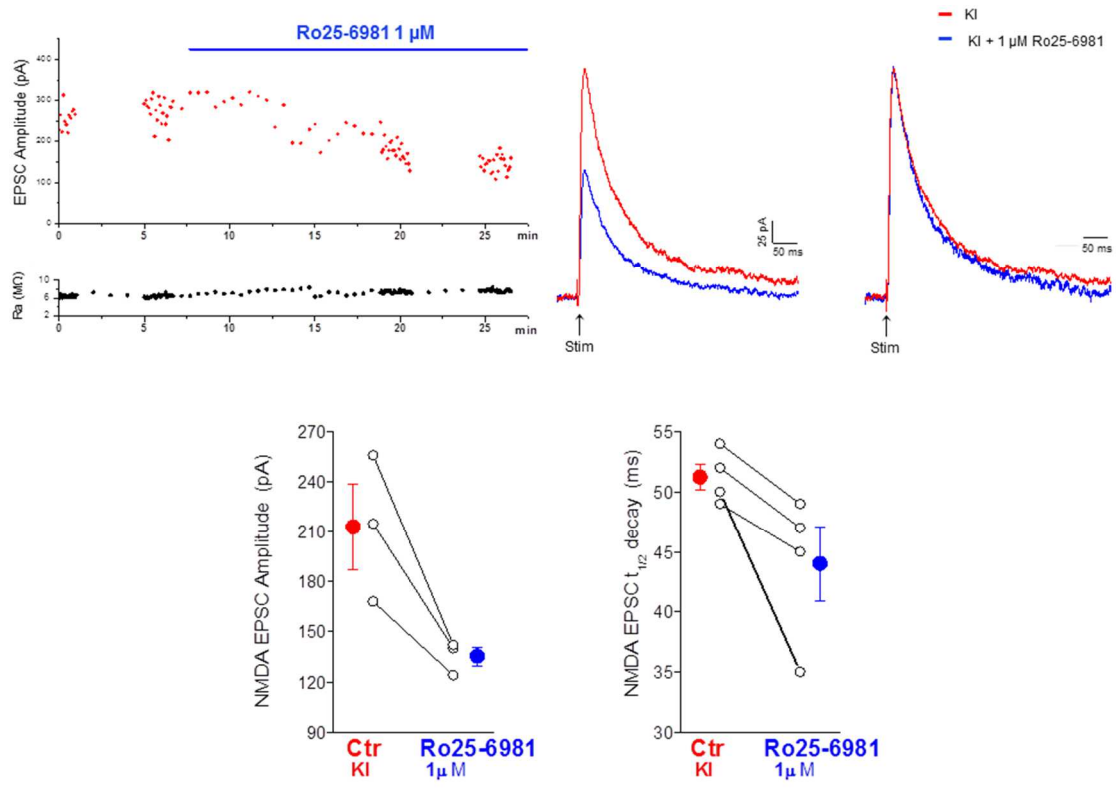

Figure 3.19 Effect of 1 μM Ro25-6981, a GluN2B-selective NMDAR antagonist, in FHM2 KI mice.
Upper panel: representative time course of the NMDARs-EPSC elicited in L2/3 Pyr, by single pulse extracellular stimulation in L1 of the barrel cortex in acute cortical slices from P22-23 FHM2 KI mice in control conditions and during the application of 20 μM Ro25-6981 (horizontal blue bar). At the bottom: the time course of the series resistance (Ra) during the experiment (left). Representative superimposed original and normalized traces of the NMDARs-EPSC from the same experiment, elicited as described in 3.2, in Ctr KI (red trace) and after 20 minutes from the application of 1 μM Ro25-6981 (Ro25-6981 1 μM) (blue trace) (right).
Bottom panel: amplitude (n =3; N = 3) and decay kinetics (n =4; N = 4), measured as half time of decay, of the NMDARs-EPSC evoked, as described in 3.2, in Ctr KI and after 1 μM Ro25-6981 application.

The quantitative comparison between the effect of 1 μM Ro25-6981 and the effect of the FHM2 mutation on the amplitude and decay kinetics of the NMDARs-EPSC suggests that the increased activation of GluN2BRs might quantitatively account for most, if not all, the increased activation of NMDARs in FHM2 KI compared to WT mice (although to adequately support this quantitative conclusion I should increase the number of pharmacological experiments).

The small slowing of the decay kinetics in FHM2 KI mice seems in apparent contrast with this conclusion. Indeed if the diheteromers GluN2BRs have a slow decay kinetics as those reported for recombinant receptors it would be expected a larger slowing of the decay kinetics in FHM2 KI. A possible explanation could be the expression of diheteromers GluN2BRs with faster decay kinetics in Pyrs. An indication that this could be the case comes from a pharmacological experiment in which I tested the effect of PEAQX, a competitive antagonist of NMDARs containing the GluN2A subunit. I used PEAQX at a concentration of 400 nM, which should completely inhibit the diheteromers GluN2ARs and the majority (although not all) of the triheteromers GluN2A-2B receptors but also a large fraction of diheteromers GluN2BRs (Tovar *et al*., 2013). PEAQX inhibited the amplitude of NMDARs-EPSC by 85% (57 versus 374 pA) and slowed by 31% the time constant of decay, measured as τ_w, (136 versus 104 ms) and by 88% the activation kinetics (11,88 versus 6,32 ms), as expected if the remaining current is due to diheteromers GluN2BRs. Although the decay kinetics are slower, they are still faster than those reported for recombinant diheteromers GluN2BRs (136 versus 314-274 ms) (Hansen *et al*., 2014). However a clear-cut conclusion cannot be drown since it is unclear whether all triheteromers GluN2A-2B receptors are inhibited and to which extent they contribute to determine the decay kinetics of the remaining current (Fig 3.20).

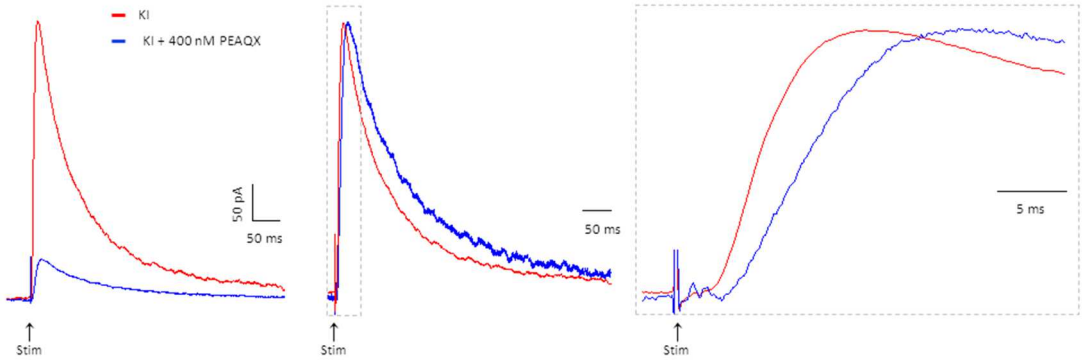

Figure 3.20 Effect of 400 nM PEAQX, a GluN2A NMDAR competitive antagonist, in FHM2 KI mice. **Left:** representative traces of NMDARs-EPSC elicited in L2/3 Pyr, by single extracellular stimulation in L1 of the barrel cortex in acute cortical slices from P22-23 WT mice in control conditions (red trace) and after the application of 400 nM PEAQX (blue trace). After 20 min, PEAQX inhibited the 85% of the NMDARs-EPSC amplitude (n = 1; N = 1). **Center:** representative normalized traces derived from those to the left, showing the effect of 400 nM PEAQX (blue trace) on the decay kinetics, measured as τw, which is slowed by 31% (n =1; N = 1). **Right:** magnification of the representative normalized traces derived from those to the left, showing the effect of 400 nM PEAQX (blue trace) on the activation kinetic of NMDARs-EPSC, which is slowed by 88% (n =1; N = 1).

3.4 Implementation and optimization of the protocol for *in utero* electroporation (IUE) for selective expression of channelrhodopsin-2 (ChR2) in layer 2/3 Pyramidal cells.

The differential effect of FHM1 mutation at excitatory and inhibitory synapses led to propose the working hypothesis that a dysfunctional excitatory/inhibitory (E/I) balance in specific cortical circuits might be the key pathogenic mechanisms in FHM (Vecchia and Pietrobon 2012; Pietrobon and Moskowitz, 2013). As a first test of this hypothesis we investigated whether FHM mutations alter the dynamic regulation of the E/I balance in L2/3 during recurrent network activity induced by optogenetic activation of L2/3 Pyrs with different types of light stimuli, that presumably mimick different types of physiological activity. Selective expression of channelrhodopsin-2 (ChR2) in L2/3 Pyrs of the barrel cortex can be obtained by performing *in utero* electroporation (IUE) at day 15.5 of gestation (Szczurkowska *et al.*, 2016). This tecnique has been described for the first time in 2001 by Saito and Nakatsuji and takes advantage of the fact that by targeting neural progenitors at

the epithelium of the ventricular system, one can address specific populations of newborns neurons that will migrate to the various brain areas. Depending on the location of the progenitors and the embryonic stage one can target cells that will integrate in different brain regions and carry the gene of interest (dal Maschio *et al*., 2012). We focused on L2/3 of the somatosensory cortex because it is thought to be a locus of integration of sensory signals arriving from thalamo-cortical (TC) pathways; it is connected with neighbouring cortical domains and project and receive information from many other cortical areas and thus can process information in a context-dependent manner (Petersen and Crochet, 2013). L2/3 cannot be selectively activated using classical extracellular stimulation because local circuit are intermixed with long-range axons. We therefore used optogenetic activation to enable selective, single-column activation of L2/3 recurrent network without contamination of fiber of passage, feed-forward input, or direct stimulation of interneurons. Furthermore, graded stimulation by increasing light intensity allowed to characterize the progressive recruitment of excitation and inhibition in the active recurrent network (Shao *et al*., 2013)

3.4.1 Optimization of the mating strategies and pups survival

In the facility where we started mating the mice and performing IUE, I encountered many problems: I) only 6% of WT and 7% of FHM1 KI mice were plug-positive (plug +) in the morning following the mating nights, II) only 16% of WT pups survived after electroporation, and no surviving pups were found among FHM1 KI mice. Furthermore, episodes of abandonment of the pups by their mother or even cannibalism have often happened, especially in FHM1 KI, which are more pronte to this type of episodes compared to WT mice. In light of these problems I decided to move to a specific pathogen free (SPF) facilty in which there were more favorable igienic and environmental conditions (eg no overcrowding of personnel, operators and animals; reduced and controlled access to the structure, reduced noise pollution etc..) to grow and mate the colonies and to perform IUE.

In this SPF facility I was able to ameliorate both aspects: I) the number of plug + females that slightly increased from 6 to 8% in WT and from 7 to 11% in FHM1 KI

mice (Fig 3.21); II) the percentage of surviving WT pups after electroporation that increased from 16 to 59%.

To the first aim I used similar mating strategies than in the previous facility apart from the fact that I paired only two females for each male in order to focalize the male's attention among a lower number of females (for details see also 5.13 in "Materials and Methods"). In order to further increase the probability of mating I also supplied each cage with environmental enrichments such as tubes, cotton wools and plastic houses.

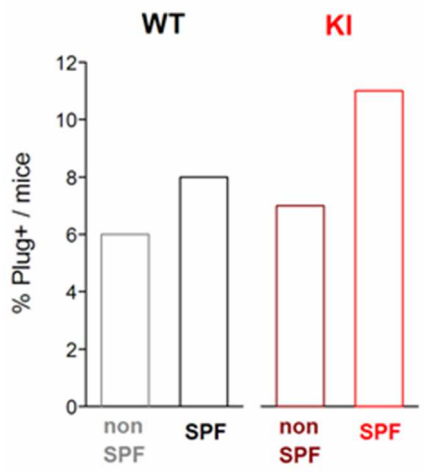

Figure 3.21 Optimization of the mating strategies
Bar graphs showing increased percentages of plug + females during the mating period comparing both phenotypes before (non SPF) and after moving in an SPF facility (SPF).
In the non SPF facility only 43 out of 726 (6%) and 26 out of 395 (7%) females were plug + among WT and FHM1 KI mice, respectively. In the SPF facility 31 out of 372 (8%) and 16 out of 149 (11%) females were plug + among WT and FHM1 KI mice, respectively.

The second aim was achieved using three main strategies: the first, of which I will discuss the details in 3.4.2, was to optimize the concentration and the volume of DNA to be injected; the second was to use non-primiparae females that presumably have already developed maternity skills, so they are more prone to breastfeeding and caring for offspring; the third was to use foster-mother in case of abandonment of the pups. CD-1 mice have been chosen as foster-mothers for mainly two reasons: first, CD-1 female exhibit high levels of maternal cares (Szczurkowska *et al*., 2016), and second CD-1 mice have white fur and are bigger in size, thus C57BL/6J are easily recognizable if added to CD-1 pups.

The second strategy allows us to increase the percentage of the surviving pups after IUE from 58 to 92% (Fig 3.22), while the third was successful only in very rare cases. Unfortunately, both these strategies were ineffective in FHM1 KI mice,

for which we need to further improve the protocol to obtain surviving electroporated pups.

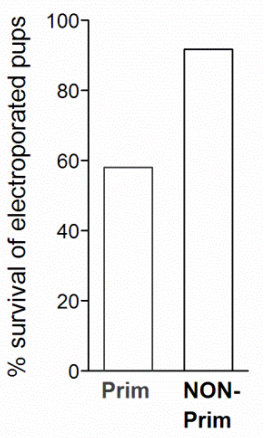

Figure 3.22 Increased survival of electroporated WT pups using non primiparae female during mating.
Bar graph showing an increased percentage of survival of the electroporated pups from 58 to 92% in SPF conditions. Such increase was obtained using non primiparae (NON-Prim) instead of primiparae females (Prim) for the mating. 19 out of 21 (*N* = 3) and 31 out of 54 (*N* = 7) electroporated embryos survived in NON-Prim and Prim, respectively.

To verify the actual pregnancy of each female and to avoid false-positives due to palpation tecnique I established a criterion based on the visual inspection of the animal and on its weight gain at 13-14 days post-coitum. Pregnant females appear with the characteristic enlargment of the abdomen easily identifiable by gently pulling their tail, and show a weight gain around 29% at 13-14 days compared to their initial weight (29,54 ± 0,98 versus 22,91 ± 0,60 g). An increase in weight by 2% is instead compatible with two weeks of aging of the animal (23,93 ± 1,22 versus 22,91 ± 0,60 g) (Fig 3.23).

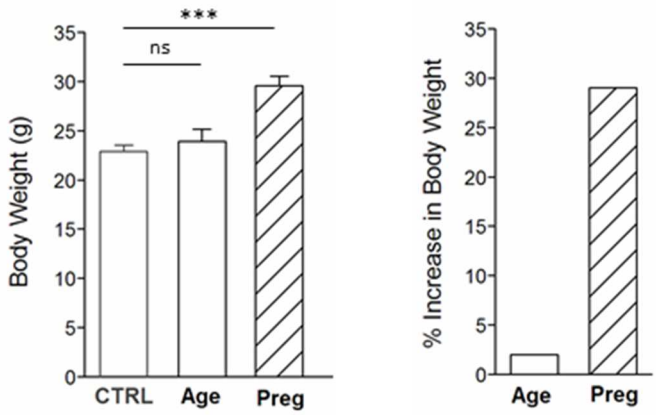

Figure 3.23 Significant increase in body weight during pregnancy.
Left: bar graphs showing the increase in body weight in two weeks (Age) (n = 7, *N* = 7) and a significant weight gain compatible with pregnancy (Preg) (n = 13, *N* = *13*) 13-14 days post-coitum, compared to the averaged weight of a 2.5 months mice (CTRL) (n = 20, *N* = *20*) (Mann-Whitney *U*-test: *P* = 0,000016). **Left:** Histograms showing the percentage relative body weight increase in Age (n = 7, *N* = 7) and Preg mice (n = 13, *N* = *13*).

3.4.2 Optimization of the concentration and volume injection of cDNA and Fast Green FCF

We started electroporating embrios using a DNA solution, added with the Fast Green dye, containing the lowest concentrations of the plasmids commonly reported in the literature: "final concentration of 1-4 µg/µl DNA solution and 0.3 mg/ml of Fast Green dye in sterile water" in Szczurkowska *et al*., 2016; "injection of 2 µg ChR2 DNA and 0.5-1 µg of GFP or mRFP DNA" in Adesnik and Scanziani, 2010; "2 µl at E 15 of coloured DNA solution containg 3-4 µg of the GFP encoding plasmid" in Baumgarth and Grebe, 2015. We started injecting a defined volume of DNA solution, 1 µl, in the lateral ventricle of each embryo containing 1 or 0.8 µg/µl of each plasmid: pCAGGS-ChR2-venus and pCAGGS-mCherry (Addgene, USA), and 0.3 µg/µl of Fast Green FCF. Unfortunately, these concentrations were too high since they produced toxicity of the slices and in most of the cases it was impossible to perform patch-clamp recordings. Moreover we had a low percentage of WT surviving electroporated pups and no surviving FHM1 KI pups. In order to obtain a good, selective expression of ChR2 in L2/3 Pyrs of the barrel cortex, to avoid toxicity of the slices and also, hopefully, to increase the percentage of surviving pups, we optimized the concentrations of DNA and Fast Green dye. We lowered the concentration of each plasmid to 0.5 µg/µl and the concentration of Fast Green FCF dye to 0.15 µg/µl. These optimized concentrations allowed us not only to obtain a selective and homogeneous expression of ChR2 in L2/3 of the barrel cortex (Fig 3.24), and hence to perform preliminary optogenetic experiments, but also to increase the percentage of the surviving pups up to the 59% from the 16% obtained using higher concentration of DNA.

The volume of injection was set and checked before starting each IUE procedure and verified at the end.

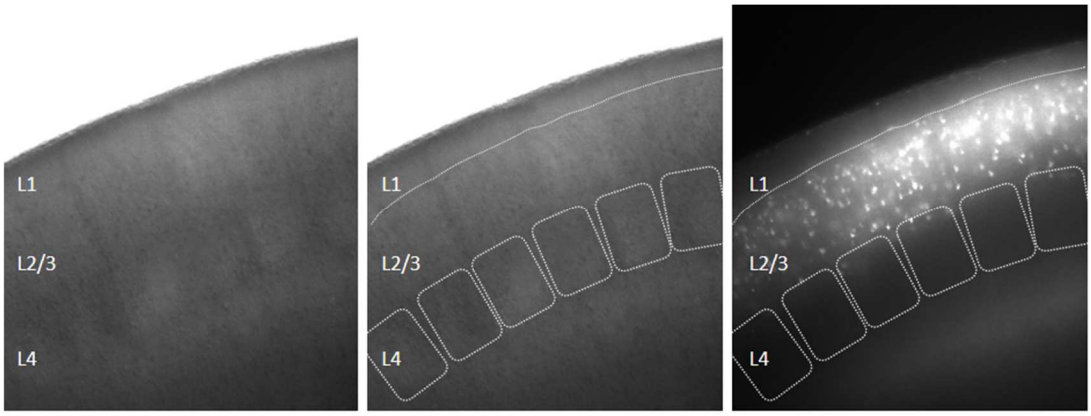

Figure 3.24 Channelrhodopsin-2 selective expression in layer 2/3 Pyrs of the barrel cortex following *in utero* electroporation.
Left panel: 10X phase-contrast representative image of the barrel cortex in a living brain slice where all the layers from 1 to 4 are recognizable from their characteristc morphology. L1 is the most superficial layer characterized by few cell bodies and mainly occupied by the dendrites of the cells located in the deeper layers. L2/3 is characterized by small spherical cells, the so called "granule cells" and a variety of cell types, many of which are pyramidally shaped. L4 is organized in typical esily recognizable structures called "barrels". In the **central panel** for an easier identification of all the layers of the barrel cortex, they are underlined by white dotted lines. **Right panel:** Ds-red epifluorescence of the same image field as the left and central panel in which one can appreciate the selective and homogeneous expression of ChR2 in L2/3 of the barrel cortex. ChR2+ or -Pyrs were identified based on the presence of mCherry which is a valid indicator for putative ChR2-expressing neurons fluorescence (Shao *et al*., 2013).

3.4.3 Preliminary experiment in WT mice with a selective expression of channelrhodopsin-2 in layer 2/3 pyramidal cells of the barrel cortex

All the improvements mentioned above allowed us to obtain, in WT mice, a good, selective expression of ChR2 in L2/3 Pyrs in thalamocortical slices of the barrel cortex in which we performed preliminary optogenetic experiments. We measured light evoked excitatory and inhibitory currents in isolation by voltage clamping individual Pyrs at +10 mV and -68 mV, the E_{rev} for EPSC and IPSC, respectively in L2/3 voltage-clamped Pyrs not expressing ChR2 (Chr2-) (For experimental setup Fig 3.25). For each measure we used single short 2 ms blue light pulses, to mimic transient sensory-driven spiking. Increasing the photostimulation intensity allows to induce spiking in an increasing number of ChR2+ Pyrs and characterize the progressive recruitment of excitation and inhibition in the active recurrent network.

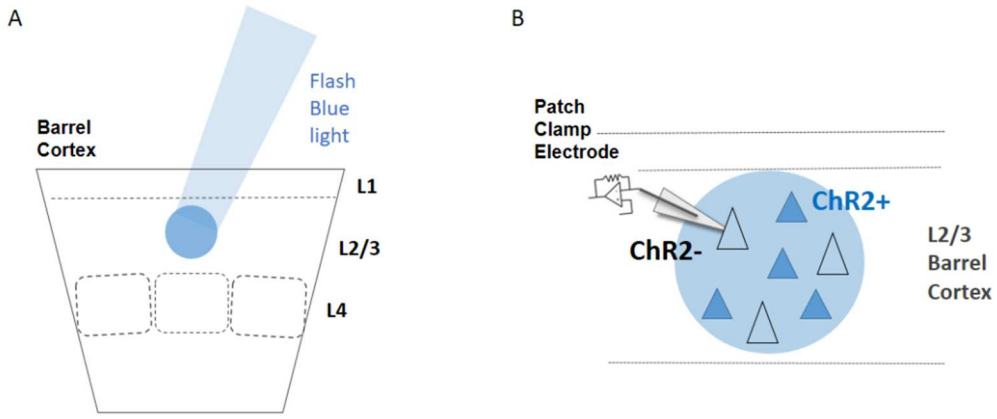

Figure 3.25 Patch-clamp configuration recordings of layer 2/3 pyramidal cells of the barrel cortex not expressing channelrhodopsin-2.
A: Image showing the scheme of optogenetic experiments setup. Thalamocortical slices were illuminated from the top with a round spot of approximately 90 µm in diameter, set adjusting a field diaphragm, in order to selectively activate ChR2+ cells in a single column of the barrel cortex. **B:** ChR2- Pyrs in L2/3 of the barrel cortex were voltage clamped at +10 mV and at -68 to record IPSC and EPSC, respectively, elicited by single short 2 ms blue light pulses at increasing photostimulation intensity.

With increasing intensity of the 2 ms light pulses above a certain light intensity, inhibitory synaptic currents increased more rapidly than excitatory synaptic currents and hence the E/(E+I) ratio, in ChR2- cells decreased (except at close to EPSC threshold light intensities), reflecting preferential recruitment of inhibition over excitation as the L2/3 network activation increases, as reported in the literature in Shao *et al*., 2013 (Fig 3.26, a preliminary representative experiment). E/(E+I) is calculated by using the synaptic charges derived by integrating the synaptic currents over the first 50 ms.

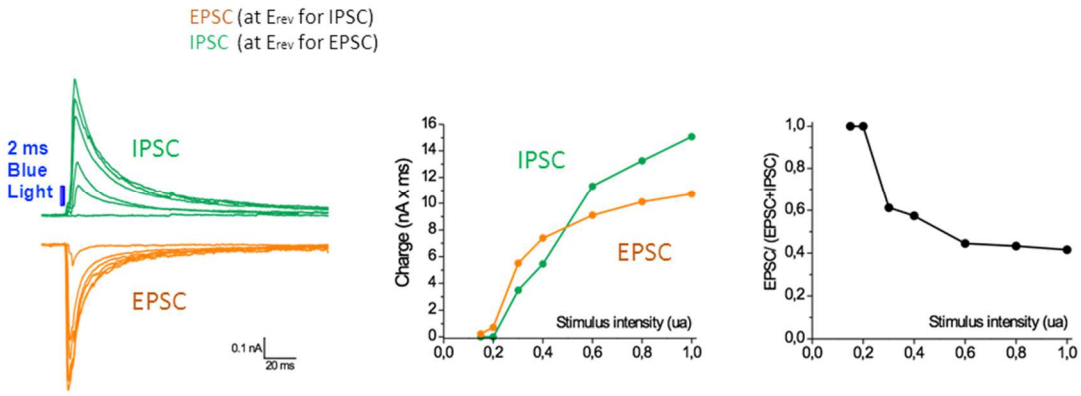

Figure 3.26 Patch-clamp configuration recordings of layer 2/3 pyramidal cells of the barrel cortex not expressing channelrhodopsin-2.
Image showing a representative optogenetic experiment in which a voltage-clamped ChR2- Pyr in L2/3 was stimulated by single short 2 ms blue light pulses at increasing photostimulation intensity. **Left:** superimposed pooled traces of IPSC (green traces, recorded at E_{rev} for EPSC) and of EPSC (orange traces, recorded at E_{rev} for IPSC) of increasing amplitude at increasing photostimulation intensity. **Centre:** graph showing the relative increase of the total charge, obtained by integrating the currents over the first 50 ms, at increasing photostimulation intensity of both IPSC and EPSC (for details see also 5.14 in "Materials and Methods"). **Right:** graph showing the E/(E+I) ratio at increasing photostimulation intensity.

If we succeed in resolving the remaining technical problems regarding the electroporation method (particularly in KI mice), we are now ready to investigate whether FHM mutations alter the dynamic regulation of the E/I balance in L2/3 during recurrent network activity.

4. DISCUSSION

The first mouse model of FHM2 has been created in 2011 by introducing the human W887R FHM2 mutation in the orthologous gene (as described in Leo *et al*., 2011); since then, studies have focused on the characterization of the phenotype of this mouse model. *In vivo* studies show that heterozygous FHM2 KI mice, with 50% reduced expression of α2 NKA, show a lower threshold for CSD induction and a higher velocity of CSD propagation compared to WT mice (Leo *et al*., 2011).

Studies recently conducted in the lab shed light on the mechanisms underlying the increased susceptibility to experimental CSD in FHM2 KI mice by demonstrating that the loss-of-function of the α2 NKA results in an activity-dependent impaired Glu and K^+ clearance by cortical astrocytes during neuronal activity (Capuani *et al*., 2016). Moreover our collaborators in parallel demonstrated, using immunogold electron microscopy (EM), that FHM2 KI mice have a 50% reduction of the GLT-1a density in the membrane of astrocytic processes surrounding glutamatergic synapses compared to WT mice, a reduction that is quantitatively equal to the reduction of the α2 NKA in mutant mice. Taken together these data suggest that α2 NKA and GLT-1a are structurally and functionally coupled (Capuani *et al*., 2016).

In light of these recent findings, during my PhD research project I further investigated the mechanisms leading to CSD facilitation in FHM2 KI mice. I firstly tested whether there is a cause-effect relationship between the reduced rate of Glu clearance by cortical astrocytes and CSD facilitation in FHM2 KI mice, using two different approaches.

In the first I investigated whether CSD facilitation could be rescued by systemic treatment of FHM2 KI mice with Cef, a drug that in WT mice increases the membrane expression of GLT-1 up to 60% (Bellesi *et al*., 2009). We found that Cef treatment was able to rescue a small fraction of CSD facilitation in FHM2 KI mice, in fact it increased slightly but significantly the threshold of CSD induction but it did not affect the velocity of CSD propagation. Immunogold EM showed that surprisingly neither the total expression of GLT-1a in the cortex nor the membrane density of GLT-1a at PAPs was significantly increased in Cef treated FHM2 KI

mice. However, Cef-treatment increased the membrane expression of GLT-1a at AxTs of FHM2 KI mice; this may provide an explanation for the small rescue of CSD by Cef in FHM2 KI mice. This result is however surprising, since if on one hand it provides an explanation for the small efficacy of Cef-treatment on the rescue of CSD facilitation, on the other hand it is well known that GLT-1 in the AxTs are only a small fraction of the total brain GLT-1a (Chen *et al*., 2004; Melone *et al*., 2009) and their selective deletion in neurons did not give rise to any apparent neurological phenotype, contrary to what happens in astrocytes (Petr *et al*., 2015). Effects unrelated to the ability of Cef to increase GLT-1 could be an alternative explanation for the small effect on CSD threshold, but they seem unlikely given that FHM2 KI mice show no alteration in the protein expression of α2 NKA, glial Glu/cystine antiporter xCT and Kir4.1 after Cef-treatment (Capuani *et al*., 2016).

In the second approach I investigated whether pharmacological reduction of the rate of Glu clearance by astrocytes in WT mice to a value similar to that in FHM2 KI mice could decrease the threshold and increase the propagation velocity of CSD to values similar to those produced by the FHM2 mutation. Subsaturating concentration of TBOA, a Glu transporter inhibitor, that slowed the rate of Glu clearance to a value similar to that in FHM2 KI, did lower the threshold to a value similar to that of FHM2 KI mice and increased the velocity of propagation but less than the FHM2 mutation. The quantitative comparison between the facilitation of CSD produced by the FHM2 mutation and by subsaturating concentrations of TBOA supports the conclusion that the reduced rate of Glu clearance by cortical astrocytes can account for most of the facilitation of CD induction in FHM2 KI mice, leaving only a few possibility for other mechanisms to participate. In contrast, impaired Glu clearance by astrocytes can account for only a fraction, even though large, of the facilitation of CSD propagation, suggesting that other mechanisms could contribute. This differential effect of TBOA on CSD threshold and propagation velocity in WT mice is consistent with the different effect of Cef-treatment on CSD threshold and propagation in FHM2 KI mice. A possible mechanism that could contribute to explain the fraction of facilitation of CSD propagation in FHM2 KI mice that remained unaccounted is the reduced rate of K^+ clearance by astrocytes uncovered in these mice by Capuani *et al*., 2016. Indeed,

strong evidences point to the diffusion of K^+ released into the interstitial space during CSD as the underlying mechanism of the typical slow rate of CSD propagation (Pietrobon and Moskowitz, 2014; Enger *et al*., 2015).

Previously the lab investigated the mechanisms leading to CSD facilitation in FHM1 KI mice, carrying a gain of function mutation in the neuronal voltage-gated calcium channel $Ca_v2.1$, and showed that facilitation of CSD in FHM1 KI mice is due to enhanced release of Glu at cortical excitatory synapses (Tottene *et al*., 2009). The data from FHM1 and FHM2 KI mice support the conclusion that excessive glutamatergic transmission, due to enhanced release of Glu in FHM1 and to its defective clearance in FHM2, is a common mechanism underlying susceptibility to CSD in FHM KI mice.

Although the mechanisms underlying ignition of the experimental CSD are still controversial, there is pharmacological support for a key role of NMDARs (but not AMPA or Kainate receptors) (Pietrobon and Moskowitz, 2014). To test the hypothesis that the reduced rate of Glu clearance and the consequent increased Glu spillover results in excessive NMDARs activation in FHM2 KI mice, I measured the NMDARs-mediated EPSC in L2/3 Pyrs elicited by extracellular stimulation in L1 of the barrel cortex in both WT and FHM2 KI mice.

Preliminary experiments in WT mice slices perfused with the concentration of TBOA able to slow the rate of Glu clearance in WT astrocytes to a similar extent as the FHM2 mutation, produced a slowing of the decay kinetics and a large increase of the amplitude of NMDARs-EPSC. The slowing of the decay kinetics of NMDARs-EPSC is in accordance with previous studies by Diamond at hippocampal synapses of WT mice, in which, however, an almost saturating concentration of TBOA was used (Diamond, 2001). Diamond interpreted the slowing of the decay kinetics as a consequence of the Glu spillover that leads to delayed, cooperative activation of synaptic NMDARs at neighboring synapses and/or the activation of extrasynaptic NMDARs (Diamond, 2001). The high affinity for Glu makes extrasynaptic NMDARs (and NMDARs at neighboring synapses) able to detect little variation in extracellular Glu concentration as those produced by Glu spillover. In contrast with the relative small increase in NMDARs-EPSC amplitude at hippocampal synapses (Diamond, 2001), I found a large increase of

NMDARs-EPSC amplitude at cortical synapses despite the much lower concentration of TBOA.

In light of these preliminary findings I investigated the NMDARs mediated EPSC in FHM2 KI mice. I found that after a single stimulus the decay kinetics of NMDARs-EPSC were slower in FHM2 KI compared to WT mice, as expected if the slowing of Glu clearance results in an increased Glu spillover and delayed activation of NMDARs at distant sites; moreover, I found an increased amplitude of NMDARs-EPSC in FHM2 KI mice. As a result of both the slowing of the decay and the increased amplitude, the total charge carried by the NMDA current, as measured by the current integral, is larger in FHM2 KI compared to WT mice. I also found a significant difference in the activation kinetics of NMDARs-EPSC, that are slower in FHM2 KI compared to WT mice. In accordance with the activity-dependent slowing of Glu clearance, also the increase in the activation of NMDARs in FHM2 KI mice is activity-dependent since it is larger after train of pulses at high frequency than after a single stimulus.

Interestingly, the quantitative comparison of the decay kinetics of the NMDARs-EPSC with those of the STC and the Glu transients suggests that the slowing of the decay kinetics of NMDARs in FHM2 KI mice reflects the reduced rate of Glu clearance by astrocytes at cortical excitatory synapses during neuronal activity. These data are consistent with delayed activation of NMDARs at distant sites (cooperative activation of NMDARs at neighboring synapses and/or extrasynaptic NMDARs) and/or with the presence of NMDARs with different subunits composition.

Since the diheteromeric GluN2B containing NMDARs are known to possess a higher affinity for Glu than both diheteromers GluN2ARs and triheteromers GluN2A-2BRs, they should be preferentially activated by Glu spillover. Investigation of the contribution of diheteromers GluN2B containing NMDARs to the NMDARs-EPSC is complicated by the fact that relatively high concentration of the specific inhibitor Ro25-6981 also inhibit triheteromeric GluN2A-2BRs, although not completely. To investigate the relative contribution of diheteromeric GluN2BRs and triheteromeric GluN2A-2BRs I used two different concentration of Ro25-6981: a low concentration (1 μM) that should inhibit specifically

diheteromers GluN2BRs, and a higher concentration (20 µM) that should inhibit also the triheteromers GluN2A-2BRs, although not completely (max 50-60%), without affecting the diheteromers GluN2ARs (Fischer *et al*., 1997; Volianskis *et al*., 2013).

I found that only a small fraction of NMDARs-EPSC is due to the activation of diheteromers GluN2BRs in WT mice, given the small decrease of the amplitude and the negligible effect on the decay kinetics exerted by the low concentration of the drug. In contrast, 20 µM Ro25-6981 inhibited a large fraction (68%) of NMDARs-EPSC, suggesting that its large majority in WT mice is due to the activation of triheteromers GluN2A-2BRs. Consistent with this conclusion are the decay kinetics of the NMDARs-EPSC in WT mice, that are much faster than those reported for recombinant diheteromers GluN2BRs and only slightly slower than those of recombinant triheteromers GluN2A-2BRs (Hansen *et al.*, 2014) and similar to those reported for native hippocampal GluN2A-2BRs (Tovar *et al.*, 2013). Although the decay kinetics of recombinant triheteromers GluN2A-2BRs resemble more those of recombinant diheteromers GluN2ARs than those of recombinant diheteromers GluN2BRs, they are slower than those of diheteromers GluN2ARs (τ_W = 32 ms, τ_f= 30 ms, τ_s = 90 ms, A_f = 70%) (Hansen *et al.*, 2014). The fact that only a very small fraction of diheteromers GluN2ARs (if any) is present is indicated by the fact that in one experiment in which the two different concentrations of Ro25-6981 were sequentially added, the decay kinetics of the current remaining after 20 µM Ro25-6981 was only slightly faster compared to that after 1 µM Ro25-6981. Taken together these data suggest that the large majority of the WT NMDARs-EPSC is due to the activation of triheteromeric GluN2A-2BRs, with only a very small fraction due to activation of diheteromers GluN2BRs and perhaps an even smaller fraction to diheteromers GluN2ARs.

In FHM2 KI mice, the inhibition of the NMDARs-EPSC by 1 µM Ro25-6981 was significantly larger than in WT mice, and the decay of the remaining NMDARs-EPSC was faster, indicating that a larger fraction of the NMDARs-EPSC is due to the activation of diheteromeric GluN2BRs in FHM2 KI compared to WT mice. This is consistent with preferential recruitment of GluN2BRs by increased Glu spillover in FHM2 KI mice. The quantitative comparison between the effect of

1 μM Ro25-6981 and the effect of the FHM2 mutation on the amplitude and decay kinetics of the NMDARs-EPSC suggests that the increased activation of GluN2BRs might quantitatively account for most, if not all, the increased activation of NMDARs in FHM2 KI compared to WT mice (although to adequately support this quantitative conclusion I should increase the number of pharmacological experiments).

In case that these preliminary data will be confirmed by a higher number of pharmacological experiments, we will investigate whether the increased activation of diheteromeric GluN2BRs in FHM2 KI mice can account, at least in part, for the CSD facilitation. If it does, selective GluN2BRs inhibitors might be further investigated and considered as a possible therapeutical approach for FHM2 patients.

Overall, the data from FHM1 and FHM2 KI mice are consistent with a model of CSD initiation in which excessive glutamatergic synaptic transmission (due to $Ca_v2.1$-dependent Glu release in FHM1 or to Glu defective clearance in FHM2) and activation of NMDARs are key elements in the positive feedback cycle that ignites CSD. In this model the α2 NKA pumps exert a dampening role owing mainly to their key role in Glu and K^+ clearance by cortical astrocytes during neuronal activity. In FHM1 KI mice it has been demonstrated that while excitatory neurotransmission is enhanced, inhibitory neurotransmission at fast spiking and other multipolar interneuron synapses is unaltered (Tottene *et al*., 2009). Interestingly, in the cortex, the α2 NKA pump is localized in astrocytic processes surrounding glutamatergic synapses, but is not present in astrocytic processes surrounding GABAergic synapses (Cholet *et al*., 2002), suggesting that FHM2 mutations likely affect excitatory but not inhibitory synaptic transmission. The differential effect of FHM mutations on excitatory and inhibitory synaptic transmission implies that, most likely, the neuronal circuits that dynamically maintain a tight balance between excitation and inhibition during cortical activity are functionally altered in both FHM1 and FHM2, and suggests that dysfunctional regulation of the cortical excitatory/inhibitory balance (E/I) may be a common feature of the FHM brain (Capuani *et al*., 2016). The view of migraine as a disorder of brain excitability characterized by dysfunctional regulation of E/I balance is

strengthened in light of these results (Vecchia and Pietrobon, 2012) and gives insights into possible mechanisms underlying the susceptibility to ignition of "spontaneous" CSD in FHM, and possibly migraine (Capuani *et al*., 2016). A possible hypothesis is that excessive glutamatergic transmission and dysfunctional regulation of the E/I balance in FHM may in certain conditions lead to overexcitation and network hyperactivity with the consequent increase of K^+ and NMDARs activation (that leads to further increase of K^+) thus creating the conditions for initiation of the positive feedback cycle that ignites CSD (Capuani *et al*., 2016).

5. MATERIALS AND METHODS

5.1 Animals

All experiments were performed on brain slices from an heterozygous knock-in (KI) mouse model of FHM2, carrying the human W887R mutation in the *ATP1A2* orthologous gene (for details Leo *et al.*, 2011) and the corresponding wild-type (WT) littermates (background C57BL/6J) or WT C57BL/6J (provided by Charles River Laboratories, Italy). Genotype identification of FHM2 KI mice was obtained by extraction of DNA from biopsy, and sequent analysis by polymerase chain reaction (PCR) using the primers described in Leo *et al.*, 2011 (see below). All the data were obtained from experiments performed on both male and female mice from postnatal day 22 to 23 (P22-23). Experiments from WT and KI mice were alternated on a daily bases.

Mice were housed in a specific pathogen free (SPF) facility under constant temperature (22 ± 1°C), humidity (50%) and acoustic isolation conditions with 12 hours light/dark cycle, and were provided with food and water *ad libitum*.

All experimental procedures involving animals and their care were conducted in accordance with National laws and policies (D.L. n. 26, March 14, 2014) and with the guidelines established by the European Community Council Directive (2010/63/UE) and were approved by the local authority veterinary service.

5.2 DNA extraction and Polimerase Chain Reaction (PCR)

Genomic DNA was extracted from mice biopsy using the Eurogold Tissue DNA Kit (Euroclone, MI, Italy), following the manufacturer's protocol, and then quantified and quality-checked on a Nanodrop 2000 spectrophotometer (Thermo Fisher Scientific, Italy). *Atp1a2* DNA was amplified using forward primer on exon 19 (5′-GGCTTCTTTACCTACTTTGTGATA-3′) and reverse primer on hexon 20 (5′-ATGCCCTGCTGGAACACTGAGTTG-3′) (BMR Genomics, Italy) with GoTaq Green Master Mix (Promega, USA) at 95°C for 2 min, 35 cycles at 95°C for 30 s, 58°C for 30 s, 65°C for 30 s and 65°C for 5 min (Leo *et al.*, 2011). PCR products were run on a 1,5% agarose gel in TAE buffer (SIGMA Aldrich, Italy). The presence of the W887R mutation was tested on PCR products: heterozygous

Atp1a2$^{+/R88}$ (FHM2 KI) showed a double band, one at 310 bp, same as *Atp1a2*$^{+/+}$ (WT) littermates, and one at 400 bp relative to the mutants allele, not present in WT mice (Fig 5.1).

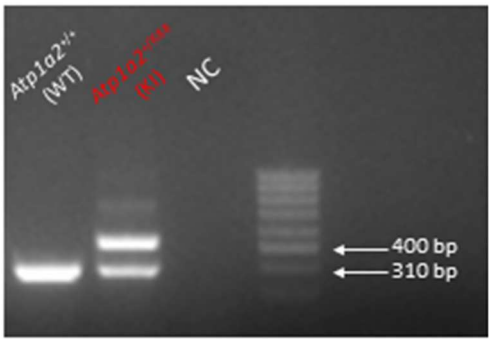

Figure 5.1 Representative image of PCR products run for genotype identification.
Agarose gel after PCR products run showing double bands (310 and 400 bp) for heterozygous FHM2 KI mutants carrying the human W887R mutation on *Atp1a2* gene, a single band (310 bp) for WT mice littermates and the negative control (NC). On the right, the molecular weight marker.

5.3 Brain slices dissection

5.3.1 Solutions for slices preparation

The slice cutting protocol provides the use of three different solutions:

standard Artificial Cerebrospinal Fluid (sACSF): 125 mM NaCl, 2.5 mM KCl, 1 mM $MgCl_2$, 2 mM $CaCl_2$, 25 mM $NaHCO_3$, 1.25 mM NaH_2PO_4, 25 mM glucose, 50 nM minocycline, saturated with 95% O_2 and 5% CO_2 (pH 7.4 with Na OH).

Gluconate Cutting Solution (GCS): 130 mM KGluconate, 15 mM KCl, 0.2 mM EGTA, 20 mM HEPES, 25 mM glucose, 2 mM kynurenic acid, 50 nM minocycline saturated with 100% O_2 (pH 7.4).

Mannitol Cutting Solution (MCS): 225 mM D-Mannitol, 25 mM glucose, 2.5 mM KCl, 1.25 mM NaH_2PO_4, 26 mM $NaHCO_3$, 0.8 mM $CaCl_2$, 8 mM $MgCl_2$, 2 mM kynurenic acid, 50 nM minocycline saturated with 95% O_2 and 5% O_2 (pH 7.4).

Minocycline, a broad-spectrum tetracycline with good permeability of the blood-brain barrier (SIGMA Aldrich, Italy), was added to prevent activated microglial immune response. Kynurenic acid (Abcam bichemicals, UK), an NMDA receptor blocker, was added to all solutions to prevent excitotoxicity during slice cutting.

5.3.2 Cortical coronal slices preparation

The protocol adopted in the laboratory refers to the one developed by Duguè *et al.*, 2005. Mice were anesthetized with Isoflurane and decapitated. The head was immediately put in ice-cold sACSF where the scalp was removed and the skull opened. The brain was quickly removed and placed with its ventral surface on a plate where a perpendicular cut to the antero-posterior axis was made in order to remove the cerebellum and to create a flat surface for fixing the brain to the slicer stage. The flat surface of the brain was glued with cyanoacrylate onto the plate of a vibratome (Leica VT1200S, Germany) with the pial surface towards the cutting blade and allowed for a few seconds to dry before quickly and totally immerging it in ice-cold GCS. 350 µm thick slices with barrel cortex were collected and the left and right hemispheres were separated, transferred at room temperature (RT) for 1-2 minutes in MCS, and then transferred into sACSF solution for the recovery at 30°C for 30 minutes. A quick passage into MCS is fundamental as it prevents the osmotic and termal shock to the slices between the cutting and the recovery, in fact MCS has an intermediate ionic composition and temperature between the GCS and the sACSF. Slices were then transferred at RT in sACSF to allow the complete recovery from the cutting procedure before using them for electrophysiological recordings. All experiments were performed within 6 hours from the decapitation of each animal.

5.3.3 Thalamocortical slices preparation

In the case of thalamocortical slices for optogenetic experiments, we used a protocol developed by Agmon and Connors in 1991. Mice were anesthetized with Isoflurane and decapitated. The head was immediately put in ice-cold sACSF where the scalp was removed and the skull opened. The brain was quickly removed and placed on a 10° ramp made of plexiglass with the ventral face towards the ramp and the anterior end downhill (Fig 5.2 A). The ramp was placed on a protractor and hand-held single edge razor blade was used to make a vertical cut throught the tissue at an angle of 55° to the right of the posterior to anterior axis of the brain, intersectioning this axis at about its anterior one-third point (Fig 5.2 B). The plane of cut was thus determined by two angles: the ramp tilt angle of 10° and the blade

rotation angle of 55°. The tissue rostral to the cut was discarded. The remaining tissue was lightly blotted on filter paper and glued with cyanoacrylate onto the stage of the Vibratome (Leica VT1200S, Germany) with the cut surface down and the pial surface toward the blade (Agmon and Connors, 1991) (Fig 5.2 C). 300 µm thick slices with the right transfected hemisphere of the barrel cortex were collected and processes as described above for the coronal slices before performing optogenetic experiments.

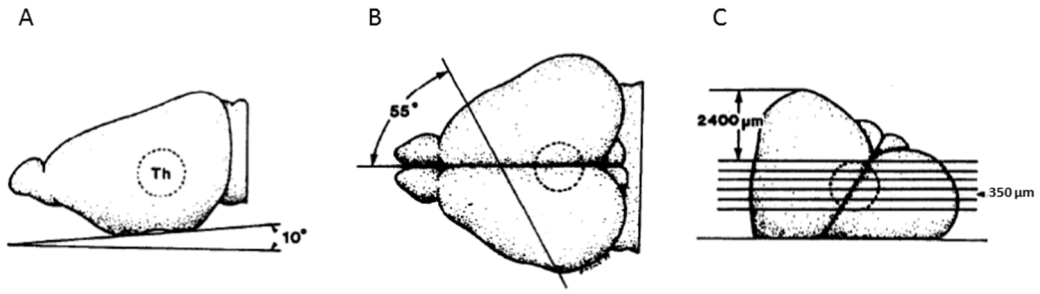

Figure 5.2 Thalamocortical slices dissection (adapted from Agmon and Connors, 1991)
A: image showing the brain laid on the 10° plexiglass ramp with its ventral face. **B:** dorsal view showing the angle of 55° and **C:** brain positioned as in the Vibratome stage.

5.4 Patch-Clamp technique

The patch-clamp technique, which was introduced by Neher and Sakmann and their colleagues in 1981, has allowed electrophysiologists to record ion channel activity from different cell types (Neher and Sakmann, 1976). The patch-clamp technique enable the measurements of ion conductance through single ion channel or all the ion channels across the cell membrane. The principle of patch-clamp recordings is to isolate from the extracellular solution a membrane patch through the formation of a seal (in order of GΩ) between the membrane and the pipette tip. The pipette contains a silver electrode covered with silver chloride connected to a feedback amplifying system which allows the control of the voltage difference across the membrane patch after seal formation. The same electrical circuit allows current measurements through the membrane patch while voltage is controlled

(voltage-clamp) or, alternatively, to measure voltage difference after current injections (current-clamp) (Molleman, 2003) (see below).

5.4.1 Patch-Clamp configurations

One of the main useful feature of patch-clamp is that it can be used with different configurations, which enables the operator to study ion channels at different levels (either whole-cell, which allows the recording of the activity of all ion channels added up, or single ion channel) and easily manipulate the composition of the intracellular and extracellular solutions during a recording. Indeed, when the tip of the recording pipette touches the plasma membrane and the seal is formed, four different configurations can be obtained: cell-attached, whole-cell, inside-out, outside-out.

1) *Cell-attached*: in this configuration the pipette is positioned against the cell membrane where the glass makes a very strong connection, resulting in a tight (high resistance GΩ) seal. This configuration allows measurements of a single channel current (if the channel of interest is present in the patch) without altering cytosolic environment. Because the pipette is on the extracellular side of the membrane, it is usually filled with bathing solution.
2) *Whole-cell*: in this configuration, if a suction is applied to the pipette tip, the patch of membrane under the pipette tip in cell-attached configuration is ruptured, then the pipette solution and the electrode make direct electrical contact with the cytoplasm. As patch pipette tip is sufficiently wide to allow washout of the cytoplasm by the pipette-filling solution, the composition of intracellular fluid can be considered equal to that of the pipette-filling solution. The pipette is filled with a solution that resemble, as close as possible, the cytoplasm in terms of ionic composition, in order to record in physiological conditions. This configuration allows the measurements of the current flowing through all the channels expressed in the plasma membrane.
3) *Inside-out*: this configuration is obtained from a cell-attached configuration, where the pipette is slowly pulled away. The result is a vesicle attached to the pipette tip. The vesicle can be destroyed by exposure to air, i.e. the pipette is briefly lifted above the bath. Inside-out patches are useful for

studying the effects of cytosolic factors on channels but to do this the bath solution must be replaced with intracellular solution in each experiment.

4) *Outside-out*: this configuration is obtained by simply pulling away the patch pipette from a whole-cell configuration. The membrane will eventually breake and, owing to the properties of the phospholipids, fold back on itself into a patch covering the pipette. To obtain a physiological condition the pipette solution should resemble the intracellular ionic environment because it is facing the intracellular side of the membrane. Outside-out patches can be used to study the effects of extracellular factors on the ion channels or receptors, because the bath composition can be easily altered during recordings.

5.4.2 Patch-Clamp recording mode

The patch-clamp technique offers the possibility to perform experiments in two different modes: the voltage clamp recording mode and the current-clamp recording mode.

1) *The voltage-clamp mode* allows the recording of ionic currents across the cell membrane at a defined potential set by the operator (holding potential); the measured potential and the holding potential are continuously compared and any deviation of the recorded from the holding potential is instantly corrected by compensatory current injection from the amplifier. This current is an accurate representation (but opposite in sign) of the ionic current over the membrane under investigation.
2) *The current-clamp mode* allows the recording of the membrane potential variations after injections into a cell of a certain amount of current or without injecting any current through the recording electrode. In the current clamp mode the membrane potential is not clamped but can vary freely and the amplifier records spontaneous voltage variations or voltage deflections evoked by different types of stimulations.

All the electrophysiological recordings presented in “Results” 3.1.2, 3.2, 3.2.1, 3.3.1, 3.3.2 and 3.4.3 were performed using patch-clamp technique in voltage-clamp mode and in whole-cell configuration.

5.5 Patch-Clamp setup for electrophysiological recordings

All the electrophysiological recordings were performed in acute cortical brain slices put into a submerged recording chamber mounted on the stage of an upright microscope (Eclipse E600FN, Nikon Instruments, Japan). The slices were continuously perfused by a peristaltic pump (Gilson, Minipuls 3, USA), with fresh extracellular solution (for composition see 5.7.1) saturated with 95% O_2 and 5% CO_2, at a flow rate of 3 mL/min for voltage-clamp experiments in whole-cell configuration in cortical astrocytes and Pyrs. All the electrophysiological recordings were performed at a temperature of 30°C using an automatic temperature controller (TC-324B, Warner Instruments, USA).

Slices observations and recordings were performed with the microscope mentioned above, that is equipped with infrared light and DIC optics. Slices were first visually inspected with a 10X air Plan Fluor objective (Nikon Instruments, Japan) and then cells were visualized for a detailed observation and identified before performing electrophysiological recordings with a 60X Fluor water immersion objective (Nikon Instruments, Japan). Two cameras (acA1920-155 µm, Basler, Germany; Electro Retiga, Photometrics, USA) were fitted on the microscope and connected to a monitor for live view acquisition on two different displays.

The microscope and the manipulators were placed in an anti-vibration table (Micro-g, TMC) and isolated by a homemade Faraday cage.

Electrical signals were recorded through a Multiclamp 700B patch-clamp amplifier connected to an analogical to digital converter (Digidata 1550) interface and pClamp software (Axon Instruments, USA).

The CV-7B headstage contains both resistor feedback voltage-following circuitry for current-clamp operation, and voltage-to-current circuitry for voltage-clamp operation. The recording electrode, filled with intracellular solution (for composition see 5.7.2) is introduced in an appropriate holder (1-HL-U, Molecular Devices, USA) containing a silver chloride wire linking the electrode to the headstage. A silver chloride earth electrode links the bath to the headstage. The headstage is connected to a motorized micromanipulator (Luigs&Neumann, Germany) allowing precise positioning of the electrode under microscopic control.

5.6 Electrodes

5.6.1 Recording Electrode

Patch-clamp pipettes were obtained from borosilicate capillaries (Wiretrol II 5-1000-2050), after being polished by fire and cleaned with alcohol, using both pullers: P-95 (Sutter Instruments, USA) and PC-100 (Narishige, Japan). The resistance of the pipettes in the bath ranged between 5-7 MΩ and between 3-5 MΩ to record from astrocytes and Pyrs, respectively.

5.6.2 Stimulating Electrode

The cortical layer 1 (L1) neuronal fibers were stimulated using a concentric bipolar electrode (WPI TM33CCINS Tungsten 3'' 76 Imp 10-15K Probe outer diameter 0.016 insulated 400 microm, core diameter 003'' 76 microm y 0.4 mm, X dim w/polyimide .005'' 127 microm. World Precision Instruments Inc., USA).

Precise positioning of the stimulating electrode was obtained using motorized micromanipulator (Luigs&Neumann, Germany) under microscopic control. The stimulating electrode was positioned in L1, 200 µm apart from the patch pipette in the case of recordings from astrocytes in L1 (Fig 5.6), and 200 µm apart from the projection in L1 of the patch pipette in the case of recordings from Pyrs in L2/3 (Fig 5.7). The stimulating electrode was connected to a digital stimulus isolator (AM System, Canada) and neuronal afferent fibers were stimulated by applying a single (100 µs length) or repetitive stimulation (50 and 100 Hz frequency). A stimulation intensity of 100 and 50 µA was used for astrocytic and NMDARs-EPSC recordings, respectively.

5.7 Solutions

5.7.1 Extracellular solutions

The extracellular solution used for recordings from astrocytes and neurons is composed as follows: 125 mM NaCl, 2.5 mM KCl, 1 mM $MgCl_2$, 1 mM $CaCl_2$, 25 mM $NaHCO_3$, 1.25 mM NaH_2PO_4, 25 mM glucose, saturated with 95% O_2 and 5% CO_2 (pH 7.4 with NaOH).

For NMDARs-EPSC recordings from Pyrs 10 or 30 µM D-Serine was added to the extracellular solution in order to limit run-down of the current.

The extracellular solution used to measure CSD threshold and velocity, *modified Artificial Cerebrospinal Fluid* (mACSF), is composed as follows: 125 mM NaCl, 3.5 mM KCl, 1 mM $MgCl_2$, 1 mM $CaCl_2$, 25 mM $NaHCO_3$, 1.25 mM NaH_2PO_4, 25 mM glucose, saturated with 95% O_2 and 5% CO_2 (pH 7.4 with Na OH).

5.7.2 Intracellular solutions

The patch electrodes were filled with different types of intracellular solutions depending on the type of experiment, the cell patched and the recording mode:

For voltage-clamp recordings from astrocytes the pipette contained: 115 mM K-gluconate, 6 mM KCl, 4 mM MgATP, 0.3 mM NaGTP, 10 mM Na-Phosphocretine, 10 mM HEPES, 5 mM glucose (pH = 7.25 with KOH, osmolarity 295 mOsm with sucrose).

For voltage-clamp recordings from Pyrs to measure the NMDARs-EPSC the pipette contained: 129 mM Cs-methanesulfonate, 6 mM KCl, 4 mM MgATP, 0.3 mM NaGTP, 10 mM Na-Phosphocretine, 10 mM HEPES, 0.2 mM EGTA, 3 mM QX-314, 0.2% p/v Biocytine, (pH = 7.25 with CsOH, osmolarity 320 mOsm with sucrose). Cs is used to block potassium channels while QX-314 to block sodium channels and prevent unwanted unclamped action potentials.

For voltage-clamp recordings from Pyrs in optogenetic experiments the pipette contained: 125 mM Cs-methanesulfonate, 8 mM TEA-Cl, 10 mM HEPES, 4 mM MgATP, 0.3 mM NaGTP, 10 mM Na-Phosphocretine, 0.2 mM EGTA, 5 mM BAPTA, 3 mM QX-314, 0.2% p/v Biocytine (pH = 7.25 with KOH, osmolarity 292 mOsm with sucrose).

All intracellular solutions were filtered using a 0.2 µm filter (Minisaret RC 4, Sartorius stedim biotech, Germany).

5.8 Reagents, drugs and toxins

All reagents used for the intracellular and extracellular solutions were supplied by Sigma Aldrich (Italy) except for QX-314 purchased by Abcam Biochemicals (UK).

Ceftriaxone used by intraperitoneal injection in WT and FHM2 KI mice, in experiments presented in "Results 3.1.2" was supplied by Roche (Italy).

For patch clamp recordings from astrocytes (experiments presented in "Results" 3.1.2): D-AP5, NBQX, Gabazine and MK-801 were supplied by Abcam Biochemicals (UK), while DL-TBOA by Tocris (Italy).

For patch clamp recordings from Pyrs (experiments presented in "Results" 3.2, 3.2.1, 3.3.1 and 3.3.2): NBQX, Gabazine and DL-TBOA (same as for astrocyte recordings); Ro25-6981 and PEAQX were supplied by Tocris (Italy).

5.9 Cell identification within the barrel cortex

All the experiments (except for optogenetics) were performed on coronal slices of somatosensory cortex, the so called "barrel cortex". The somatosensory cortex is easily recognizable by the presence of barrel-like structures in L4 (Fig 5.3).
In order to compare the results we standardized the quality of the slices on the basis of cell vitality at 45 µm depth. Slices were used to perform the experiments only if more than 50% of the cells were alive at 45 µm in a 228 X 172 µm field.

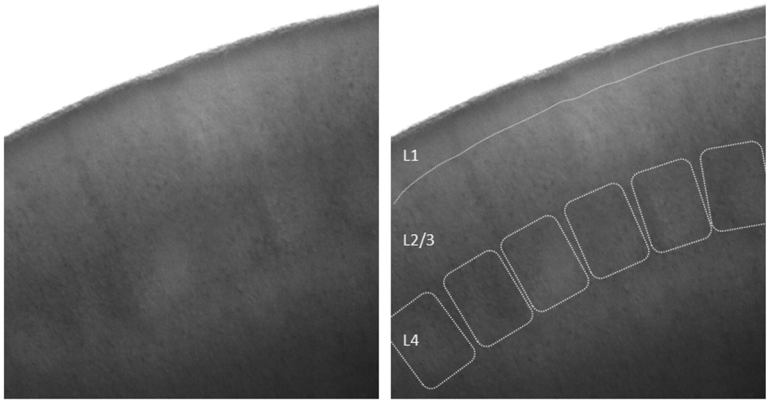

Figure 5.3 Representative image of the somatosensory cortex in a coronal mouse brain slice.
Left panel: Coronal section of somatosensory cortical mouse brain slice.
Right panel: same as the left panel with the different cortical layers defined by dotted lines (note the characteristic barreloid structures recognizable in L4).

5.9.1 Astrocytes identification

Astrocytes were first visually identified, as described in Capuani *et al.*, 2016, in L1 deeper than 45 µm from the slice surface and recognized by their typical morphological shape: small soma (<10 µm diameter) and their electrophysiological properties: low input resistances, very negative resting membrane potential, inability to generate action potentials and linear current-voltage relation (Bergles and Jahr, 1997; Bernardinelli and Chatton, 2008; Scimemi and Diamond, 2013). For the study of the pharmacological effect of TBOA on STC measurements only cells exhibiting passive electrophysiological properties were used, as these astrocytes subtype are known to mediate glutamate uptake as they express active glutamate transporters (Matthias *et al*., 2003).

5.9.2 Pyramidal cell identification

Pyramidal cells (Pyrs) were first visually identified in L2/3 deeper than 45 µm from the slice surface and recognized by their typical morphological pyramidal shape and the presence of a prominent apical dendrite. Given the impossibility to identify Pyrs from their firing properties since the patch pipette is filled with an intracellular solution containing Cs-methanesulfonate and QX-314, in the aftermath is necessary to perform immunohistochemistry to confirm the identity of the recorded cell (see next paragraph and relative Fig).

5.10 Immunohistochemistry

After *in vitro* recordings, slices were transferred into a fixative solution containing 4% paraformaldehyde in phosphate buffer (PB) with 30% sucrose. Slices were rinsed in a PB three times every 10 minutes, then were immersed in Tris-buffered saline (TBS) containing 0.5% triton and Alexa Fluor 594 Streptavidin conjugate (1:1000; Thermofisher Scientific, USA) to detect biocytin (Sigma, Italy). Slices were incubated at room temperature for two hours and then rinsed three times every 15 minutes with PB. The sections were then mounted in Vectashield (Vector Laboratories, USA) and analyzed with a fluorescent microscope (Leica DMI 6000B, Germany) at low magnification 10X and 20X (Fig 5.4).

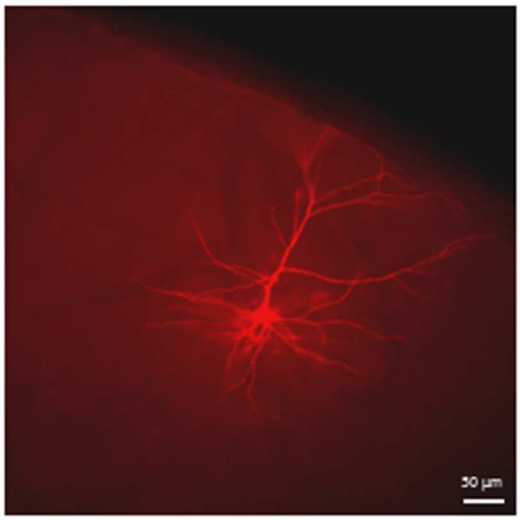

Figure 5.4 Representative image of an immunostained Pyr in L2/3 of the barrel cortex in a coronal slice of mouse brain. Coronal brain slice of the somatosensory cortex in which an immunostained Pyrs (in red) is recognizable in L2/3.

5.11 Data acquisition and analysis

Voltage-clamp recordings from astrocytes and neurons were acquired using Clampex 10.4 software at a sampling rate of 10 kHz and filtered at 2 kHz and analyzed using Clampfit 10.4 of the pClamp suite (pClamp 10.4 Axon, Molecular Devices, USA).

Liquid junction potentials (LJP) measured at the pipette tip was -10 mV and +10.5 mV for the intracellular solutions used in voltage clamp recordings from astrocytes and neurons, respectively. The addition of LJP in whole-cell recordings is necessary to obtain the correct values of the membrane potential (Neher, 1992).

5.11.1 Experimental CSD

Cortical spreading depression was elicited and measured in acute coronal slices of the somatosensory cortex of WT and FHM2 KI mice as in Tottene *et al.*, 2009. Briefly, the brain slices were placed into a submersion chamber and continuously perfused with mACSF solution at a flowing rate of 6 mL/min. Recordings were at 30°C and pressure-ejection pulses of 3 M KCl (0.5 bar) of increasing duration (at 5 min intervals in 20 ms steps) were applied through a glass micropipette (resistance ranging from 0.19 to 0.25 MΩ) onto the slice surface on L2/3, using a PDES-02DX pneumatic drug ejection system (Npi Electronic GmbH, Tamm, Germany), until a

CSD was elicited. CSD was detected by the change in intrinsic optical signal (IOS) (Fig 5.5).

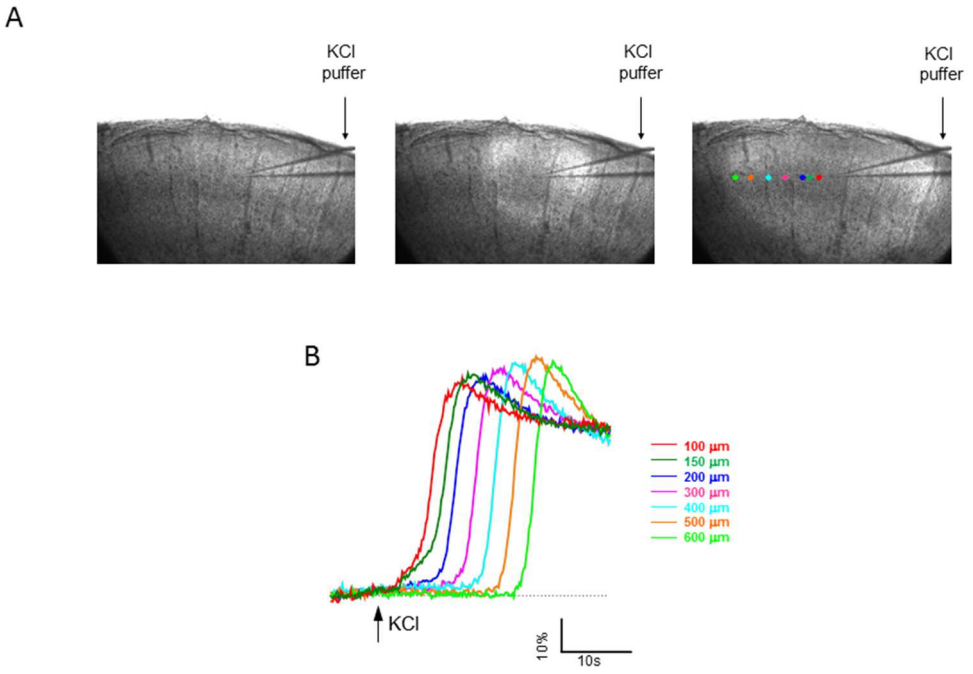

Figure 5.5 Induction of experimental CSD by high KCl pressure pulses.
A Time frames from CSD acquisition showing a coronal brain slice before (on the left) and after CSD induction onto L2/3 of somatosensory cortex by pressure ejection pulses of increasing duration with high KCl (KCl puffer) (central image). Typical change in IOS during CSD propagation (on the right) with the increasing distances (50-100 ms intervals) from the puff pipette indicated by dots of different colors. The change in IOS signal was measured at each dots.
B Representative traces showing the relative change in IOS at increasing distances (50-100 µm intervals) from the puff pipette. The IOS change is expressed as percent change in light transmittance relative to the backgroud.

The duration of the first pulse eliciting a CSD was taken as CSD threshold and the rate of horizontal spread of the change in IOS as CSD velocity. IOS was recorded using a CCD camera (KP-M2A, Hitachi, Tokio, Japan) connected with an upright microscope (Nikon Eclipse; 10X magnification, Nikon, Tokio, Japan). Images were recorded at 200 ms intervals as 640 x 480 pixels images (pixel size: 2.15 µm). MBF ImageJ software was used for the off line analysis of the digitalized images. The IOS change is expressed as percent change in light trasmittance (ΔT)

relative to the background signal: %ΔT/T. All CSD experiments and analyses in saline-treated and cef-treated mice were performed by a blinded observer.

5.11.2 Glutamate imaging

6 weeks old FHM2 knock-in mice and WT littermates were injected with 0.3-0.5 µl of AAV2/1.GFAP.iGluSnFr.WPRE.SV40 (Penn Vector; provided by Dr Loren Looger, Janelia Farm) into the barrel cortex through a glass pipette. Stereotaxic co-ordinates with respect to Bregma were (in mm): 1 posterior, 3.5 lateral, 0.3 ventral. 15 to 18 days following the viral injections, coronal brain slices (350 µm) containing the barrel cortex were obtained as described previously (Santello and Nevian, 2015). A galvanometer-based two-photon laser scanning system was used to image extrasynaptic glutamate (16X objective, zoom 6, excitation wavelength 900 nm, 64x64 pixels/image, acquisition rate 19.2 Hz). Astrocytes were visualized using the sulforhodamine 101 dye (SR101, 1 µM, incubation 15 minutes at 34° C). Synaptic glutamate release was elicited by single pulse stimulation and by trains of 10 pulses at high frequency (50 or 100 Hz) every 20 s delivered via a theta-glass pipette (bipolar, 100 µs, stimulation intensity 3-5 V) placed in the inner L1. In order to visualize the theta-glass pipette, the latter was filled with ACSF containing 5 µM SR-101. All solutions contained 10 µM NBQX, 50 µM APV, 100 µM picrotoxin and temperature was kept between 33 and 34°C while imaging. 10 consecutive sweeps were acquired and subsequently analyzed using Image J. Fluorescence emission was collected from a region of interest (diameter 34 µm) 10-40 µm away from the stimulation pipette. The average background values (derived from a region within the field of view which was free of clearly visible iGluSnFr, typically outside the slice) were then subtracted from the fluorescence intensity of the ROIs for each frame. Traces were then averaged and decay Tau was calculated by fitting a single exponential function using Igor Pro (wavemetrics). Genotypes were blinded to the experimenter until the analysis was completed.

5.11.3 Recordings and analysis of the STC from cortical L1 astrocytes

Only astrocytes with a resting potential between –85 and –95 mV (after LJP correction) and an access resistance below 25 MΩ (with less than 25% variation) were included in the analysis.

In voltage-clamp recordings, astrocytes were clamped at –90 mV. To record the STC, during whole-cell patch recordings from astrocytes in the L1 of somatosensory cortex slices (Fig 5.6), AMPA, NMDA, and GABAA receptors were blocked using specific antagonists (10 μM NBQX, 50 μM D-AP5, 20 μM MK-801 and 20 μM bicuculline) (Bergles and Jahr, 1997; Bernardinelli and Chatton, 2008). Under these conditions, stimulation of the fibers in L1 generates an inward current comprising fast and slow components. The transporter antagonist TFB-TBOA (15 μM) blocked the fast component, identifying it as the STC. The slower component mainly reflects a K^+ conductance caused by an increase in extracellular K^+ due to K^+ efflux through voltage-gated K^+ channels during the APs (Bergles and Jahr, 1997; Meeks and Mennerick, 2007; Bernardinelli and Chatton, 2008; Dallérac *et al.*, 2013) and through the NMDA receptors (in the case in which they are not blocked, see below) (Poolos *et al.*, 1987; De Saint and Westbrook, 2005; Shih *et al.*, 2013; Sibille *et al.*, 2014).

To isolate the STC of the single pulse, the response to single pulse in the presence of TFB-TBOA was subtracted to the response in control condition. The STC decay was fitted with a single exponential function ($y = A * \exp(-x/\tau) + y0$, where A is the amplitude, y0 is the value at steady state, τ is the time constant, x is the time at which the decay starts) and the time constant (τ) was obtained, providing a measure of the rate of Glu clearance. The K^+ current has been recorded in separated experiments with a protocol similar as the STC but in the absence of synaptic receptor blockers. The decay of this slow current was fitted, as for the STC, and provides a measure of the rate of K^+ clearance. The decay time constant of the K^+ currents has been measured both, in the absence and in the presence of Glu transporter blockers, showing similar time constants of decay in both genotypes and similar slowing of K^+ clearance in FHM2 KI compared to WT mice (data not shown, for details see Capuani *et al.*, 2016).

.

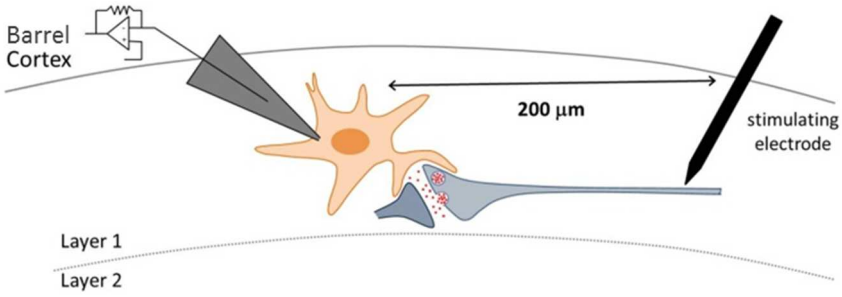

Figura 5.6 Patch-clamp configuration recordings of L1 astrocyte of the barrel cortex (Capuani *et al.*, 2016).
Image showing the scheme of the STC recording paradigm. The currents elicited by extracellular stimulation in L1 were measured in voltage-clamped L1 astrocyte located at 200 µm from the stimulating electrode in an acute cortical slice of mouse barrel cortex.

5.11.4 Recordings and analysis of the NMDARs-EPSC from L2/3 pyramidal neurons of the barrel cortex

Pyramidal neurons (Pyrs) were identified by their morphology in the upper L2/3 of the somatosensory cortex and were whole-cell patch clamped using a 3-5 MΩ electrode. Access resistance was accepted only if below 15 MΩ and monitored throughout the whole experiments and eventually compensated using Multiclamp 700B software (Axon Instruments, USA).

In voltage-clamp mode, neurons were held at + 40 mV to relive the Mg^{2+} block of the NMDARs and allowed to stabilize for 6 minutes. To record the NMDAR-EPSC in isolation AMPA and GABAA receptors were blocked using specific antagonists: 10 µM NBQX and Gabazine, respectively (Fig 5.7 A). Under these conditions, stimulation (50 µA of intensity) of the fibers in L1 generates an outward current that was completely abolished by 100 µM D-APV, a specific NMDARs antagonist. The NMDARs-EPSC activation kinetics were derived from the time course of the rising phase and calculated from the time in which the current reaches the 95% of the peak. NMDARs-EPSC amplitude was calculated at the peak of the evoked current (Fig 5.7 B, upper panel), the decay kinetics were derived by measuring the half time of decay (Fig 5.7 B, middle panel) or by fitting with a

double exponential function ($y = y0 + A_f * \exp(-(-x-x0)/\tau_f) + A_s * \exp(-(-x-x0)/\tau_s)$, where A_f and A_s are the relative amplitudes and τ_f and τ_s are the time constants of the fast and the slow exponential, respectively. Weighted time constants were calculated as follows: $\tau_w = [(A_f * \tau_f) + (A_s * \tau_s)]/(A_f + A_s)]$, where A_f and A_s are the relative amplitudes and τ_f and τ_s are the time constants of the fast and the slow exponential, respectively. The total charge transfer mediated by NMDARs was calculated by integrating the 90% of the area under the curve (Fig 5.7 B, bottom panel).

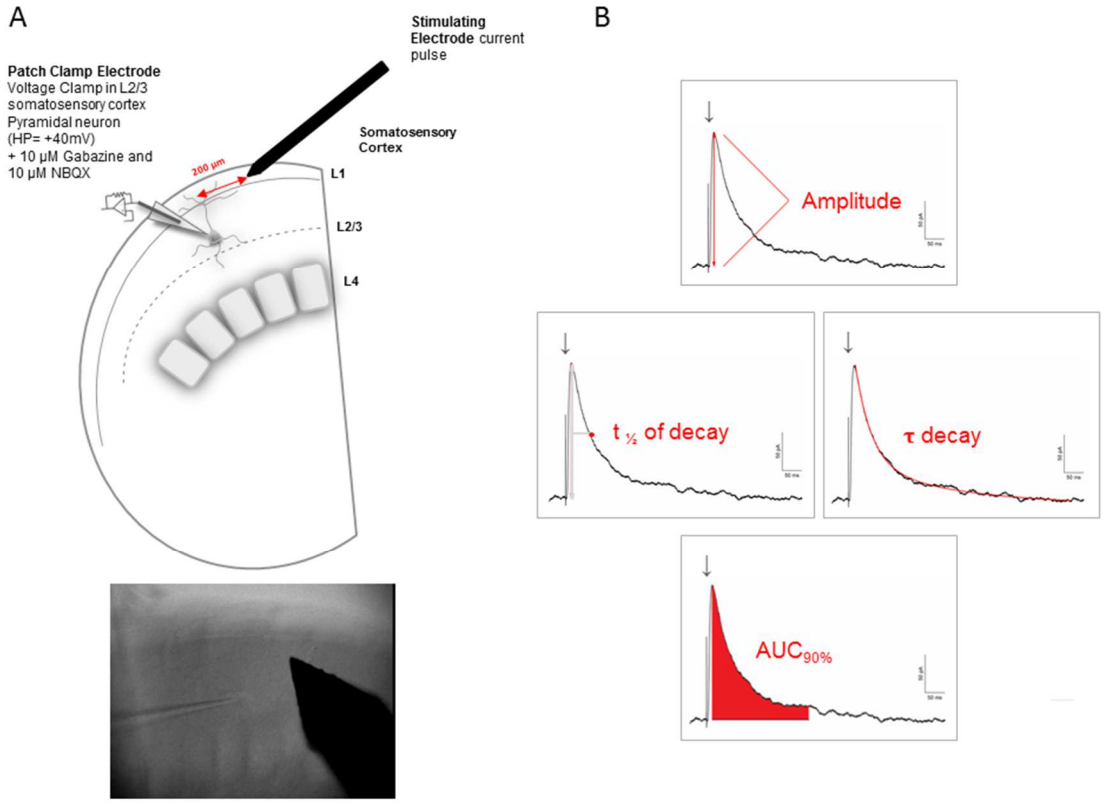

Figure 5.7 Patch-clamp configuration recordings of L2/3 pyramidal neuron of the barrel cortex
A Image showing the scheme of the NMDARs-EPSC recording paradigm. The NMDARs-mediated currents were measured in voltage-clamped L2/3 Pyrs and elicited by extracellular stimulation in L1 positioning the stimulating electrode at 200 µm from the projection of the patched Pyrs in L1, in an acute cortical slice of mouse barrel cortex.
B Measures of the amplitude, the decay kinetics and the total charge carried by NMDARs from the original or normalized recorded traces.

5.12 *In Utero* electroporation

The protocol we used to perform in utero electroporation was developed by Szczurkowska *et al*., 2016. Time pregnant mice (15.5 days post-coitum, as revealed by the presence of a sperm plug in the female at early morning post-mating (for details see below, 5.13), were anesthetized with Isoflurane (for induction: 4% Isoflurane and 1.5 ml/min) and maintained in anesthesia (2.5% Isoflurane and 1.5 ml/min Oxygen) for maximum 30 minutes for each electroporation procedure. The mouse was placed on its back on a heated (30°C) surgery pad, covered with a sterile towels. Artificial tears were gently applied to the eyes of the animal to prevent them from drying during anesthesia. Front paws were fixed with tape and hind paws were intramuscularly injected on the left with painkiller (5 mg/Kg Toradol, Recordati, Italy) and on the right with antibiotic (5 mg/Kg Baytril, Bayer, New Zeland). The abdomen was gently stretched out and shaved with an electrical shaver and fur was removed with a vacuum cleaner. The shaved abdomen was cleaned using both cotton balls soaked with ethanol and Betadine (Meda Pharma, Italy) repeatedly for three times. Only after the operator has worn sterile gloves, a surgical drape with a hole in the middle was positioned onto mouse's abdomen in order to create both, a sterile field and a quick access to the abdomen. The skin was cut with a scissor near the *linea alba* to prevent from excessive bleeding. By using two grabbers the skin was gently separated from the abdominal muscle and, once established that there are no embryos underneath, the muscle was cut until the hole was large enough to easily expose the uterus. The first two-three embryos of one side of the uterine horn were pulled off the abdomen by using a ring forceps positioned in the uterine wall (corresponding to the gap between the yolk sacs of two neighboring embryos), and the remaining embryos were carefully pulled using fingers. The right lateral ventricle of each embryo was injected, using a 30G needle perpendicular to the head surface, with a pressure controller (Picospritzer III, Parker, USA) connected to a foot-switch. Each embryo received 1 µl of plasmidic DNA solution containing 0.5 µg/µl of plasmid (pCAGGS-ChR2-Venus and pCAGGS-mCherry, Addgene, USA) and 0,15 µg/µl of Fast Green FCF (SIGMA, Italy) for site injection visualization (Fig 5.8). Once injected, each embryo was wet with 27°C sterile PBS to avoid excessive cooling before being electroporated.

Moreover, sterile PBS solution facilitate current flow during the electroporation. Electroporation is performed as soon as possible after injection using warm bipolar tweezertrodes (5 mm Ø) connected to a pulse generator (BTX, Harvard Apparatus, USA) and optimized parameters encompass: 6 pulses of 30 V in amplitude, lasting 50 ms each and delivered every second. The forceps-type electrodes were positioned at the sides of the embryo's head with the anode positioned to selectively target the cortical L2/3 progenitor cells (Fig 5.8). To prevent the embryo's death, the operator should not squeeze the uterus and yolk sac containing the embryos during electroporation. Afterward, embryos were carefully returned back into mouse's abdominal cavity and the procedure repeated for the embryos of the other side of the uterine horn. Once completed the electroporation of all the embryos, first the abdominal muscle and then the skin were sutured using vicryl-coated suture thread (5-0 gauge). Betadine was locally applied onto the wound and the stitches.

After the surgery, Isoflurane was shutted down and the oxygen was led flow for 5 minutes to favor the recovery of the animal from anesthesia. The operated animal was then placed belly-down into a clean cage with some wet food inside the cage to favor feeding and hydration. The cage was kept under an heating lamp until the animal fully recovered from anesthesia and afterward returned into the animal husbandry. The operated animals were kept separate from any stress source (smell, noise, etc) (Szczurkowska *et al*., 2016).

Figure 5.8 Representative image of *in utero* electroporation of mouse embryo (E 15.5)
Forceps-type electrodes configuration used at 15.5 days to selectively target the cortical L2/3 progenitor cells. The green spot (indicated by the white arrow) represents succesful filling of the lateral ventricle with DNA. + and – indicate the polarities of the forceps-type electrodes.

5.13 Mating strategy

For all the animals of both phenotypes I planned a mating for 3 nights a week, pairing one male (from 2-3 months of age) and three females (from 2-2.5 months of age), and transferring the females into the male's cage during the mating period. The presence of a sperm plug was verified for each female every morning at 8 am. The morning in which the sperm plug was observed was considered day 0.5 since mice are nocturnal animals and the mating is supposed to happen during the night.

5.14 Channelrhodopsin-2 activation

Optogenetic stimulation of the somatosensory cortex was performed using an infinity cube (CAIRN Research, UK) consisting of a 470-nm filter system mounted on the upright microscope described in 5.5. Light intensity and timing were controlled by a Dual OptoLed power supply (CAIRN Research, UK). Slices were illuminated from the top and a round spot was created, adjusting a field diaphragm, with a diameter of approximately 90 µm in order to illuminate a single barrel column. Excitatory and inhibitory light-evoked currents were measured in L2/3 Pyrs not expressing ChR2 (Chr2-), by voltage clamping individual Pyrs at +10 mV and -68 mV, the reversal potential (E_{rev}) for EPSP (excitatory post-synaptic potential) and IPSP (inhibitory post-synaptic potential), respectively. A protocol consisting in single short 2 ms blue light pulses to mimic transient sensory-driven spiking (Shao *et al*., 2012) was delivered at increasing light intensity. Net synaptic charge was derived by integrating the currents over the first 50 ms, and used to calculate the E/(E+I) ratio.

5.15 Statistics

All averages were calculated using Microsoft Excel software. All the graphs, the plots and the exponential fitting were obtained with the Origin 8 software (Microcal Software, Inc.). Statistical comparison were obtained with both Origin 8 and Statgraphics Centurion XVII (Statgraphics Technologies, Inc.) software. After assessing for normal distribution of the data using Shapiro-Wilk, comparison between two groups was made using unpaired or paired *t*-test for normal distributed

data or the Mann-Whitney *U*-test for nonparametric data, equal variance were always assumed. Data are given as mean ± standard error of the mean (SEM); differences were considered statistically significant if $P < 0.05$ (*$P < 0.05$; ** $P < 0.01$; *** $P < 0.001$).

ABBREVIATION

ABD: Agonist binding domain

AMPA: α-amino-3-hydroxy-5-methyl-4-isoxazole-propionic acid

AxTs: Axon terminals

BOLD: Blood-oxygen-level-dependent

Ca^{2+}: Calcium ion

Ca_v: Voltage-gated Ca^{2+} channels

Cef: Ceftriaxone

CGRP: Calcitonin gene-related peptide

ChR2: Channelrhodopsin 2

ChR2+: Channelrhodopsin 2-expressing neurons

ChR2-: Channelrhodopsin 2-non expressing neurons

Cl^-: Chloride ion

CNS: Central nervous system

CTD: carboxyl (C)-terminal domain

Ctr: Control conditions

CSD: Cortical spreading depression

FHM: Familial hemiplegic migraine

FHM1: Familial hemiplegic migraine type 1

FHM2: Familial hemiplegic migraine type 2

FHM3: Familial hemiplegic migraine type 3

EM: Electron microscopy

EPSC: Excitatory post-synaptic current

FS: Fast spiking

GABA: γ-aminobutirric acid

GCS: Gluconate cutting solution

GLT-1: Glial glutamate transporter 1

Glu: Glutamate

GluN2AR: Dieteromeric GluN2A subunit containing NMDA receptor

GluN2BR: Dieteromeric GluNBA subunit containing NMDA receptor

GluN2A-2BR: Trieteromeric GluN2A and GluN2B subunits containing NMDA receptor

GluTs: Glutamate transporters

H^+: Hydrogen ion

iGluRs: Ionotropic glutamate receptors

Ins: Insular

IOS: Intrinsic optic signal

IUE: *In utero* electroporation

ir: Immunoreactivity

K^+: Potassium ion

KI: Knock-in

L1: Layer 1

L2/3: Layer 2/3

MA: Migraine with aura

Mg^{2+}: Magnesium ion

MO: Migraine without aura

Na^+: Sodium ion

Na_v: Voltage-gated Na^+ channels

MCS: Mannitol cutting solution

NMDA: N-methyl-D-aspartate

NMDAR: N-methyl-D-aspartate receptor

NMDARs-EPSC: NMDARs-mediated excitatory postsynaptic currents

NO: Nitric oxide

NTD: Amino (N)-terminal domain

PAPs: Perisynaptic astrocytic processes

PB: Phosphate buffer

Plug +: Plug positive

Pyr: Pyramidal neuron

PV: Parvalbumin expressing interneurons

RT: Room temperature

RVM: Rostral ventromedial medulla

S1: Somatosensory 1

sACSF: standard Artificial cerebrospinal fluid

SOM: Somatostatin expressing interneurons

SP: Single pulse stimulation

STC: Synaptically activated transporter current

T_{100Hz}: Train of 10 pulses at 100 Hz frequency

TBS: Tris-buffered saline

TC: Thalamo-cortical

TCC: Trigeminocervical complex

TCN: Spinal trigeminal nucleus

TGVS: Trigeminovascular system

VGLUT1: Vescicolar glutamate transporter 1

TMD: Trans-membane domain

vlPAG: Ventro lateral periacqueductal gray

VPM: Ventro postero medial

WT: Wild type

$\alpha 2$ NKA: $\alpha 2$ subunit of the Na^+/K^+ ATPase

REFERENCES

Adesnik H, Scanziani M (2010) Lateral competiton for cortical space by layer-specific horizontal circuits. Nature 464:1155-1160.

Agmon A, Connors BW (1991) Thalamocortical responses of mouse somatosensory (barrel) cortex in vitro. Neurosci 41:365-379.

Aiba I and Shuttleworth CW (2012) Sustained NMDA receptor activation by spreading depolarization can initiate excitotoxic injury in metabolically compromised neurons. J Physiol 590:5877-5893.

Anderson CM, Swanson RA (2000) Astrocyte glutamate transport: review of properties, regulation, and physiological functions. Glia 32:1–14.

Araque A, Parpura V, Sanzgiri RP, Haydon PG (1999) Tripartite synapses: glia, the unacknowledged partner. Trends Neurosci 22:208–215.

Armbruster M, Hanson E, Dulla CG (2016) Glutamate Clearance Is Locally Modulated by Presynaptic Neuronal Activity in the Cerebral Cortex. J Neurosci 36:10404–10415.

Ayata C (2009) Spreading depression: from serendipity to targeted therapy in migraine prophylaxis. Cephalalgia 29:1095–1114.

Ayata C, Jin H, Kudo C, Dalkara T, Moskowitz MA (2006) Suppression of cortical spreading depression in migraine prophylaxis. Ann Neurol 59:652–661.

Ayata C, Shimizu-Sasamata M, Lo EH, Noebels JL, Moskowitz MA (2000) Impaired neurotransmitter release and elevated threshold for cortical spreading depression in mice with mutations in the alpha1A subunit of P/Q type calcium channels. Neuroscience 95:639–645.

Barbour B, Keller BU, Llano I, Marty A (1994) Prolonged presence of glutamate during excitatory synaptic transmission to cerebellar Purkinje cells. Neuron 12:1331–1343.

Baumgart J, Grebe N (2015) C57BL/6-specific conditions for efficient in utero eletctroporation of the central nervous system. J Neurosci 240:116-124.

Bellesi M, Melone M, Gubbini A, Battistacci S, Conti F (2009) GLT-1 upregulation impairs prepulse inhibition of the startle reflex in adult rats. Glia 57:703–713.

Bergles DE, Jahr CE (1997) Synaptic activation of glutamate transporters in hippocampal astrocytes. Neuron 19:1297–1308.

Bernardinelli Y, Chatton J-Y (2008) Differential effects of glutamate transporter inhibitors on the global electrophysiological response of astrocytes to neuronal stimulation. Brain Res 1240:47–53.

Bøttger P, Doğanlı C, Lykke-Hartmann K (2012) Migraine- and dystonia-related disease-mutations of Na+/K+-ATPases: relevance of behavioral studies in mice to disease symptoms and neurological manifestations in humans. Neurosci Biobehav Rev 36:855–871.

Bourne HR, Nicoll R (1993) Molecular machines integrate coincident synaptic signals. Cell 72 Suppl:65–75.

Bozdagi O, Shan W, Tanaka H, Benson DL, Huntley GW (2000) Increasing numbers of synaptic puncta during late-phase LTP: N-cadherin is synthesized, recruited to synaptic sites, and required for potentiation. Neuron 28:245–259.

Bragina L, Melone M, Fattorini G, Torres-Ramos M, Vallejo-Illarramendi A, Matute C, Conti F (2006) GLT-1 down-regulation induced by clozapine in rat frontal cortex is associated with synaptophysin up-regulation. J Neurochem 99:134–141.

Brennan KC, Charles A (2010) An update on the blood vessel in migraine. Curr Opin Neurol 23:266–274.

Brennan KC, Pietrobon D (2018) A Systems Neuroscience Approach to Migraine. Neuron 97:1004–1021.

Campbell SL, Hablitz JJ (2004) Glutamate transporters regulate excitability in local networks in rat neocortex. Neuroscience 127:625–635.

Campbell SL, Hablitz JJ, Olsen ML (2014) Functional changes in glutamate transporters and astrocyte biophysical properties in a rodent model of focal cortical dysplasia. Front Cell Neurosci 8:425.

Canals S, Makarova I, López-Aguado L, Largo C, Ibarz JM, Herreras O (2005) Longitudinal depolarization gradients along the somatodendritic axis of CA1 pyramidal cells: a novel feature of spreading depression. J Neurophysiol 94:943–951.

Capuani C, Melone M, Tottene A, Bragina L, Crivellaro G, Santello M, Casari G, Conti F, Pietrobon D (2016) Defective glutamate and K+ clearance by cortical astrocytes in familial hemiplegic migraine type 2. EMBO Mol Med 8:967–986.

Carreño O, Corominas R, Serra SA, Sintas C, Fernández-Castillo N, Vila-Pueyo M, Toma C, Gené GG, Pons R, Llaneza M, Sobrido M-J, Grinberg D, Valverde MÁ, Fernández-Fernández JM, Macaya A, Cormand B (2013) Screening of CACNA1A and ATP1A2 genes in hemiplegic migraine: clinical, genetic, and functional studies. Mol Genet Genomic Med 1:206–222.

Cestèle S, Scalmani P, Rusconi R, Terragni B, Franceschetti S, Mantegazza M (2008) Self-limited hyperexcitability: functional effect of a familial hemiplegic migraine mutation of the Nav1.1 (SCN1A) Na+ channel. J Neurosci 28:7273–7283.

Chen W, Mahadomrongkul V, Berger UV, Bassan M, DeSilva T, Tanaka K, Irwin N, Aoki C, Rosenberg PA (2004) The glutamate transporter GLT1a is expressed in excitatory axon terminals of mature hippocampal neurons. J Neurosci 24:1136–1148.

Cholet N, Pellerin L, Magistretti PJ, Hamel E (2002) Similar perisynaptic glial localization for the Na+,K+-ATPase alpha 2 subunit and the glutamate transporters GLAST and GLT-1 in the rat somatosensory cortex. Cereb Cortex 12:515–525.

Chuquet J, Hollender L, Nimchinsky EA (2007) High-resolution *in vivo* imaging of the neurovascular unit during spreading depression. J Neurosci 27:4036-4044.

Clements JD, Lester RA, Tong G, Jahr CE, Westbrook GL (1992) The time course of glutamate in the synaptic cleft. Science 258:1498–1501.

Coppola G, Pierelli F, Schoenen J (2007) Is the cerebral cortex hyperexcitable or hyperresponsive in migraine?. Cephalalgia 27(12):1427-1439.

dal Maschio M, Ghezzi D, Bony G, Alabastri A, Deidda G, Brondi M, Sato SS, Zaccaria RP, Di Fabrizio E, Ratto GM, Cancedda L (2012) High-performance and site-directed in utero electroporation with a triple-electrode probe. Nat Commun 3:960.

Dallérac G, Chever O, Rouach N (2013) How do astrocytes shape synaptic transmission? Insights from electrophysiology. Front Cell Neurosci 7:159.

Danbolt NC (2001) Glutamate uptake. Prog Neurobiol 65:1–105.

De Fusco M, Marconi R, Silvestri L, Atorino L, Rampoldi L, Morgante L, Ballabio A, Aridon P, Casari G (2003) Haploinsufficiency of ATP1A2 encoding the Na+/K+ pump alpha2 subunit associated with familial hemiplegic migraine type 2. Nat Genet 33:192–196.

De Saint Jan D, Westbrook GL (2005) Detecting activity in olfactory bulb glomeruli with astrocyte recording. J Neurosci 25:2917-2924.

Diamond JS (2001) Neuronal glutamate transporters limit activation of NMDA receptors by neurotransmitter spillover on CA1 pyramidal cells. J Neurosci 21:8328–8338.

Diamond JS (2005) Deriving the glutamate clearance time course from transporter currents in CA1 hippocampal astrocytes: transmitter uptake gets faster during development. J Neurosci 25:2906–2916.

Dichgans M, Freilinger T, Eckstein G, Babini E, Lorenz-Depiereux B, Biskup S, Ferrari MD, Herzog J, van den Maagdenberg AM, Pusch M, Strom TM (2005) Mutation in the neuronal voltage-gated sodium channel SCN1A in familial hemiplegic migraine. Lancet 366:371–377.

Ducros A, Denier C, Joutel A, Cecillon M, Lescoat C, Vahedi K, Darcel F, Vicaut E, Bousser MG, Tournier-Lasserve E (2001) The clinical spectrum of familial hemiplegic migraine associated with mutations in a neuronal calcium channel. N Engl J Med 345:17–24.

Dugué GP, Dumoulin A, Triller A, Dieudonné S (2005) Target-dependent use of co-released inhibitory transmitters at central synapses. J Neurosci 25:6490–6498.

Enger R, Tang W, Vindedal GF, Jensen V, Johannes HP, Sprengel R, Looger LL, Nagelhus EA (2015) Dynamics of ionic shifts in cortical spreading depression. Cereb Cortex 25:4469-4476.

Farhy-Tselnicker I, Allen NJ (2018) Astrocytes, neurons, synapses: a tripartite view on cortical circuit development. Neural Dev 13:7.

Fellin T, Pascual O, Haydon PG (2006) Astrocytes coordinate synaptic networks: balanced excitation and inhibition. Physiology (Bethesda) 21:208–215.

Fink D, Knapp PE, Mata M (1996) Differential expression of Na,K-ATPase isoforms in oligodendrocytes and astrocytes. Dev Neurosci 18:319–326.

Fischer G, Mutel V, Trube G, Malherbe P, Kew JN, Mohacsi E, Heitz MP, Kemp JA (1997) Ro 25-6981, a highly potent and selective blocker of N-methyl-D-aspartate receptors containing the NR2B subunit. Characterization in vitro. J Pharmacol Exp Ther 283:1285–1292.

Footitt DR, Newberry NR (1998) Cortical spreading depression induces an LTP-like effect in rat neocortex in vitro. Brain res 781:339-342.

Furness DN, Dehnes Y, Akhtar AQ, Rossi DJ, Hamann M, Grutle NJ, Gundersen V, Holmseth S, Lehre KP, Ullensvang K, Wojewodzic M, Zhou Y, Attwell D, Danbolt NC (2008) A quantitative assessment of glutamate uptake into hippocampal synaptic terminals and astrocytes: new insights into a neuronal role for excitatory amino acid transporter 2 (EAAT2). Neuroscience 157:80–94.

Furuta A, Rothstein JD, Martin LJ (1997) Glutamate transporter protein subtypes are expressed differentially during rat CNS development. J Neurosci 17:8363–8375.

Giffin NJ, Ruggiero L, Lipton RB, Silberstein SD, Tvedskov JF, Olesen J, Altman J, Goadsby PJ, Macrae A (2003) Premonitory symptoms in migraine: an electronic diary study. Neurology 60:935–940.

Goadsby PJ, Lipton RB, Ferrari MD (2002) Migraine-current understanding and treatment. N Engl J Med 346:257-270.

Golovina VA, Song H, James PF, Lingrel JB, Blaustein MP (2003) Na+ pump alpha 2-subunit expression modulates Ca2+ signaling. Am J Physiol, Cell Physiol 284:C475-486.

Grafstein B (1956) Mechanism of spreading cortical depression. J Neurophysiol 19:154–171.

Hadjikhani N, Sanchez Del Rio M, Wu O, Schwartz D, Bakker D, Fischl B, Kwong KK, Cutrer FM, Rosen BR, Tootell RB, Sorensen AG, Moskowitz MA (2001) Mechanisms of migraine aura revealed by functional MRI in human visual cortex. Proc Natl Acad Sci USA 98:4687–4692.

Hans M, Luvisetto S, Williams ME, Spagnolo M, Urrutia A, Tottene A, Brust PF, Johnson EC, Harpold MM, Stauderman KA, Pietrobon D (1999) functional consequences of mutations in the human a1A calcium channel subunit linked to familial hemiplegic migraine. J Neurosci 19:1610-1619.

Hansen KB, Ogden KK, Yuan H, Traynelis SF (2014) Distinct functional and pharmacological properties of Triheteromeric GluN1/GluN2A/GluN2B NMDA receptors. Neuron 81:1084–1096.

Hansen KB, Yi F, Perszyk RE, Menniti FS, Traynelis SF (2017) NMDA Receptors in the Central Nervous System. Methods Mol Biol 1677:1–80.

Hauge AW, Kirchmann M, Olesen J (2011) Characterization of consistent triggers of migraine with aura. Cephalalgia 31:416–438.

Haugeto O, Ullensvang K, Levy LM, Chaudhry FA, Honoré T, Nielsen M, Lehre KP, Danbolt NC (1996) Brain glutamate transporter proteins form homomultimers. J Biol Chem 271:27715–27722.

Haydon PG (2001) GLIA: listening and talking to the synapse. Nat Rev Neurosci 2:185–193.

Hederich UBS, Liautard C, Kirschenbaum D, Pofahl M, Lavigne J, Liu Y, Theiss S, Slotta J, Escayg A, Dihnè M, Beck H, Mantegazza M, Lerche H (2014) Impaired action potential initiation in GABAergic interneurons causes hyperexcitable networks in an hepileptic mouse model carrying a human $Na_v1.1$ mutation. J Neurosci 34:14874-14889.

Herreras O, Largo C, Ibarz JM, Somjen GG, Martín del Río R (1994) Role of neuronal synchronizing mechanisms in the propagation of spreading depression in the in vivo hippocampus. J Neurosci 14:7087–7098.

Hestrin S (1992) Activation and desensitization of glutamate-activated channels mediating fast excitatory synaptic currents in the visual cortex. Neuron 9:991–999.

Hestrin S, Perkel DJ, Sah P, Manabe T, Renner P, Nicoll RA (1990) Physiological properties of excitatory synaptic transmission in the central nervous system. Cold Spring Harb Symp Quant Biol 55:87–93.

Ilarianova NB, Brismar H, Aperia A, Gunnarson E (2014) Role of Na,K-ATPase α1 and α2 Isoforms in the Support of Astrocyte Glutamate Uptake. PLOS One 9(6):1-10.

Ikeda K, Onimaru H, Yamada J, Inoue K, Ueno S, Onaka T, Toyoda H, Arata A, Ishikawa T, Taketo MM, Fukuda A, Kawakami K (2004) Malfunction of respiratory-related neuronal activity in Na+, K+-ATPase alpha2 subunit-deficient mice is attributable to abnormal Cl- homeostasis in brainstem neurons. J Neurosci 24:10693–10701.

Jing J, Aitken PG, Somjen GG (1993) Role of calcium channels in spreading depression in rat hippocampal slices. Brain Res 604:251–259.

Jonas P, Racca C, Sakmann B, Seeburg PH, Monyer H (1994) Differences in Ca2+ permeability of AMPA-type glutamate receptor channels in neocortical neurons caused by differential GluR-B subunit expression. Neuron 12:1281–1289.

Jorgensen PL, Hakansson KO, Karlish SJD (2003) Structure and mechanism of Na,K-ATPase: functional sites and their interactions. Annu Rev Physiol 65:817–849.

Juhaszova M, Blaustein MP (1997) Distinct distribution of different Na+ pump alpha subunit isoforms in plasmalemma. Physiological implications. Ann N Y Acad Sci 834:524–536.

Kahlig KM, Rhodes TH, Pusch M, Freilinger T, Pereira-Monteiro JM, Ferrari MD, van den Maagdenberg AMJM, Dichgans M, George AL (2008) Divergent sodium channel defects in familial hemiplegic migraine. Proc Natl Acad Sci USA 105:9799–9804.

Kaneko T, Fujiyama F, Hioki H (2002) Immunohistochemical localization of candidates for vesicular glutamate transporters in the rat brain. J Comp Neurol 444:39–62.

Koenderink JB, Zifarelli G, Qiu LY, Schwarz W, De Pont JJHHM, Bamberg E, Friedrich T (2005) Na,K-ATPase mutations in familial hemiplegic migraine lead to functional inactivation. Biochim Biophys Acta 1669:61–68.

Kors EE, Terwindt GM, Vermeulen FL, Fitzsimons RB, Jardine PE, Heywood P, Love S, van den Maagdenberg AM, Haan J, Frants RR, Ferrari MD (2001) Delayed cerebral edema and fatal coma after minor head trauma: role of the CACNA1A calcium channel subunit gene and relationship with familial hemiplegic migraine. Ann Neurol 49:753–760.

Kraus RL, Sinnegger M, Koschak A, Glossmann H, Stenirri S, Carrera P, Striessnig J (2000) Three new familial hemiplegic migraine mutants affect P/Q-type Ca^{2+} channel kinetics. J Biol Chem 275:9239-9243.

Kraus RL, Sinnegger MJ, Glossmann H, Hering S, Striessnig J (1998) Familial hemiplegic migraine mutations change a1A Ca^{2+} channel kinetics. J Biol Chem 273: 5586-5590.

Krnjević K (1974) Some neuroactive compounds in the substantia nigra. Adv Neurol 5:145–152.

Lau CG, Zukin RS (2007) NMDA receptor trafficking in synaptic plasticity and neuropsychiatric disorders. Nat Rev Neurosci 8:413–426.

Leão AAP (1944) Spreading depression of activity in the cerebral cortex. J Neurophysiol 7:359-390.

Lehre KP, Danbolt NC (1998) The number of glutamate transporter subtype molecules at glutamatergic synapses: chemical and stereological quantification in young adult rat brain. J Neurosci 18:8751–8757.

Lencesova L, O'Neill A, Resneck WG, Bloch RJ, Blaustein MP (2004) Plasma membrane-cytoskeleton-endoplasmic reticulum complexes in neurons and astrocytes. J Biol Chem 279:2885–2893.

Leo L, Gherardini L, Barone V, De Fusco M, Pietrobon D, Pizzorusso T, Casari G (2011) Increased susceptibility to cortical spreading depression in the mouse model of familial hemiplegic migraine type 2. PLoS Genet 7:e1002129.

Leonardi M, Steiner TJ, Scher AT, Lipton RB (2005) The global burden of migraine: measuring disability in headache disorders with WHO's Classification of Functioning, Disability and Health (ICF). J Headache Pain 6:429–440.

Lester RA, Clements JD, Westbrook GL, Jahr CE (1990) Channel kinetics determine the time course of NMDA receptor-mediated synaptic currents. Nature 346:565–567.

Lester RA, Jahr CE (1992) NMDA channel behavior depends on agonist affinity. J Neurosci 12:635–643.

Lipton RB, Bigal ME, Diamond M, Freitag F, Reed ML, Stewart WF, AMPP Advisory Group (2007) Migraine prevalence, disease burden, and the need for preventive therapy. Neurology 68:343–349.

Matthias K, Kirchhoff F, Seifert G, Hüttmann K, Matyash M, Kettenmann H, Steinhäuser C (2003) Segregated expression of AMPA-type glutamate receptors and glutamate transporters defines distinct astrocyte populations in the mouse hippocampus. J Neurosci 23:1750–1758.

May A, Schulte LH (2016) Chronic migraine: risk factors, mechanisms and treatment. Nat Rev Neurol 12:455–464.

Meeks JP, Mennerick S (2007) Astrocyte membrane responses and potassium accumulation during neuronal activity. Hippocampus 17:1100–1108.

Melliti K, Grabner M, Seabrook GR (2003) The familial hemiplegic migraine mutation R192Q reduces G-protein-mediated inhibition of P/Q-type (Ca(v)2.1) calcium channels expressed in human embryonic kidney cells. J Physiol 546:337-347.

Melone M, Bellesi M, Conti F (2009) Synaptic localization of GLT-1a in the rat somatic sensory cortex. Glia 57:108–117.

Melone M, Bellesi M, Ducati A, Iacoangeli M, Conti F (2011) Cellular and Synaptic Localization of EAAT2a in Human Cerebral Cortex. Front Neuroanat 4:151.

Melone M, Ciriachi C, Pietrobon D, Conti F (2018) Heterogeneity of Astrocytic and Neuronal GLT-1 at Cortical Excitatory Synapses, as Revealed by its Colocalization With Na+/K+-ATPase α Isoforms. Cereb Cortex.

Mitani A, Tanaka K (2003) Functional changes of glial glutamate transporter GLT-1 during ischemia: an in vivo study in the hippocampal CA1 of normal mice and mutant mice lacking GLT-1. J Neurosci 23:7176–7182.

Molleman A (2003) Patch Clamping: an introductory guide to patch clamp electrophysiology. John Wiley & Sons, Ltd

Moseley AE, Lieske SP, Wetzel RK, James PF, He S, Shelly DA, Paul RJ, Boivin GP, Witte DP, Ramirez JM, Sweadner KJ, Lingrel JB (2003) The Na,K-ATPase alpha 2 isoform is expressed in neurons, and its absence disrupts neuronal activity in newborn mice. J Biol Chem 278:5317–5324.

Mullner C, Broos LA, van den Maagdenberg AM, Striessnig J (2004) Familial hemiplegic migraine type 1 mutations K1336E, W1684R, and W1696I alter $Ca_v2.1$ Ca^{2+} channel gating: evidence for beta-subunit isoform-specific effects. J Biol Chem 279:51844-51850.

Murphy-Royal C, Dupuis J, Groc L, Oliet SHR (2017) Astroglial glutamate transporters in the brain: Regulating neurotransmitter homeostasis and synaptic transmission. J Neurosci Res 95:2140–2151.

Navarrete M, Araque A (2014) The Cajal school and the physiological role of astrocytes: a way of thinking. Front Neuroanat 8:33.

Neher E (1992) Correction for liquid junction potentials in patch clamp experiments. Meth Enzymol 207:123–131.

Neher E, Sakmann B (1976) Single-channel currents recorded from membrane of denervated frog muscle fibres. Nature 260:799–802.

Obrenovitch TP, Zilkha E (1995) High extracellular potassium, and not extracellular glutamate, is required for the propagation of spreading depression. J Neurophysiol 73:2107–2114.

Ogiwara I, Miyamoto H, Morita N, Atapour N, Mazaki E, Inoue I, Takeuchi T, Itohara S, Yanagawa Y, Obata K, Furuichi T, Hensch TK, Yamakawa K (2007) $Na_v1.1$ localizes to axons of paravalbumin-positive inhibitory interneurons: a circuit basis

for epileptic seizures in mice carrying an Scn1a gene mutation. J Neurosci 27:5903-5914.

Okubo Y, Iino M (2011) Visualization of glutamate as a volume transmitter. J Physiol (Lond) 589:481–488.

Olesen J, Diener HC, Bousser MG, Dodick DW,Goadsby PJ, Lipton RB, Schoenen J, Silberstain SD, Nappi G, Sakai F (2013) The international classification of headache disordrs, 3rd edition (beta version). Cephalalgia 33:629-808.

Omrani A, Melone M, Bellesi M, Safiulina V, Aida T, Tanaka K, Cherubini E, Conti F (2009) Up-regulation of GLT-1 severely impairs LTD at mossy fibre--CA3 synapses. J Physiol (Lond) 587:4575–4588.

Ophoff RA, Terwindt GM, Vergouwe MN, van Eijk R, Oefner PJ, Hoffman SM, Lamerdin JE, Mohrenweiser HW, Bulman DE, Ferrari M, Haan J, Lindhout D, van Ommen GJ, Hofker MH, Ferrari MD, Frants RR (1996) Familial hemiplegic migraine and episodic ataxia type-2 are caused by mutations in the Ca2+ channel gene CACNL1A4. Cell 87:543–552.

Paoletti P, Bellone C, Zhou Q (2013) NMDA receptor subunit diversity: impact on receptor properties, synaptic plasticity and disease. Nat Rev Neurosci 14:383–400.

Perea G, Araque A (2010) GLIA modulates synaptic transmission. Brain Res Rev 63:93–102.

Perea G, Navarrete M, Araque A (2009) Tripartite synapses: astrocytes process and control synaptic information. Trends Neurosci 32:421–431.

Peters O, Schipke CG, Hashimoto Y, Kettenmann H (2003) Different mechanisms promote astrocyte $Ca2^{+}$ waves and spreading depression in the mouse neocortex. J Neurosci 23:9888–9896.

Petersen CC, Crochet S (2013) Synaptic computation and sensory processing in neocortical layer 2/3. Neuron 78:28-48.

Petr GT, Sun Y, Frederick NM, Zhou Y, Dhamne SC, Hameed MQ, Miranda C, Bedoya EA, Fischer KD, Armsen W, Wang J, Danbolt NC, Rotenberg A, Aoki CJ, Rosenberg PA (2015) Conditional deletion of the glutamate transporter GLT-1 reveals that astrocytic GLT-1 protects against fatal epilepsy while neuronal GLT-1 contributes significantly to glutamate uptake into synaptosomes. J Neurosci 35:5187–5201.

Pietrobon D (2005) Function and dysfunction of synaptic calcium channels: insights from mouse models. Curr Opin Neurobiol 15:257–265.

Pietrobon D (2007) Familial hemiplegic migraine. Neurotherapeutics 4:274–284.

Pietrobon D (2010) Biological science of headache channels. Handb Clin Neurol 97:73–83.

Pietrobon D (2010) CaV2.1 channelopathies. Pflugers Arch 460:375–393.

Pietrobon D (2017) Chapter 15: "Lessons from familial hemiplegic migraine and cortical spreading depression". Neurobiological Basis of Migraine, First Edition. Edited by Dalkara T and Moskowitz MA, Wiley & Sons, Inc.

Pietrobon D (2013) Calcium channels and migraine. Biochim Biophys Acta 1828:1655–1665.

Pietrobon D, Moskowitz MA (2013) Pathophysiology of migraine. Annu Rev Physiol 75:365–391.

Pietrobon D, Moskowitz MA (2014) Chaos and commotion in the wake of cortical spreading depression and spreading depolarizations. Nat Rev Neurosci 15:379–393.

Pietrobon D, Striessnig J (2003) Neurobiology of migraine. Nat Rev Neurosci 4:386–398.

Poolos NP, Mauk MD, Kocsis JD (1987) Activity-evoked increases in extracellular potassium modulate presynaptic excitability in the CA1 region of the hippocampus. J Neurophysiol 58:404-416.

Reyes N, Oh S, Boudker O (2013) Binding thermodynamics of a glutamate transporter homolog. Nat Struct Mol Biol 20:634–640.

Rogers DC, Fisher EM, Brown SD, Peters J, Hunter AJ, Martin JE (1997) Behavioural and functional analysis of mouse phenotype: SHIRPA, a proposed protocol for comprehensive phenotype assessment. Mamm Genome 8:711-713.

Rose EM, Koo JCP, Antflick JE, Ahmed SM, Angers S, Hampson DR (2009) Glutamate transporter coupling to Na,K-ATPase. J Neurosci 29:8143–8155.

Rothstein JD, Dykes-Hoberg M, Pardo CA, Bristol LA, Jin L, Kuncl RW, Kanai Y, Hediger MA, Wang Y, Schielke JP, Welty DF (1996) Knockout of glutamate transporters reveals a major role for astroglial transport in excitotoxicity and clearance of glutamate. Neuron 16:675–686.

Rothstein JD, Patel S, Regan MR, Haenggeli C, Huang YH, Bergles DE, Jin L, Hoberg MD, Vidensky S, Chung DS, Toan SV, Bruijn LI, Su ZZ, Gupta P, Fisher PB (2005) β-Lactam antibiotics offer neuroprotection by increasing glutamate transporter expression. Nature 433(7021):73–77.

Rumbaugh G, Prybylowski K, Wang JF, Vicini S (2000) Exon 5 and spermine regulate deactivation of NMDA receptor subtypes. J Neurophysiol 83:1300–1306.

Russell MB, Ducros A (2011) Sporadic and familial hemiplegic migraine: pathophysiological mechanisms, clinical characteristics, diagnosis, and management. Lancet Neurol 10:457–470.

Saito T, Nakatsuji (2001) Efficient gene transfer into the embryonic mouse brain using in vivo electroporation. Dev Biol 240:237-246.

Santello M, Nevian T (2015) Dysfunction of cortical dendritic integration in neuropathic pain reversed by serotoninergic neuromodulation. Neuron 86:233–246.

Scimemi A, Diamond JS (2013) Deriving the time course of glutamate clearance with a deconvolution analysis of astrocytic transporter currents. J Vis Exp.

Shao YR, Isett BR, Miyashita T, Chung J, Pourzia O, Gasperini RJ, Feldman DE (2013) Plasticity of recurrent L2/3 inhibition and gamma oscillations by whisker experience. Neuron 80(1):210-222.

Shih PY, Savtchenko LP, Kamasawa N, Dembitskaja Y, McHugh TJ, Rusakov DA, Shigemoto R, Semyanov A (2013) Retrograde synaptic signaling mediated by K^+ efflux through postsynaptic NMDA receptors . Cell Rep 5:941-951.

Sibille J, Pannasch U, Rouach N (2014) Astroglial potassium clearance contributes to short-term plasticity of synaptically evoked currents at the tripartite synapse. J Physiol 592:87-102.

Silver RA, Cull-Candy SG, Takahashi T (1996) Non-NMDA glutamate receptor occupancy and open probability at a rat cerebellar synapse with single and multiple release sites. J Physiol (Lond) 494 (Pt 1):231–250.

Somjen GG (2001) Mechanisms of spreading depression and hypoxic spreading depression-like depolarization. Physiol Rev 81:1065–1096.

Stroebel D, Casado M, Paoletti P (2018) Trieteromeric NMDA receptors: from structure to synaptic physiology. Curr Opin Physiol 2: 1-12.

Su ZZ, Leszczyniecka M, Kang DC, Sarkar D, Chao W, Volsky DJ, Fischer PB (2003) Insights into glutamate transport regulation in human astrocytes: Cloning of the promoter for excitatory amino acid transporter 2 (EAAT2). Proc Natl Acad Sci USA 100(4):1955-1960.

Sutherland HG, Griffiths LR (2017) Genetics of Migraine: Insights into the Molecular Basis of Migraine Disorders. Headache 57:537–569.

Szczurkowska J, Cwetsch AW, dal Maschio M, Ghezzi D, Ratto GM, Cancedda L (2016) Targeted in vivo genetic manipulation of the mouse or rat brain by in utero electroporation with a triple-electrode probe. 11(3):399-412.

Takasaki C, Okada R, Mitani A, Fukaya M, Yamasaki M, Fujihara Y, Shirakawa T, Tanaka K, Watanabe M (2008) Glutamate transporters regulate lesion-induced plasticity in the developing somatosensory cortex. J Neurosci 28:4995–5006.

Tanaka K, Watase K, Manabe T, Yamada K, Watanabe M, Takahashi K, Iwama H, Nishikawa T, Ichihara N, Kikuchi T, Okuyama S, Kawashima N, Hori S, Takimoto M, Wada K (1997) Epilepsy and exacerbation of brain injury in mice lacking the glutamate transporter GLT-1. Science 276:1699–1702.

Tavraz NN, Dürr KL, Koenderink JB, Freilinger T, Bamberg E, Dichgans M, Friedrich T (2009) Impaired plasma membrane targeting or protein stability by certain ATP1A2 mutations identified in sporadic or familial hemiplegic migraine. Channels (Austin) 3:82–87.

Tavraz NN, Friedrich T, Dürr KL, Koenderink JB, Bamberg E, Freilinger T, Dichgans M (2008) Diverse functional consequences of mutations in the Na+/K+-ATPase alpha2-subunit causing familial hemiplegic migraine type 2. J Biol Chem 283:31097–31106.

Thomas CG, Tian H, Diamond JS (2011) The relative roles of diffusion and uptake in clearing synaptically released glutamate change during early postnatal development. J Neurosci 31:4743–4754.

Thomsen LL, Olesen J, Russell MB (2003) Increased risk of migraine with typical aura in probands with familial hemiplegic migraine and their relatives. Eur J Neurol 10:421–427.

Tottene A, Conti R, Fabbro A, Vecchia D, Shapovalova M, Santello M, van den Maagdenberg AM, Ferrari MD, Pietrobon D (2009) Enhanced excitatory

transmission at cortical synapses as the basis for facilitated spreading depression in Ca(v)2.1 knockin migraine mice. Neuron 61:762–773.

Tottene A, Fellin T, Pagnutti S, Luvisetto S, Striessnig J, Fletcher C, Pietrobon D (2002) Familial hemiplegic migraine mutations increased Ca^{2+} influx through single human $Ca_v2.1$ channels and decrease maximal $Ca_v2.1$ current density in neurons. Proc Natl Acad Sci USA 99:13284-13289.

Tottene A, Pivotto F, Fellin T, Cesetti T, van den Maagdenberg AM, Pietrobon D (2005) Specific kinetic alterations of human $Ca_v2.1$ calcium channels produced by mutation S218L causing familial hemiplegic migraine and delayed cerebral edema and coma after minor head trauma. J Biol Chem 280:17678-17686.

Tovar KR, McGinley MJ, Westbrook GL (2013) Triheteromeric NMDA receptors at hippocampal synapses. J Neurosci 33:9150–9160.

Tzingounis AV, Wadiche JI (2007) Glutamate transporters: confining runaway excitation by shaping synaptic transmission. Nat Rev Neurosci 8:935–947.

Ullensvang K, Lehre KP, Storm-Mathisen J, Danbolt NC (1997) Differential developmental expression of the two rat brain glutamate transporter proteins GLAST and GLT. Eur J Neurosci 9:1646–1655.

van den Maagdenberg AM, Pietrobon D, Pizzorusso T, Kaja S, Broos LAM, Cesetti T, van de Ven RCG, Tottene A, van der Kaa J, Plomp JJ, Frants RR, Ferrari MD (2004) A Cacna1a knockin migraine mouse model with increased susceptibility to cortical spreading depression. Neuron 41:701–710.

van den Maagdenberg AM, Pizzorusso T, Kaja S, Terpolilli N, Shapovalova M, Hoebeek FE, Barrett CF, Gherardini L, van de Ven RC, Todorov B, Broos LA, Tottene A, Gao Z, Fodor M, De Zeeuw CI, Frants RR, Plesnila N, Plomp JJ, Pietrobon D, Ferrari MD (2010) High cortical spreading depression susceptibility and migraine-associated symptoms in $Ca_{(v)}2.1$ S218L mice. Ann Neurol 67(1):85-98.

van Harreveld A (1959) Compounds in brain extracts causing spreading depression of cerebral cortical activity and contraction of crustacean muscle. J Neurochem 3:300–315.

Vance KM, Hansen KB, Traynelis SF (2012) GluN1 splice variant control of GluN1/GluN2D NMDA receptors. J Physiol (Lond) 590:3857–3875.

Vecchia D, Pietrobon D (2012) Migraine: a disorder of brain excitatory-inhibitory balance? Trends Neurosci 35:507–520.

Volianskis A, Bannister N, Collett VJ, Irvine MW, Monaghan DT, Fitzjohn SM, Jensen MS, Jane DE, Collingridge GL (2013) Different NMDA receptor subtypes mediate induction of long-term potentiation and two forms of short-term potentiation at CA1 synapses in rat hippocampus in vitro. J Physiol (Lond) 591:955–972.

Volianskis A, France G, Jensen MS, Bortolotto ZA, Jane DE, Collingridge GL (2015) Long-term potentiation and the role of N-methyl-D-aspartate receptors. Brain Res 1621:5–16.

Watkins JC, Evans RH (1981) Excitatory amino acid transmitters. Annu Rev Pharmacol Toxicol 21:165–204.

Yu FH, Mantegazza M, Westenbroek RE, Robbins CA, Kalume F, Burton KA, Spain WJ, McKnight GS, Scheuer T, Catterall WA (2006) Reduced sodium current in GABAergic interneurons in a mouse model of severe myoclonic epilepsy in infancy. Nat Neurosci 9:1142–1149.

Zerangue N, Kavanaugh MP (1996) Flux coupling in a neuronal glutamate transporter. Nature 383:634–637.

Zhang X, Levy D, Kainz V, Noseda R, Jakubowski M, Burstein R (2011) Activation of central trigeminovascular neurons by cortical spreading depression. Ann Neurol 69:855–865.

Zhang X, Levy D, Noseda R, Kainz V, Jakubowski M, Burstein R (2010) Activation of meningeal nociceptors by cortical spreading depression: implications for migraine with aura. J Neurosci 30:8807–8814.

Zhu S, Paoletti P (2015) Allosteric modulators of NMDA receptors: multiple sites and mechanisms. Curr Opin Pharmacol 20:14–23.

Defective glutamate and K^+ clearance by cortical astrocytes in familial hemiplegic migraine type 2.

Clizia Capuani[1*], Marcello Melone[2,3*], Angelita Tottene[1*], Luca Bragina[2,3], Giovanna Crivellaro[1], Mirko Santello[4], Giorgio Casari[5], Fiorenzo Conti[2,3,6], Daniela Pietrobon[1].

[1] Department of Biomedical Sciences, University of Padova, and CNR Institute of Neuroscience, 35121 Padova, Italy

[2]Department of Experimental and Clinical Medicine, Università Politecnica delle Marche, 60026 Ancona, Italy

[3]Center for Neurobiology of Aging, INRCA IRCCS, 60127 Ancona, Italy

[4] Institute of Pharmacology and Toxicology, University of Zurich, 8057 Zürich, Switzerland

[5] Vita-Salute San Raffaele University and San Raffaele Scientific Institute, 20132 Milano, Italy

[6] Fondazione di Medicina Molecolare, Università Politecnica delle Marche, 60026 Ancona, Italy

*These authors contributed equally to the work

Corresponding author: daniela.pietrobon@unipd.it

Running title: **Defective glutamate and K clearance in FHM2 cortex**

Characters (excluding title page and references): 73953

Abstract

Migraine is a common disabling brain disorder. A subtype of migraine with aura (familial hemiplegic migraine type 2: FHM2) is caused by loss-of-function mutations in α_2 Na^+,K^+ ATPase (α_2NKA), an isoform almost exclusively expressed in astrocytes in adult brain. Cortical spreading depression (CSD), the phenomenon that underlies migraine aura and activates migraine headache mechanisms, is facilitated in heterozygous FHM2 knockin mice with reduced expression of α_2NKA. The mechanisms underlying increased susceptibility to CSD in FHM2 are unknown. Here, we show reduced rates of glutamate and K^+ clearance by cortical astrocytes during neuronal activity and reduced density of GLT-1a glutamate transporters in cortical perisynaptic astrocytic processes in heterozygous FHM2 knockin mice, demonstrating key physiological roles of α_2NKA and supporting tight coupling with GLT-1a. Using ceftriaxone treatment of FHM2 mutants and partial inhibition of glutamate transporters in wild-type mice, we obtain evidence that defective glutamate clearance can account for most of the facilitation of CSD initiation in FHM2 knockin mice, pointing to excessive glutamatergic transmission as a key mechanism underlying vulnerability to CSD ignition in migraine.

Migraine/spreading depression/Na^+,K^+ ATPase/glutamate transporter/ceftriaxone

Introduction

Migraine is a common disabling brain disease, which manifests itself as recurrent attacks of typically throbbing and unilateral headache with certain associated features such as nausea and hypersensitivity to sensory stimuli. In a third of patients the headache is preceded by transient focal symptoms that are most frequently visual (migraine with aura: MA). Increasing evidence supports a key role of cortical spreading depression (CSD) in migraine pathogenesis in that CSD underlies migraine aura (Lauritzen, 1994; Noseda & Burstein, 2013; Pietrobon & Moskowitz, 2013; Pietrobon & Moskowitz, 2014) and may trigger the headache mechanisms (Ayata et al, 2006; Bolay et al, 2002; Karatas et al, 2013; Pietrobon & Moskowitz, 2014; Zhang et al, 2011; Zhang et al, 2010; Zhao & Levy, 2015). CSD is a slowly propagating wave of rapid nearly complete depolarization of brain cells lasting about 1 min that silences brain activity for several min (Pietrobon & Moskowitz, 2014; Somjen, 2001). The mechanisms of the primary brain dysfunction underlying the susceptibility to CSD ignition in the human brain and the onset of a migraine attack remain largely unknown and are a major open issue in the neurobiology of migraine.

Migraine has a strong multifactorial genetic component (de Vries et al, 2009; Ferrari et al, 2015; Russell & Ducros, 2011). As for many other multifactorial diseases, rare monogenic forms that phenocopy most or all the clinical features of the disorder are helpful for elucidating the molecular and cellular mechanisms of the disease. Familial hemiplegic migraine (FHM) is a rare monogenic autosomal dominant form of MA. Apart from motor features and longer duration of the aura, typical FHM attacks resemble MA attacks and both types of attacks may alternate in patients and co-occur within families (de Vries et al, 2009; Ferrari et al, 2015; Russell & Ducros, 2011).

FHM type 2 (FHM2) is caused by mutations in ATP1A2, the gene encoding the α_2 subunit of the Na^+,K^+ ATPase (NKA) (Bøttger et al, 2012; De Fusco et al, 2003). The α_2 NKA is expressed primarily in neurons during embryonic development and at the time of birth and almost exclusively in astrocytes in the adult brain (Cholet et al, 2002; Ikeda et al, 2003; McGrail et al, 1991; Moseley et al, 2003). The α_2 NKA is thought to play an important role in K^+ clearance during neuronal activity, but direct evidence is missing mainly because selective inhibitors allowing to distinguish the contributions of the glial α_2 and the neuronal α_3 NKA are still lacking (D'Ambrosio et al, 2002; Larsen et al, 2014; Larsen & MacAulay, 2014; Ransom et al, 2000). An important role of α_2 NKA in glutamate (Glu) clearance is suggested by its co-localization with the Glu transporters (GluTs) GLT-1 and GLAST in astrocytic processes surrounding glutamatergic synapses in adult somatic sensory cortex (Cholet et al, 2002) and by the association of GluTs and α_2 NKA in the same macromolecular complex (Rose et al, 2009). However, this association is not specific for the α_2 NKA (Genda et al, 2011; Illarionava et al, 2014; Rose et al, 2009) and, although ouabain pharmacology indicates a preferential functional coupling of GluTs with α_2 NKA in cultured astrocytes ((Illarionava et al, 2014; Pellerin & Magistretti, 1997); but see (Rose et al, 2009)), the role of the α_2 pump in clearance of synaptically released Glu during neuronal activity remains unclear, given the lack of functional data in brain slices.

FHM2 mutations cause complete or partial loss-of-function of α_2 NKA (Bøttger et al, 2012; De Fusco et al, 2003; Leo et al, 2011; Pietrobon, 2007; Schack et al, 2012; Swarts et al, 2013; Tavraz et al, 2009; Tavraz et al, 2008; Weigand et al, 2014). α_2 NKA protein is barely detectable in the brain of homozygous knockin (KI) mice carrying the pathogenic W887R FHM2 mutation, and is halved in the brain of heterozygous W887R/+ mutants (Leo et al, 2011). These FHM2 KI mice show a lower threshold for CSD induction and an increased velocity of CSD propagation, *in vivo* (Leo et al, 2011), similarly to KI mouse

models of FHM type 1 (FHM1) (Eikermann-Haerter et al, 2009; van den Maagdenberg et al, 2004; van den Maagdenberg et al, 2010) and to a mouse model of a familial advanced sleep syndrome in which all patients also suffered from MA (Brennan et al, 2013).

The mechanisms underlying increased susceptibility to CSD in FHM2 are unknown, although impaired Glu and/or K^+ clearance by astrocytes have been suggested as hypothetical mechanisms (Moskowitz et al, 2004; Pietrobon, 2007).

Here, to test these hypotheses and to gain insights into the physiological role of the α_2 NKA, we investigated the functional consequences of the W887R FHM2-causing mutation on Glu and K^+ clearance by cortical astrocytes during neuronal activity in acute cortical slices. We show that the rates of Glu and K^+ clearance by cortical astrocytes are reduced in heterozygous W887R/+ KI mice, and that the density of GLT-1a in the membrane of astrocytic processes surrounding cortical glutamatergic synapses is reduced by 50 % in the FHM2 mutants. Using an *in vitro* model of CSD and ceftriaxone treatment in FHM2 KI mice as well pharmacological inhibition of a fraction of GluTs in wild-type (WT) mice, we provide evidence that the defective Glu clearance can account for most of the facilitation of CSD initiation in the FHM2 mouse model.

Results

To investigate whether the reduced membrane expression of the α_2 NKA in heterozygous W887R/+ FHM2 KI mice causes a reduced rate of Glu clearance by cortical astrocytes during neuronal activity, we took advantage of the fact that i) Glu uptake into astrocytes by GluTs is electrogenic, and therefore can be monitored electrophysiologically; and ii) the time course of the Glu transporter current elicited in astrocytes upon extracellular neuronal stimulation in hippocampal slices (the so called synaptically activated transporter current, STC) reflects the time course of Glu clearance by astrocytes and provides a measure of

how rapidly synaptically released Glu is taken up from extracellular space (Bergles & Jahr, 1997; Diamond, 2005).

We measured the STC in cortical astrocytes by recording the inward current evoked in layer 1 astrocytes (held at -90 mV, close to the resting potential) by stimulation of neuronal afferents with an extracellular electrode located in layer 1, 200 µm from the patch-clamped astrocyte, in acute slices of the somatic sensory cortex from P22-23 WT and FHM2 KI mice, in the presence of antagonists of Glu and GABA receptors (Fig 1A) (Bergles & Jahr, 1997; Bernardinelli & Chatton, 2008). The inward current evoked in astrocytes by a single pulse stimulation comprised a rapidly rising and decaying component (complete decay in few tens of ms) and a sustained component (Fig 1B, trace a). The rapidly decaying component was completely inhibited by the GluTs inhibitor TFB-TBOA (TBOA), identifying it as the STC (Fig 1B). The STC can thus be obtained by subtracting the residual current remaining in the presence of TBOA from the total inward current (trace a-b in Fig 1B) (Scimemi & Diamond, 2013). The STC can also be obtained by subtracting from the total inward current an exponential waveform (trace c in Fig 1C) that approximates the average TBOA-insensitive current (Fig 1C, top trace) obtained as described in Methods (Devaraju et al, 2013; Scimemi and Diamond, 2013).

Previous studies have shown that the decay kinetics of the STC reflects the rate of Glu clearance filtered by the electrotonic properties of astrocytes (Diamond, 2005) and provides a measure of the rate of Glu clearance that is independent of the amount of Glu released (Diamond, 2005; Diamond & Jahr, 2000; Unichenko et al, 2012). As in hippocampal slices (Diamond, 2005; Diamond & Jahr, 2000), also in barrel cortex slices the decay kinetics of the STC slowed down when the density of GluTs was reduced by subsaturating concentrations of DL-TBOA (Appendix Fig S1A), as expected for a reduced rate of Glu clearance and a longer lifetime of synaptically released Glu in the extracellular

space. Moreover, changing the intensity of extracellular stimulation (and hence the number of stimulated fibers and the amount of Glu released) changed the STC amplitude without affecting the STC decay kinetics (Appendix Fig S1B). Thus, to obtain a measure of the rate of clearance of synaptically released Glu by cortical astrocytes, which is not affected by the amount of Glu released by extracellular stimulation, we fitted with an exponential function the decay of the STC (Fig 1).

The STC isolated pharmacologically in cortical astrocytes of WT mice decayed with an exponential time course with time constant τ = 6.80 ± 0.19 ms (Fig 1B). The STC isolated in a larger number of cells using the exponentially rising function that approximates the average TBOA-insensitive current (Fig 1C) decayed with a similar time course (6.46 ± 0.13 ms; unpaired t-test, P = 0.15). The decay kinetics of the STC elicited in cortical astrocytes of heterozygous W887R/+ FHM2 KI mice were slower compared to those in WT astrocytes, as shown by the significantly larger time constant of decay of both the STC isolated pharmacologically (τ = 7.97 ± 0.31 ms) and the STC isolated non-pharmacologically in a larger number of cells (τ = 7.82 ± 0.16 ms) (Fig 1). These data indicate that the rate of clearance of synaptically released Glu by cortical astrocytes is slower in FHM2 KI compared to WT mice.

We next investigated whether the slowing down of Glu clearance in FHM2 KI mice was larger after repetitive stimulation with trains of 10 pulses at 50 or 100 Hz, as e.g. might be expected if the binding capacity of the GluTs in layer 1 astrocytes is overwhelmed during the train. In this case, the decay kinetics of the STC elicited by the 10th pulse in the train should be slower than those of the STC elicited by a single pulse stimulation (Diamond & Jahr, 2000). Indeed, in experiments in which single stimuli were alternated with trains of 9 and 10 pulses at 50 or 100 Hz, the time constants of decay of the STCs elicited by the 10th pulse of the high-frequency trains (isolated as described in Methods: Fig 2A) were

168 significantly larger than those of the corresponding STC elicited by a single pulse. For
169 example, the time constant of the STC elicited in WT astrocytes by the 10th pulse of a 50
170 Hz train, $\tau_{10\ (50\ Hz)}$, was 7.56 ± 0.16 ms (n = 23) while that elicited by a single pulse in the
171 same cells was τ_1 = 6.45 ± 0.15 ms (n = 23; paired t-test, P < 0.0001) and the average
172 ratio τ_{10} / τ_1 (50 Hz) was 1.18 ± 0.02 (n = 23). The slowing of the STC after the train was
173 larger in FHM2 KI compared to WT mice (in KI: τ_{10} /τ_1 (50 Hz) = 1.26 ± 0.03, n = 21;
174 unpaired t-test, P = 0.021). The relative slowing and the difference between WT and KI
175 mice were more pronounced after a 100 Hz train (τ_{10} /τ_1 (100 Hz) = 1.25 ± 0.03, n=18, in
176 WT vs τ_{10} /τ_1 (100 Hz) = 1.40 ± 0.05, n=14, in KI, P = 0.009).
177 As a consequence, the slowing down of Glu clearance in FHM2 KI compared to WT mice
178 was quantitatively larger after repetitive stimulation than after single pulse stimulation and
179 increased with increasing stimulation frequency (Fig 2B). The time constants of decay of
180 the STCs elicited by the 10th pulse of 50 and 100 Hz trains in FHM2 KI mice ($\tau_{10(50\ Hz)}$ =
181 9.82 ± 0.24; $\tau_{10(100\ Hz)}$ = 11.08 ± 0.41 ms) were 30 % and 37 % larger than those in WT
182 mice, respectively ($\tau_{10(50\ Hz)}$ = 7.56 ± 0.16 ms; $\tau_{10(100\ Hz)}$ = 8.09 ± 0.23 ms) (Fig 2B). For
183 comparison, the time constant of decay of the STC elicited by a single pulse was 21%
184 larger in FHM2 KI compared to WT mice (Fig 1).

185

186 Given the evidence of association in the same protein complex of the glial GluTs (GLT-1
187 and GLAST) and the α_2 NKA pump (Illarionava et al, 2014; Rose et al, 2009) and of co-
188 localization of the glial GluTs with α_2 NKA in astrocytic processes surrounding neocortical
189 glutamatergic synapses (Cholet et al, 2002), we investigated whether the slower rate of
190 Glu clearance by cortical astrocytes in the FHM2 KI mice was due, at least in part, to a
191 reduced density of GLT-1 in the membrane of astrocytic processes surrounding cortical
192 excitatory synapses (perisynaptic astrocytic processes: PAPs). GLT-1 is the quantitatively

dominant GluT in the brain and mediates the majority of Glu clearance in the adult murine neocortex (Campbell et al, 2014; Danbolt, 2001; Haugeto et al, 1996; Rothstein et al, 1996; Tanaka et al, 1997).

We obtained a first indication that GLT-1 expression in the vicinity of cortical glutamatergic synapses was decreased in FHM2 KI mice from double labeling immunofluorescence of GLT-1a and the vesicular glutamate transporter VGLUT1 in neocortical sections. GLT-1a is the predominant brain GLT-1 isoform (Berger et al, 2005; Chen et al, 2004; Holmseth et al, 2009) and VGLUT1 is expressed in the large majority of cortical excitatory terminals (Kaneko et al, 2002). Quantitative analysis of GLT-1a immuno-reactivity (ir) showed that the mean size of the GLT-1a positive (GLT-1a+) ir puncta (green) that overlapped with VGLUT1+ ir puncta (red) was reduced by 18 % in FHM2 KI mice (0.47 ± 0.03 μm^2) compared to WT (0.57 ± 0.03 μm^2) (Fig 3). The percentages of GLT-1a+ puncta overlapping with VGLUT1+ puncta were comparable (49 ± 3% in KI; 46 ± 4% in WT). As a change in size of ir puncta has been considered strongly suggestive of a change in protein expression (Bozdagi et al, 2000; Bragina et al, 2006; Omrani et al, 2009), the reduced size of the GLT-1a+ puncta overlapping with VGLUT1+ puncta is consistent with a reduced GLT-1a expression in the vicinity of cortical glutamatergic synapses in W887R/+ KI mice.

The majority of overlapping GLT-1a/VGLUT1 puncta co-localized with α_2 NKA (81 ± 2%), as revealed by triple labeling immunofluorescence of GLT-1a, VGLUT1 and α_2 NKA in WT cortical sections (Fig EV1). This suggests a strict co-localization of GLT-1a and α_2 NKA in the astrocytic processes close to glutamatergic synapses, given that in the adult brain α_2 NKA is expressed almost exclusively in astrocytes and is not present in cortical axon terminals (Cholet et al, 2002; McGrail et al, 1991).

We then used post-embedding immunogold electron microscopy (EM) in cerebral cortex sections to study the density of GLT-1a gold particles associated with the membrane of PAPs. In line with previous studies (e.g., (Melone et al, 2009; Omrani et al, 2009)), GLT-1a particles were at the membrane and in the cytoplasm of both PAPs (Fig 4A) and axon terminals (AxT) forming asymmetric synaptic contacts (Fig 4B); the density of gold particles was significantly higher on the plasma membrane (i.e., within 15 nm of the extracellular side of the membrane) than in the cytoplasm (Table I). The total and plasma membrane density of GLT-1a gold particles in PAPs were reduced by 41% and 48%, respectively, in FHM2 KI compared to WT mice (Fig 4A, Table I). The reduction of GLT-1a density in the membrane of PAPs is quantitatively similar to the reduction of α2 NKA protein level in cortical crude synaptic membranes from W887R/+ KI mice revealed by Western blotting (about 50%: (Leo et al, 2011)). Interestingly, in contrast with the decreased density of GLT-1a in PAPs, both the total and the plasma membrane density of GLT-1a were unaltered in FHM2 KI AxTs (Fig 4B, Table I). The similar density of GLT-1a in FHM2 and WT AxTs correlates with, and likely reflects, the absence of α_2 NKA in cortical AxTs (Cholet et al, 2002).

The EM data, together with the strict co-localization of α_2 NKA and GLT-1a in the vicinity of glutamatergic synapses (Fig EV1), suggest a necessary tight coupling between α_2 NKA and GLT-1a in PAPs, and point to reduced expression of GluTs in PAPs as the main mechanism underlying the reduced rate of Glu clearance by astrocytes in FHM2 KI mice.

To investigate whether the reduced expression of the α_2 NKA in W887R/+ KI mice causes a reduced rate of K^+ clearance by astrocytes during neuronal activity, we took advantage of the fact that i) as a consequence of the very high expression of K^+ channels that are open at negative resting voltages, the astrocyte passive conductance is essentially K^+-

selective and the astrocyte membrane potential behaves as a good K^+ electrode, rendering astrocytes useful $[K^+]_e$ biosensors (Hwang et al, 2014; Meeks & Mennerick, 2007; Zhou et al, 2009); ii) the slowly decaying inward current elicited in astrocytes upon extracellular neuronal stimulation in acute brain slices is largely a K^+ current that reflects $[K^+]_e$ accumulation due to neuronal K^+ efflux and the accompanying change in driving force through glial K^+ channels (mainly inward rectifier Kir channels judging from the sensitivity of the slow current to low Ba^{2+} concentrations and to Kir4.1 knockout) (Bernardinelli & Chatton, 2008; De Saint Jan & Westbrook, 2005; Djukic et al, 2007; Meeks & Mennerick, 2007; Shih et al, 2013; Sibille et al, 2014). The time constant of decay of this slow current (hereafter called I_K) provides a measure of the rate of K^+ clearance, that has been shown to be equivalent to that obtained with $[K^+]_e$-sensitive microelectrodes (Meeks & Mennerick, 2007).

Therefore, to investigate the effect of the FHM2 mutation on K^+ clearance we recorded the current evoked in layer 1 astrocytes by extracellular stimulation in layer 1, a protocol similar to that used for the STC. However, the recordings were performed in the absence of synaptic receptor blockers because postsynaptic Glu receptors, in particular the NMDA receptors (NMDARs), represent a major source of K^+ efflux during neuronal activity (De Saint Jan & Westbrook, 2005; Poolos et al, 1987; Shih et al, 2013; Sibille et al, 2014). The I_K current elicited by repetitive stimulation (10 pulses at 50 Hz) in WT astrocytes decayed with a time constant of 2.36 ± 0.10 s, more than 2 orders of magnitude more slowly than the STC (Fig 5). The decay kinetics of I_K elicited by the same stimulation in FHM2 KI cortical slices were slower, as shown by the 22% larger time constant (2.87 ± 0.10 s) (Fig 5). This indicates that the reduced membrane expression of the α_2 NKA in W887R/+ FHM2 KI mice causes a reduced rate of K^+ clearance by cortical astrocytes following neuronal activity.

The measurement of the time constant of decay of I_K following stimulation with 10 pulses at 50 Hz in the presence of Glu receptor blockers in WT (I_k τ_{decay} = 2.38 ± 0.09 s, n=18) and FHM2 KI astrocytes (I_k τ_{decay} = 2.95 ± 0.08 s, n=16) confirms this conclusion. In both genotypes, the time constants of decay of I_K are similar in the absence and presence of Glu receptors blockers, and the slowing of K^+ clearance in FHM2 KI cortical slices is also similar in the two conditions.

We next investigated whether the slower rate of Glu clearance during neuronal activity contributes to the facilitation of CSD in W887R/+ FHM2 KI mice (Leo et al, 2011). First we verified that, in the conditions in which we recorded the STC (P22 - 23 mice, T = 30°C), CSD induced in acute cortical slices by brief pulses of high K^+ (as in (Tottene et al, 2009)) was facilitated in FHM2 KI mice, as shown in vivo in adult mice (Leo et al, 2011). Brief pressure-ejection KCl pulses of increasing duration were applied (at 5 min intervals) onto the slice surface (layer 2/3) until a CSD was elicited, as revealed by the associated changes in intrinsic optic signal (IOS). The duration of the first pulse eliciting a CSD was taken as CSD threshold and the rate of horizontal spread of the change in IOS as CSD velocity (Fig 6A). The threshold for CSD induction was 28% lower in FHM2 KI relative to WT (170 ± 4 vs 236 ± 8 ms) and the velocity of CSD propagation was 21% higher (3.94 ± 0.04, vs 3.26 ± 0.05 mm/min) (Fig 6B). Thus, experimental CSD in acute cortical slices from FHM2 KI mice was facilitated in the conditions in which a slowing of the rate of Glu clearance compared to WT was shown. The smaller extent of facilitation compared to *in vivo* situation (where the CSD threshold was decreased about 50% and the velocity increased about 40%) is at least in part due to the younger age of the animals and the lower temperature. In fact, the facilitation of CSD was larger in cortical slices from older (P34 - 35) mice: the threshold for CSD induction (T = 30°C) was 39% lower and the

294 velocity of CSD propagation 26% higher in FHM2 KI relative to WT mice (Appendix Fig
295 S2A). In contrast with the very small number of spontaneous CSDs in both WT and KI
296 slices from P22 - 23 mice (2 out of 26 and 1 out of 28, respectively), it was necessary to
297 increase the perfusion rate of P34 - 35 cortical slices (to 13 ml/min) to prevent the frequent
298 ignition of spontaneous CSDs in KI slices; in the latter the frequency of spontaneous CSDs
299 (5 out of 31) remained larger than in WT (1 out of 21) even at this high flow rate. On the
300 other hand, the facilitation of CSD was smaller in cortical slices from P34 - 35 mice at
301 lower temperature: the threshold for CSD induction (room T) was 22% lower and the
302 velocity of CSD propagation 20% higher in FHM2 KI relative to WT mice (Appendix Fig
303 S2B); no spontaneous CSDs were observed.
304
305 As a first approach to study whether there is a causative relationship between reduced
306 rate of Glu clearance by astrocyes and CSD facilitation, we investigated whether the
307 facilitation of CSD in the FHM2 mice could be (at least partially) rescued by systemic
308 treatment with ceftriaxone (Cef), a drug that increases the membrane expression of GLT-1
309 in neocortex (Bellesi et al, 2009). Indeed, Western blotting of cortical crude synaptic
310 membranes and double labelling immunofluorescence of GLT-1a and VGLUT1 in cortical
311 sections from WT mice that had been injected for 8 days with either Cef (200 mg/Kg) or
312 saline showed a 63% increase of GLT-1a protein (Fig 7A) and a 58% increase in the mean
313 size of the GLT-1a+ puncta overlapping with VGLUT1 in Cef-treated compared to saline-
314 treated control animals (0.84 ± 0.03 µm^2 vs 0.53 ± 0.03 µm^2; Fig 7B).
315
316 Threshold of CSD induction and velocity of CSD propagation were measured in slices from
317 P30-33 FHM2 KI mice that had been injected for 7-8 days with either Cef or saline. At this
318 age the frequency of spontaneous CSDs was relatively small (in 7 out of 47 slices from
319 saline-injected KI mice) even using 6 ml/min perfusion rate. Moreover, at this age, α_2 NKA

and GLT-1 are expressed at very close to adult levels (Orlowski and Lingrel, 1988; Furuta et al, 1997; Ullenswang et al, 1997). The threshold for CSD induction was slightly (12%), but significantly, increased in cortical slices from Cef-treated compared to saline-treated FHM2 KI mice (162 ± 5 vs 145 ± 5 ms) (Fig 7C), and the frequency of spontaneous CSDs (2 out of 40 slices) was decreased in Cef-treated mice. The velocity of CSD propagation was similar in cortical slices from Cef- and saline-treated FHM2 KI mice (3.82 ± 0.08 vs 3.83 ± 0.07) (Fig 7C). These findings indicate that Cef treatment rescues a small fraction of the facilitation of CSD induction in FHM2 KI mice without affecting the facilitation of CSD propagation.

Given the findings suggesting a necessary tight coupling between α_2 NKA and GLT-1a in PAPs, we asked whether Cef effectively increased the density of GLT-1a in cortical PAPs of W8887R/+ KI mice having 50% reduced α_2 NKA expression. We used post-embedding EM to measure the density of GLT-1a gold particles associated with the membrane of PAPs in cortical sections from Cef- and saline-injected FHM2 KI mice. Interestingly, while the density of the membrane pool of GLT-1a in AxTs was larger in Cef-treated than saline-treated FHM2 KI mice, the density of GLT-1a gold particles in the membrane of PAPs was similar in Cef- and saline-treated KI mice (Fig 8A, B, Table II). Accordingly, the GLT-1a protein expression level and the size of the GLT-1a+ ir puncta that overlapped with VGLUT1 ir in the cortex of Cef- and saline-treated FHM2 KI mice were similar (Fig 8C, D). This is consistent with the Cef-induced increase of GLT-1a only at AxTs, given the relatively small fraction of GLT-1a in AxTs relative to that in PAPs (and the limit of resolution of confocal microscopy) (Chen et al, 2004; Melone et al, 2009). These findings provide an explanation for the relative inefficacy of Cef in the rescue of CSD facilitation and provide further support to the idea of a necessary tight coupling between α_2 NKA and GLT-1a in PAPs.

346 Given that Cef did not increase the density of GLT-1a in PAPs, the partial rescue of the
347 facilitation of CSD induction in Cef-treated FHM2 KI mice may be due to increase Glu
348 reuptake in AxTs (due to higher GLT-1a expression) and/or to some other effect of Cef not
349 related to GLT-1 expression. Mechanisms involving changes in expression of the α_2 NKA
350 or the glial Glu-cystine antiporter xCT (that appears to be co-regulated with GLT-1 in
351 nucleus accumbens after chronic treatment with cocaine or alcohol: (Knackstedt et al,
352 2010; Rao & Sari, 2014)) or Kir4.1 (the glial K^+ channel that plays a key role in K^+ spatial
353 buffering: (Djukic et al, 2007; Kofuji & Newman, 2004)) do not seem to play a role, since
354 the protein level of α_2 NKA, xCT and Kir4.1 was not affected by Cef treatment of FHM2 KI
355 mice (Figure EV2).
356
357 As a second approach to study whether there is a causative relationship between reduced
358 rate of Glu clearance by astrocytes and CSD facilitation, we investigated whether
359 pharmacological reduction of the rate of Glu clearance in WT mice to a value similar to that
360 of FHM2 KI mice reduces the threshold for CSD induction and increases the velocity of
361 CSD propagation to values similar to those in the FHM2 mutants.
362 To identify which concentration of drug produced a slowing of the rate of Glu clearance in
363 WT mice close to that produced by the FHM2 mutation and obtain information on the time
364 necessary to reach steady-state inhibition, we measured the STC in cortical slices from
365 P22-23 WT mice before and after application of different subsaturating concentrations of
366 DL-TBOA. We identified a concentration of DL-TBOA (2.5 µM) that increased by 32 ± 2 %
367 the time constant of decay of the STC elicited by single pulse stimulation, thus producing a
368 slowing of the rate of Glu clearance close to (although larger than) that produced by the
369 FHM2 mutation (Figure 9A). In the presence of 2.5 µM DL-TBOA, the threshold for CSD
370 induction was 36% lower than in control (142 ± 4 vs 220 ± 8 ms), and the velocity of CSD
371 propagation was 20% higher (3.84 ± 0.09 vs 3.21 ± 0.08 mm/min) (Fig 9B). Thus,

pharmacological inhibition of a fraction of GluTs does facilitate CSD induction and propagation in WT mice. In correlation with the larger slowing of the rate of Glu clearance produced by TBOA 2.5 relative to that produced by the FHM2 mutation (32 vs 21 %: Figs 9A and 1C) the facilitation of CSD induction was also larger (36% vs 28% lower CSD threshold in TBOA 2.5 vs KI, respectively: Figs 9B and 6B), suggesting that the reduced rate of Glu clearance in FHM2 KI mice may account for a large fraction of the facilitation of CSD induction.

To establish whether impaired Glu clearance in FHM2 KI mice may completely account for the facilitation of CSD induction, we measured CSD threshold and velocity in the presence of a concentration of DL-TBOA (1.5 µM) that produced a slowing of the rate of Glu clearance quantitatively similar to that produced by the FHM2 mutation (22 ± 3 %: Fig 9C). In the presence of 1.5 µM DL-TBOA, the threshold for CSD induction was 23 % lower than in control (170 ± 5 vs 220 ± 8 ms), and the velocity of CSD propagation was 13 % higher than in control WT slices (3.61 ± 0.09 vs 3.21 ± 0.08) (Fig 9D). These data support the conclusion that the reduced rate of Glu clearance in FHM2 KI mice can account for most of the facilitation of CSD induction (82%, as estimated from the ratio of the relative reductions of CSD threshold produced by TBOA 1.5 and the FHM2 mutation: 23% / 28%; cf also similar CSD thresholds in WT TBOA 1.5 and FHM2 KI in Figs 9D and 6B), while it can account for only a fraction of the facilitation of CSD propagation in FHM2 KI mice (62%, as estimated from the ratio 13/21 of the relative increases of CSD velocity produced by TBOA 1.5 and the FHM2 mutation; cf also different CSD rates in WT TBOA 1.5 and FHM2 KI: unpaired t-test, $P < 0.001$).

Discussion

We have studied the functional consequences of the reduced membrane expression of the α_2 NKA pump in heterozygous W887R/+ FHM2 KI mice on the rate of Glu clearance by

astrocytes during neuronal activity, as measured from the decay kinetics of the synaptically activated Glu transporter current recorded in cortical astrocytes. We have shown that Glu clearance by astrocytes during neuronal activity is slower in FHM2 KI compared to WT mice, and that the density of GLT-1a in the membrane of astrocytic processes surrounding cortical excitatory synapses is about 50% reduced in the FHM2 mutants, a reduction that mirrors the reduced expression of the α_2 NKA protein.

Interestingly, the relative impairment of Glu clearance in FHM2 KI mice is activity-dependent. In fact, when synaptic Glu release was induced by a train of pulses, the slowing down of the rate of Glu clearance in the FHM2 mutants was larger than that observed with a single pulse and was larger with a 100 Hz compared to 50 Hz train. This is consistent with and likely reflects the decreased Glu binding capacity of GluTs in the KI mice due to the reduced density of GLT-1a in PAPs. As a consequence, a relatively lower number of GluTs remain available to bind Glu at the end of the train in KI compared to WT astrocytes, resulting in a relatively larger slowing of the rate of Glu clearance at the end of the train.

These data provide the first direct experimental evidence, to our knowledge, for a key role of the α_2 NKA pump in the clearance of synaptically released Glu during neuronal activity. Our findings suggest that this key role is based on a necessary tight coupling between α2 pumps and GLT-1 in cortical PAPs. These findings include: i) the strict co-localization of α_2 NKA and GLT-1a in astrocytic processes in the vicinity of glutamatergic synapses; ii) the 48% reduction of the membrane density of GLT-1a in KI PAPs, quantitatively similar to the reduction in the expression of α_2 NKA, and, in contrast, the unaltered membrane density of GLT-1a in AxTs where α_2 is not expressed; iii) the insignificant increase in membrane density of GLT-1a in PAPs in Cef-treated FHM2 KI mice, in contrast with the increased density of GLT-1a in AxTs.

By using astrocytes as $[K]_e$ biosensors, we have also studied the functional consequences of the reduced expression of α_2 NKA in heterozygous W887R/+ KI mice on the rate of K^+ clearance, as measured from the decay kinetics of the $[K^+]_e$-dependent slow inward current elicited in astrocytes by neuronal activity and the ensuing K^+ efflux. The finding that the rate of K^+ clearance after a train of pulses at 50 Hz is slower in FHM2 KI mice provides the first direct experimental support for an important role of the α_2 NKA pump in K^+ clearance following neuronal activity.

Can impaired Glu and K^+ clearance during neuronal activity explain the facilitation of initiation and propagation of experimental CSD in the FHM2 mouse model and the episodic vulnerability to CSD ignition in FHM2? Despite important progress, the mechanisms underlying the initiation of experimental CSD remain incompletely understood and controversial (Pietrobon & Moskowitz, 2014). Experimental data and computational models support the ideas that an increase in $[K^+]_e$ above a critical value is a key initiating event, and that generation of a net self-sustaining inward current and a regenerative local K^+ release are essential components of the positive feedback cycle that confers to CSD its all-or-none characteristics and causes complete neuronal depolarization if removal of K^+ from the interstitium does not keep pace with its release (Pietrobon & Moskowitz, 2014; Somjen, 2001). The ion channels involved in the generation of the net self-sustaining inward current and in the regenerative local K^+ release essential for CSD ignition remain incompletely understood, although there is strong pharmacological support for a key role of NMDARs (Pietrobon & Moskowitz, 2014). Investigation of the mechanisms underlying the facilitation of experimental CSD in FHM1 KI mice, carrying a gain-of-function mutation in neuronal $Ca_V2.1$ channels, revealed enhanced excitatory synaptic transmission at cortical pyramidal cell synapses (Tottene et al, 2009; Vecchia et al, 2015), and showed a

450 causative link between enhanced glutamatergic transmission at cortical synapses and
451 facilitation of initiation and propagation of experimental CSD (Tottene et al, 2009).
452
453 Here , we investigated whether there is a causative relationship between reduced rate of
454 Glu clearance at cortical synapses and facilitation of CSD in FHM2 KI mice, using two
455 different approaches.
456 In the first approach we investigated whether the facilitation of CSD in FHM2 KI mice
457 could be rescued by systemic treatment with Cef, a drug that increased around 60% the
458 expression of GLT-1a in neo-cortex of WT mice. Cef was able to rescue a small portion of
459 the facilitation of CSD induction without affecting the facilitation of CSD propagation. The
460 findings that neither the total expression of GLT-1a in the cortex nor the membrane density
461 of GLT-1a in PAPs were significantly increased in Cef-treated FHM2 KI mice, made it
462 difficult to draw a clearcut conclusion regarding the role of impaired Glu clearance by
463 astrocytes in CSD facilitation. The observation that Cef increased GLT-1a expression in
464 AxTs in FHM2 KI mice suggests the possibility that the small increase in CSD threshold
465 produced by Cef may be due to increased reuptake of Glu in AxTs. If correct, this would be
466 remarkable because GLT-1a in AxTs is only a small fraction of the total brain GLT-1a
467 (Chen et al, 2004; Furness et al, 2008; Melone et al, 2009); accordingly, selective deletion
468 of GLT-1a in neurons does not give rise to any apparent neurological abnormality in
469 contrast with selective deletion in astrocytes (Petr et al, 2015). Alternatively, some other
470 effect of Cef, not related to GLT-1 expression, might underlie its small effect on CSD
471 threshold, although the unaltered protein levels of α_2 NKA, XCT and Kir4.1 in Cef-treated
472 FHM2 KI mice make the involvement of mechanisms mediated by these proteins unlikely.
473 In the second approach we investigated whether pharmacological reduction of the rate of
474 Glu clearance by astrocytes in WT mice to values similar to those in FHM2 KI mice could
475 lead to a similar facilitation of CSD induction and propagation. Pharmacological inhibition

476 of a fraction of GluTs in WT mice did lower the threshold for CSD induction and increased
477 the velocity of CSD propagation. The quantative comparison between the changes in CSD
478 threshold and velocity produced by the FHM2 mutation and by subsaturating
479 concentrations of DL-TBOA, supports the conclusion that the reduced rate of Glu
480 clearance by astrocytes can account for most of the facilitation of CSD initiation in FHM2
481 KI mice, leaving little room for other contributing mechanisms. In contrast, impaired Glu
482 clearance by astrocytes can account for only a (relatively large) fraction of the facilitation of
483 CSD propagation, suggesting that other mechanisms contribute. The observation that also
484 Cef treatment in FHM2 KI mice had a differential effect on CSD threshold and velocity
485 appears consistent with the interpretation that increased reuptake of Glu in AxTs might
486 account for the small rescue of facilitation of CSD induction produced by Cef.
487
488 The present data, together with the findings in FHM1 KI mice (Tottene et al, 2009), support
489 a model of CSD initiation in which i) excessive glutamatergic synaptic transmission and
490 activation of NMDARs are key elements in the positive feedback cycle that ignites CSD
491 and ii) the α_2 NKA pumps exert a dampening role owing mainly to their key role in Glu
492 clearance by astrocytes.
493 There is evidence that cooperative activation of postsynaptic NMDARs by independent
494 excitatory synapses due to Glu spillover occurs with e.g. high frequency stimulation or by
495 increasing the probability of Glu release or with pharmacological inhibition of GluTs, i.e. in
496 conditions in which the binding capacity of GluTs is overwhelmed by high extracellular Glu
497 (Arnth-Jensen et al, 2002; Lozovaya et al, 1999; Tsukada et al, 2005). Most likely,
498 cooperative activation of postsynaptic NMDARs also occurs with the experimental stimuli
499 that ignite CSD, since they induce a large release of Glu (Enger et al, 2015; Pietrobon &
500 Moskowitz, 2014). Within the framework of the proposed CSD model, one predicts a lower
501 threshold for CSD induction in FHM2 KI compared to WT mice because in the FHM2

mutants depolarizing stimuli of lower intensity will release enough Glu to overwhelm the binding capacity of GluTs and lead to cooperative activation of a sufficient number of NMDARs to initiate the positive feedback cycle that ignites CSD. The findings discussed above indicate that the contribution of the reduced rate of K^+ clearance by astrocytes to the facilitation of CSD initiation in FHM2 KI mice, if present, is quite small. This would be consistent with a more relevant role of the neuronal α_3 NKA relative to the glial α_2 NKA in K^+ buffering during the CSD-inducing stimuli. Evidence that this is the case during the CSD depolarization is provided by reports that the duration of the CSD depolarization is increased in heterozygous KI mice carrying a mutation that reduces the activity of α_3 NKA (Hunanyan et al, 2015), whereas, in contrast, the CSD duration is not affected in FHM2 KI mice with reduced α_2 NKA (Leo et al, 2011).

The typical slow rate of CSD propagation implies that it is mediated by diffusion of a chemical substance. Although it has long been debated whether the diffusing substance is K^+ or Glu, most evidence points to diffusion of K^+ released into the interstitial space during CSD as the underlying mechanism (Enger et al, 2015; Pietrobon & Moskowitz, 2014). The very fast rate of Glu clearance compared to that of K^+ clearance is consistent with and supports this notion. The faster rate of CSD propagation in FHM2 KI mice is consistent with the idea that CSD propagation is mediated by K^+ diffusion because, in the framework of our CSD model, one predicts that in KI mice the $[K^+]_e$-dependent Glu release necessary to activate a number of NMDARs sufficient for ignition of CSD in contiguous regions is obtained when the propagating K^+ ions reach a lower concentration than in WT mice. Moreover, it is plausible to expect that the reduced rate of K^+ clearance by astrocytes in FHM2 KI mice increases the rate of CSD spread and thus contribute to the facilitation of CSD propagation.

Since activity-dependent intracellular Na^+ transients in hippocampal and cortical astrocytes are predominantly due to Na^+ influx mediated by GluTs (Chatton et al, 2000; Lamy & Chatton, 2011; Langer & Rose, 2009), and since in our FHM2 KI mice the reduced expression of α_2 NKA is accompanied by a similar reduction of GLT-1 in PAPs, it remains unclear if and to what extent activity-dependent Na^+ transients are altered in astrocytes of FHM2 KI mice. However, if the reduced α_2 NKA expression in FHM2 KI mice significantly affects Na^+ homeostasis in cortical astrocytes, other possible hypothetical mechanisms that might contribute to CSD facilitation (to be possibly investigated in future studies) could result from slowing (or even reversal) of Na^+-dependent transporters such as the electrogenic Na^+- $HCO3^-$ cotransporters or the Na^+-Ca^{2+} exchangers (Kirischuk et al, 2012; Rose & Karus, 2013) (See Appendix Supplementary Discussion).

Both FHM2 and FHM1 mouse models are characterized by excessive glutamatergic transmission, due to either increased Glu release (FHM1) or reduced Glu clearance (FHM2). In contrast with enhanced excitatory synaptic transmission at pyramidal cell synapses, inhibitory transmission at fast-spiking and other multipolar interneuron synapses was unaltered in FHM1 KI mice (Tottene et al, 2009; Vecchia et al, 2014; Vecchia et al, 2015). Interestingly, in the cortex, the α_2 NKA pump is localized in astrocytic processes surrounding glutamatergic synapses but is not present in astrocytic processes surrounding GABAergic synapses (Cholet et al, 2002), suggesting that FHM2 mutations likely affect excitatory but not inhibitory synaptic transmission. The differential effect of FHM1 and FHM2 mutations on excitatory and inhibitory synaptic transmission implies that, most likely, the neuronal circuits that dynamically maintain a tight balance between excitation and inhibition during cortical activity are functionally altered in FHM1 and FHM2, and suggests that dysfunctional regulation of the cortical excitatory inhibitory balance (E/I) may be a common feature of the FHM brain. This supports the view of migraine as a

disorder of brain excitability characterized by dysfunctional regulation of the cortical E/I balance (Ferrari et al, 2015; Vecchia & Pietrobon, 2012) and gives insights into possible mechanisms underlying the susceptibility to ignition of "spontaneous" CSDs in FHM, and possibly migraine. It seems plausible to hypothesize that excessive glutamatergic transmission and dysfunctional regulation of the E/I balance in FHM may in certain conditions (e.g. with sensory overload or with other migraine triggers) lead to overexcitation and network hyperactivity with consequent excessive K^+ increase and NMDAR activation (that leads to further K^+ increase) thus creating the conditions for initiation of the positive feedback cycle that ignites CSD. Similar mechanisms may underlie the susceptibility to CSD ignition in common forms of migraine for which there is indirect evidence consistent with enhanced cortical excitatory transmission (Pietrobon & Moskowitz, 2013) and for which genome-wide association studies have identified susceptibility loci potentially leading to enhanced glutamatergic transmission and/or dysregulated brain E/I balance (Anttila et al, 2010; Anttila et al, 2013; Chasman et al, 2011; Freilinger et al, 2012).

Materials and Methods

Animals

Experiments were performed using heterozygous knockin (KI) mice harbouring the W887R FHM2 mutation ($Atp1a2^{+/R887}$ mice: (Leo et al, 2011)) and their wild type (WT) littermates (background C57BL6J, male and female in equal or near equal number). Animals were housed in Specific Pathogen Free conditions, maintained on a 12 h light/dark cycle, with free access to food and water. Animals were anaesthetized with isoflurane or an i.p. injection of chloral hydrate (300 mg/kg) and brains removed for acute slices preparation or prepared for immunocytochemistry and western blotting studies. For Cef studies, mice received a daily intraperitoneal (i.p.) injection (8-10 A.M) of saline or Cef (Rocefin, Roche

S.p.A., Milano, Italy; 200 mg $kg^{-1}day^{-1}$ dissolved in saline) for 7-8 days. Twenty-four hours after the final injection, animals were anaesthetized and brains removed.

All experimental procedures involving animals and their care were carried out in accordance with National laws and policies (D.L. n. 26, march 14, 2014) and with the guidelines established by the European Community Council Directive (2010/63/UE), and were approved by the local authority veterinary services.

Statistics

After assessing for normal distribution (using the Shapiro-Wilk or the Kolmogorov-Smirnov test), comparison between two groups was performed using two-tailed unpaired or paired t-test for normal distributed data or the Mann-Withney U test for non-parametric data. Equal variances were assumed. Data are given as mean ± SEM; Differences were considered statistically significant if $P<0.05$ (*, $P<0.05$; **, $P<0.01$; ***, $P<0.001$). No statistical methods were used to choose sample size, that were estimated based on previous experience and are in line with those in the literature. No animals were excluded from the analysis.

Whole-cell patch-clamp recordings from astrocytes in acute brain slices

Acute coronal slices of the somatosensory cortex were prepared from P22-23 mice (unless otherwise specified) of either sex as described in (Tottene et al, 2009) and in Appendix Supplementary Methods.

Patch-clamp recordings were made following standard techniques. Brain slices were continuously perfused in a submersion chamber with fresh extracellular solution at 30 °C at a flow rate of 3 ml/min. Recordings were made from layer 1 astrocytes deeper than 45 µm from the slice surface. The cell bodies of astrocytes were visualized using an upright microscope equipped with infrared light and DIC optics and identified by their small soma size (< 10 µm), low input resistance (< 20 MΩ; WT:_13.2 ± 0.7 MΩ, n= 42; KI: 14.2 ± 1.2 MΩ,

606 n=24; p=0.42), very negative resting membrane potential (WT:_-91 ± 0.6 mV, n= 42; KI: -91 ±
607 0.6 , n=24, , after LJP correction of -10 mV), inability to generate action potentials and
608 linear current-voltage relationships, typical of so called passive astrocytes (Bergles & Jahr,
609 1997; Bernardinelli & Chatton, 2008) (Scimemi & Diamond, 2013).
610 Astrocyte internal solution contained (in mM): 115 K-gluconate, 6 KCl, 4 MgATP, 0.3
611 NaGTP, 10 Na-Phosphocreatine, 10 HEPES, 5 glucose (pH 7.25 with KOH, osmolarity
612 295 mOsm with sucrose)**.**
613 The extracellular solution contained 125 mM NaCl, 2.5 mM KCl, 1 mM $MgCl_2$, 1 mM $CaCl_2$,
614 25 mM $NaHCO_3$, 1.25 mM NaH_2PO_4, 25 mM glucose, saturated with 95% O_2 and 5% CO_2.
615 For recording of Glu transporter-mediated currents, the extracellular solution also
616 contained antagonists of AMPA receptors (10 µM NBQX), NMDA receptors (NMDARs; 50
617 µM D-AP5 and 20 µM (+)-MK801) and $GABA_A$ receptors (20 µM (+)-Bicuculline or 5 µM
618 gabazine) to block neuronal postsynaptic current flow (Bergles & Jahr, 1997).
619 Currents were evoked in astrocytes (held close to the resting potential at -90 mV, after LJP
620 correction) by passing constant current pulses (100 µA, 100 µs) every 15 s (or 20 s with
621 train of pulses) through a concentric bipolar tungsten electrode (TM33CCINS, World
622 precision Instruments, Inc., Sarasota, FL, USA) placed in layer 1 at least 200 µm away
623 from the recorded astrocyte (Fig 1A).
624 Access resistance was monitored continuously throughout the experiments and was
625 typically less than 20 MΩ (without compensation)**;** experiments where it changed more
626 than 20% (or had access resistance >25 MΩ) were excluded from the data. The recorded
627 WT and KI astrocytes had similar access resistance (WT: 14.7 ± 0.6 MΩ, n= 66; KI: 16.0 ±
628 0.8 MΩ, n=47; p=0.15). Pipette resistance: 5-6 MΩ. Currents were sampled at 10 kHz and
629 filtered at 2 kHz.
630
631 *Analysis of patch-clamp recordings*

Synaptically activated Glu transporter currents (STCs) elicited by single pulse stimulation were isolated pharmacologically using saturating concentrations of the GluTs inhibitor (3*S*)-3-[[3-[[4-(Trifluoromethyl)benzoyl]amino]phenyl]methoxy]-L-aspartic acid (TFB-TBOA; Tocris Cookson Ltd., Bristol, UK) (0.5 - 15 uM). The STC was obtained by subtracting the residual current remaining in the presence of TFB-TBOA (TBOA) from the total control current (Scimemi and Diamond, 2013). To obtain a measure of the rate of clearance of synaptically released Glu by cortical astrocytes, the decay of the STC was best fitted by a single exponential function (Diamond, 2005). STCs elicited by single pulse stimulation were also isolated non pharmacologically by using an exponential waveform approximating the average TBOA-insensitive current (Devaraju et al, 2013; Diamond, 2005; Scimemi & Diamond, 2013). The average normalized residual current recorded in the presence of TBOA was obtained by pooling the normalized TBOA-insensitive currents recorded in 16 slices (recordings from 7 WT and 9 FHM2 astrocytes were pooled together because the time course of the residual current in WT and KI slices was similar). The rising phase of the average normalized TBOA-insensitive current was approximated by a mono-exponential function (1-exp (-t/τ_{rise})) with τ_{rise} = 2.35 ms (Fig 1C). The STC was obtained by subtracting from the total current elicited in astrocytes an exponential function A(1-exp (-t/τ_{rise})) with τ_{rise} = 2.35 ms and with A equal to the maximal current measured in individual astrocytes at about 60 ms after stimulation when the transient transporter current had decayed to zero (Devaraju et al, 2013; Diamond, 2005; Scimemi & Diamond, 2013). When STCs were elicited by trains of 10 pulses at high frequency (50 or 100 Hz), it was not possible to isolate them pharmacologically (by subtracting the residual current in the presence of TBOA from the control current elicited by the train) because in the presence of TBOA the residual current measured after the train was larger than in control. Therefore, the STC elicited by the 10th pulse in the train was obtained from experiments in which single stimuli were alternated with trains of 9 and 10 pulses at 50 or 100 Hz

(Diamond & Jahr, 2000) as follows. First, the current elicited by 9 pulses was subtracted from that elicited by 10 pulses (Fig 2A, left) to obtain the 10-9 pulses difference current (trace a-b); then, the STC elicited by the 10^{th} pulse (Fig 2A, right: trace a-b-c) was obtained in isolation by subtracting the exponential function that simulates the TBOA-insensitive current elicited by a single pulse (trace c, obtained as explained above) from the 10-9 pulses difference current (trace a-b) (Fig 2A, right). This could be done because the amplitude of the TBOA-insensitive current elicited by a single pulse was similar to the amplitude of the steady component of the 10-9 pulses difference current (e.g WT: 23 ± 3 pA vs 21 ± 3 pA with 50 Hz train, n = 19; 21 ± 3 pA vs 20 ± 2 pA with 100 Hz train, n = 14; similar finding for KI: 25 ± 6 pA vs 24 ± 5 pA with 50 Hz train, n = 15; 32 ± 7 pA vs 27 ± 5 pA with 100 Hz train, n = 11).

Sweeps are averages of at least 5 responses**.** Stimulation artifacts have been truncated.

Cortical spreading depression

Cortical spreading depression was elicited and measured in acute coronal slices of the somatosensory cortex of WT and FHM2 KI mice as in (Tottene et al, 2009), but most recordings were at 30°C rather than room temperature and the rate of perfusion of the slices was higher (6 mL/min, unless otherwise specified). See Appendix Supplementary Methods for details.

Immunocytochemical studies

Mice were anesthetized with an intraperitoneal (i.p.) injection of chloral hydrate (300 mg/kg) and perfused transcardially with a flush of saline solution followed by 4% freshly depolimerized paraformaldehyde in 0.1 M phosphate buffer (PB; pH 7.4). Brains were removed, post-fixed in the same fixative (4 weeks for both double-labeling immunofluorescence and immunogold studies; 2 hours for triple-labeling

684 immunofluorescence observations), and cut in coronal sections on a Vibratome in 50 µm
685 sections which were collected in PB until processing (Melone et al, 2009).

686 *Immunofluorescence.* GLT-1a/VGLUT1 double-labeling studies were performed in
687 sections from WT and KI mice and then, in a second set of experiments, in sections from
688 saline- or Cef-treated WT mice and saline- or Cef-treated KI mice. To minimize the effects
689 of procedural variables, GLT-1a/VGLUT1 double-labeling staining of sections from WT and
690 KI groups and then of WT saline, WT Cef, KI saline and KI Cef groups was performed in
691 parallel using well-characterized antibodies (Melone et al, 2005; Omrani et al, 2009;
692 Rothstein et al, 1994) and standard procedures as described in (Melone et al, 2009) and
693 detailed in Appendix Supplementary Methods.

694 *Confocal microscopy and data analysis.* Collection and data analysis of confocal
695 microscopic fields were performed by a blinded observer. Procedures were as described
696 previously (Bragina et al, 2006; Melone et al, 2009; Melone et al, 2005) and are detailed in
697 Appendix Supplementary Methods.
698
699 *Immunogold.* Sections from WT and KI animals and from KI mice that received saline or
700 Cef were processed for the osmium-free method (Phend et al, 1995). Procedures were as
701 described previously (Melone et al, 2009) and are detailed in Appendix Supplementary
702 Methods. To minimize the effects of procedural variables, post-embedding procedure of
703 grids from WT and KI groups and then from KI saline and KI Cef groups was performed in
704 parallel.
705

706 *Electron microscopy and data analysis.* Collection and analysis of electron microscopic
707 fields were performed by a blinded observer as described (Melone et al, 2009) and

detailed in Appendix Supplementary Methods.

Western blotting

For western blotting studies mice were anesthetized with chloral hydrate (300 mg/kg i.p.) and decapitated. Cerebral cortex was quickly separated, tissue was homogenized (Melone et al, 2001), and crude synaptic membranes were prepared (Danbolt et al, 1990). To minimize procedural variables, homogenates from Cef and saline mice were loaded onto the same gel and in a blinded manner. Procedures were as described (Bragina et al, 2006) and detailed in Appendix Supplementary Methods, together with antibodies and controls.

Acknowledgements

We thank Michele Bellesi for help with Western blotting. This work was supported by Telethon Italy grant GGP14234 (to D.P.), the Italian Ministry of University and Research (PRIN2010) (to D.P.) and the University of Padova (Progetto Ateneo 2012) to D.P.

Author contributions

CC, MM and AT performed the experiments, analysed the data, discussed interpretation of the data and revised critically the manuscript. LB and GC contributed to the acquisition, analysis and discussion of the data. MS and GC contributed to the experimental design, discussed interpretation of the data and revised critically the manuscript. GC also provided the FHM2 mouse model. FC and DP designed the study, supervised the experiments, the analysis and interpretation of the data. DP conceived the study and wrote the paper.

Conflict of interest

The authors declare that they have no conflict of interest

The paper explained

Problem

Migraine is a common disabling brain disease. Cortical spreading depression (CSD) is thought to play a key role in migraine pathogenesis in that it underlies migraine aura and may trigger migraine headache. The mechanisms of the primary brain dysfunction underlying the susceptibility to CSD ignition in the human brain and the onset of a migraine attack remain largely unknown and are a major open issue in the pathophysiology of migraine. To gain insights into this question we studied the mechanisms underlying facilitation of CSD in a knockin (KI) mouse model of familial hemiplegic migraine type 2 (FHM2), a rare monogenic form of migraine with aura caused by loss-of-function mutations in the gene encoding the α_2 subunit of the Na^+, K^+ ATPase (α_2 NKA), an isoform almost exclusively expressed in astrocytes in the adult brain.

Results

Combining patch-clamp recordings from astrocytes in acute cortical slices with immunohistochemistry and immunogold electron microscopy we show that i) the rates of glutamate and K^+ clearance by cortical astrocytes during neuronal activity are reduced in heterozygous KI mice which carry the W887R FHM2 mutation and have 50% reduced α_2 NKA protein in the brain, thus providing direct evidence for a key role of α_2 NKA in clearance of synaptically released glutamate and in extracellular K+ buffering during neuronal activity and ii) the density of GLT-1a glutamate transporters in the membrane of astrocytic processes surrounding cortical excitatory synapses is about 50% reduced in the FHM2 mouse model, pointing to specific tight coupling between α_2 NKA and GLT-1a in the astrocytic processes. Measurements of CSD threshold and velocity in cortical slices from FHM2 KI mice treated with ceftriaxone and from wild-type mice after pharmacological

inhibition of a fraction of glutamate transporters provide evidence that the defective glutamate clearance by astrocytes underlies most of the facilitation of CSD initiation (and a large fraction of the facilitation of CSD propagation) in the FHM2 mouse model.

Impact

By uncovering the key mechanism underlying facilitation of CSD in the FHM2 mouse model, this study moves forward our understanding of the molecular and cellular mechanisms that may underlie the brain susceptibility to CSD ignition in migraine and point out a direction in which to search for novel migraine therapies. In particular, it points to excessive cortical glutamatergic synaptic transmission as a key mechanism underlying vulnerability to CSD ignition in migraine and to enhancement of astrocytic glutamate transporter function as a possible new therapeutic strategy.

Figure legends

Figure 1. The rate of glutamate clearance by cortical astrocytes, as deduced from the decay kinetics of the synaptically activated glutamate transporter current (STC) elicited by single pulse stimulation, is slower in W887R/+ FHM2 knockin (KI) relative to wild-type (WT) mice.

(A) Scheme of the STC recording paradigm. The currents elicited by extracellular stimulation in layer 1 were measured in a voltage-clamped layer 1 astrocyte located at 200 µm from the stimulating electrode in an acute slice of mouse barrel cortex.

(B) Time constants of decay, τ_{decay}, of the STC isolated pharmacologically in WT and FHM2 KI mice. Top, superimposed representative traces of the inward current evoked in an astrocyte (held at -90 mV) by a single pulse stimulation (indicated by the arrow) in a WT slice, before (trace a) and after (trace b) application of a saturating concentration of the GluT inhibitor TFB-TBOA (TBOA). The STC was obtained by subtracting the residual current remaining in the presence of TBOA from the total inward current (trace a-b); the decay of the STC was best fitted by a single exponential function with τ_{decay} = 6.53 ms (in red). The bar plot shows the average values of τ_{decay} of the STC isolated pharmacologically in cortical slices (n=13) from P22-23 WT (N=7) and KI mice (n=9; N=3). STC τ_{decay} is 17% higher in KI compared to WT astrocytes (unpaired t-test: P = 0.003). Hereafter, n indicates the number of slices and N indicates the number of mice.

(C) τ_{decay} of the STC isolated using an exponential waveform approximating the average TBOA-insensitive current in WT and KI mice. Top trace, average normalized TBOA-insensitive current obtained by pooling the normalized TBOA-insensitive currents recorded in 16 WT and KI cells. This current was best fitted by an exponentially rising function ($1-\exp(-t/\tau_{rise})$) with τ_{rise}= 2.35 ms (in green). The STC was obtained by subtracting from the total current elicited in the astrocyte (a: same representative trace as in (B)) the

exponential function A(1-exp (-t/τ_{rise})) with τ_{rise} = 2.35 ms and A equal to the maximal current measured in the astrocyte at about 60 ms after stimulation (trace c); the decay of the STC (trace a-c) was best fitted by a single exponential function with τ_{decay} = 6.49 ms (in red). The bar plot shows the average values of τ_{decay} of the STC isolated as shown in the top panel in cortical slices from P22-23 WT (n = 28; N=11) and KI mice (n = 27; N=9). STC τ_{decay} is 21% higher in KI compared to WT astrocytes (unpaired t-test: $P < 0.0001$). Data are mean ± SEM.

Figure 2. The slowing down of glutamate clearance in FHM2 KI relative to WT mice is larger after a train of action potentials at high frequency than after a single action potential.

(A) Isolation of the STC elicited by the last pulse of a high-frequency train of action potentials. Left: superimposed representative traces of the inward current evoked in an astrocyte (held at -90 mV) by extracellular stimulation with a train of 10 pulses (trace a: black) and a train of 9 pulses (trace b: brown) at 50 Hz in a WT cortical slice. The inward current elicited by the 10th pulse was obtained by subtracting the current elicited by 9 pulses from that elicited by 10 pulses (trace a-b). Right: The STC elicited by the 10th pulse (trace a-b-c) was obtained by subtracting the exponential function that simulates the TBOA-insensitive current elicited by a single pulse (trace c, obtained as in Figure 1C) to the 10-9 pulses difference current (trace a-b). The decay of the STC elicited by the 10th pulse was best fitted by a single exponential function with τ_{decay} = 8.04 ms (in red).

(B) τ_{decay} of the STC elicited by the 10th pulse of 50 Hz ($\tau_{10\ (50\ Hz)}$, left panel) and 100 Hz ($\tau_{10\ (100\ Hz)}$, right panel) trains in layer 1 astrocytes in acute cortical slices from P22-23 WT (n = 23; N=10 for 50 Hz; n = 18; N=8 for 100 Hz) and KI (n = 21; N=9 for 50 Hz and n = 14; N=7 for 100 Hz) mice. The STC elicited by the 10th pulse was obtained as described in (A). STC $\tau_{10\ (50\ Hz)}$ and $\tau_{10\ (100\ Hz)}$ are 30% and 37% higher in KI compared to WT mice,

respectively (unpaired t-test: $P < 0.0001$ in both cases).

Data are mean ± SEM.

Figure 3. **The size of GLT-1a immunoreactive (ir) puncta overlapping with VGLUT1 ir puncta is reduced in the cortex of W887R/+ FHM2 KI mice, suggesting a reduced expression of the glutamate transporter GLT-1a in the vicinity of cortical glutamatergic synapses.**

(A) Simultaneous visualization of GLT-1a+ (green) and VGLUT1+ puncta (red) in first somatic sensory cortex (SI) of a WT and a KI mouse (P35). Arrows point to some GLT-1a+ puncta overlaying with VGLUT1+ puncta (i.e., GLT-1a/VGLUT1 related puncta); framed regions (enlarged below) are examples of GLT-1a/VGLUT1 related puncta (arrowheads). All microscopic fields are from layers II/III. Scale bars: 3.5 µm for left and right panels and 1 µm for enlarged framed areas.

(B) Percentage and size of GLT-1a+ puncta overlaying with VGLUT1 in P35 WT and KI mice. Left, percentage of GLT-1a+ puncta overlaying with VGLUT1 is comparable in WT and KI mice (data were obtained from 14 and 18 fields of 20 µm x 20 µm from 2 WT and 2 KI mice (4 sections/animal), respectively) (unpaired t-test: $P = 0.52$). Right, size of GLT-1a/VGLUT1 related puncta is 19 % reduced in KI mice (169 GLT-1a+ puncta analyzed from 2 mice) compared to WT (174 GLT-1a+ puncta analyzed from 2 mice) (Mann-Withney U test: $P = 0.016$).

Data are mean ± SEM.

Figure 4. **The density of GLT-1a in the membrane of cortical perisynaptic astrocytic processes is reduced in W887R/+ FHM2 KI mice, while the density of GLT-1a in axon terminals is unaltered.**

(**A**) Distribution of GLT-1a gold particles in astrocytic processes contacting asymmetric

synapses (perisynaptic astrocytic processes: PAP) in SI of 5 WT and 5 KI (2 male, 3 female) mice (P34-35). In cortical PAP of KI mice the density (particles/μm^2) of total and membrane-associated gold particles (arrowheads) are reduced compared to WT mice, whereas the density of cytoplasmic gold particles (arrows) is comparable to that in WT (cf Table I for numerical values and statistics).

(B) Distribution of GLT-1a gold particles in excitatory axon terminals forming asymmetric synaptic contact (AxT) in SI of P34-35 WT and KI mice. In cortical AxT of KI and WT mice, GLT-1a density is comparable (arrowheads: membrane-associated gold particles; arrows: cytoplasmic gold particles) (cf Table I*)*.

All microscopic fields in (A) and (B) are from layers II/III. t, total density; cyt, cytoplasmic density; mem, membrane density. Scale bar: 100 nm.

Data are mean ± SEM.

Figure 5. The rate of K^+ clearance by cortical astrocytes after a train of action potentials is reduced in W887R/+ FHM2 KI compared to WT mice.

Left, superimposed representative traces of the normalized inward current evoked in a WT (black trace) and a KI cortical astrocyte (blue trace) by extracellular stimulation with a train of 10 pulses at 50 Hz in cortical slices. The inset shows in an expanded time scale the portion of the traces indicated by the dotted line. The slowly decaying current (τ_{decay} = 2.00 s and 3.04 s for the WT and KI trace, respectively) is largely a $[K^+]_e$-dependent K^+ current (I_K) whose decay kinetics provide a measure of the rate of K^+ clearance by astrocytes (see text). Right, time constant of decay of I_K elicited by trains of 10 pulses at 50 Hz in cortical astrocytes from P22-23 WT (n = 21; N=12) and KI mice (n = 20; N=8). I_K τ_{decay} is 22% higher in KI compared to WT astrocytes (unpaired t-test: P = 0.001).

Data are mean ± SEM.

Figure 6. Facilitation of CSD induction and propagation in acute cortical slices of W887R/+ FHM2 KI mice.

(A) Images of a cortical slice before (t = 0) and after (t = 15.6 s) pressure ejection of a high KCl pulse that elicits a CSD (top panels), showing that the propagating CSD is associated with a change in light transmittance. Scale bar*:* 500 µm. The traces below show representative changes in intrinsic optical signal (IOS) relative to background measured in a WT and a KI cortical slice during CSD propagation at increasing times and distances from the KCl puff, as indicated in color code in the right image on the top. The velocity of CSD propagation, obtained from the rate of horizontal spread of the change in IOS, in these two representative WT and KI slices is 3.11 and 4.14 mm/min, respectively.

(B) Stimulation threshold for CSD induction (CSD threshold) and rate of CSD propagation (CSD velocity) in WT (n = 24; N=3) and KI (n = 27; N=8) cortical slices from P22-23 mice. CSD threshold is expressed as duration of the first KCl pulse eliciting a CSD. CSD threshold is 28% lower (Mann Whitney U test, $P < 0.0001$) and CSD velocity 21% higher (unpaired t-test: $P< 0.0001$) in KI compared to WT mice.

Data are mean ± SEM.

Figure 7. **The CSD threshold is increased in cortical slices of FHM2 KI mice after Cef treatment that increases the GLT-1a expression in WT mice.**

(A) Western blottings of GLT-1a in cortical crude synaptic membranes of P39 WT mice following Cef treatment for 8 days. GLT-1a levels are significantly increased in mice treated with Cef (Cef WT, N = 4) compared to control saline-injected mice (Ctr WT, N = 4) (Mann-Withney U test: $P = 0.028$).

(**B**) Visualization of GLT-1a+ puncta (green) and VGLUT1+ puncta (red) in sections from SI of P45-46 WT mice that were treated with saline (Ctr WT) or Cef (Cef WT). Arrows point to some GLT-1a/VGLUT1 related puncta. Framed regions (enlarged below) are examples

of GLT-1a/VGLUT1 related puncta (arrowheads). Right, Cef treatment increased significantly the size of GLT-1a+ puncta overlaying VGLUT1 (142 and 186 GLT-1a+ puncta analyzed from 4 Ctr WT and 4 Cef WT mice, respectively; 3 sections/animal) (Mann-Withney U test: $P < 0.0001$). All microscopic fields are from layers II/III. Scale bars: 3.5 µm for left and right panels and 1 µm for enlarged framed areas.

(C) CSD threshold and CSD velocity in cortical slices from P30-33 KI mice that were injected with saline (Ctr KI, n = 38; N=7) or Cef (Cef KI, n = 31; N=6). CSD threshold is 12% higher (Mann-Withney U test: $P = 0.02$) in Cef-treated compared to saline-treated KI mice. CSD velocity is not altered by Cef treatment ($P = 0.90$).

Data are mean ± SEM.

Figure 8. The density of GLT-1a in the membrane of cortical perisynaptic astrocytic processes is not altered by ceftriaxone treatment in W887R/+ FHM2 KI mice, while the density of GLT-1a in the axon terminals is increased.

(A) Distribution of GLT-1a gold particles in PAP of saline-injected (Ctr KI, N=4) and Cef-treated KI mice (Cef KI, N=4) (P45-46). Cef treatment does not modify the density of total, cytoplasmic (arrows) and membrane-associated (arrowheads) gold particles in PAP of KI mice (cf Table II).

(B) Distribution of GLT-1a gold particles in AxT in SI of Ctr KI and Cef KI KI mice. The density of the membrane-associated gold particles (arrowheads) is increased in Cef-treated KI mice (cf Table II).

All microscopic fields in (A) and (B) are from layers II/III. t, total density; cyt, cytoplasmic density; mem, membrane density. Scale bar: 100 nm.

(C) Western blottings of GLT-1a in cortical crude synaptic membranes of P39 KI mice following Cef treatment. GLT-1a levels are similar in Cef-treated (Cef KI, N=4) and and saline-injected (Ctr KI, N=4) (Mann-Withney U test: $P = 0.83$).

(D) Visualization of GLT-1a+ puncta (green) and VGLUT1+ puncta (red) in KI mice that received saline (Ctr KI) and in Cef-treated KI mice (Cef KI) (P45-46). Arrows point to some GLT-1a/VGLUT1 related puncta; framed regions are examples of GLT-1a/VGLUT1 related puncta (arrowheads). Right, Cef treatment does not increase the size of GLT-1a+ puncta overlaying with VGLUT1 (160 and 175 GLT-1a+ puncta analyzed from the same 4 Ctr KI and 4 Cef KI used for post-embedding electron microscopy analysis; 3 sections/animal) (Mann-Withney U test: P = 0.31). Scale bar: 3.5 µm for left and right panels and 1 µm for enlarged framed areas. All microscopic fields are from layers II/III.

Data are mean ± SEM.

Figure 9. **Facilitation of CSD induction and propagation after pharmacological inhibition of a fraction of glutamate transporters in WT mice.**

(A) τ_{decay} of the STC evoked by single pulse stimulation in layer 1 astrocytes in acute cortical slices from P22-23 WT mice before (Ctr WT) and after application of 2.5 µM DL-TBOA (TBOA 2.5) (n = 4; N=2) (right panel). The traces on the left are the corresponding average normalized STCs, isolated as in Figure 1C. The STC τ_{decay} in TBOA 2.5 is 32 ± 2 % higher than in Ctr WT (paired t-test: P = 0.002). The left top panel shows the time course of τ_{decay} of the transient component (due to the STC) of the current recorded in an astrocyte during a representative experiment in which TBOA 2.5 was applied at the time indicated by the horizontal bar. The steady-state effect was reached within 10-15 minutes from the beginning of the drug perfusion. **(B)** CSD threshold and velocity measured in cortical slices from P22-23 WT mice after perfusion for 20 minutes with extracellular solution without (Ctr WT: n = 23; N = 15) and with 2.5 µM DL-TBOA (TBOA 2.5: n = 25; N = 8). CSD threshold in TBOA 2.5 is 36 % lower than in Ctr WT (Mann-Withney U test test: P < 0.0001) and CSD velocity is 20% higher (unpaired t-test: P < 0.0001).

(C) τ_{decay} of the STC evoked by single pulse stimulation in layer 1 astrocytes in acute

cortical slices from P22-23 WT mice before (Ctr WT) and after application of 1.5 µM DL-TBOA (TBOA 1.5) (n = 4; N=4). The STC τ_{decay} in TBOA 1.5 is 22 ± 3 % higher than in Ctr WT (paired t-test: P = 0.004).

(D) CSD threshold and velocity measured in cortical slices from P22-23 WT mice after perfusion for 20 minutes with extracellular solution without (Ctr WT: n = 23; N = 15) and with 1.5 µM DL-TBOA (TBOA 1.5: n = 18; N = 6). CSD threshold in TBOA 1.5 is 23 % lower than in Ctr WT (Mann-Withney U test test: P < 0.0001) and CSD velocity is 13 % higher (unpaired t-test: P = 0.003).

Data are mean ± SEM.

Table legends

Table I. Density values are mean ± SEM; n=number of profiles. Comparison of densities between WT (N = 5) and KI (N = 5) and comparison of densities of perisynaptic astrocytic processes, axon terminals and background were performed using Mann-Withney U test: º density of gold particles was significantly higher than background in PAPs and AxTs (P<0.0001 for both WT and KI).

The mean areas of PAP and AxT of all sampled profiles used for immunogold analysis were comparable in WT and KI (PAP: 0.33 ± 0.09 vs 0.38 ± 0.05 µm^2; Mann-Withney U test, P = 0.53); AxT: 0.71 ± 0.17 vs 0.56 ± 0.10 µm^2; Mann-Withney U test, P = 0.55).

Table II. Density values are mean ± SEM; n=number of profiles. Comparison of densities between saline-treated (N = 4) and Cef-treated (N = 4) FHM2 KI mice was performed using Mann-Withney U test.

Expanded view Figure Legends

Figure EV1

Simultaneous visualization of GLT-1a (green), α_2 Na^+,K^+ ATPase (α_2 NKA) (red) and VGLUT1 (blue) immuno-reactivity puncta in a section of first somatic sensory cortex (SI) of a WT mouse. Confocal microscopy inspection of fields reveals a high degree of co-localization between GLT-1a and α_2 NKA in GLT-1a+ puncta overlaying with VGLUT1+ puncta (arrows). Framed regions (enlarged below) show examples of overlapping GLT-1a/VGLUT1 puncta that are co-localized with α_2 NKA. Data obtained from 32 fields of 20 µm x 20 µm from 2 P32 WT mice (3 sections/animal) revealed that 81 ± 2% of overlapping GLT-1a/VGLUT1 puncta co-localized with α_2. Scale bar: 3.5 µm and 1 µm for enlarged framed areas. All microscopic fields are from layers II/III.

Figure EV2

Western blotting of α_2 NKA, Kir 4.1 and xCT in cortical crude synaptic membranes of P39 FHM2 KI mice following Cef treatment for 8 days. Protein levels are similar in Cef-treated (Cef KI, N = 4) and saline-injected (Ctr KI, N =4); Mann withney U test: P = 0.34, 0.83 and 0.83 for α_2 NKA, Kir 4.1 and xCT, respectively.

1006

1007

1008 **Table I.** Density of GLT-1a gold particles in perisynaptic astrocytic processes and axon
1009 terminals of asymmetric synapses of WT and W887R/+ FHM2 KI mice.

1010

Localization	**WT** (particles/μm^2)	**FHM2 KI** (particles/μm^2)	**WT *vs* FHM2 KI**
Nucleus (background)	0.59 ± 0.02 (n=30)	0.68 ± 0.03 (n=30)	
Astrocytic processes[º]	26.14 ± 1.80 (n=481)	15.39 ± 1.04 (n=524)	P<0.0001
Plasma membrane	48.79 ± 2.66	25.40 ± 1.38	P<0.0001
Cytoplasm	13.40 ± 1.76	11.26 ± 1.06	P=0.058
Axon terminals[º]	7.05 ± 0.65 (n=148)	6.00 ± 0.43 (n=121)	P=0.44
Plasma membrane	20.15 ± 1.77	17.34 ± 1.57	P=0.47
Cytoplasm	4.94 ± 0.60	4.14 ± 0.46	P=0.45

1011

TableII. Density of GLT-1a gold particles in perisynaptic astrocytic processes and axon terminals of asymmetric synapses of saline-(Ctr) and ceftriaxone-(Cef) treated W887R/+ FHM2 KI mice.

Localization	**Ctr KI** (particles/μm^2)	**Cef KI** (particles/μm^2)	**Ctr *vs* Cef**
Nucleus (background)	0.51 ± 0.03 (n=25)	0.54 ± 0.01 (n=25)	
Astrocytic processes	12.98 ± 0.60 (n=354)	13.26 ± 0.71 (n=380)	P=0.27
Plasma membrane	21.13 ± 1.16	23.31 ± 1.19	P=0.27
Cytoplasm	11.70 ± 0.86	10.52 ± 0.83	P=0.009
Axons terminal	5.10 ± 0.30 (n=158)	6.56 ± 0.50 (n=166)	P= 0.002
Plasma membrane	14.40 ± 1.22	18.50 ± 1.18	P=0.007
Cytoplasm	3.42 ± 0.29	4.85 ± 0.70	P=0.068

References

Anttila V, Stefansson H, Kallela M, Todt U, Terwindt GM, Calafato MS, Nyholt DR, Dimas AS, Freilinger T, Muller-Myhsok B, Artto V, Inouye M, Alakurtti K, Kaunisto MA, Hamalainen E, de Vries B, Stam AH, Weller CM, Heinze A, Heinze-Kuhn K, et al. (2010) Genome-wide association study of migraine implicates a common susceptibility variant on 8q22.1. *Nat Genet* **42:** 869-873

Anttila V, Winsvold BS, Gormley P, Kurth T, Bettella F, McMahon G, Kallela M, Malik R, de Vries B, Terwindt G, Medland SE, Todt U, McArdle WL, Quaye L, Koiranen M, Ikram MA, Lehtimaki T, Stam AH, Ligthart L, Wedenoja J, et al. (2013) Genome-wide meta-analysis identifies new susceptibility loci for migraine. *Nat Genet* **45:** 912-917

Arnth-Jensen N, Jabaudon D, Scanziani M (2002) Cooperation between independent hippocampal synapses is controlled by glutamate uptake. *Nat Neurosci* **5:** 325-331

Ayata C, Jin H, Kudo C, Dalkara T, Moskowitz MA (2006) Suppression of cortical spreading depression in migraine prophylaxis. *Ann Neurol* **59:** 652-661

Bellesi M, Melone M, Gubbini A, Battistacci S, Conti F (2009) GLT-1 upregulation impairs prepulse inhibition of the startle reflex in adult rats. *Glia* **57:** 703-713

Berger UV, DeSilva TM, Chen W, Rosenberg PA (2005) Cellular and subcellular mRNA localization of glutamate transporter isoforms GLT1a and GLT1b in rat brain by in situ hybridization. *J Comp Neurol* **492:** 78-89

Bergles DE, Jahr CE (1997) Synaptic activation of glutamate transporters in hippocampal astrocytes. *Neuron* **19:** 1297-1308

Bernardinelli Y, Chatton JY (2008) Differential effects of glutamate transporter inhibitors on the global electrophysiological response of astrocytes to neuronal stimulation. *Brain Res* **1240:** 47-53

Bolay H, Reuter U, Dunn AK, Huang Z, Boas DA, Moskowitz MA (2002) Intrinsic brain activity triggers trigeminal meningeal afferents in a migraine model. *Nat Med* **8:** 136-142

Bøttger P, Doğanlı C, Lykke-Hartmann K (2012) Migraine- and dystonia-related disease-mutations of Na+/K+-ATPases: Relevance of behavioral studies in mice to disease symptoms and neurological manifestations in humans. *Neuroscience & Biobehavioral Reviews* **36:** 855-871

Bozdagi O, Shan W, Tanaka H, Benson DL, Huntley GW (2000) Increasing numbers of synaptic puncta during late-phase LTP: N-cadherin is synthesized, recruited to synaptic sites, and required for potentiation. *Neuron* **28:** 245-259

Bragina L, Melone M, Fattorini G, Torres-Ramos M, Vallejo-Illarramendi A, Matute C, Conti F (2006) GLT-1 down-regulation induced by clozapine in rat frontal cortex is associated with synaptophysin up-regulation. *J Neurochem* **99:** 134-141

Brennan KC, Bates EA, Shapiro RE, Zyuzin J, Hallows WC, Huang Y, Lee HY, Jones CR, Fu YH, Charles AC, Ptacek LJ (2013) Casein kinase idelta mutations in familial migraine and advanced sleep phase. *Science translational medicine* **5:** 183ra156, 181-111

Campbell SL, Hablitz JJ, Olsen ML (2014) Functional changes in glutamate transporters and astrocyte biophysical properties in a rodent model of focal cortical dysplasia. *Front Cell Neurosci* **8:** 425

Chasman DI, Schurks M, Anttila V, de Vries B, Schminke U, Launer LJ, Terwindt GM, van den Maagdenberg AM, Fendrich K, Volzke H, Ernst F, Griffiths LR, Buring JE, Kallela M, Freilinger T, Kubisch C, Ridker PM, Palotie A, Ferrari MD, Hoffmann W, et al., (2011) Genome-wide association study reveals three susceptibility loci for common migraine in the general population. *Nat Genet* **43:** 695-698

Chatton J-Y, Marquet P, Magistretti PJ (2000) A quantitative analysis of l-glutamate-regulated Na+ dynamics in mouse cortical astrocytes: implications for cellular bioenergetics. *European Journal of Neuroscience* **12:** 3843-3853

Chen W, Mahadomrongkul V, Berger UV, Bassan M, DeSilva T, Tanaka K, Irwin N, Aoki C, Rosenberg PA (2004) The glutamate transporter GLT1a is expressed in excitatory axon terminals of mature hippocampal neurons. *J Neurosci* **24:** 1136-1148

Cholet N, Pellerin L, Magistretti PJ, Hamel E (2002) Similar perisynaptic glial localization for the Na+,K+-ATPase alpha 2 subunit and the glutamate transporters GLAST and GLT-1 in the rat somatosensory cortex. *Cereb Cortex* **12:** 515-525

D'Ambrosio R, Gordon DS, Winn HR (2002) Differential role of KIR channel and Na(+)/K(+)-pump in the regulation of extracellular K(+) in rat hippocampus. *J Neurophysiol* **87:** 87-102

Danbolt NC (2001) Glutamate uptake. *Prog Neurobiol* **65:** 1-105

Danbolt NC, Pines G, Kanner BI (1990) Purification and reconstitution of the sodium- and potassium-coupled glutamate transport glycoprotein from rat brain. *Biochemistry* **29:** 6734-6740

De Fusco M, Marconi R, Silvestri L, Atorino L, Rampoldi L, Morgante L, Ballabio A, Aridon P, Casari G (2003) Haploinsufficiency of ATP1A2 encoding the Na+/K+ pump alpha2 subunit associated with familial hemiplegic migraine type 2. *Nat Genet* **33:** 192-196

De Saint Jan D, Westbrook GL (2005) Detecting activity in olfactory bulb glomeruli with astrocyte recording. *J Neurosci* **25:** 2917-2924

de Vries B, Frants RR, Ferrari MD, van den Maagdenberg AM (2009) Molecular genetics of migraine. *Hum Genet* **126:** 115-132

Devaraju P, Sun MY, Myers TL, Lauderdale K, Fiacco TA (2013) Astrocytic group I mGluR-dependent potentiation of astrocytic glutamate and potassium uptake. *J Neurophysiol* **109:** 2404-2414

Diamond JS (2005) Deriving the glutamate clearance time course from transporter currents in CA1 hippocampal astrocytes: transmitter uptake gets faster during development. *J Neurosci* **25:** 2906-2916

Diamond JS, Jahr CE (2000) Synaptically Released Glutamate Does Not Overwhelm Transporters on Hippocampal Astrocytes During High-Frequency Stimulation. *Journal of Neurophysiology* **83:** 2835-2843

Djukic B, Casper KB, Philpot BD, Chin LS, McCarthy KD (2007) Conditional knock-out of Kir4.1 leads to glial membrane depolarization, inhibition of potassium and glutamate uptake, and enhanced short-term synaptic potentiation. *J Neurosci* **27:** 11354-11365

Eikermann-Haerter K, Dilekoz E, Kudo C, Savitz SI, Waeber C, Baum MJ, Ferrari MD, van den Maagdenberg AMJM, Moskowitz MA, Ayata C (2009) Genetic and hormonal factors modulate spreading depression and transient hemiparesis in mouse models of familial hemiplegic migraine type 1. *Journal of Clinical Investigation* **119:** 99-109

Enger R, Tang W, Vindedal GF, Jensen V, Johannes Helm P, Sprengel R, Looger LL, Nagelhus EA (2015) Dynamics of Ionic Shifts in Cortical Spreading Depression. *Cereb Cortex* ***25:***4469-4476

Ferrari MD, Klever RR, Terwindt GM, Ayata C, van den Maagdenberg AMJM (2015) Migraine pathophysiology: lessons from mouse models and human genetics. *The Lancet Neurology* **14:** 65-80

Freilinger T, Anttila V, de Vries B, Malik R, Kallela M, Terwindt GM, Pozo-Rosich P, Winsvold B, Nyholt DR, van Oosterhout WP, Artto V, Todt U, Hamalainen E, Fernandez-Morales J, Louter MA, Kaunisto MA, Schoenen J, Raitakari O, Lehtimaki T, Vila-Pueyo M, et al. (2012) Genome-wide association analysis identifies susceptibility loci for migraine without aura. *Nat Genet* **44:** 777-782

Furness DN, Dehnes Y, Akhtar AQ, Rossi DJ, Hamann M, Grutle NJ, Gundersen V, Holmseth S, Lehre KP, Ullensvang K, Wojewodzic M, Zhou Y, Attwell D, Danbolt NC (2008) A quantitative assessment of glutamate uptake into hippocampal synaptic terminals and astrocytes: new insights into a neuronal role for excitatory amino acid transporter 2 (EAAT2). *Neuroscience* **157:** 80-94

Genda EN, Jackson JG, Sheldon AL, Locke SF, Greco TM, O'Donnell JC, Spruce LA, Xiao R, Guo W, Putt M, Seeholzer S, Ischiropoulos H, Robinson MB (2011) Co-compartmentalization of the astroglial glutamate transporter, GLT-1, with glycolytic enzymes and mitochondria. *J Neurosci* **31:** 18275-18288

Haugeto O, Ullensvang K, Levy LM, Chaudhry FA, Honore T, Nielsen M, Lehre KP, Danbolt NC (1996) Brain glutamate transporter proteins form homomultimers. *J Biol Chem* **271:** 27715-27722

Holmseth S, Scott HA, Real K, Lehre KP, Leergaard TB, Bjaalie JG, Danbolt NC (2009) The concentrations and distributions of three C-terminal variants of the GLT1 (EAAT2; slc1a2) glutamate transporter protein in rat brain tissue suggest differential regulation. *Neuroscience* **162:** 1055-1071

Hunanyan AS, Fainberg NA, Linabarger M, Arehart E, Leonard AS, Adil SM, Helseth AR, Swearingen AK, Forbes SL, Rodriguiz RM, Rhodes T, Yao X, Kibbi N, Hochman DW, Wetsel WC, Hochgeschwender U, Mikati MA (2015) Knock-in mouse model of alternating hemiplegia of childhood: behavioral and electrophysiologic characterization. *Epilepsia* **56:** 82-93

Hwang EM, Kim E, Yarishkin O, Woo DH, Han KS, Park N, Bae Y, Woo J, Kim D, Park M, Lee CJ, Park JY (2014) A disulphide-linked heterodimer of TWIK-1 and TREK-1 mediates passive conductance in astrocytes. *Nature communications* **5:** 3227

Ikeda K, Onaka T, Yamakado M, Nakai J, Ishikawa TO, Taketo MM, Kawakami K (2003) Degeneration of the amygdala/piriform cortex and enhanced fear/anxiety behaviors in sodium pump alpha2 subunit (Atp1a2)-deficient mice. *J Neurosci* **23:** 4667-4676

Illarionava NB, Brismar H, Aperia A, Gunnarson E (2014) Role of Na,K-ATPase α1 and α2 Isoforms in the Support of Astrocyte Glutamate Uptake. *PLoS ONE* **9:** e98469

Kaneko T, Fujiyama F, Hioki H (2002) Immunohistochemical localization of candidates for vesicular glutamate transporters in the rat brain. *J Comp Neurol* **444:** 39-62

Karatas H, Erdener SE, Gursoy-Ozdemir Y, Lule S, Eren-Kocak E, Sen ZD, Dalkara T (2013) Spreading depression triggers headache by activating neuronal Panx1 channels. *Science* **339:** 1092-1095

Kirischuk S, Parpura V, Verkhratsky A (2012) Sodium dynamics: another key to astroglial excitability? *Trends in Neurosciences* **35:** 497-506

Knackstedt LA, Melendez RI, Kalivas PW (2010) Ceftriaxone Restores Glutamate Homeostasis and Prevents Relapse to Cocaine Seeking. *Biological Psychiatry* **67:** 81-84

Kofuji P, Newman EA (2004) Potassium buffering in the central nervous system. *Neuroscience* **129:** 1045-1056

Lamy CM, Chatton J-Y (2011) Optical probing of sodium dynamics in neurons and astrocytes. *NeuroImage* **58:** 572-578

Langer J, Rose CR (2009) Synaptically induced sodium signals in hippocampal astrocytes in situ. *The Journal of Physiology* **587:** 5859-5877

Larsen BR, Assentoft M, Cotrina ML, Hua SZ, Nedergaard M, Kaila K, Voipio J, MacAulay N (2014) Contributions of the Na+/K+-ATPase, NKCC1, and Kir4.1 to hippocampal K+ clearance and volume responses. *Glia* **62:** 608-622

Larsen BR, MacAulay N (2014) Kir4.1-mediated spatial buffering of K(+): experimental challenges in determination of its temporal and quantitative contribution to K(+) clearance in the brain. *Channels (Austin)* **8:** 544-550

Lauritzen M (1994) Pathophysiology of the migraine aura. The spreading depression theory. *Brain* **117 (Pt 1):** 199-210

Leo L, Gherardini L, Barone V, De Fusco M, Pietrobon D, Pizzorusso T, Casari G (2011) Increased susceptibility to cortical spreading depression in the mouse model of familial hemiplegic migraine type 2. *PLoS Genet* **7:** e1002129

Lozovaya NA, Kopanitsa MV, Boychuk YA, Krishtal OA (1999) Enhancement of glutamate release uncovers spillover-mediated transmission by N-methyl-D-aspartate receptors in the rat hippocampus. *Neuroscience* **91:** 1321-1330

McGrail KM, Phillips JM, Sweadner KJ (1991) Immunofluorescent localization of three Na,K-ATPase isozymes in the rat central nervous system: both neurons and glia can express more than one Na,K-ATPase. *J Neurosci* **11:** 381-391

Meeks JP, Mennerick S (2007) Astrocyte membrane responses and potassium accumulation during neuronal activity. *Hippocampus* **17:** 1100-1108

Melone M, Bellesi M, Conti F (2009) Synaptic localization of GLT-1a in the rat somatic sensory cortex. *Glia* **57:** 108-117

Melone M, Burette A, Weinberg RJ (2005) Light microscopic identification and immunocytochemical characterization of glutamatergic synapses in brain sections. *J Comp Neurol* **492:** 495-509

Melone M, Vitellaro-Zuccarello L, Vallejo-Illarramendi A, Perez-Samartin A, Matute C, Cozzi A, Pellegrini-Giampietro DE, Rothstein JD, Conti F (2001) The expression of glutamate transporter GLT-1 in the rat cerebral cortex is down-regulated by the antipsychotic drug clozapine. *Molecular psychiatry* **6:** 380-386

Moseley AE, Lieske SP, Wetzel RK, James PF, He S, Shelly DA, Paul RJ, Boivin GP, Witte DP, Ramirez JM, Sweadner KJ, Lingrel JB (2003) The Na,K-ATPase alpha 2 isoform is expressed in neurons, and its absence disrupts neuronal activity in newborn mice. *J Biol Chem* **278:** 5317-5324

Moskowitz MA, Bolay H, Dalkara T (2004) Deciphering migraine mechanisms: Clues from familial hemiplegic migraine genotypes. *Annals of Neurology* **55:** 276-280

Noseda R, Burstein R (2013) Migraine pathophysiology: anatomy of the trigeminovascular pathway and associated neurological symptoms, cortical spreading depression, sensitization, and modulation of pain. *Pain* **154 Suppl 1:** S44-53

Omrani A, Melone M, Bellesi M, Safiulina V, Aida T, Tanaka K, Cherubini E, Conti F (2009) Up-regulation of GLT-1 severely impairs LTD at mossy fibre--CA3 synapses. *J Physiol* **587:** 4575-4588

Pellerin L, Magistretti PJ (1997) Glutamate uptake stimulates Na+,K+-ATPase activity in astrocytes via activation of a distinct subunit highly sensitive to ouabain. *J Neurochem* **69:** 2132-2137

Petr GT, Sun Y, Frederick NM, Zhou Y, Dhamne SC, Hameed MQ, Miranda C, Bedoya EA, Fischer KD, Armsen W, Wang J, Danbolt NC, Rotenberg A, Aoki CJ, Rosenberg PA (2015) Conditional deletion of the glutamate transporter GLT-1 reveals that astrocytic GLT-1 protects against fatal epilepsy while neuronal GLT-1 contributes significantly to glutamate uptake into synaptosomes. *J Neurosci* **35:** 5187-5201

Phend KD, Rustioni A, Weinberg RJ (1995) An osmium-free method of epon embedment that preserves both ultrastructure and antigenicity for post-embedding immunocytochemistry. *The journal of histochemistry and cytochemistry : official journal of the Histochemistry Society* **43:** 283-292

Pietrobon D (2007) Familial hemiplegic migraine. *Neurotherapeutics* **4:** 274-284

Pietrobon D, Moskowitz MA (2013) Pathophysiology of migraine. *Annu Rev Physiol* **75:** 365-391

Pietrobon D, Moskowitz MA (2014) Chaos and commotion in the wake of cortical spreading depression and spreading depolarizations. *Nat Rev Neurosci* **15:** 379-393

Poolos NP, Mauk MD, Kocsis JD (1987) Activity-evoked increases in extracellular potassium modulate presynaptic excitability in the CA1 region of the hippocampus. *J Neurophysiol* **58:** 404-416

Ransom CB, Ransom BR, Sontheimer H (2000) Activity-dependent extracellular K+ accumulation in rat optic nerve: the role of glial and axonal Na+ pumps. *J Physiol* **522 Pt 3:** 427-442

Rao PSS, Sari Y (2014) Effects of Ceftriaxone on Chronic Ethanol Consumption: a Potential Role for xCT and GLT1 Modulation of Glutamate Levels in Male P Rats. *Journal of Molecular Neuroscience* **54:** 71-77

Rose CR, Karus C (2013) Two sides of the same coin: Sodium homeostasis and signaling in astrocytes under physiological and pathophysiological conditions. *Glia* **61:** 1191-1205

Rose EM, Koo JC, Antflick JE, Ahmed SM, Angers S, Hampson DR (2009) Glutamate transporter coupling to Na,K-ATPase. *J Neurosci* **29:** 8143-8155

Rothstein JD, Dykes-Hoberg M, Pardo CA, Bristol LA, Jin L, Kuncl RW, Kanai Y, Hediger MA, Wang Y, Schielke JP, Welty DF (1996) Knockout of glutamate transporters reveals a major role for astroglial transport in excitotoxicity and clearance of glutamate. *Neuron* **16:** 675-686

1289 Rothstein JD, Martin L, Levey AI, Dykes-Hoberg M, Jin L, Wu D, Nash N, Kuncl RW (1994)
1290 Localization of neuronal and glial glutamate transporters. *Neuron* **13:** 713-725

1291
1292 Russell MB, Ducros A (2011) Sporadic and familial hemiplegic migraine: pathophysiological
1293 mechanisms, clinical characteristics, diagnosis, and management. *Lancet Neurol* **10:** 457-470

1294
1295 Schack VR, Holm R, Vilsen B (2012) Inhibition of Phosphorylation of Na+,K+-ATPase by Mutations
1296 Causing Familial Hemiplegic Migraine. *Journal of Biological Chemistry* **287:** 2191-2202

1297
1298 Scimemi A, Diamond JS (2013) Deriving the Time Course of Glutamate Clearance with a
1299 Deconvolution Analysis of Astrocytic Transporter Currents. *Jove* e50708

1300
1301 Shih PY, Savtchenko LP, Kamasawa N, Dembitskaya Y, McHugh TJ, Rusakov DA, Shigemoto R,
1302 Semyanov A (2013) Retrograde synaptic signaling mediated by K+ efflux through postsynaptic
1303 NMDA receptors. *Cell reports* **5:** 941-951

1304
1305 Sibille J, Pannasch U, Rouach N (2014) Astroglial potassium clearance contributes to short-term
1306 plasticity of synaptically evoked currents at the tripartite synapse. *J Physiol* **592:** 87-102

1307
1308 Somjen GG (2001) Mechanisms of spreading depression and hypoxic spreading depression-like
1309 depolarization. *Physiol Rev* **81:** 1065-1096

1310
1311 Swarts HGP, Weigand KM, Venselaar H, van den Maagdenberg AMJM, Russel FGM, Koenderink
1312 JB (2013) Familial hemiplegic migraine mutations affect Na,K-ATPase domain interactions.
1313 *Biochimica et Biophysica Acta (BBA) - Molecular Basis of Disease* **1832:** 2173-2179

1314
1315 Tanaka K, Watase K, Manabe T, Yamada K, Watanabe M, Takahashi K, Iwama H, Nishikawa T,
1316 Ichihara N, Kikuchi T, Okuyama S, Kawashima N, Hori S, Takimoto M, Wada K (1997) Epilepsy
1317 and exacerbation of brain injury in mice lacking the glutamate transporter GLT-1. *Science* **276:**
1318 1699-1702

1319
1320 Tavraz NN, Durr KL, Koenderink JB, Freilinger T, Bamberg E, Dichgans M, Friedrich T (2009)
1321 Impaired plasma membrane targeting or protein stability by certain ATP1A2 mutations identified in
1322 sporadic or familial hemiplegic migraine. *Channels (Austin)* **3:** 82-87

1323
1324 Tavraz NN, Friedrich T, Durr KL, Koenderink JB, Bamberg E, Freilinger T, Dichgans M (2008)
1325 Diverse Functional Consequences of Mutations in the Na+/K+-ATPase alpha(2)-Subunit Causing
1326 Familial Hemiplegic Migraine Type 2. *Journal of Biological Chemistry* **283:** 31097-31106

1327
1328 Tottene A, Conti R, Fabbro A, Vecchia D, Shapovalova M, Santello M, van den Maagdenberg
1329 AMJM, Ferrari MD, Pietrobon D (2009) Enhanced Excitatory Transmission at Cortical Synapses as
1330 the Basis for Facilitated Spreading Depression in Ca(v)2.1 Knockin Migraine Mice. *Neuron* **61:**
1331 762-773

1332

Tsukada S, Iino M, Takayasu Y, Shimamoto K, Ozawa S (2005) Effects of a novel glutamate transporter blocker, (2S, 3S)-3-[3-[4-(trifluoromethyl)benzoylamino]benzyloxy]aspartate (TFB-TBOA), on activities of hippocampal neurons. *Neuropharmacology* **48:** 479-491

Unichenko P, Myakhar O, Kirischuk S (2012) Intracellular Na+ concentration influences short-term plasticity of glutamate transporter-mediated currents in neocortical astrocytes. *Glia* **60:** 605-614

van den Maagdenberg AM, Pietrobon D, Pizzorusso T, Kaja S, Broos LA, Cesetti T, van de Ven RC, Tottene A, van der Kaa J, Plomp JJ, Frants RR, Ferrari MD (2004) A Cacna1a knockin migraine mouse model with increased susceptibility to cortical spreading depression. *Neuron* **41:** 701-710

van den Maagdenberg AM, Pizzorusso T, Kaja S, Terpolilli N, Shapovalova M, Hoebeek FE, Barrett CF, Gherardini L, van de Ven RC, Todorov B, Broos LA, Tottene A, Gao Z, Fodor M, De Zeeuw CI, Frants RR, Plesnila N, Plomp JJ, Pietrobon D, Ferrari MD (2010) High cortical spreading depression susceptibility and migraine-associated symptoms in Ca(v)2.1 S218L mice. *Ann Neurol* **67:** 85-98

Vecchia D, Pietrobon D (2012) Migraine: a disorder of brain excitatory–inhibitory balance? *Trends in Neurosciences* **35:** 507-520

Vecchia D, Tottene A, van den Maagdenberg AMJM, Pietrobon D (2014) Mechanism underlying unaltered cortical inhibitory synaptic transmission in contrast with enhanced excitatory transmission in CaV2.1 knockin migraine mice. *Neurobiology of Disease* **69:** 225-234

Vecchia D, Tottene A, van den Maagdenberg AMJM, Pietrobon D (2015) Cortical synaptic transmission in CaV2.1 knockin mice with the S218L missense mutation which causes a severe familial hemiplegic migraine syndrome in humans. *Frontiers in Cellular Neuroscience* **9**

Weigand KM, Swarts HGP, Russel FGM, Koenderink JB (2014) Biochemical characterization of sporadic/familial hemiplegic migraine mutations. *Biochimica et Biophysica Acta (BBA) - Biomembranes* **1838:** 1693-1700

Zhang X, Levy D, Kainz V, Noseda R, Jakubowski M, Burstein R (2011) Activation of central trigeminovascular neurons by cortical spreading depression. *Ann Neurol* **69:** 855-865

Zhang X, Levy D, Noseda R, Kainz V, Jakubowski M, Burstein R (2010) Activation of meningeal nociceptors by cortical spreading depression: implications for migraine with aura. *J Neurosci* **30:** 8807-8814

Zhao J, Levy D (2015) Modulation of intracranial meningeal nociceptor activity by cortical spreading depression: a reassessment. *J Neurophysiol* 113: 2778-2785

Zhou M, Xu G, Xie M, Zhang X, Schools GP, Ma L, Kimelberg HK, Chen H (2009) TWIK-1 and TREK-1 are potassium channels contributing significantly to astrocyte passive conductance in rat hippocampal slices. *J Neurosci* **29:** 8551-8564

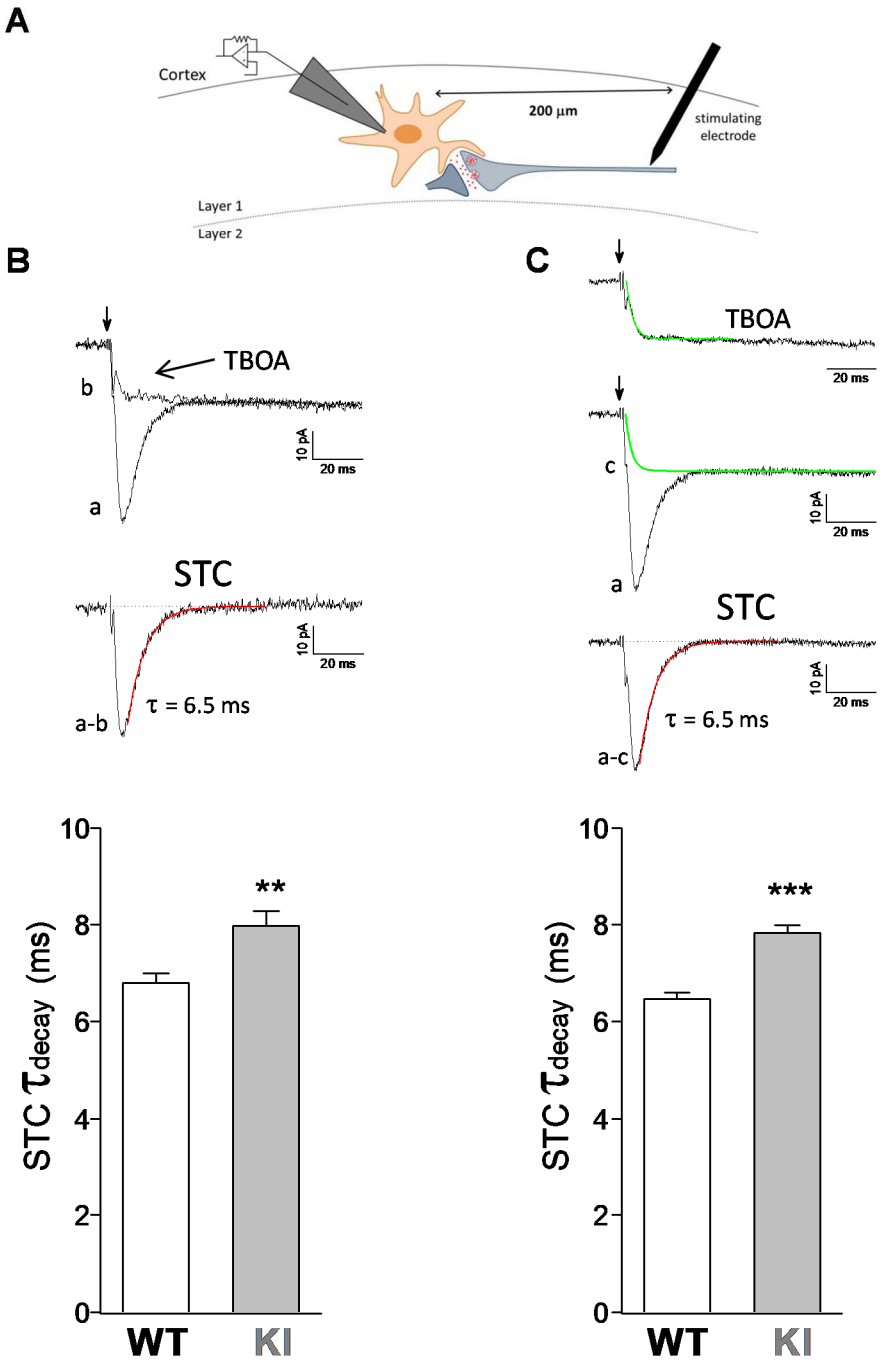
A
Cortex
200 µm
stimulating electrode
Layer 1
Layer 2
B
TBOA
b
a
10 pA
20 ms
STC
a-b
τ = 6.5 ms
C
TBOA
20 ms
c
a
STC
a-c
τ = 6.5 ms
STC τdecay (ms)
**
***
WT
KI

Figure 1

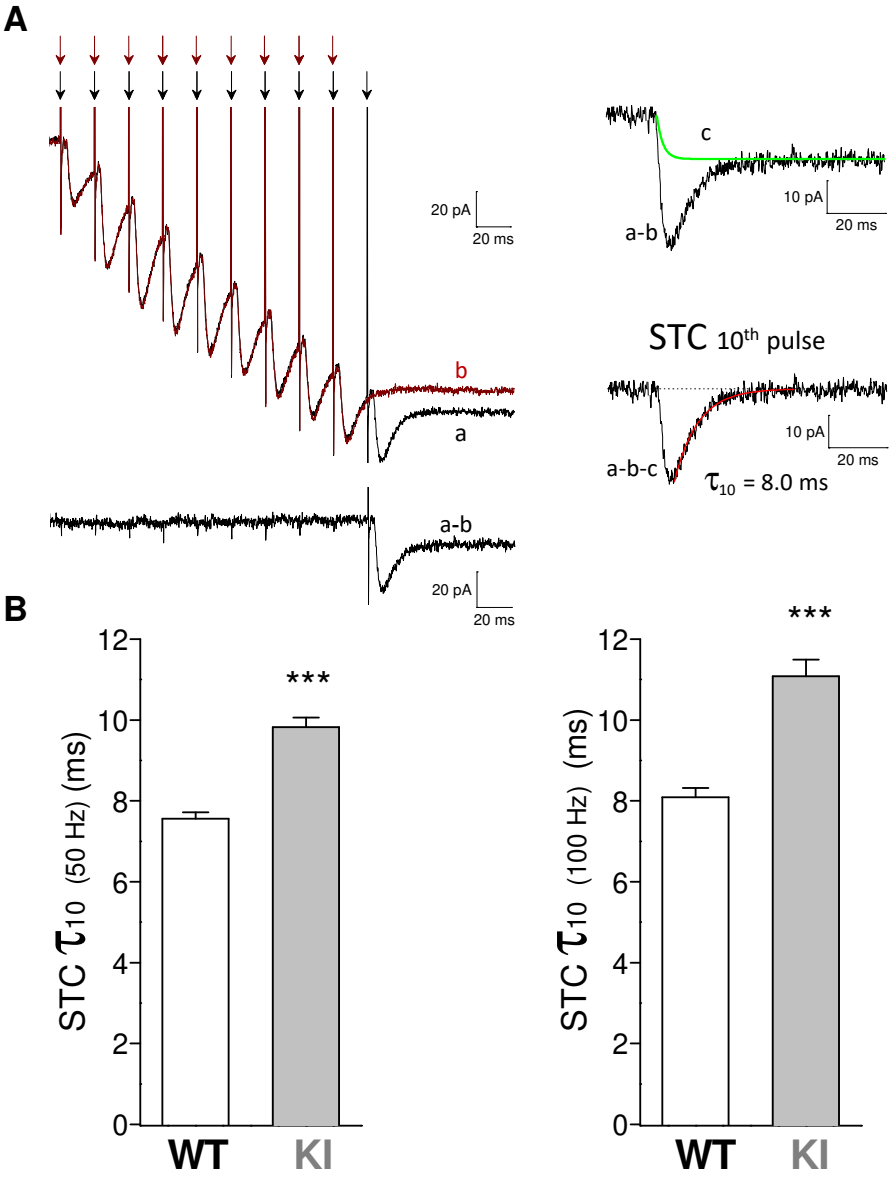
A
20 pA
20 ms
b
a
a-b
20 pA
20 ms
c
10 pA
20 ms
a-b
STC 10th pulse
10 pA
20 ms
a-b-c
τ10 = 8.0 ms
B
STC τ10 (50 Hz) (ms)
12
10
8
6
4
2
0
***
WT
KI
STC τ10 (100 Hz) (ms)
12
10
8
6
4
2
0
***
WT
KI

Figure 2

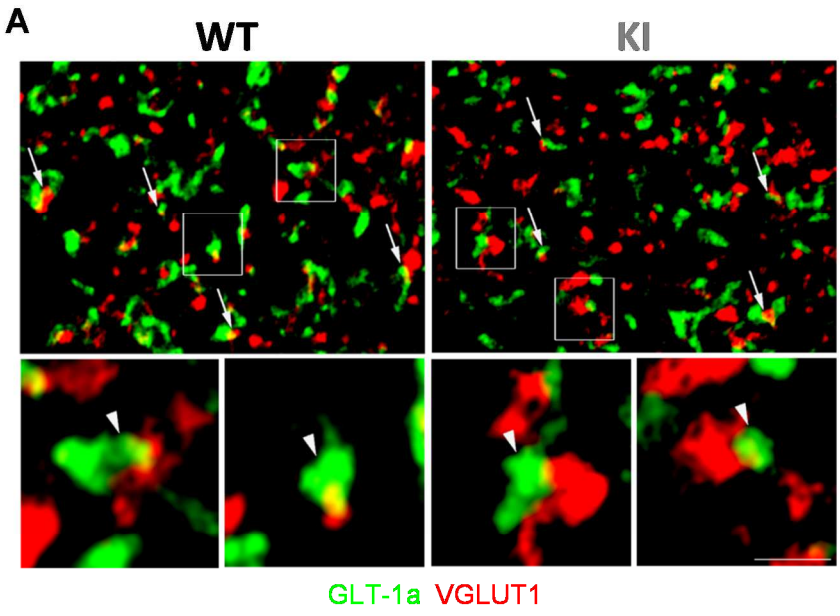
A
WT
KI
GLT-1a VGLUT1
B
% GLT-1a+ overlaying VGLUT1+
60
50
40
30
20
10
0
WT
KI
size GLT-1a+ overlaying VGLUT1+ (µm²)
0.6
0.4
0.2
0.0
*
WT
KI

Figure 3

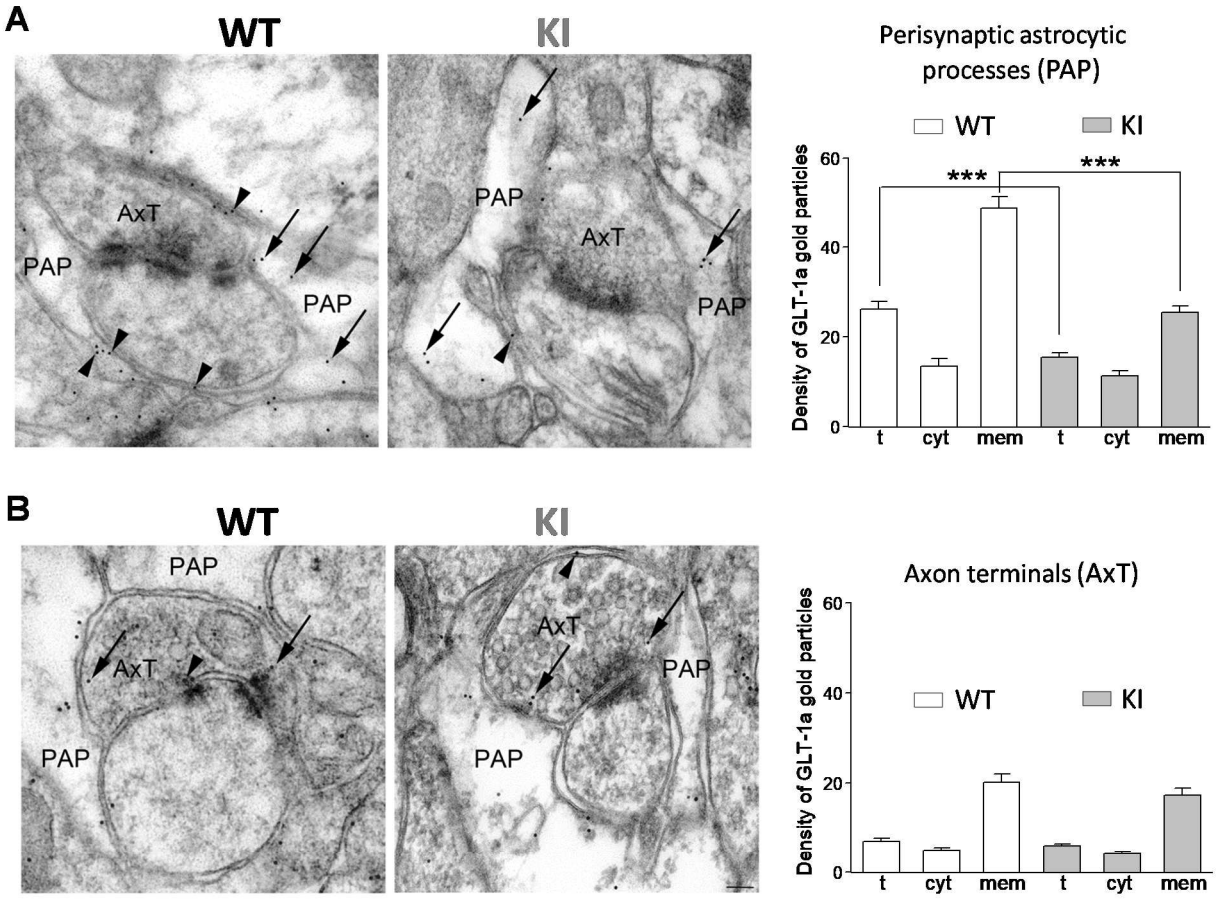
A
WT
KI
AxT
PAP
PAP
PAP
AxT
PAP
Perisynaptic astrocytic processes (PAP)
WT
KI
***
***
Density of GLT-1a gold particles
60
40
20
0
t
cyt
mem
t
cyt
mem
B
WT
KI
PAP
AxT
PAP
AxT
PAP
PAP
Axon terminals (AxT)
WT
KI
Density of GLT-1a gold particles
60
40
20
0
t
cyt
mem
t
cyt
mem

Figure 4

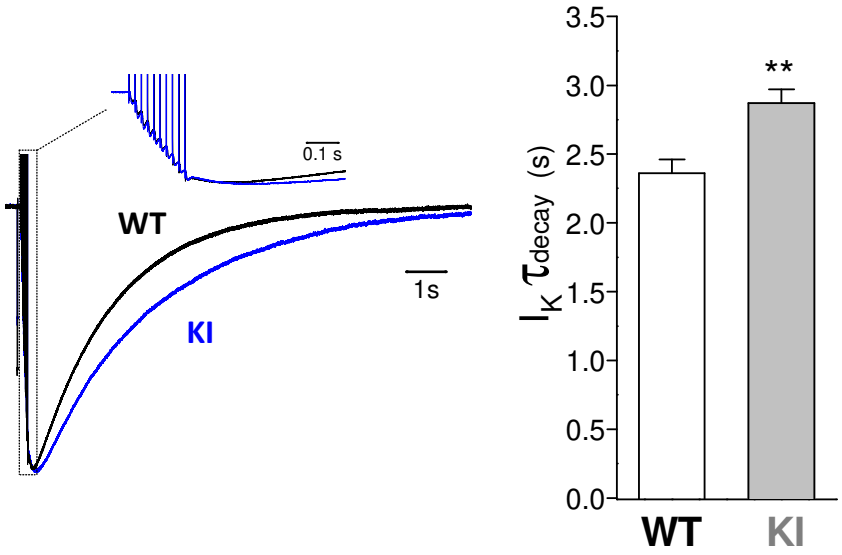

Figure 5

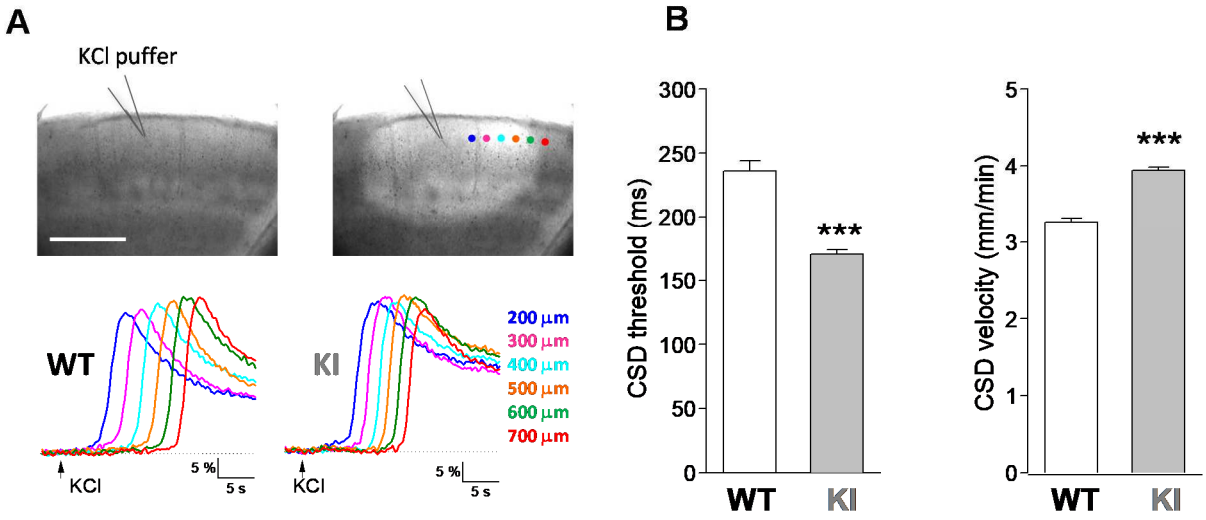
A
KCl puffer
WT
KI
200 µm
300 µm
400 µm
500 µm
600 µm
700 µm
KCl
5 %
5 s
KCl
5 %
5 s
B
CSD threshold (ms)
300
250
200
150
100
50
0
***
WT
KI
CSD velocity (mm/min)
5
4
3
2
1
0
***
WT
KI

Figure 6

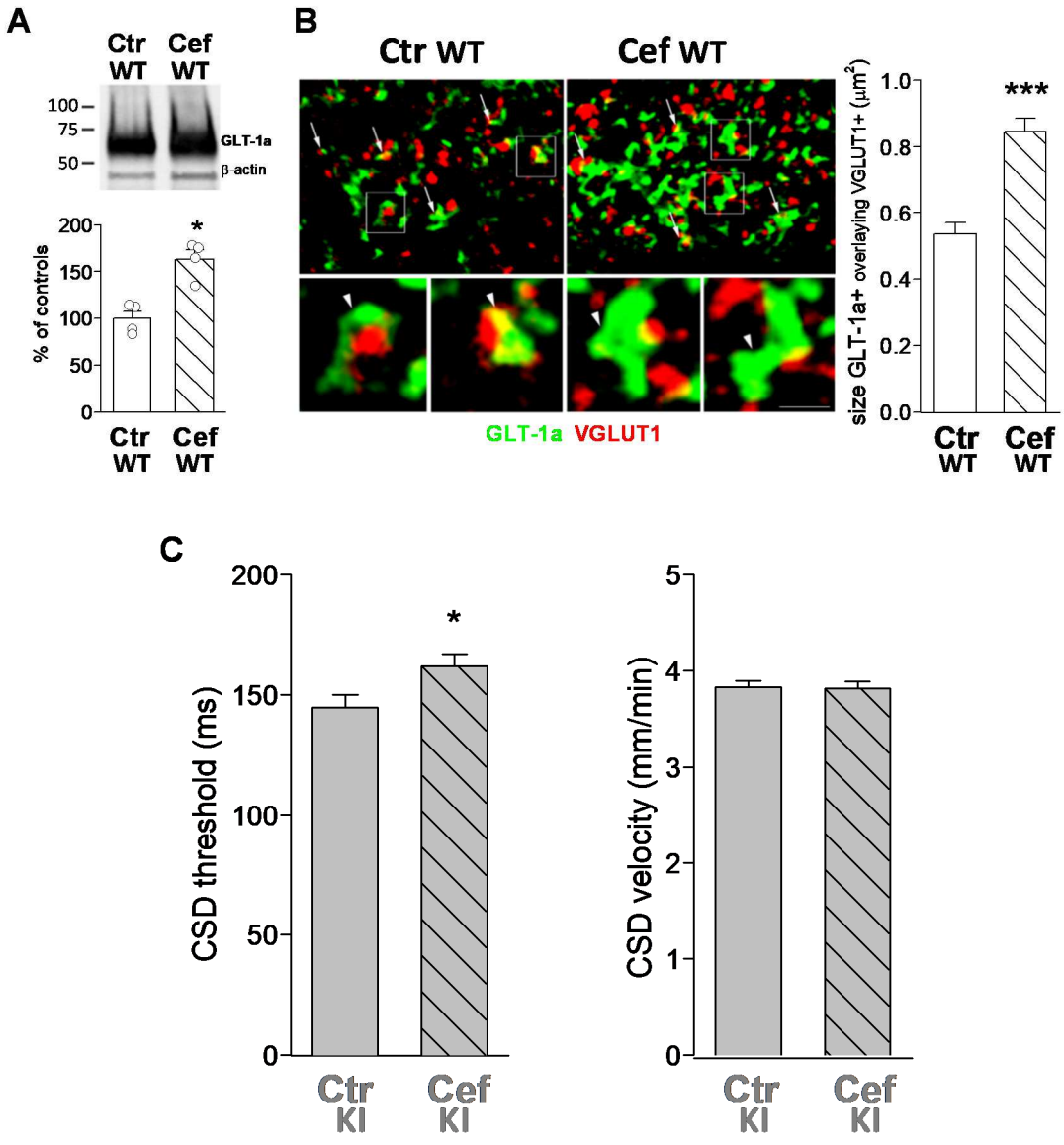
A
Ctr WT
Cef WT
100
75
50
GLT-1a
β-actin
200
150
100
50
0
% of controls
*
Ctr WT
Cef WT
B
Ctr WT
Cef WT
GLT-1a VGLUT1
size GLT-1a+ overlaying VGLUT1+ (µm²)
1.0
0.8
0.6
0.4
0.2
0.0
***
Ctr WT
Cef WT
C
CSD threshold (ms)
200
150
100
50
0
*
Ctr KI
Cef KI
CSD velocity (mm/min)
5
4
3
2
1
0
Ctr KI
Cef KI

Figure 7

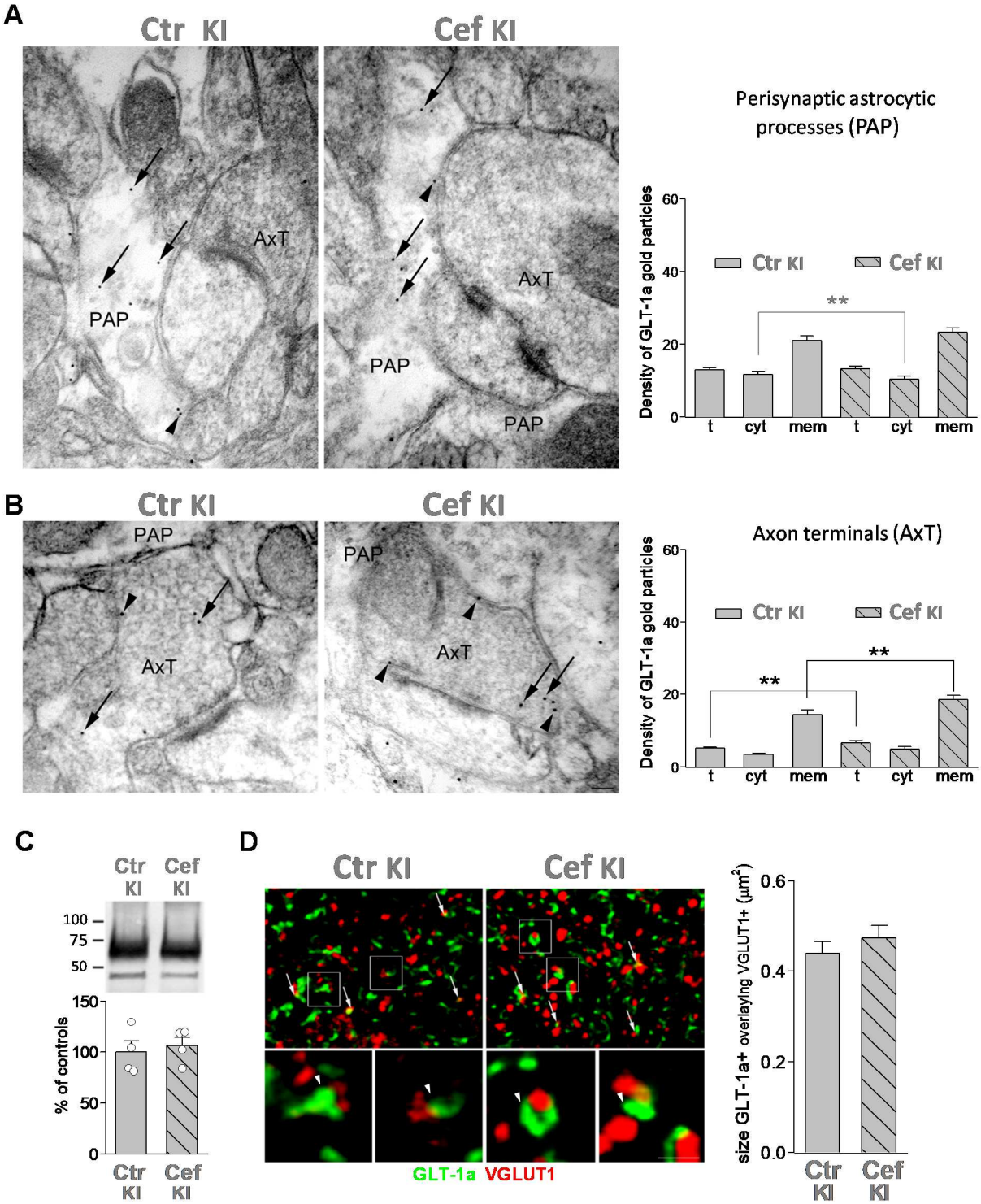
A
Ctr KI
Cef KI
AxT
PAP
AxT
PAP
PAP
Perisynaptic astrocytic processes (PAP)
Density of GLT-1a gold particles
60
40
20
0
Ctr KI
Cef KI
**
t
cyt
mem
t
cyt
mem
B
Ctr KI
Cef KI
PAP
AxT
PAP
AxT
Axon terminals (AxT)
Density of GLT-1a gold particles
60
40
20
0
Ctr KI
Cef KI
**
**
t
cyt
mem
t
cyt
mem
C
Ctr KI
Cef KI
100
75
50
150
100
50
0
% of controls
Ctr KI
Cef KI
D
Ctr KI
Cef KI
GLT-1a VGLUT1
size GLT-1a+ overlaying VGLUT1+ (µm²)
0.6
0.4
0.2
0.0
Ctr KI
Cef KI

Figure 8

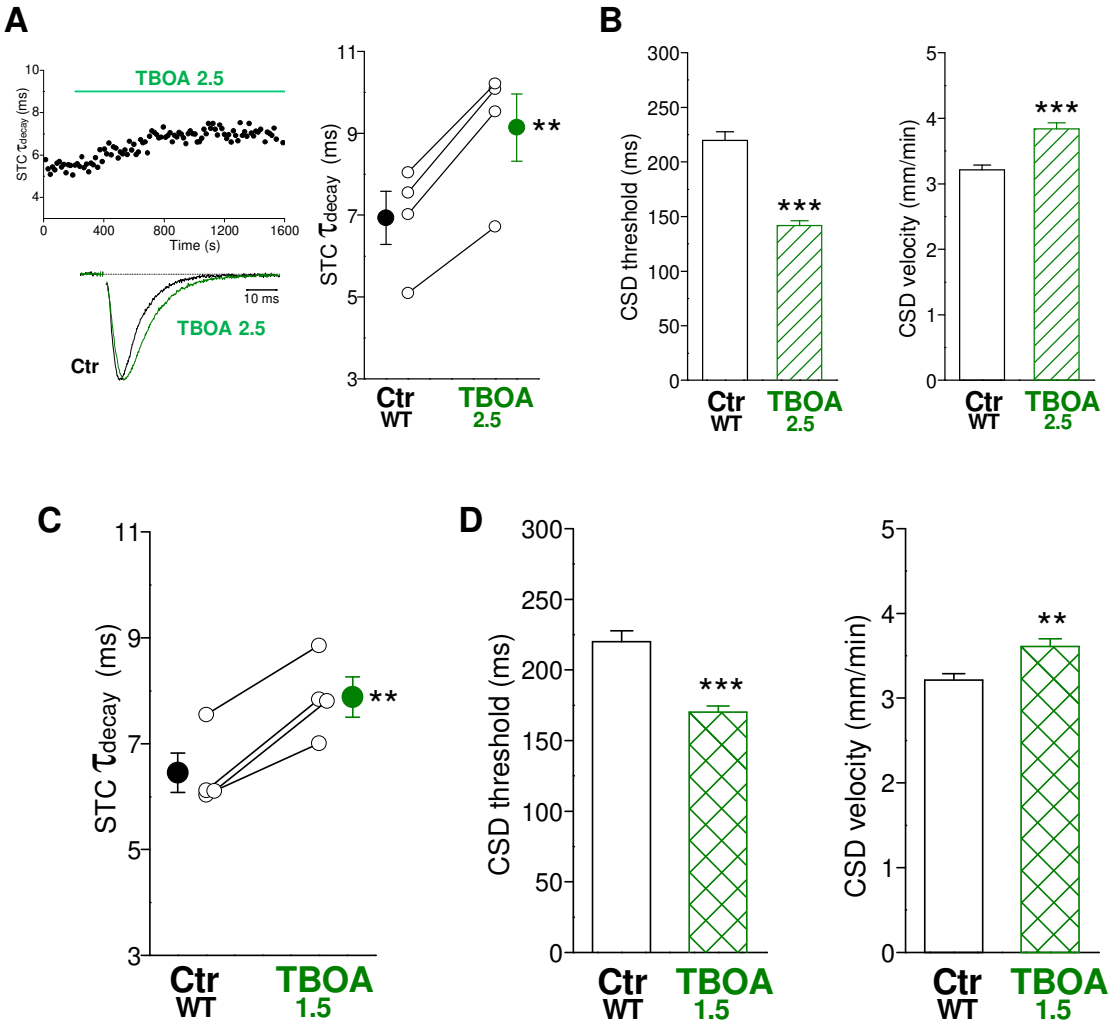
A
TBOA 2.5
STC τdecay (ms)
Time (s)
10 ms
TBOA 2.5
Ctr
STC τdecay (ms)
**
Ctr WT
TBOA 2.5
B
CSD threshold (ms)
***
Ctr WT
TBOA 2.5
CSD velocity (mm/min)
***
Ctr WT
TBOA 2.5
C
STC τdecay (ms)
**
Ctr WT
TBOA 1.5
D
CSD threshold (ms)
***
Ctr WT
TBOA 1.5
CSD velocity (mm/min)
**
Ctr WT
TBOA 1.5

Figure 9

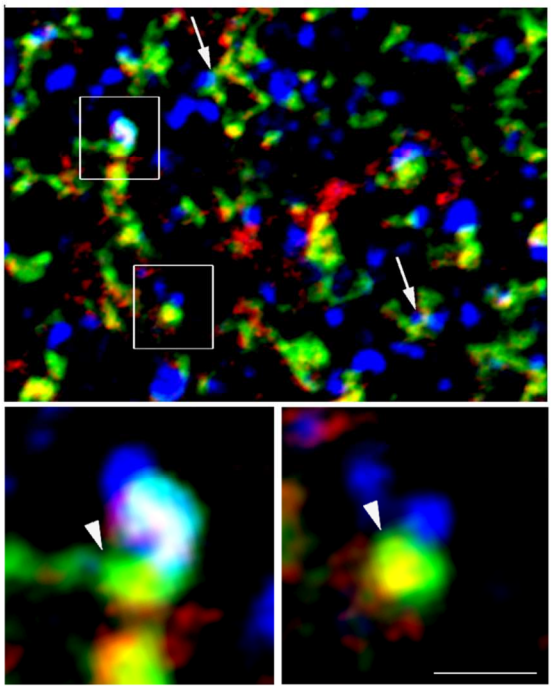

Expanded view figure 1

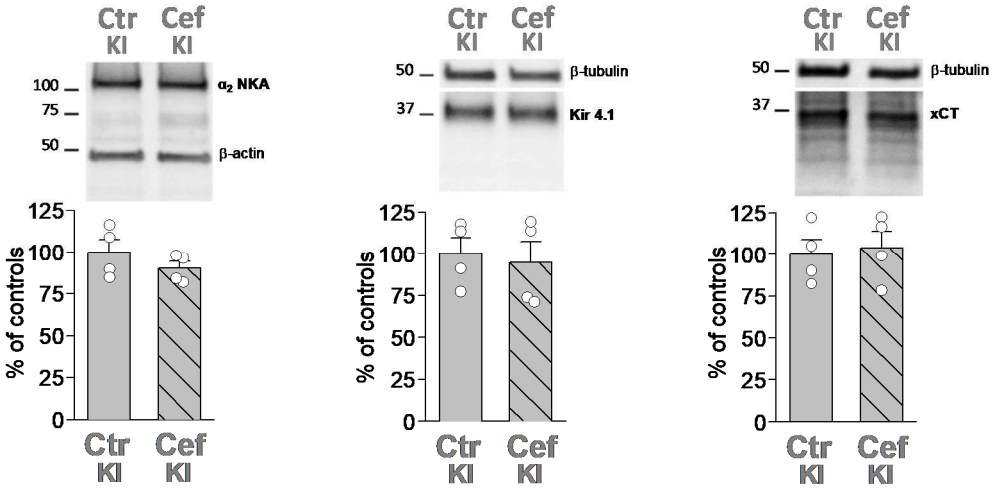

Expanded view figure 2

Table of content

Supplementary Figures

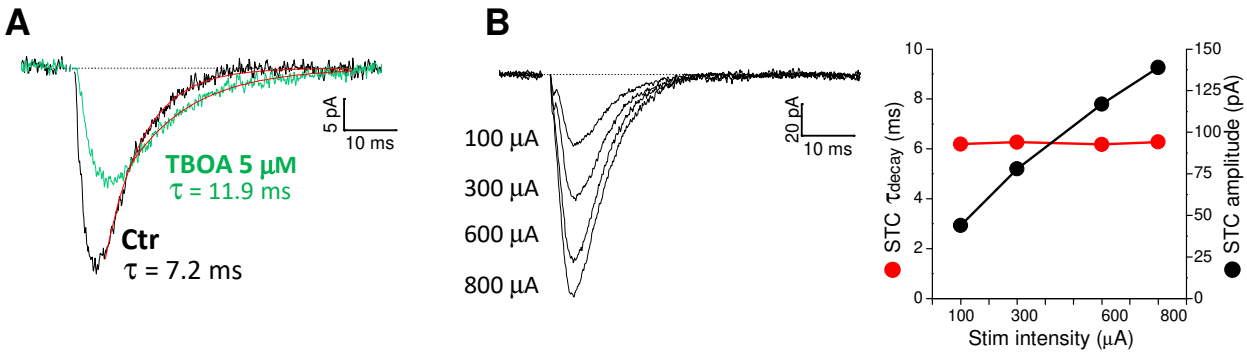

Supplementary figure 1

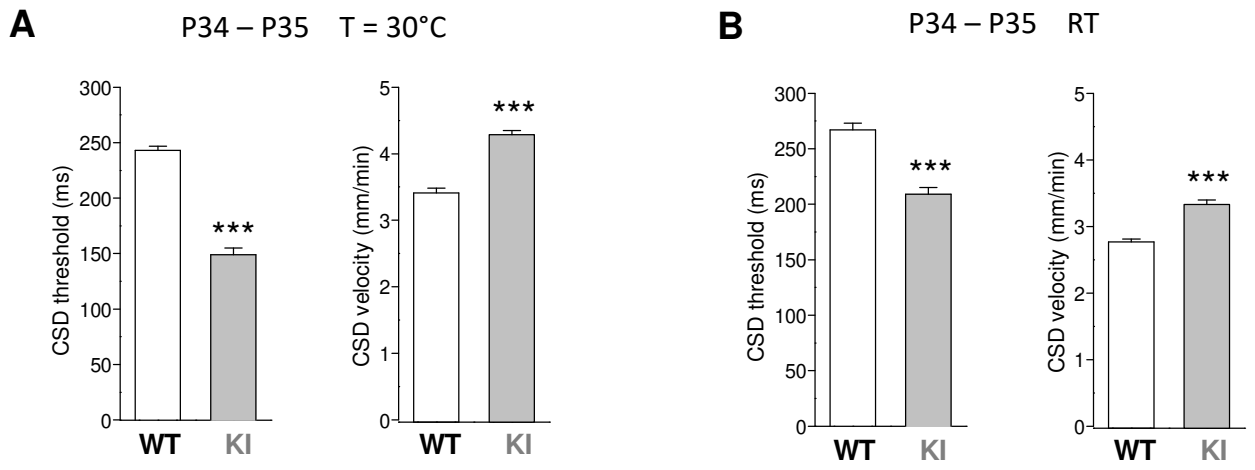

Supplementary Fig 2

Legends to supplementary Figures

Supplementary Figure 1. The decay kinetics of the STC reflect the rate of glutamate clearance by astrocytes and provide a measure of the rate of glutamate clearance which is independent of the amount of glutamate released.

(A) Inhibition of a fraction of glutamate transporters with DL-TBOA increases τ_{decay} of the STC elicited by single pulse stimulation in layer 1 astrocytes in WT cortical slices. In the representative experiment shown here, 5 µM DL-TBOA increased by 65% τ_{decay} of the STC (from 6.6 ms to 12.6 ms) and decreased the STC amplitude by 42%. The STC was isolated pharmacologically by subtracting the current recorded in the presence of saturating concentrations of DL-TBOA (100 µM) from the total control current and the total current recorded in the presence of 5 µM DL-TBOA (see Fig 1B of main text). P23 (n=3; N=2).

(B) Increasing the intensity of the extracellular stimulation increases the amplitude without affecting the decay kinetics of the STC elicited by single pulse stimulation in layer 1

astrocytes in WT cortical slice. STC traces at increasing intensity of extracellular stimulation (left) together with τ_{decay} and amplitude of the STC as a function of the intensity of stimulation (right) in a representative experiment in which the stimulation intensity was increased from 100 to 800 µA. The STC was isolated by subtracting from the total inward current an exponential waveform that approximates the average TBOA-insensitive current (see Fig 1C of main text). P21 (n=3; N=3).

Supplementary Figure 2. Facilitation of CSD induction and propagation in acute cortical slices of P34-35 W887R/+ FHM2 KI mice at different temperatures.

(A) CSD threshold and CSD velocity in WT (n = 20; N=3) and FHM2 KI (n = 26; N=4) cortical slices from P34-35 mice (T = 30 °C, flow rate 13 ml/min). CSD threshold is 39% lower in FHM2 KI relative to WT mice (149 ± 6 vs 243 ± 4 ms; Mann-Whitney U test, $P < 0.0001$). CSD velocity is 26% higher in FHM2 KI relative to WT mice (4.29 ± 0.06 vs 3.41 ± 0.07 mm/min; unpaired t test, $P < 0.0001$).

(B) CSD threshold and CSD velocity in WT (n = 15; N=2) and FHM2 KI (n = 17; N=2) cortical slices from P34-35 mice (room temperature, flow rate 3 ml/min). CSD threshold is 22% lower in FHM2 KI relative to WT mice (209 ± 6 vs 267 ± 6 ms; Mann-Whitney U test, $P < 0.0001$). CSD velocity is 20% higher in FHM2 KI compared to WT mice (3.33 ± 0.07 vs 2.77 ± 0.04 mm/min; unpaired t test: $P < 0.0001$).

Supplementary Discussion

A slowing of the Na^+-$HCO3^-$ cotransport is expected to increase activity-dependent alkaline shifts and, as a consequence, possibly lead to increased activation of NMDARs (CHESLER, 2003), thus providing an additional mechanism that could contribute to facilitate CSD in FHM2 KI mice. Given that the Na^+-Ca^{2+} exchanger (NCX) reversal potential lies close to the resting membrane potential, reduced expression of the α_2 NKA might favor the reverse mode of the NCX in FHM2 astrocytes, which could generate local Ca^{2+} increases in perisynaptic processes (where NCX is prominently localized: (Minelli et al, 2007)) and in the microdomains at the plasma membrane-endoplasmic reticulum (ER) junctions (where NCX colocalizes with α_2 NKA in cultured astrocytes: (Juhaszova & Blaustein, 1997)), hence increasing ER Ca content; this could result in increased release of gliotransmitters, including Glu, that might be involved in CSD facilitation. Interestingly, evidence for increased Ca^{2+} in the ER of astrocytes cultured from α2 NKA knockout mice has been reported (Golovina et al, 2003).

Finally, considering that the α2 NKA appears expressed primarily in neurons during embryonic development (Ikeda et al, 2003; Moseley et al, 2003), possible alterations of cortical network development produced by the FHM2 mutation and consequent effects on cortical synaptic function might be additional hypothetical mechanisms contributing to CSD facilitation in FHM2 KI mice.

However, as discussed in the main text, if present, the contribution of mechanisms involving Na+- dependent transporters (or deriving from hypothetical alterations of cortical network development) to the facilitation of CSD initiation is small and one should assume that they may contribute more to facilitation of CSD propagation.

Supplementary Materials and Methods

Acute slices preparation

Acute coronal slices of somatosensory cortex were prepared from wild-type (WT) and heterozygous W887R/+ knockin (KI) mice from the same litter as described in (Tottene et al, 2009). Briefly, animals were anestethized and decapitated. The brain was quickly removed and put in an ice-cold cutting solution (in mM: 130 K gluconate, 15 KCl, 0.2 EGTA, 20 HEPES, 25 glucose, 2 kynurenic acid, 5 x 10^{-5} minocycline, pH 7.4 with NaOH, oxygenated with 100% O_2) (Dugue et al, 2005). 350 µm-thick slices were then cut on the coronal plane with a vibratome (VT1200S, Leica Biosystems, Germany) and were transferred for 1 min in a solution containing (in mM) 225 D-mannitol, 2.5 KCl, 1.25 NaH_2PO_4, 26 $NaHCO_3$, 25 glucose, 0.8 $CaCl_2$, 8 $MgCl_2$, 2 kynurenic acid, 5 x 10^{-5} minocycline, saturated with 95% O_2 and 5% CO_2. Slices were then maintained at 30 °C for 30 min in standard artificial cerebrospinal fluid saturated with 95% O_2 and 5% CO_2 (sACSF in mM: 125 NaCl, 2.5 KCl, 25 $NaHCO_3$, 1.25 NaH_2PO_4, 1 $MgCl_2$, 2 $CaCl_2$, 25 glucose) plus 50 nM minocycline, and then transferred at room temperature in the same solution for a minimum of 30 min.

Acute cortical slices prepared as described above were used for measurement of either the current elicited in layer 1 astrocytes by extracellular stimulation (comparison WT vs KI) or of threshold and velocity of cortical spreading depression induced by high KCl pulses (comparison WT vs KI or ceftriaxone-treated vs untreated). In most CSD measurements (including all those testing the ceftriaxone effect) the investigator was blinded to the genotype. The investigator was not blinded to the genotype in the astrocyte current measurements.

Cortical spreading depression

Cortical spreading depression was elicited and measured in acute coronal slices of the somatosensory cortex of WT and FHM2 KI mice as in (Tottene et al, 2009), but most recordings were at 30°C rather than room temperature and the rate of perfusion of the slices was higher. Briefly, the brain slices were placed into a submersion chamber and continuously perfused with fresh extracellular solution (as that used for astrocyte patch-clamp recordings but with 3.5 mM KCl) at 30 °C at a flow rate of 6 mL/min (unless otherwise specified), and pressure-ejection pulses of 3 M KCl (0.5 bar) of increasing duration (at 5 min intervals in 20 ms steps) were applied through a glass micropipette (R = 0.19-0.25 MΩ) onto the slice surface on layer 2/3, using a PDES-02DX pneumatic drug ejection system (Npi Electronic GmbH, Tamm, Germany), until a CSD was elicited. CSD was detected by monitoring the associated change in intrinsic optical signal (IOS). The duration of the first pulse eliciting a CSD was taken as CSD threshold and the rate of horizontal spread of the change in IOS as CSD velocity. IOS was recorded using a CCD camera (KP-M2A, Hitachi, Tokio, Japan) connected with an upright microscope (Nikon Eclipse; 10X magnification, Nikon, Tokio, Japan). Images were recorded at 200 ms intervals as 640 x 480 pixels images (pixel size: 2.15 µm). MBF ImageJ software was used for the off line analysis of the digitalized images. The IOS change is expressed as percent change in light trasmittance (ΔT) relative to the background signal: %ΔT/T.

All CSD experiments and analyses in saline-treated and cef-treated mice and most of the CSD experiments in WT and KI mice were performed by a blinded observer.

Immunocytochemical studies

Immunofluorescence. After washing in PB, sections to be used for GLT-1/VGLUT1 double-labeling studies were directly incubated in 10% normal goat serum (NGS) in PB (1 h), whereas those to be used for GLT-1a/α_2/VGLUT1 triple-labeling studies were pre-treated

with 10%, 20% and 10% alcohol in PB (5 min each) and then incubated in NGS. Then, sections were exposed (2 h at RT and then overnight at 4 C°) to a solution containing a mixture of antibodies directed against the synthetic peptide corresponding to AA 559-573 (SADCSVEEEPWKREK) of GLT-1a rat C-terminus (0.3 µg/mL; made in rabbit) kindly provided by Dr J.D. Rothstein, Johns Hopkins University, Baltimore, MD (Omrani et al, 2009; Rothstein et al, 1994) and raised against a C-terminus synthetic peptide of rat VGLUT1 protein (GATHSTVQPPRPPPPVRDY) (1:800; made in guinea pig; AB5905, Merck Millipore, Billerica, MA; Melone et al., 2005) for double-labeling studies, or to a solution containing a mixture of antibodies direct against a synthetic peptide corresponding to AA 554–573 (AANGKSADCSVEEEPWKREK) of GLT-1a rat C-terminus (1: 250; made in guinea pig, AB1783, Merck Millipore; (DeSilva et al, 2012)), against a synthetic peptide corresponding to AA 432-445 of human α_2 Na^+,K^+ ATPase (CKAGQENISVSKRDT; immunizing sequence is identical in rat and mouse; 1:200, made in rabbit; AB07-674, Merck Millipore), and against Strep-Tag® fusion protein of the rat VGLUT1 (AA 456-560), specific for rat and mouse VGLUT1 (1:50, made in mouse; Synaptic System, Goettingen, Germany) for triple-labeling studies. Sections were washed and incubated in 10% NGS in PB (15 min) and then in a solution containing a mixture of affinity-purified Alexa 488- (1:250; 111-545-003, Jackson ImmunoResearch Europe, Ltd, Suffolk, UK) or Alexa 555- (1:250; TRITC, T-2762/6691-11:250; Molecular Probes, PoortGebouw, The Netherlands)-conjugated secondary antibodies made in goats (90 min) for double-labeling studies or Alexa 488-555- and 647-(1:200, Jackson) conjugated secondary antibodies made in goats for triple-labeling studies. Sections were washed, mounted, air-dried, and coverslipped using Vectashield mounting medium (H-1000; Jackson), and finally examined with a Leica confocal laser microscope (TCS SP2; Leica Microsystems, Wetzlar, Germany). Control experiments with single-labeled sections and sections incubated with two or three primary antibodies and one secondary antibody or with one primary and two or three secondary

antibodies revealed neither bleed-through nor cross-reactivity.

Confocal microscopy and data analysis. Microscopic fields from layers II/III of SI were randomly collected. Analysis of positive (+) puncta (i.e. GLT-1a, VGLUT1+ puncta in double-labeled material and GLT-1a, α_2, VGLUT1+ puncta in triple-labeled material) was performed in randomly selected subfields of 20 × 20 μm. Images of selected subfields were processed according to (Melone et al, 2005). The percentage of GLT-1a in close relationship with excitatory terminals in WT and FHM2 mice was estimated by the number of GLT-1a+ puncta overlapping with VGLUT1+ puncta: the channel corresponding to GLT-1a was examined first and all positive puncta were identified; the channel corresponding to VGLUT1 was viewed next and the presence or absence of overlap was noted (Melone et al, 2009). For GLT-1a/α_2/VGLUT1 analysis in WT mice, before examining the overlap between GLT-1a and VGLUT1, the presence or the absence of colocalization of GLT-1a with α_2 was noted. Finally, size of GLT-1a+ puncta overlaying with VGLUT1 was calculated in all subfields of double-labeled material from all experimental groups (Bozdagi et al, 2000; Bragina et al, 2006). Statistical analysis was performed using GraphPrism v.4.0 (GraphPad Software, La Jolla, CA); a = 0.05.

Equipment, settings and image analysis. For confocal microscopy a TCS SL Leica confocal microscope (Leica Microsystems, Wetzlar, Germany) coupled with a Leica Microsystem Confocal software v.2.61 and equipped with Argon and He-Neon lasers, was used to acquire double-and triple-labeled microscopical fields. Each fluorescent was acquired separately as 512 x 512 pixel images (pixel size of 120 nm) with a planapo x63 objective (numerical aperture 1.4) and pinhole 1.0 Airy unit and with a xy scan mode. Excitation and emission wavelenghts of fluorochromes used were: 488 and 490-540, 543 and 570-630, 633 and 670-800 respectively for green (Alexa 488), red (cy-3 and Alexa

555) and blue (Alexa 647) fluorescents. Original images collected on the surface of stained sections (Melone et al., 2005) were in color scale method (tiff format), 8 bit/channel with an original resolution of 72 dpi (512 x 512 pixels; 18.06 x 18.06 cm).

For each acquired field, a merged image (called composite) was obtained using ImageJ v.1.46r (NIH, USA). Then, randomly selected subfields of 20 × 20 μm were obtained (by ImageJ) from the composite image and, analysis of positive (+) puncta (i.e. GLT-1a, VGLUT1+ puncta in double-labeled material and GLT-1a, α_2, VGLUT1+ puncta in triple-labeled material) was performed (all steps indicate below were performed by ImageJ). The analysis of the selected subfields, required several steps of processing, according to previous studies (Melone et al, 2005). Optimal visualization of punctate staining (good separation between contiguous puncta, along with clear contours for each immunopositive puncta) was achieved by setting a threshold for each color channel to the mean pixel value over the field under study (as previously reported, this is a reliable procedure; indeed with threshold values set anywhere between 0.5 and 2 times the mean pixel brightness had virtually no influence on the extent of overlay between puncta) (Melone et al, 2005). In particular, for studying the size of GLT-1/VGLUT-1 related puncta, threshold was set at 1 times the mean pixel brightness of each color channel and applied to all field for GLT-1a and VGLUT1 and for control and experimental groups. Thresholded images were converted to binary images (binary.tif images), watershed function applied and GLT-1a+ puncta overlapping with VGLUT1+ puncta identified by the observer (using yellow pixels as a sign of overlay). From binary images, size of GLT-1a+ puncta (in pixels) was determined by ImageJ functions (software automatically excluded puncta on the edges of fields and puncta below 5 pixels). Then, size of puncta was converted in μm^2 based on the pixel size of acquisition.

Image processing for final illustrations. For final qualitative high resolution illustrations of double- and triple-labeled fields representative of data obtained, original merged

composite (in color scale method, see above) images were converted into RGB method (tiff format; 8 bit/channel) by ImageJ. Then, using Adobe Photoshop CS5 extended (v.12.1), RGB images were properly dimensioned and converted into high resolution images (600 dpi; tiff format, 8 bit/channel). Selected areas of interest were cropped and levels of each color channel of final images were obtained by using the level function; for each color channel a threshold was applied to all field based on its mean pixel brightness (consistently with the method used to quantify puncta; see above).

Immunogold. For epoxy embedding, dehydrated sections were immersed in propylene oxide, infiltrated with an Epon/Spurr resin mixture, sandwiched between Aclar films, and polymerized at 60°C for 48 h. Chips including layers II/III of SI cortex (at least 2/animal), were cut and sectioned, and ultrathin sections (60–80 nm) were mounted on nickel grids. All rinse and diluent solutions were filtered through a 0.45 µm membrane filter before use. To minimize the effects of procedural variables, post-embedding procedure of grids from WT and KI groups and then from KI saline and KI Cef groups was performed in parallel. Briefly, after treatment with 1% para-phenyenediamine in Tris-buffered saline (0.1 M Tris, pH 7.6, with 0.005% Tergitol N P-10 (TBST)), grids were washed in distilled water, incubated for 15 min in blocking solution (1% bovine serum albumine (BSA) in TBST, pH 7.6) and then transferred in TBST (pH 7.6) solution containing GLT-1a made in rabbit primary antibodies (6 µg/mL). The next day, grids were washed in TBST pH 7.6, incubated for 15 min in blocking solution (1% BSA in TBST pH 8.2), transferred to TBST (pH 8.2; 2 h) containing secondary antibodies conjugated to 12 nm gold particles (1:20; 111-205-144, Jackson), washed, stained with uranyl acetate and Sato's lead, and examined with a Philips EM 208 and CM10 electron microscope (Eindhoven, The Netherlands) coupled to a MegaView-II high resolution CCD camera (Soft Imaging System, Münster, Germany). Gold

particles were not detected when the primary antiserum was omitted; when normal serum was substituted for the immune serum, parse and scattered particles were observed. Optimal concentration of anti-GLT-1a antibodies was sought by testing several dilutions; the concentration yielding the lowest background labeling and immunopositive elements was used for final studies.

Electron microscopy and data analysis. Microscopic fields (original magnification: 50000–85000X; at least 80-100 fields/animal from 10-15 ultrathin sections/animal) were selected when they included at least one immunolabeled astrocytic profile and/or axon terminal associated with an asymmetric synapse with a clear active zone–postsynaptic density complex (Tyler & Pozzo-Miller, 2001). Background was calculated by estimating labeling density over nuclei (Racz & Weinberg, 2004). For determining the relative density of GLT-1a, gold particles within astrocytic profiles, axon terminals and cell nuclei were counted and areas calculated. Gold particles were considered membrane-associated if they were within 15 nm of its extracellular side, and cytoplasmic if they were > 25 nm from the membrane extracellular side (Melone et al, 2009). Comparison of particle densities (i.e., background, total, cytoplasmic and membrane-associated densities) of immunopositive profiles between WT and FHM2 and between FHM2 saline and cetriaxone groups was then performed using GraphPrism.

Equipment, settings and image analysis. For electron microscopy, Philips EM 208 and CM10 electron microscopes (Eindhoven, The Netherlands) coupled to a MegaView-II high resolution CCD camera with Soft Imaging System (Münster, Germany) and iTEM software v 5.1 (Olympus Soft Imaging Solutions, GmbH) were used to acquire microscopical fields from immunogold processed ultrathin sections. Original collected images were in gray scale method (jpg format), 8 bit/channel with an original resolution of 150 dpi (1376 x 1032 pixels; 23.3 x 17.48 cm) for those of the Philips EM 208, and of 300 dpi (2048 x 2048

pixels; 17.34 x 17.34 cm) for those of CM10. For determining the relative density of GLT-1a gold particles, original images were opened with ImageJ; set scale function was applied and then total, cytoplasmic and membrane areas of profiles were calculate, gold particles within the areas counted and data collected.

Image processing for final illustrations. For final qualitative high resolution illustrations of fields representative of data obtained, original images were properly dimensioned and converted into high resolution images (600 dpi; gray scale method, tiff format, 8 bit/channel) by using Adobe Photoshop CS5 extended (v.12.1). Selected areas of interest were cropped and gray levels of final images, were obtained by using the level function with minimal degree of processing.

Western blotting

Total amount of protein in cortical crude synaptic membranes was determined according to the Bradford method (Bradford, 1976) using the Bio-Rad Protein Assay (Bio-Rad Laboratories, GmbH, Munchen, Germany) and a Beckman DU 530 spectrophotometer (Beckman Coulter, Fullerton, CA; 3–4 measurements/homogenate). A standard curve with 2-10 µg of bovine serum albumin was drawn for each dosing run. Curves of increasing concentration were drawn to define a linear range for densitometric analysis (Bragina et al, 2006). Aliquots of homogenates were subjected to SDS-PAGE (3 µg of total protein [tp] for GLT-1 studies; 7 of [tp] for α_2 Na^+,K^+ ATPase studies; and 5 of [tp] for both xCT and Kir4.1 studies). To control potein loading, β-actin and β-tubulin were used as housekeeping proteins (Li & Shen, 2013). Based on the known molecular weight of each protein studied and to avoid possible overlaps between bands, β-actin was used as housekeeping protein for GLT-1a and α_2 Na^+,K^+ ATPase studies, whereas β-tubulin for xCT, and Kir4.1 experiments. Separated proteins were electroblotted onto nitrocellulose

filters, which were initially washed in phosphate buffered saline with 0.1% Tween 20 (PBS-T; pH7.4); subsequently, they were exposed first to a blocking buffer solution (5% Bio-Rad non-fat dry milk in PBS-T; 1 h), and incubated (2 h at room temperature and then overnight at 4°C) in a solution of 0.1% BSA in PBS-T containing anti-GLT-1a made in rabbit (0.12 µg/ml) and anti-β-actin made in mouse (1:5000; A5441, Sigma-Aldrich, St Louis, MO), or anti-α_2 Na^+,K^+ ATPase made in rabbit (1:350; Merck-Millipore) and anti-β–actin made in mouse (1:5000) primary antibodies, or anti-xCT made in rabbit (1:250; ab93030, Abcam; Cambrige, UK; raised against a synthetic peptide corresponding to N-terminal residues (between 1-50) of mouse xCT; (Van Liefferinge et al, 2016)) and anti-β-tubulin made in mouse (1:2000; T5293, Sigma-Aldrich) primary antibodies or anti-Kir4.1 (1:700; H00003766-M01, Novus Biological, Abingdon, UK; raised against KCNJ10 (NP_002232, A.A.276-380) partial recombinant protein with GSTtag (DFELVLILSGTVESTSATCQVRTSYLPEEILWGYEFTPAISLSASGKYIADFSLFDQVVKVA SPSGLRDSTVRYGDPEKLKLEESLREQAEKEGSALSVRISNV); (Tong et al, 2014)) and anti-β-tubulin made in mouse (1:2000) primary antibodies. The following day, filters were washed with PBS-T and then exposed to appropriate secondary antibodies (Jackson) dissolved in PBS-T. Bands were visualized by the SuperSignal West Pico chemiluminescent substrate (Bragina et al., 2006). Homogenates from each animal were experimented 4-6 times for each antigen. Intensity data were calculated as ratios of GLT1a/β-actin, α_2 Na^+,K^+ ATPase/β-actin, xCT/β-tubulin, and Kir4.1/β-tubulin (Alhaddad et al, 2014; Melzer et al, 2008). Comparison between saline and cetriaxone measures for each antigen was performed using GraphPrism.

Acquisition and quantification of bands. Immnunoreactive bands were visualized by Bio-Rad Chemidoc and Quantity One software v.4.1. Optimal time of exposure during acquisition, was set for each antigen based on the appearance of few saturated pixel in

immunoreactive bands with a visible gray background. For GLT-1a and α_2 Na^+,K^+ ATPase studies, optimal exposure time for GLT-1a and α_2 Na^+,K^+ ATPase corresponded to that of β-actin detection whereas for both xCT and Kir4.1, exposure time was different to that of β-tubulin detection (for this reason illustrative images of western blottings of GLT-1a and α_2 Na^+,K^+ ATPase and β-actin there is no cropping between bands, whereas for those of xCT and Kir4.1 and β-tubulin there is cropping between bands). Original images of acquisition (1sc format) were used to quantify the intensity of bands by Quantity One tools. Collected values were used to calculate ratios of GLT1a/βactin, α_2 Na^+,K^+ ATPase/β-actin, xCT/β-tubulin, and Kir4.1/β-tubulin.

Image processing for final illustrations. Original images (1sc format) were exported in tiff format (resolution of 97.5 dpi, gray scale method, 8 bit/channel, 20 x 13.3 cm) by Quantity One software. For final qualitative illustrations of data, original images were properly cropped (without excluding additional bands), dimensioned and converted into high resolution images (600 dpi; gray scale method, tiff format, 8 bit/channel) by using Adobe Photoshop CS5 extended (v.12.1). Gray levels of final images, were obtained by using the level function with minimal degree of processing.

References

Alhaddad H, Das SC, Sari Y (2014) Effects of ceftriaxone on ethanol intake: a possible role for xCT and GLT-1 isoforms modulation of glutamate levels in P rats. *Psychopharmacology* **231:** 4049-4057

Bozdagi O, Shan W, Tanaka H, Benson DL, Huntley GW (2000) Increasing numbers of synaptic puncta during late-phase LTP: N-cadherin is synthesized, recruited to synaptic sites, and required for potentiation. *Neuron* **28:** 245-259

Bragina L, Melone M, Fattorini G, Torres-Ramos M, Vallejo-Illarramendi A, Matute C, Conti F (2006) GLT-1 down-regulation induced by clozapine in rat frontal cortex is associated with synaptophysin up-regulation. *J Neurochem* **99:** 134-141

CHESLER M (2003) Regulation and Modulation of pH in the Brain. *Physiological Reviews* **83:** 1183-1221

DeSilva TM, Borenstein NS, Volpe JJ, Kinney HC, Rosenberg PA (2012) Expression of EAAT2 in neurons and protoplasmic astrocytes during human cortical development. *J Comp Neurol* **520:** 3912-3932

Dugue GP, Dumoulin A, Triller A, Dieudonne S (2005) Target-dependent use of co-released inhibitory transmitters at central synapses. *J Neurosci* **25:** 6490-6498

Golovina VA, Song H, James PF, Lingrel JB, Blaustein MP (2003) Na+ pump alpha 2-subunit expression modulates Ca2+ signaling. *Am J Physiol Cell Physiol* **284:** C475-486

Ikeda K, Onaka T, Yamakado M, Nakai J, Ishikawa TO, Taketo MM, Kawakami K (2003) Degeneration of the amygdala/piriform cortex and enhanced fear/anxiety behaviors in sodium pump alpha2 subunit (Atp1a2)-deficient mice. *J Neurosci* **23:** 4667-4676

Juhaszova M, Blaustein MP (1997) Na+ pump low and high ouabain affinity alpha subunit isoforms are differently distributed in cells. *Proc Natl Acad Sci U S A* **94:** 1800-1805

Li R, Shen Y (2013) An old method facing a new challenge: Re-visiting housekeeping proteins as internal reference control for neuroscience research. *Life Sciences* **92:** 747-751

Melone M, Bellesi M, Conti F (2009) Synaptic localization of GLT-1a in the rat somatic sensory cortex. *Glia* **57:** 108-117

Melone M, Burette A, Weinberg RJ (2005) Light microscopic identification and immunocytochemical characterization of glutamatergic synapses in brain sections. *J Comp Neurol* **492:** 495-509

Melzer N, Meuth SG, Torres-Salazar D, Bittner S, Zozulya AL, Weidenfeller C, Kotsiari A, Stangel M, Fahlke C, Wiendl H (2008) A ?-Lactam Antibiotic Dampens Excitotoxic Inflammatory CNS Damage in a Mouse Model of Multiple Sclerosis. *PLoS ONE* **3:** e3149

Minelli A, Castaldo P, Gobbi P, Salucci S, Magi S, Amoroso S (2007) Cellular and subcellular localization of Na+–Ca2+ exchanger protein isoforms, NCX1, NCX2, and NCX3 in cerebral cortex and hippocampus of adult rat. *Cell Calcium* **41:** 221-234

Moseley AE, Lieske SP, Wetzel RK, James PF, He S, Shelly DA, Paul RJ, Boivin GP, Witte DP, Ramirez JM, Sweadner KJ, Lingrel JB (2003) The Na,K-ATPase alpha 2 isoform is expressed in neurons, and its absence disrupts neuronal activity in newborn mice. *J Biol Chem* **278:** 5317-5324

Omrani A, Melone M, Bellesi M, Safiulina V, Aida T, Tanaka K, Cherubini E, Conti F (2009) Up-regulation of GLT-1 severely impairs LTD at mossy fibre--CA3 synapses. *J Physiol* **587:** 4575-4588

Racz B, Weinberg RJ (2004) The subcellular organization of cortactin in hippocampus. *J Neurosci* **24:** 10310-10317

Rothstein JD, Martin L, Levey AI, Dykes-Hoberg M, Jin L, Wu D, Nash N, Kuncl RW (1994) Localization of neuronal and glial glutamate transporters. *Neuron* **13:** 713-725

Tong X, Ao Y, Faas GC, Nwaobi SE, Xu J, Haustein MD, Anderson MA, Mody I, Olsen ML, Sofroniew MV, Khakh BS (2014) Astrocyte Kir4.1 ion channel deficits contribute to neuronal dysfunction in Huntington's disease model mice. *Nat Neurosci* **17:** 694-703

Tottene A, Conti R, Fabbro A, Vecchia D, Shapovalova M, Santello M, van den Maagdenberg AMJM, Ferrari MD, Pietrobon D (2009) Enhanced Excitatory Transmission at Cortical Synapses as the Basis for Facilitated Spreading Depression in Ca(v)2.1 Knockin Migraine Mice. *Neuron* **61:** 762-773

Tyler WJ, Pozzo-Miller LD (2001) BDNF enhances quantal neurotransmitter release and increases the number of docked vesicles at the active zones of hippocampal excitatory synapses. *J Neurosci* **21:** 4249-4258

Van Liefferinge J, Bentea E, Demuyser T, Albertini G, Follin-Arbelet V, Holmseth S, Merckx E, Sato H, Aerts JL, Smolders I, Arckens L, Danbolt NC, Massie A (2016) Comparative analysis of antibodies to xCT (Slc7a11): Forewarned is forearmed. *Journal of Comparative Neurology* **524:** 1015-1032

1793

1794

1795